Broadband view of blast wave physics : a study of gamma-ray burst afterglows

van der Horst, A.J.

Publication date
2007

Document Version
Final published version

Citation for published version (APA):
van der Horst, A. J. (2007). *Broadband view of blast wave physics : a study of gamma-ray burst afterglows*. [Thesis, fully internal, Universiteit van Amsterdam].

Broadband View of Blast Wave Physics
A Study of Gamma-Ray Burst Afterglows

Broadband View of Blast Wave Physics
A Study of Gamma-Ray Burst Afterglows

Academisch Proefschrift

Ter verkrijging van de graad van doctor
aan de Universiteit van Amsterdam
op gezag van de Rector Magnificus prof. dr. J.W. Zwemmer
ten overstaan van een door het college voor promoties ingestelde commissie,
in het openbaar te verdedigen in de Aula der Universiteit

op

vrijdag 7 september 2007, te 12:00 uur

door

Alexander Jonathan van der Horst

geboren te Singapore, Singapore

Promotiecommissie

Promotor	Prof. Dr. R.A.M.J. Wijers
Overige leden	Prof. Dr. E.P.J. van den Heuvel Prof. Dr. L.B.F.M. Waters Prof. Dr. R. Strom Prof. Dr. L. Kaper Dr. L.J. van den Horn Dr. C. Kouveliotou

Faculteit der Natuurwetenschappen, Wiskunde en Informatica
Universiteit van Amsterdam

Voor Mama

Contents

1

Introduction

Gamma-Ray Bursts (GRBs) are short flashes of gamma rays, typically lasting tens of seconds, but actually spanning a range of durations from less than one tenth up to hundreds of seconds. They are extraordinarily powerful phenomena, with extreme observed brightnesses in gamma rays. Since their discovery in 1967 the origin of these events was unknown for three decades. The discovery in 1997 of their counterparts at X-ray, optical and radio wavelengths, the so-called afterglow, made it possible to reveal the nature of these enigmatic phenomena. GRBs are thought to be products of the formation of compact objects and are laboratories for studying ultra-relativistic outflows. The ultra-relativistic shock waves, also known as blast waves, that are formed when these outflows interact with the medium surrounding the GRB progenitor, are the main topic of this thesis. Modeling of GRB blast waves and comparing the models with broadband observations of GRBs and their afterglows, provide a wealth of information on GRB progenitors, their surroundings, the physics of relativistic flows and shock waves, and particle acceleration and the formation of magnetic fields in astrophysical objects. In this introduction I give an overview of the most relevant observational facts about GRBs and their afterglows, and discuss the standard models for GRB progenitors and afterglow physics. I will conclude with a summary of the work presented in this thesis on the multi-wavelength study of (GRB) blast waves.

1.1 The discovery of gamma-ray bursts and the afterglow revolution

GRBs were discovered with the Vela satellites (Klebesadel et al. 1973), which were US military satellites used in the Cold War to verify that no country would carry out nuclear tests in the upper atmosphere or in space. They found flashes of gamma rays, not coming from the Earth's atmosphere or spacecraft, but from extraterrestrial sources. The existence of GRBs originating from supernovae, the collapse of massive stars at the end of their lives, was already predicted by Colgate (1968). This hypothesis could not be tested, because the localisation accuracy of the gamma-ray satellites in those days was not good enough to identify GRB counterparts (quiescent or transient) at longer wavelengths. The crucial missing parameter was the distance: were GRBs explosions in our own Milky Way, or even in our own solar system, or did they have a cosmological origin? Because of the lack of knowledge of the distance, a myriad of theoretical models was developed; there were basically as many models as there were GRBs.

The situation changed dramatically in the early 1990s, when the Burst And Transient Source Experiment (BATSE) on board the Compton Gamma-Ray Observatory showed that GRBs have an isotropic sky distribution. This ruled out the models that placed GRBs in our solar system or in the disk of our Galaxy. It was still possible that GRBs originated from the halo of our Galaxy (Lamb 1995) or that they had a cosmological origin (Paczyński 1995). Further indications on the distance came when BATSE showed that the cumulative peak flux distribution deviated from a power-law with index -3/2 due to a lack of relatively faint bursts, which points to a cosmological origin of GRBs (Meegan et al. 1992).

The final solution to the distance debate came with the discovery of the first afterglow. On the 28th of February 1997 the Wide-Field Cameras on board the Italian-Dutch X-ray satellite BeppoSAX obtained their first quickly available accurate position of a GRB. The optical afterglow of this GRB 970228 (the nomenclature for GRBs is GRB YYMMDD, with YY=year, MM=month, and DD=date), was found with the William Herschel Telescope (WHT) and the Isaac Newton Telescope (INT) on La Palma (Van Paradijs et al. 1997). At the same time, the soft X-ray afterglow was discovered with the Narrow-Field Instruments of BeppoSAX (Costa et al. 1997). The light curve of this GRB showed a steep power-law decay. This clarified that observations had to be performed very quickly in order to find a counterpart to a GRB in other wave bands. The next GRB afterglow was discovered on May 8 in that same year, GRB 970508, for which a radio counterpart was found for the first time (Frail et al. 1997a). Taking spectra of this GRB 970508 with the Keck telescope, Metzger et al. (1997) identified absorption lines which pinpointed the event at $z = 0.835$, i.e. 10^{10} light years away. After 30 years of GRB studies, this settled the distance controversy: GRBs originate at cosmological distances. Knowing this, the observations revealed that they are by far the most luminous sources of photons in the Universe, and GRB research entered a new era.

1.2 Gamma-ray burst progenitors

Besides the important role that BATSE played in the distance debate, the large sample of more than 2700 GRBs that BATSE observed was also crucial in the

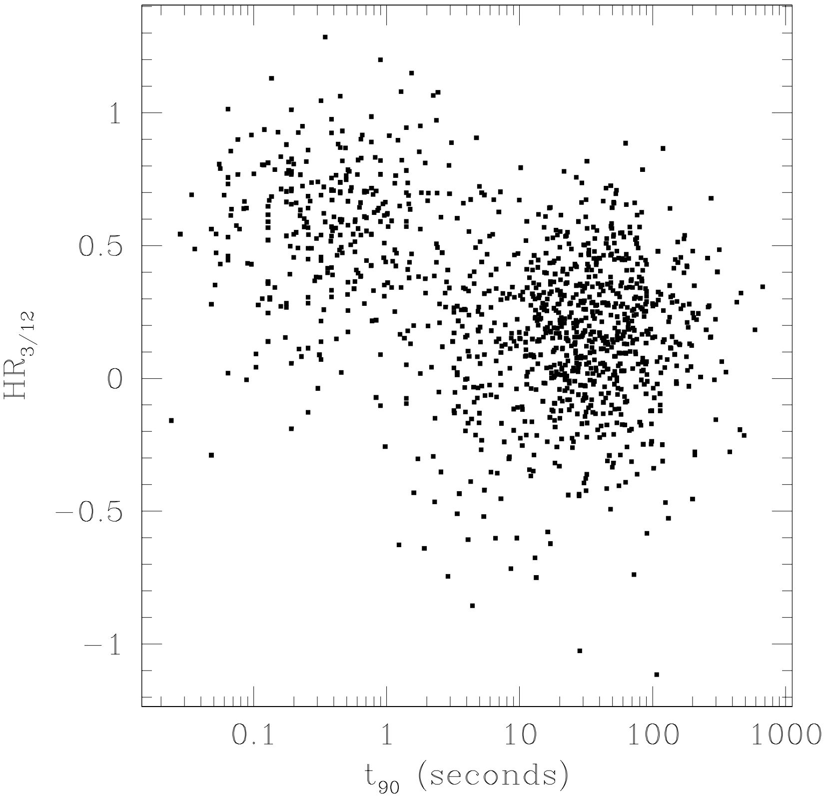

Figure 1.1 — The hardness ratio of GRBs detected by BATSE, versus their duration (Kouveliotou et al. 1993). There is clear evidence for two separate classes of burst: long-soft and short-hard GRBs.

debate on GRB progenitors. BATSE showed that the distribution of GRBs in temporal and spectral properties is bimodal (Kouveliotou et al. 1993). The total population of GRBs can be divided into two classes: long-soft bursts and short-hard bursts (see Figure 1.1). The long-soft bursts, or long GRBs, have durations larger than roughly 2 seconds, while the duration of the short-hard bursts, or short GRBs, is shorter than that; the short GRBs show a higher peak energy in their spectrum than long GRBs, i.e. they are harder. Both long and short GRBs show the isotropic sky distribution discovered by BATSE, but their different temporal and spectral properties indicate that they have different progenitors. There have been statistical studies suggesting that there is even a third, intermediate, class of GRBs (Horváth 1998); the existence of this third class is, however, under debate.

In the first eight years of afterglow research, afterglows were only detected for long GRBs. Photometric and spectroscopic observations of afterglows and their host galaxies, provided a plethora of clues on the origin of this class of GRBs. Two years ago the Swift satellite discovered the afterglow of a short burst for the first time (Gehrels et al. 2005). More detections of short GRB afterglows and studies of their immediate environment, showed that the two classes of GRBs do not only differ in the properties of their prompt gamma-ray emission, but also in their afterglow emission and host galaxy properties. This confirmed the idea that long and short GRBs originate from different progenitors: long GRBs are formed by the collapse of massive stars at the end of their lives, while there are a few possible origins of short GRBs, among which the merger of two compact objects is the most popular one.

1.2.1 Long gamma-ray bursts

The first indication of what the origin of long GRBs is, came with the discovery of supernova SN 1998bw at the same position where GRB 980425 had gone off (Galama et al. 1998b). There was apparently a connection between supernovae and GRBs, but since this object resided at a redshift of 0.0085, while all the other GRBs had redshifts of at least 0.1, this could still be some odd-ball phenomenon, and not representative for the total GRB population. There was, however, more evidence for the GRB-supernova connection: GRBs that were close by enough, i.e. with redshifts below 0.5, showed a small bump in their late-time optical afterglow light curves (e.g. Bloom et al. 1999; Galama et al. 2000), the so-called supernova-bump. Furthermore, the long GRBs were found to have blue host galaxies, that are actively forming stars and have a large population of young and massive stars. The definitive answer came with the discovery of GRB 030329 and its associated supernova SN 2003dh (Hjorth et al. 2003; Stanek et al. 2003). This was one of the brightest GRB afterglows ever, and when the optical afterglow had faded enough, the supernova signature became visible, not only in the light curve, but more importantly in the spectra. In optical spectra of the afterglow a supernova Type Ib/c spectrum emerged after a few days, which became more pronounced in the following weeks (see Figure 1.2). The resemblance of these supernova spectra with the spectra of SN 1998bw was remarkable, making this the conclusive evidence for the GRB-supernova connection: the prediction of Colgate (1968) had come true.

In the early 1990s a detailed model of the death of a rapidly rotating, massive star had been constructed by Woosley (1993). In the collapsar model, as it was called, a GRB accompanied by a supernova was produced in the collapse of a massive stellar core into a central compact object. This compact object is

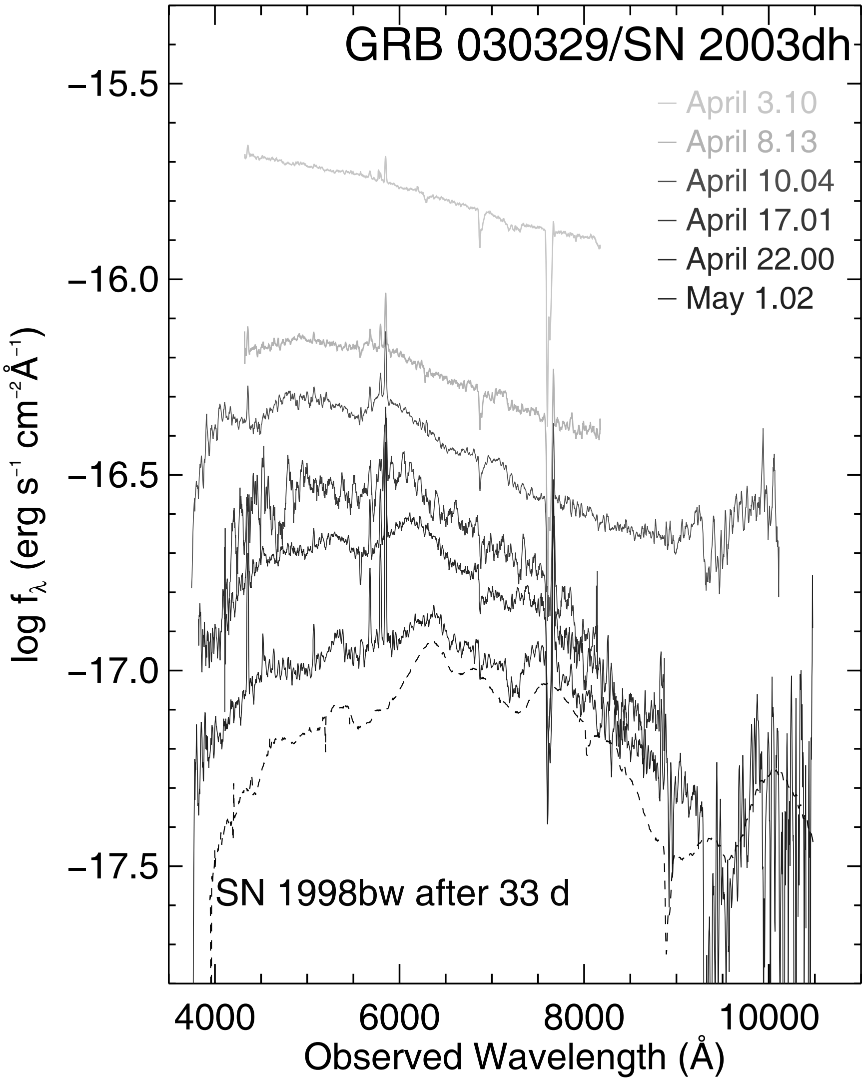

Figure 1.2 — The optical spectra of GRB 030329 / SN 2003dh at various epochs (Hjorth et al. 2003). The upper spectrum is well fitted by a power-law, as is expected for GRB afterglows. Later spectra show deviations from this power-law and resemble the spectrum of the very energetic Type Ic supernova 1998bw. These supernova signatures in the afterglow spectrum of GRB 030329 provide conclusive evidence for the connection between GRBs and supernovae, and support the collapsar model for the long GRBs.

generally considered to be a black hole, although it has been suggested that at first a super-massive rapidly rotating neutron star is formed, which collapses to a black hole after it has lost the angular momentum it needs to support the mass against gravity. In both cases the end-product of the collapse is a black hole and a torus of stellar material surrounding it, which produce a collimated outflow, the jet, which is the source of the GRB. The fact that the jet has to escape the stellar envelope puts constraints on the massive star: the star must have undergone severe mass loss by means of a stellar wind, e.g. a Wolf-Rayet star. Spectroscopic evidence of Wolf-Rayet wind characteristics has been found in afterglow observations.

After GRB 980425 and GRB 030329 there have been two more GRBs with a spectroscopically identified supernova associated with them: GRB 031203 with SN 2003lw and GRB 060218 with SN 2006aj. The four supernovae have similar spectra, all of them are Type Ib/c, and also their energetics are comparable: the range of total energy in the four supernovae spans at most a factor of 10: 10^{51} – 10^{52} erg. Their optical luminosities at the peak are much brighter than average Type Ib/c supernovae (see Figure 1.3). Although these four supernovae are quite similar, their associated GRBs are completely different (see e.g. Kaneko et al. 2007). GRB 980425 had an isotropic equivalent prompt emission energy that is four orders of magnitude lower than the typical values obtained for GRBs, of the order of 10^{52} erg. For this burst an afterglow was actually not found: all the emission, except for the prompt gamma-ray emission, came from the supernova. The gamma-ray energetics of GRB 060218 was somewhat comparable to GRB 980425, and the optical afterglow was completely masked by the optical light from the supernova. The X-ray and radio afterglow were, however, detected in the case of GRB 060218. GRB 030329 showed a completely different picture: the supernova light was in this case masked by the extreme optical brightness of the GRB afterglow, and was only detected spectroscopically in the GRB optical light curve. The gamma-ray energy of GRB 030329 was at the low end of the typical GRB range, but much higher than the other three. The energy release of GRB 031203 was in between GRB 980425 and typical GRB values. A comparison of the energetics of these four particular GRBs with other GRBs is shown in Figure 1.3.

The comparison of these four GRBs and their associated supernovae shows that the energetics of the supernovae show a much smaller scatter than those of the GRBs. This indicates that the energy released inside the progenitor star is roughly standard, while the fraction of that energy that ends up in the GRB jet outside the star can vary dramatically between different events. Just after this picture was established, two nearby long GRBs were discovered which both

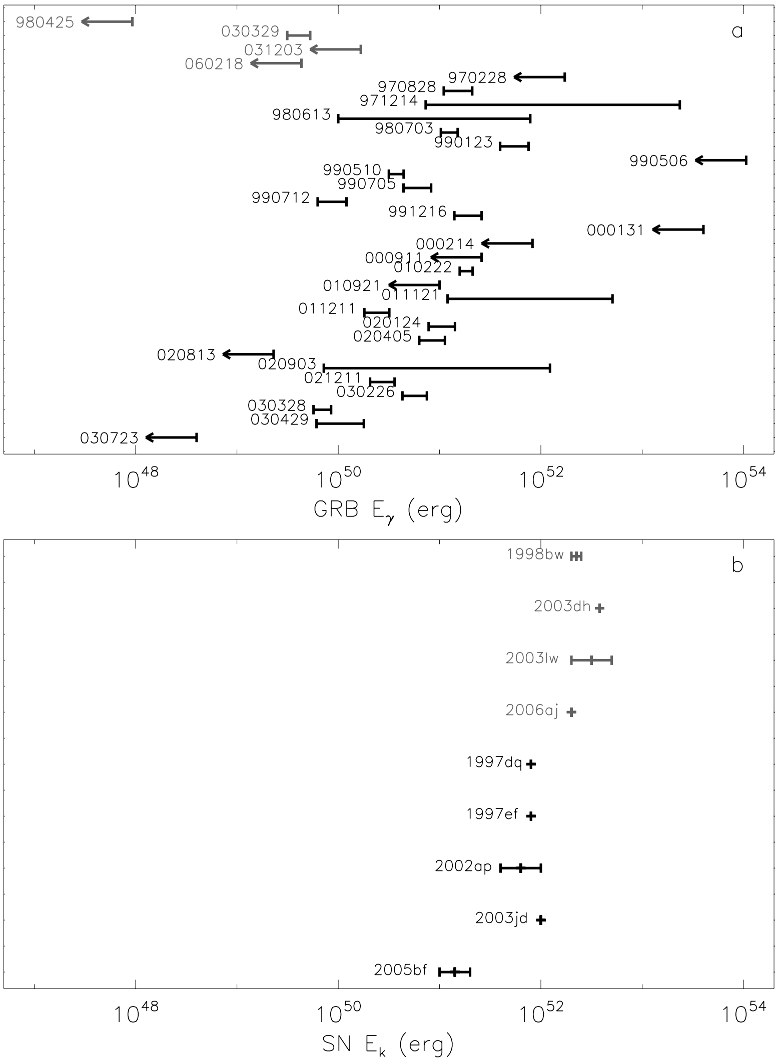

Figure 1.3 — *Top panel* Comparison of the collimation corrected energy in the prompt emission of the four GRBs with spectroscopically identified supernovae and other GRBs. *Bottom panel* Comparison of the supernova kinetic energy of these four GRB supernovae and other supernovae of the same Type Ib/c. The figure shows that the energetics of the supernovae show a much smaller scatter than those of the GRBs, indicating that the energy released inside the progenitor star is roughly standard, while the fraction of that energy that ends up in the GRB jet outside the star can vary dramatically between different events (Kaneko et al. 2007).

showed no evidence of an associated supernova: GRB 060505 and GRB 060614 (Fynbo et al. 2006b), with redshifts of 0.089 and 0.125 respectively. The lack of supernova emission in these bursts indicated that if they had an associated supernovae, the peak luminosity had to be at least 10^2 times smaller than the one of GRB 980425. This has shed a new light upon the GRB-supernova connection, in particular the question has risen whether all long GRBs are really coming from the collapse of a massive star. Host galaxy studies for these two GRBs have shown that their environment is similar to typical long GRB host galaxies (Thoene et al. 2007), hinting at a massive stellar progenitor. Some kind of failed supernova can be accommodated within the collapsar model, but if that is so then these two GRBs show that caution is needed when making statements about the lack of supernova emission and the possible progenitors of a given GRB.

1.2.2 Short gamma-ray bursts

Much less is known about the progenitors of short GRBs than those of long GRBs. Because there is such a clear distinction in their temporal and spectral characteristics, it has been widely adopted that they have different origins. The discovery of the first X-ray afterglow with the Swift satellite of a short GRB, GRB 050509B, showed that this GRB is most probably associated with a giant elliptical galaxy, in which hardly any star formation is still present, see Figure 1.4 (Gehrels et al. 2005). After this one, more short GRB afterglows have been found, also at optical and radio wavelengths (e.g. Fox et al. 2005; Hjorth et al. 2005; Berger et al. 2005b). Optical observations of their environments show that there is a wide variety of host galaxies for short GRBs: old galaxies without any significant star formation, and young galaxies similar to those found for long GRBs. Short GRBs found in the latter host galaxies might be explained by the collapsar model, but a model with a binary merger of two compact objects, neutron star-neutron star or neutron star-black hole, is the most favoured one. In this binary merger model, the GRB is expected to often occur far from the place of birth of the binary, since the supernova explosions, that made the compact objects, will give kick velocities that move the binary away from its place of birth, maybe even outside of its host galaxy given the timescale for the merger process, 10^5 – 10^{10} years.

The fact that a significant fraction of short GRBs is found in the outskirts of their host galaxies, or even entirely outside them, but in any event not in the star-forming region where they were born, means that the immediate environment of short GRBs on average has a lower density than that of long GRBs (Nakar 2007). The ambient medium density has a significant influence on the brightness of the afterglow: a lower ambient density causes a fainter afterglow. This, together

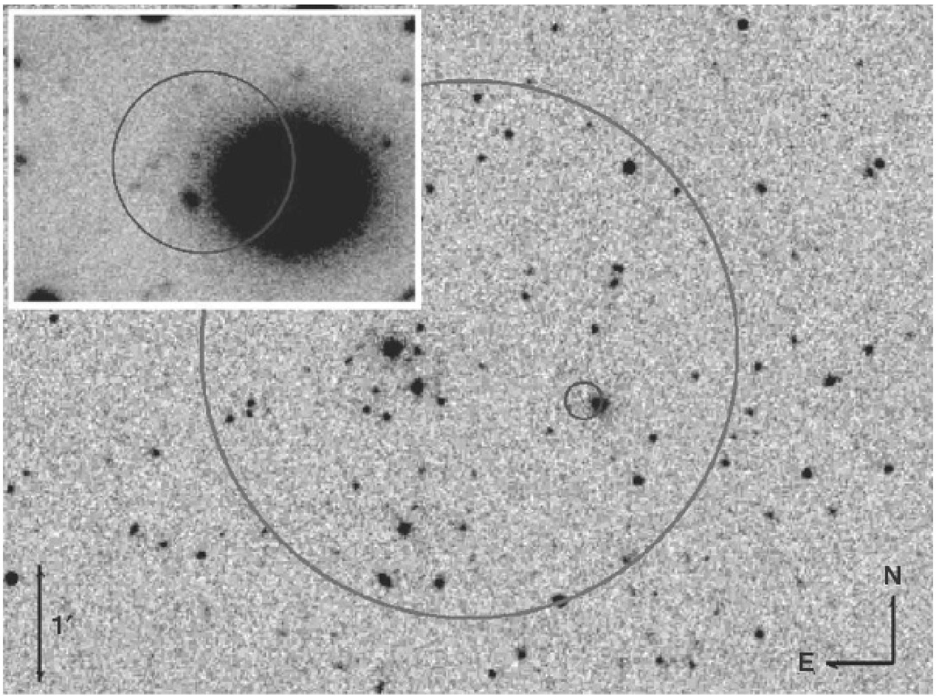

Figure 1.4 — The Digitized Sky Survey image of the field of GRB 050509B, the first short GRB with an X-ray afterglow. The large circle is the Swift Burst Alert Telescope (BAT) position error circle, and the smaller circle is the Swift X-Ray Telescope (XRT) position error circle (Gehrels et al. 2005). The inset shows a blow-up of the region of the XRT error circle from an R-band image obtained with the Very Large Telescope in Chili. The luminous elliptical galaxy to the right (west) is the likely host galaxy of this GRB.

with the fact that the typical energies of short GRBs are lower than the energies of long GRBs (Berger 2007), makes the afterglows of short GRBs fainter than the long GRB afterglows, and thus harder to detect. For instance, while it is already hard to detect radio afterglows of long GRBs because of their faintness, there have only been two short GRBs for which there has been a radio afterglow detection (Berger et al. 2005b; Soderberg et al. 2006). So, to obtain a better understanding of the progenitors of short GRBs, we have to observe many more of them, and possibly wait for the short GRB equivalent of the Rosetta stone that GRB 030329 was for long GRBs.

1.3 Broadband afterglow physics

After the burst in gamma rays, the afterglow of a GRB is observed at wavelengths ranging from hard X rays to radio waves spanning 9 orders of magnitude in frequency range, i.e. from 10^{18} Hz down to 10^{9} Hz. From modeling the afterglow emission over this extremely broad spectral range, the emission mechanisms and physics of the afterglow can be explored. This modeling results in a clear picture of the physics of the jet and its immediate environment, and addresses fundamental physical issues on, for example, particle acceleration. To perform studies of this kind, the blast wave model is the standard model in GRB afterglow physics.

1.3.1 Blast wave model

The gamma-ray prompt emission spectrum is non-thermal and indicates that the observed emission emerges from an optically thin region. The large distances for cosmological GRBs imply that the bursts release a large amount of energy in gamma rays of the order of $\sim 10^{52}$ erg. Given the finite speed of light, the millisecond variability observed in the prompt emission implies a compact source with a radius of the order of 1000 km. These two observational facts show that the source of radiation must be extremely optically thick to pair creation. Such a source should emit a blackbody form of radiation, whereas the observed spectra are non-thermal. This contradiction is known as the compactness problem. This problem can be overcome by assuming that the source is moving ultra-relativistically towards us. This has led to the so-called relativistic fireball model, first proposed by Cavallo & Rees (1978) and Rees & Mészáros (1992). Because of relativistic effects the size of the source is a factor of two times the Lorentz factor squared larger than the compact size inferred from the millisecond variability. The Lorentz factors involved are > 100, so the real size of the source would then be $10^{8} - 10^{10}$ km. Observed durations of the burst vary from $1 - 100$ seconds. These durations are of the order of days or even years at the source, because of the same relativistic effects.

According to the fireball model decelerating relativistic ejecta produce the GRB and its afterglow (see Figure 1.5). In this model the central source produces a relativistic outflow. Since the opacity is very high, this inner engine is hidden and can not be observed directly. This makes it difficult to constrain GRB models and leaves only circumstantial evidence on the nature of the sources. The energy from the central source is transported relativistically to distances larger than 10^{11} km, where the system becomes optically thin. The fireball is believed to be contaminated with baryons and a conversion of radiation energy into ki-

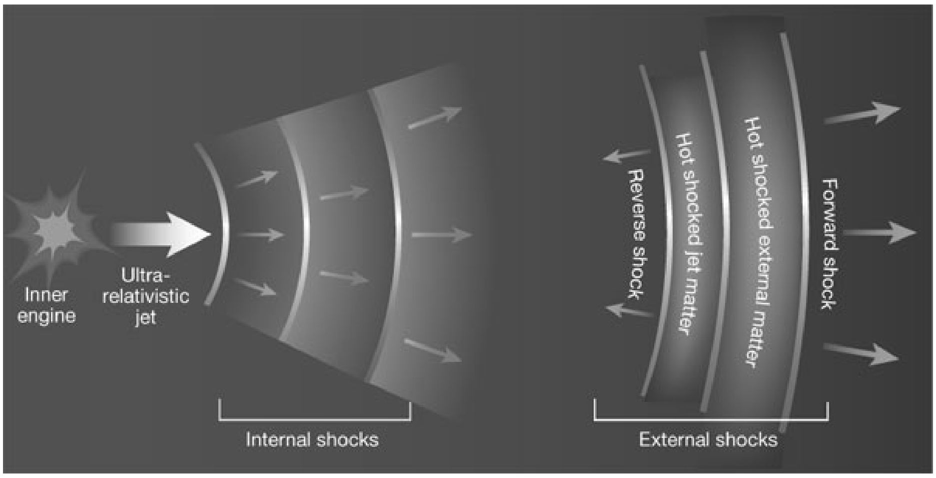

Figure 1.5 — Schematic view (Piran 2003) of the blast wave model for GRB afterglows. In this model the central source produces a relativistic outflow. If this central source is active for some time, shells with different Lorentz factors can be produced. Collisions between these shells, the so-called internal shocks, are generally assumed to power the GRB itself. The relativistic external shock, the blast wave, causes the GRB afterglow. When the external forward shock is formed, a reverse shock is also produced moving back into the ejecta, which can produce bright optical flashes minutes after the burst.

netic energy takes place. If the inner engine is active for some time, shells with different Lorentz factors can be produced. Collisions between these shells, the so-called internal shocks, are generally assumed to power the GRB itself. After the acceleration phase the fireball continues in a coasting phase with constant Lorentz factor.

At the front of the jet a relativistic external shock is present, the blast wave, that decelerates because it is ploughing its way through the ambient medium. This can be the interstellar medium, or the dense stellar wind produced by the progenitor of the GRB in the case of long GRBs. The dynamics of the blast wave is described by the solutions of Blandford & McKee (1976). These blast waves cause the GRB afterglows, and are the relativistic analogues of supernova remnants. Magnetic fields cause the swept-up electrons to produce synchrotron radiation. When the external forward shock is formed, a reverse shock is also produced moving back into the ejecta. This reverse shock can produce a bright optical flash minutes after the burst. The brightness of the reverse shock emission decays very rapidly, after which the forward shock dominates. Since the shock decelerates while it is sweeping up mass, the blast wave will become sub-relativistic and eventually even non-relativistic. From that point on the dynamics of the blast wave follows the Sedov-Taylor solutions, similar to supernova remnants. Although the blast wave emission is very well studied, the properties of the initial fireball and its energy source are very uncertain, because there are few observational clues to its nature. Therefore, when describing the modeling of afterglows, it is more appropriate to refer to the blast wave model instead of the fireball model.

1.3.2 Broadband modeling of relativistic blast waves

In general, observations of GRBs and their afterglows are in good agreement with the blast wave model (e.g. Wijers et al. 1997; Wijers & Galama 1999; Granot et al. 1999b). Light curves at various wavelengths have been obtained for many afterglows, and from these light curves, broadband spectral energy distributions (SEDs) have been constructed. Synchrotron radiation turns out to be the dominant radiation mechanism producing the afterglow SEDs, which can be derived from the broken power-law shape of the SEDs. The relativistic electrons are accelerated by the blast wave to a power-law energy distribution with index p and a cut-off energy at the low end. An afterglow SED can be characterised by the peak flux and three break frequencies (e.g. Sari et al. 1998): the peak frequency ν_m, that corresponds to the cut-off energy in the electron energy distribution; the cooling frequency ν_c, caused by the fact that some electrons have such high energies that their cooling time scale is shorter than the dynamical time scale of the source; and the self-absorption frequency ν_a, corresponding to the absorption and stimulated emission by electrons affecting the synchrotron photons. The values of the peak flux and the break frequencies evolve in time, because the dynamics of the blast wave changes in time. This, in turn, determines the evolution of the SEDs with time, i.e. gives the light curves at all observing frequencies. These light curves can, like the SEDs, be described as broken power-laws, because the break frequencies and peak flux evolve as power-laws in time.

Depending on the ordering of the break frequencies in the SED, the SED can have various shapes. In practice, there are three possible orderings observed: $\nu_\mathrm{a} < \nu_\mathrm{c} < \nu_\mathrm{m}$, $\nu_\mathrm{a} < \nu_\mathrm{m} < \nu_\mathrm{c}$, and $\nu_\mathrm{m} < \nu_\mathrm{a} < \nu_\mathrm{c}$ (see Figure 1.6). In the first case the cooling frequency lies below the peak frequency, which means that all the electrons lose a significant fraction of their energy rapidly, and this situation is called fast cooling. This is only observed, if observed at all, at very early times. In the other two cases the cooling frequency lies above the peak frequency, which means that the largest fraction of electrons hardly lose any energy by synchrotron cooling (if $p > 2$), and this is called slow cooling. The two slow cooling cases are different in ordering of the peak frequency and the self-absorption frequency.

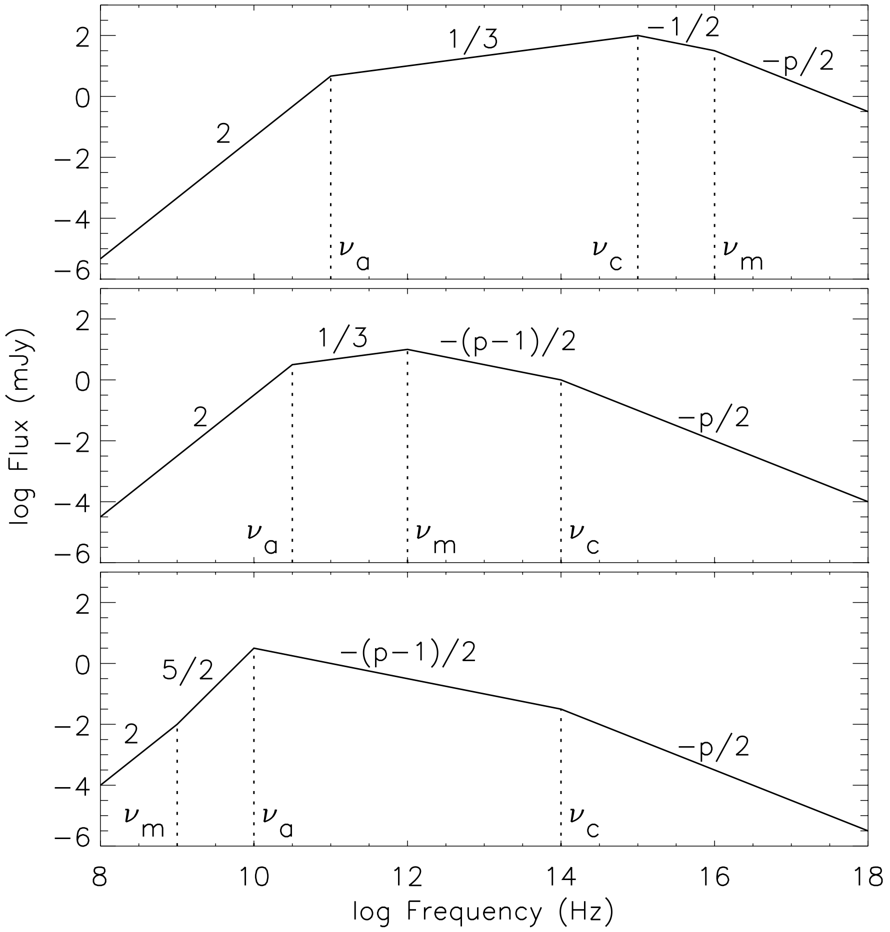

Figure 1.6 — Schematic log-log spectral energy distributions (SEDs) which are typically observed in GRB afterglows. The dominant emission mechanism is synchrotron radiation, caused by relativistic electrons which are accelerated by a relativistic blast wave. The SEDs are determined by the peak flux and three break frequencies: the peak frequency ν_{m}, the cooling frequency ν_{c}, and the synchrotron self-absorption frequency ν_{a}. Some of the slopes are determined by the power-law index p of the electron energy distribution. The shape of the SEDs depends on the ordering of the three break frequencies. Because of the temporal behaviour of the break frequencies, there are in practice three possible orderings observed: $\nu_{\mathrm{a}} < \nu_{\mathrm{c}} < \nu_{\mathrm{m}}$ (top panel; fast cooling regime; observed $\sim$ 1 hour after the burst), $\nu_{\mathrm{a}} < \nu_{\mathrm{m}} < \nu_{\mathrm{c}}$ (middle panel; slow cooling regime; $\sim$ 1 day after the burst), and $\nu_{\mathrm{m}} < \nu_{\mathrm{a}} < \nu_{\mathrm{c}}$ (bottom panel; slow cooling regime; $\sim$ 1 month after the burst).

In the situation with $\nu_\mathrm{m} < \nu_\mathrm{a}$ the peak of the SED is actually the self-absorption frequency, which can only be observed at radio frequencies at very late times, i.e. on time scales of weeks to months after the burst. From the SEDs and light curves the evolution of the break frequencies and peak flux can be deduced, and from them the physical parameters of the blast wave and its surroundings can be determined, e.g. the blast wave kinetic energy, the density and structure of the circumburst medium, the fractional energy density of the blast wave in electrons and magnetic field, and the power-law index of the electron energy distribution. From some extra light curve information the opening angle of the jet can also be determined.

1.3.3 Jets and energetics

As outlined in Section 1.2, the energetics of GRBs and their afterglows is an important issue. From gamma-ray spectral analysis the energetics of the prompt emission can be determined, provided that the peak of the spectrum is known. The kinetic energy of the blast wave can be determined from broadband modeling of the afterglow emission. The observed fluences, combined with the cosmological distance to GRBs, imply an enormous energy output, in both the prompt and afterglow emission, up to 10^{54} erg for some GRBs, assuming that the emission is isotropic. This is an extreme energy to be produced by a compact object, challenging all GRB progenitor models, but can be overcome by assuming that the outflow is not spherical but collimated, which may reduce the energy output by a factor of $10^2 - 10^3$. Observational evidence for such a collimated outflow, or jet, is the presence of an achromatic break in the light curves of several GRB afterglows. When observing the outflow roughly along the jet axis, the GRB at first appears to be isotropic, due to the ultra-relativistic motion that causes the emission to be beamed in the forward direction. The opening angle of this relativistic beaming is of the order one over the Lorentz factor. As the collimated blast wave decelerates, the Lorentz factor becomes smaller, and at some time the beaming angle becomes larger than the physical opening angle of the outflow. From that time on an observer will start to see past the edge of the jet and thus receive less flux compared to the isotropic case, which causes a steepening of the light curves. The jet break is achromatic because the change is observed at all frequencies at the same time, in contrast with the passage of a break frequency through one of the observing bands, which is chromatic.

At the jet break time there is another dynamical effect that becomes important: because the bulk velocity of the outflow has decreased to the local sound speed, the sideways expansion becomes significant. It is, however, not clear whether the velocity of this sideways expansion is roughly the velocity of light

(Rhoads 1997, 1999) or a small fraction of that (Granot 2007). In both cases the blast wave becomes non-relativistic at some point. In the first case the blast wave is (quasi-)spherical at the time that it becomes non-relativistic, and from that moment on the evolution of the blast wave follows the Sedov-Taylor solutions. In the second case, when the blast wave becomes non-relativistic, it has roughly the same opening angle as it had at the jet break time, so it first has to spread sideways, being non-relativistic, before the blast wave follows the Sedov-Taylor solutions.

Correcting the isotropic equivalent energies of the prompt emission and afterglow for the collimation effect gives energies for different bursts in the range of 10^{50} to a few times 10^{51} erg (Frail et al. 2001), which can be much more easily accommodated in GRB progenitor models. An independent measurement of the kinetic energy of the blast wave can be obtained from late time radio observations, on time scales of months to years, when the blast wave is non-relativistic (Frail et al. 2000b), and thus no collimation or beaming effects are in play anymore, and the afterglow cannot be detected anymore at optical or X-ray frequencies. This can only be done for a few GRBs that have bright enough radio afterglows. Since the cooling frequency is not in the radio regime, and thus we miss a piece of information in constructing the full SED, certain assumptions have to be made about the equipartition of energy between the electrons and the magnetic field. Making such assumptions, energies have been found that are comparable to or a bit higher than the energies from the analysis of the blast wave in the relativistic phase.

An important issue in the analysis of GRB jet phenomena is the sideways structure of the jet. In most studies the energy is assumed to be homogeneously distributed over the jet surface, but other possibilities have also been proposed, in which the energy per solid angle along the jet axis is larger than what is emitted off-axis, or the other way around, while the Lorentz factor off-axis has a lower value than along the jet axis. The light curves of these different configurations are very similar to each other, with only small differences in the smoothness of the jet break. The polarization curves, on the other hand, are different, especially around the jet break time (e.g. Sari 1999; Rossi et al. 2004). The polarization levels are unfortunately only a few percent, making it difficult to obtain polarization curves good enough to distinguish between the various models.

1.3.4 Shock physics lab

Broadband modeling of GRB afterglows enables us to perform physics experiments under extreme conditions in the Universe. As is usual in astrophysics, but in contrast with physics experiments on Earth, we cannot control the experiments ourselves. We may, however, learn a lot about relativistic particle acceleration and the generation of magnetic fields. The three micro-physical parameters that are relevant in this context are the fractional energy densities of the blast wave in electrons and magnetic field, $\varepsilon_{\rm e}$ and $\varepsilon_{\rm B}$ respectively, and the power-law index p of the electron energy distribution. The fractional energy in the electrons is usually found to be $\varepsilon_{\rm e} \sim 0.1$, while the values for $\varepsilon_{\rm B}$ range from the same value down to 10^{-4}. The latter is not really well constrained, and is due to the large uncertainties in magnetic field generation mechanisms, but also due to some preconceived opinions on what the other physical parameter should be. This is caused by the fact that there are not many GRB afterglows that are well-sampled both temporally and spectrally, in order to draw firm conclusions about the precise values of the physical parameters. In many afterglow studies one or more of the observing bands is lacking, which then usually leads to the conclusion that most of the parameters are consistent with the typical parameters, and $\varepsilon_{\rm B}$ is then the parameter that is moved around in parameter space to make all the available observations fit the models.

The origin of the magnetic fields in the blast wave is quite uncertain. They have been attributed to some turbulent dynamo mechanism behind the shock front, a two-stream instability of the relativistic plasma (Usov 1994), or the presence of an intrinsically magnetized ambient medium (Königl & Granot 2002). A big issue is not only generating these magnetic fields, but also retaining them across the whole emitting region. A different important issue is the particle acceleration mechanism. The widely accepted mechanism is that particles are accelerated via repeatedly crossing the shock front, and in that way obtain a power-law energy distribution through the Fermi-acceleration mechanism. Values of $\varepsilon_{\rm e}$ and p can give us information on those mechanisms. Important to note in this respect is that, if the micro-physics is the same from burst to burst, the micro-physical parameters should also be the same, or at least similar. As already mentioned, this is not the case for $\varepsilon_{\rm B}$, although there are quite a number of uncertainties in the derived values. The electron energy distribution index p has a large range of derived values, $\sim 1.5 - 3$, from spectral and temporal slopes at X-ray and optical frequencies. This large range in p can be obtained from particle acceleration simulations (Baring 2004), although a large fraction of the GRB community favours the idea of a universal value of $2.2 - 2.3$ coming from different simulations with more stringent assumptions (Achterberg et al. 2001).

1.3.5 Circumburst medium

The circumburst medium can in general be very complex in nature. Since typically the blast wave traverses a fairly small range in radii during its observable

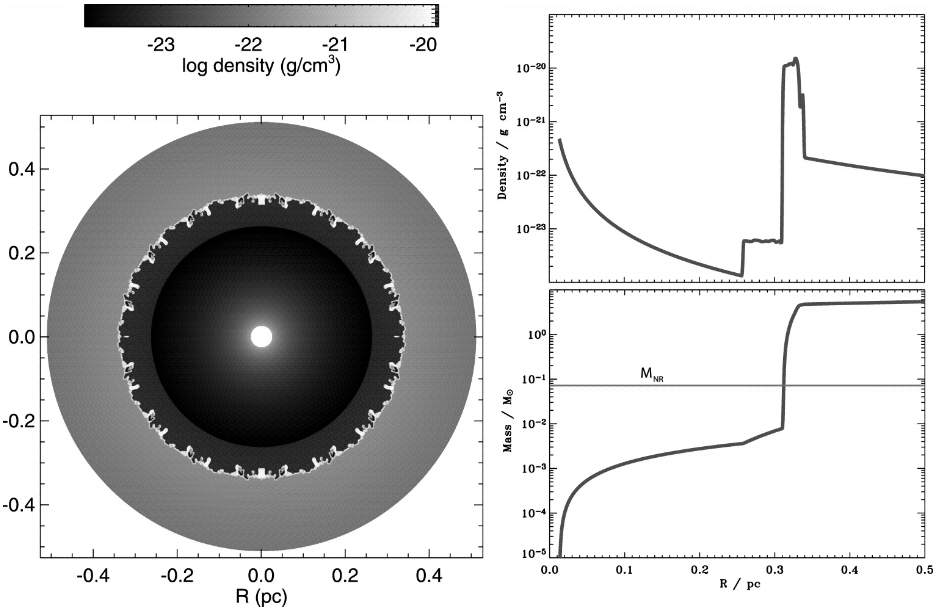

Figure 1.7 — State of the circumstellar medium around a massive star in the W-R phase (Ramirez-Ruiz et al. 2005). *Left:* Logarithm of the circumstellar density around the massive star. *Right:* Density and cumulative mass as a function of radius along the polar axis. These simulations show that interactions of the wind with the ISM can alter the structure of the wind, in particular in the region where the blast wave resides in the afterglow phase, i.e. 10^{16} – 10^{18} cm $\simeq$ 0.003 – 0.3 parsec from the center. The exact position of the transition between the unshocked stellar wind and the shocked wind depends on the density of the wind and the ISM. Determining the circumburst medium structure from afterglow modeling therefore gives important clues about the progenitor and environment of GRBs.

phase, it is customary to approximate the density structure in that region as a power-law of the radius of the blast wave. The structure of the medium is usually assumed to be either homogeneous or structured like a stellar wind, i.e. the density is inversely proportional to the radius of the blast wave squared. In early modeling efforts the ambient medium was assumed to be the interstellar medium (ISM), which is homogeneous (Wijers & Galama 1999; Granot et al. 1999b). When the first clues came that, in the case of long GRBs, we are dealing with massive stars that have lost a significant fraction of their mass through a stellar wind, the possibility of a stellar wind like environment of the blast wave was also considered (Chevalier & Li 1999). For some afterglows a homogeneous ambient medium seemed to be the best way to fit the observations (Panaitescu & Kumar 2002). In these cases, particle number densities varying from 0.01 to

10 cm^{-3} were derived. For those afterglows that showed the characteristics of a wind-like medium, ratios of the mass-loss rate and the terminal wind velocity could be derived, which are consistent with mass-loss rates of 10^{-6} solar masses per year and terminal wind velocities of 10^3 km/s.

Although we now know that long GRBs originate in massive stars, we do not necessarily need to derive a stellar wind medium from the afterglow modeling. Interactions of the wind with the ISM can alter the structure of the wind, in particular in the region where the blast wave resides in the afterglow phase, i.e. 10^{16} – 10^{18} cm from the center, see Figure 1.7 (Wijers 2001; Ramirez-Ruiz et al. 2001, 2005). At the point where the wind meets the ISM a shock moving forward in the ISM is formed, but more importantly also a reverse shock going back into the wind. This reverse shock changes the wind medium structure such that it becomes homogeneous. For typical wind and ISM parameters, the blast wave may be outside or inside the reverse shock during the period we observe the afterglow. There are, however, some uncertainties in the exact position of the transition between the unshocked stellar wind and the shocked wind, which depends on the density of the wind and the ISM. Therefore, determining the circumburst medium density and its structure gives important clues about the progenitor and environment of GRBs.

1.4 Afterglows in the Swift era

The Swift satellite was built to primarily observe GRBs at gamma-ray, X-ray, and ultraviolet and optical frequencies. The fast slewing capabilities and wide spectral range covered, make Swift the perfect satellite to bridge the gap between the prompt emission and the afterglow. Before the launch of Swift there was usually a gap of a few hours between the prompt emission and the first observations of the afterglow. Early-time observations with robotic optical telescopes in the pre-Swift era showed some spectacular optical flashes in the first minutes after the burst (e.g. Akerlof et al. 1999), sometimes also accompanied by a radio flare at $\sim$ 1 day (Kulkarni et al. 1999). Swift was expected to observe many of these optical flashes, but this turned out not to be the case. What Swift did provide was a plethora of extremely well-sampled X-ray light curves, often overlapping with the gamma-ray emission. These light curves showed all kinds of unexpected behaviour.

Figure 1.8 shows the canonical X-ray light curve (Nousek et al. 2006; Zhang et al. 2006) observed by the Swift X-Ray Telescope (XRT). The light curve shows the following characteristics: an initial very steep decay, followed by a very shallow decay, and finally the normal decay that was observed before the

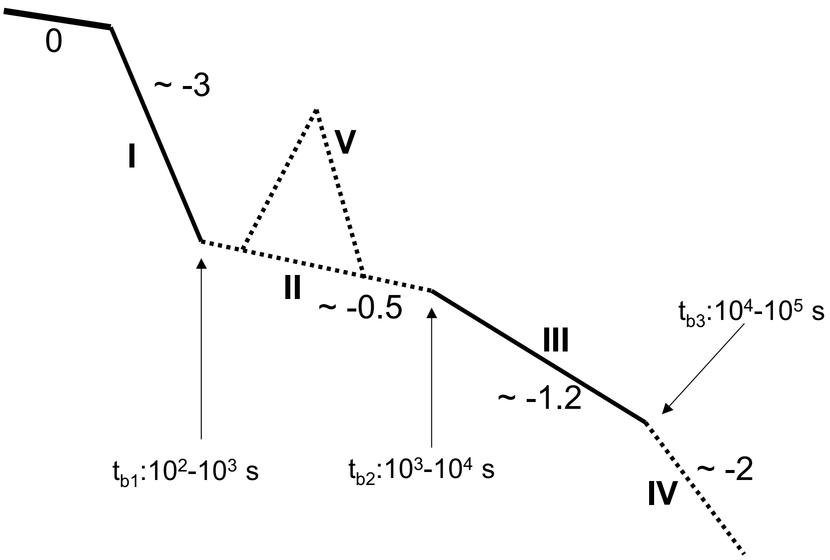

Figure 1.8 — Canonical X-ray light curve based on the observational data from the Swift X-Ray Telescope (Zhang et al. 2006). The phase 0 denotes the prompt emission. Four power-law light-curve segments together with a flaring component are identified in the afterglow phase. Typical temporal indices in the four segments and break times are indicated. Segments III (normal decay phase) and IV (jet break phase) have been observed in the pre-Swift era, while the other segments have been discovered by Swift. Segments I (steep decay phase) and III are most common, and they are marked with solid lines. The other three components are only observed in a fraction of bursts, so they are marked as dashed lines; segment II denotes the shallow decay phase and V denotes X-ray flares.

launch of Swift. On top of this canonical light curve behaviour, many early-time afterglows show X-ray flares that are in some cases as energetic as the prompt flash of gamma rays, see Figure 1.9. The initial steep decay can be attributed to the tail of the prompt emission, from photons that are emitted at large angles relative to our line of sight, the so-called high-latitude emission. The transition from the steep decay to the shallow decay, at $10^2 - 10^3$ seconds, marks the time when the emission from the forward moving blast wave becomes dominant. The shallowness of the decay can be explained by refreshment of the blast wave up to $10^3 - 10^4$ seconds after the burst. This might be caused by either energy injection of a long-lived central engine or slow shells in the relativistic outflow catching up with and refreshing the decelerating blast wave. X-ray flares are explained by the GRB central engine being still active after the prompt gamma-ray emission is over, releasing significant amounts of energy and material quite irregularly for a long period of time, sometimes up to days after the initial burst, but with a

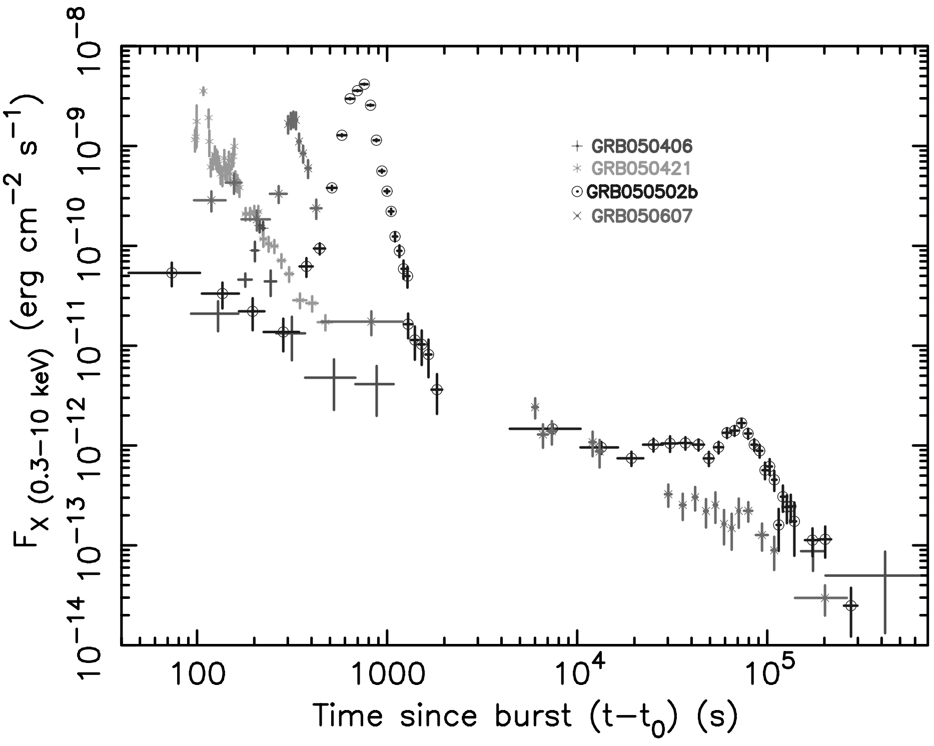

Figure 1.9 — X-ray flux (0.3-10 keV in the observer frame) as a function of the observed time for a few Swift GRBs with X-ray flares (Nousek et al. 2006). In some cases the X-ray flares are as energetic as the prompt flash of gamma rays, e.g. GRB 050502B.

reduced activity at later times. The decay of these flares is also very steep, like the first steep decay phase, and the decay slope values can also be explained by high-latitude emission (Liang et al. 2006).

The early-time light curves in the optical, from Swift and robotic telescopes on Earth, display very different behaviour between bursts. They do not show the very steep decay phase or very bright flares, but some of them do show a shallow decay phase simultaneously with the X-ray shallow decay phase. The distinct differences in behaviour between bursts is rather puzzling. These differences are also seen for those bursts that have optical observations during the prompt emission phase (Yost et al. 2007): some of the optical light curves follow the prompt emission, while in other cases there seem to be two emission components. Another puzzle in the Swift era is the proposed lack of jet breaks in the X-ray light curves. Before the launch of Swift most of the jet breaks were determined from achromatic breaks at $\sim$ 1 day, or a few days, in the optical light curves, but the X-ray light curves were in many cases not sampled well enough to either confirm or refute them with high statistical significance. Nowadays we have well-sampled X-ray light curves up to a few days, but the number of X-ray light curves going up to weeks after the burst is limited. Also the late-time follow-up with large (> 2 meter) optical telescopes has only been done for a few bursts, which makes it difficult to definitively state that the lack of observed jet breaks in the Swift era is inconsistent with the distribution of observed jet breaks in the pre-Swift era. A reason for this lack of late-time optical follow-up is the fact that Swift GRBs are on average fainter than pre-Swift bursts, because the average redshift is ~ 2.8 instead of ~ 1 (Jakobsson et al. 2006b) due to the sensitivity of Swift.

Besides all these new pieces of information and puzzles on afterglow light curves, Swift had other important discoveries; the detection of short GRB afterglows is one of the most significant ones. The X-ray light curves of short GRB afterglows display the same canonical behaviour as the long GRB afterglows. X-ray flares are observed in short GRB afterglows as well, which means that the central engines of short GRBs also have to stay active for quite a long time. Short GRB afterglows tend to be fainter than long GRB afterglows, but in a few cases they are bright enough to perform follow-up observations up to weeks after the burst. This made the detection of achromatic breaks, interpreted as jet breaks, possible. Broadband modeling of the short GRB afterglows indicates that their opening angles are on average larger than those of long GRBs, and that their energies and circumburst medium densities are lower. These statements are, however, not very secure because of the low number of well-sampled broadband afterglows of short GRBs.

1.5 Soft gamma repeaters and giant flares

Soft gamma repeaters (SGRs) were discovered in 1979, when the Venera spacecraft detected a burst of soft gamma rays from an object we now know as SGR 1806-20. After this burst, others were discovered, and they were at first classified as a class of GRBs, with a short duration and a soft spectrum (Mazets & Golenetskii 1981). When SGR 1806-20 showed an intense reactivation in 1983, it was clear that this SGR, and the others that were discovered, formed a new class of transients (Laros et al. 1987), not a class of GRBs, since GRBs never showed multiple bursts on time scales of years. SGRs turned out to be young ($10^3 - 10^4$ years old) neutron stars with extremely high magnetic fields ($\gtrsim 10^{15}$ Gauss), so-called magnetars (Duncan & Thompson 1992; Kouveliotou et al. 1998). The extreme magnetic conditions cause the recurrent SGR bursts. SGRs show bursting activity at irregular intervals with variable duration and in-

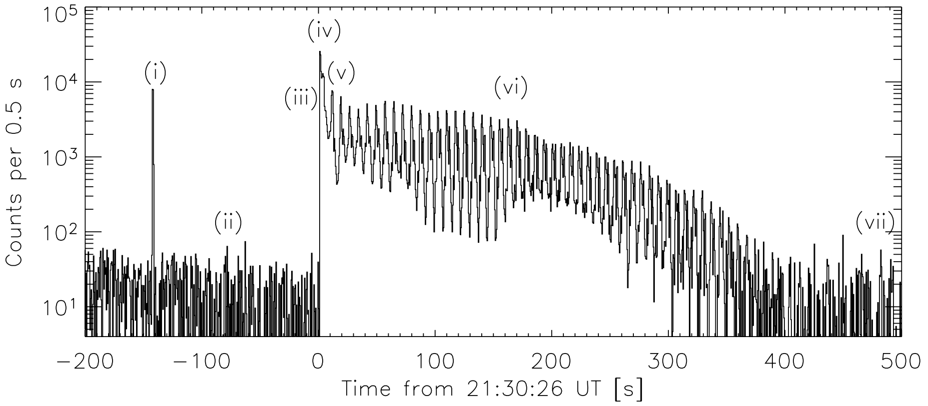

Figure 1.10 — RHESSI 20-100 keV background-subtracted time history of the giant flare, plotted with 0.5 second resolution (Boggs et al. 2007). The main peak begins at 0.64 seconds, where the RHESSI detectors are saturated and effectively dead. RHESSI recovered ~ 0.5 seconds later to observe the rest of the giant flare in detail.

tensity, and there are three types of bursts: regular bursts, lasting 0.1 seconds and peak luminosities of < 10^{41} erg/s; intermediate bursts with peak luminosities of > 10^{41} erg/s, and most commonly observed in the months following the third type of bursts, namely giant flares (Woods & Thompson 2006). SGR giant flares are thought to result from shearing and reconnection of extreme magnetic fields near the neutron star surface. The first SGR giant flare was discovered a couple of months after the first detection of a SGR burst. On March 5 of 1979, SGR 0526-66, the only SGR found in the Large Magellanic Cloud, displayed an extremely bright spike peaking at ~ 10^{45} erg/s which decayed rapidly into a pulsating tail that persisted for hundreds of seconds (Mazets et al. 1979). There have been two other detections of these giant flares: SGR 1900+14 on August 27 of 1998 (Hurley et al. 1999a), and SGR 1806-20 (Figure 1.10) on December 27 of 2004 (Hurley et al. 2005; Palmer et al. 2005). The giant flare of SGR 1900+14 was a bit more energetic than the one of SGR 0526-66, but SGR 1806-20 had a giant flare that was 2 orders of magnitude more energetic than the other two. This extreme giant flare was actually the brightest extra-solar transient event ever recorded. As a striking example of its brightness: the gamma-ray detector on board the Swift satellite was completely saturated while the detectors were illuminated from the back of the satellite. It even caused an ionospheric disturbance in the Earth's upper atmosphere (Campbell et al. 2005).

For two out of giant flares an associated radio transient was found: SGR 1900+14 and SGR 1806-20. The radio afterglow of SGR 1806-20 was

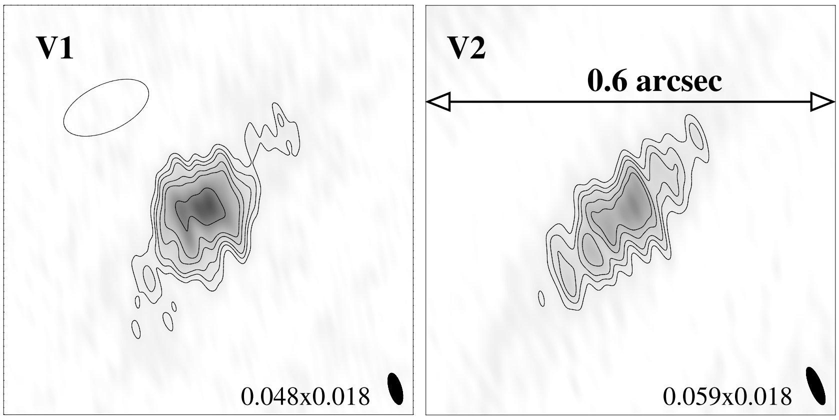

Figure 1.11 — Very Long Baseline Array images at 1.4 GHz of the radio afterglow of the SGR 1806-20 giant flare, 9 (V1) and 10 (V2) days after the gamma-ray event (Fender et al. 2006b). The grey-scale range is the same in each epoch to illustrate the fading of the source. Solid ellipses are the synthesized beams (with dimensions in arcsec); the open ellipse at epoch V1 is the Gaussian fit to the VLA data at roughly the same epoch.

spectacular, just like the flare in gamma rays, displaying a radio nebula expanding at approximately a quarter of the speed of light. This event instigated follow-up observations by radio telescopes around the world in order to construct well-sampled light curves at a broad range of radio wavelengths. The observations could be explained by a model in which the radio emission is due to the outflow ejected during the giant flare energizing a thin shell surrounding a pre-existing cavity. The shocked ejecta and external shell move outward together, driving a forward shock into the ambient medium, and are eventually decelerated by a reverse shock. This event was thus a scaled-down version of a GRB explosion, which, due to its proximity, could be resolved spatially with Merlin and VLBA, indicating that the outflow was actually asymmetric, see Figure 1.11 (Fender et al. 2006b). There is a second link between SGRs and GRBs, namely the suggestion that SGR giant flares can explain part of the population of short GRBs. If the giant flare of SGR 1806-20 had been observed from a larger distance, up to 40 Mpc, only the initial spike of $\sim$ 0.5 seconds would have been seen, and this event would have been identified as a short GRB (Palmer et al. 2005).

1.6 Extending the broadband view

Multi-wavelength studies of GRBs and their afterglows have provided a wealth of information on GRB progenitors, host galaxies, relativistic blast wave physics, particle acceleration, etcetera. These studies will become even broader in wavelength range in the near future, with a new generation of radio telescopes that will observe in the meter wave band, like the Low Frequency Array (LOFAR), and the new high energy gamma-ray satellite, the Gamma-Ray Large Area Space Telescope (GLAST). GLAST will be launched early 2008 and will have a burst monitor (GBM) with a wide field-of-view to detect GRBs, but also other phenomena like SGRs. The high energy instrument (LAT) on board GLAST will extend the gamma-ray observations of the prompt emission to very high energies, up to 300 GeV, making it possible to test the prompt emission mechanisms and models at these energies. LOFAR will observe at the complete opposite side of the electromagnetic spectrum, from 10 to 250 MHz, with an unprecedented sensitivity. Observations at these low frequencies will extend the radio afterglow observations at current observatories, making it possible to observe GRB afterglows on timescales of years to decades. Furthermore, predictions have been made that coherent radio emission at these low frequencies is produced in the internal shocks in the relativistic outflow, which would make LOFAR a GRB triggering telescope if the assumptions made in these calculations are correct.

Besides broadening our electromagnetic view on GRBs, current and future projects of other kinds will increase our understanding of the GRB phenomenon. While observations in the electromagnetic domain show only the processes in the jet, we can get a more direct view on the physics of the progenitor and central engine by observing neutrinos, high-energy cosmic rays or gravitational waves. In the shock acceleration models for GRBs it is generally believed that charged particles are accelerated to high energies, and that neutrinos and high-energy cosmic rays are formed due to interactions between these particles and the high-energy photons present in the medium. By observing them the nature of the outflow can be tested, in particular the presence of protons and neutrons in the outflow, and the role that magnetic fields play in the formation and confinement of the jet. Gravitational waves will give a direct signature of the formation of the black hole in a GRB event. In progenitor models for both long and short GRBs gravitational wave signals are expected; in the case of short GRBs they could give the decisive evidence on what the progenitors of short GRBs are.

1.7 Thesis outline

In this thesis I present broadband modeling studies of astrophysical blast waves, in particular of several GRBs and the giant flare of SGR 1806-20. *Chapter 2* provides the theoretical background of all the modeling work presented in the subsequent chapters. We present a method to perform broadband modeling of GRB afterglows from radio to X-ray frequencies, on timescales from hours to years after the GRB event. To illustrate the modeling method, we take the well-sampled GRB 970508 as a case study, and compare our results with previous studies. Central in our approach is taking the structure of the circumburst medium as a free fitting parameter, besides all the other macro- and micro-physical parameters of the blast wave and its surroundings that we obtain. In *Chapter 3* we continue this work by determining some of the physical parameters for a sample of 10 GRB afterglows. For this sample we only use the optical and X-ray observations, and focus on the ambient medium structure and the energy distribution of synchrotron electrons. We obtain a statistical distribution of circumburst density structures, and we explore the universality of the electron energy distribution index.

Chapters 4 & 5 describe our three year monitoring campaign of the radio afterglow of GRB 030329, one of the brightest afterglows ever. In *Chapter 4* we present our observations with the Westerbork Synthesis Radio Telescope (WSRT) in 2003 and the results of modeling this afterglow in the GHz regime. In *Chapter 5* we present our observations with WSRT up to 1100 days after the burst, combined with observations at the Giant Metrewave Radio Telescope (GMRT). With these observations, that range from 325 MHz up to 8.4 GHz, we explore the physics at late times when the blast wave is non-relativistic. We compare these results with early-time studies, source size measurements, and constrain the counter-jet that is expected to be formed in the stellar collapse.

In *Chapter 6* we present the results of our observing campaign of the dark GRB 051022. Although this afterglow was quite bright at radio (WSRT) and X-ray (Swift & Chandra) frequencies, the afterglow was not detected in the optical down to very deep limits. We perform broadband modeling of the radio and X-ray observations, and calculate the expected optical fluxes given the modeling results. In this way we constrain the severe optical extinction in the host galaxy, which is probably causing this lack of optical emission.

In *Chapters 7 & 8* we present a multi-wavelength analysis of two Swift afterglows, both at optical and X-ray frequencies. The first is GRB 060206, which we test for the presence or absence of an achromatic break that could be identified as a jet break, and we discuss the apparent lack of achromatic jet breaks in the Swift X-ray afterglows. GRB 060210 is discussed in the following Chapter, in particular a method is presented to perform a simultaneous temporal fit to the multi-wavelength optical data. We explore the physics behind this early-time light curve, including effects of energy injection and the circumburst medium.

Finally, our radio observing campaign during the first month of the SGR 1806-20 giant flare afterglow is presented in *Chapter 9*. We show the light curves we obtained with the Very Large Array (VLA), Australia Telescope Compact Array (ATCA), Molonglo Observatory Synthesis Telescope (MOST) and WSRT. We describe the fading radio afterglow and the resolved, polarized, radio nebula. A model is proposed for this afterglow in terms of a sub-relativistic shock producing synchrotron radiation, as a scaled-down version of a GRB blast wave.

2

Broadband modeling of gamma-ray burst afterglows & the circumburst medium: GRB 970508 revisited

A.J. van der Horst, R.A.M.J. Wijers & L.J. van den Horn

Submitted to Astronomy & Astrophyscs

Abstract Broadband modeling of gamma-ray burst (GRB) afterglows provides detailed information on the physics of relativistic blast waves, particle acceleration, and the immediate surroundings of GRBs. Obtaining the circumburst medium structure from modeling afterglow light curves constrains GRB progenitor models. We present a method to perform broadband modeling of GRB afterglows from radio to X-ray frequencies, on timescales from hours to years after the GRB event. The density structure index of the circumburst medium is treated as a free fitting parameter. We model the broadband afterglow of the classical GRB 970508 as a case study to illustrate our method, and find the best fit parameters and their uncertainties. Of particular interest is our finding that the circumburst medium is quite accurately determined to be homogeneous.

2.1 Introduction

Since the discovery of afterglow emission of gamma-ray bursts (GRBs) at X-ray, optical and radio wavelengths (Costa et al. 1997; Van Paradijs et al. 1997; Frail et al. 1997a), it has become clear that broadband observations are needed to determine the physical processes producing the afterglow emission in the context of the available models, the most popular being the blast wave model (e.g., Rees & Mészáros 1992; Mészáros & Rees 1997; Wijers et al. 1997). Obtaining the overall shape of the spectral energy distribution (SED) and the time evolution of the GRB afterglow provides information about micro- and macro-physical parameters of the relativistic blast wave and its surroundings (see, e.g., Sari et al. 1998; Wijers & Galama 1999; Granot & Sari 2002). Although optical observations alone can give the value of some of these parameters, observations covering the radio to X-ray wavelength regions are required to determine all these physical parameters.

An important factor that influences the appearance of GRB afterglows is the structure of the circumburst medium. Since we have evidence that long-duration GRBs originate in the core-collapse of a massive star, we expect to see a signature of the massive stellar wind structure, in which the blast wave propagates, in the afterglow light curves. Previous studies of broadband afterglow light curves have given us an ambiguous picture: some authors adopt a homogeneous circumburst medium in their broadband modeling of afterglows, while others assume that the medium has a typical stellar wind structure. To study this further, in this paper we treat the circumburst medium structure as a free fitting parameter. We model the classical well-sampled afterglow of GRB 970508 as a case study to find the physical parameters and their uncertainties with our method, in particular the circumburst density profile. A statistical study of 10 afterglows, including GRB 970508, has been presented in Starling et al. (2007a), in which the circumburst density profile was determined from only optical and X-ray observations. The afterglow of GRB 970508 was only the second afterglow ever observed, and the first GRB for which a (spectroscopic) redshift was obtained (Metzger et al. 1997). Frail et al. (1997a) detected a GRB radio counterpart for the first time, which was detectable up to 450 days after the burst. This afterglow is up to today still one of the best sampled broadband afterglows.

The outline of the paper is as follows: in Section 2.2, and in the Appendices 2.7, 2.8 and 2.9, we give a theoretical description of the SEDs and light curves. In Section 2.3 we describe the modeling method, and in Section 2.4 we present the results of our case study of GRB 970508. We discuss our results in the context of previous studies in Section 2.5, and conclude in Section 2.6.

2.2 Theory

In the blast wave model GRB afterglows are produced by decelerating relativistic ejecta. The source produces a relativistic outflow which bumps into an external medium. This can be the interstellar medium, or the dense stellar wind produced by the progenitor of the GRB. External shocks arise due to the interaction of the relativistic matter with the surrounding medium, and cause the GRB afterglow. Magnetic fields cause the swept-up electrons to produce synchrotron radiation, which gives the broadband spectrum. The shock dynamics determines the evolution of the radiating medium, which in turn determines the evolution of the spectrum, which gives the light curves at a given observing frequency.

We treat synchrotron emission as the radiation mechanism for GRB afterglows. We do not take inverse Compton scattering into account, but we do include synchrotron self-absorption. The basic theory of synchrotron radiation is described in Ginzburg & Syrovatskii (1965) and Rybicki & Lightman (1979). In the blast wave model it is assumed that electrons are accelerated in a relativistic shock to a power-law distribution of Lorentz factors, with a certain minimal Lorentz factor and power-law index p. Integrating the spectral power of one electron over this distribution function gives the broadband synchrotron spectrum. The relativistic electrons that radiate also absorb and re-emit radiation, giving rise to synchrotron self-absorption. The broadband spectrum is characterised by the peak frequency ν_m that corresponds to the minimal Lorentz factor of the electron distribution function, the cooling frequency ν_c that emerges from the electrons that lose their energy by emitting synchrotron radiation on a timescale shorter than the dynamical timescale, the self-absorption frequency ν_a below which synchrotron self-absorption is important, and the peak flux $F_{\nu,\mathrm{max}}$. A detailed description of the broadband spectral energy distribution (SED) is given in Appendix 2.7 (for similar studies, see also Sari et al. 1998; Granot & Sari 2002).

To calculate the SED we adopt the single-electron synchrotron spectrum from Kaplan & Tsytovich (1973), which is an asymptotic form of the integral over a modified Bessel funtion of a fractional order, which is used by Ginzburg & Syrovatskii (1965) and Rybicki & Lightman (1979). We describe the electron energy distribution function as a smoothly broken power-law with a break at ν_c, and we calculate the synchrotron self-absorption self-consistently assuming that the blast wave is a homogeneous slab of material. All of this gives an analytical expression for the flux as a function of frequency in terms of incomplete Gamma functions, which is practical in modeling the data.

We assume that the instantaneous synchrotron spectra do not depend on the hydrodynamical evolution of the blast wave. The light curves at a given observing frequency ν depend on the temporal evolution of $F_{\nu,\mathrm{max}}$ and the characteristic frequencies ν_m, ν_c and ν_a. The temporal evolution of these four parameters is given by the radius and velocity of the blast wave as a function of time, see Appendix 2.8. We adopt the asymptotic behaviour in the three stages of the blast wave evolution: the extreme relativistic phase, in which the dynamics of the blast wave is given by the self-similar solutions of Blandford & McKee (1976); the jet-spreading phase in which the jet spreads sideways (Rhoads 1997, 1999); the non-relativistic phase, in which the blast wave has become spherical and non-relativistic, following the Sedov-Taylor self-similar solutions. The transitions between the three phases are characterised by the jet break time t_j and the non-relativistic time t_nr. The radius and the Lorentz factor (in the non-relativistic phase the velocity) of the blast wave in the three phases are power-laws in time, which are connected at the two transition times as smoothly broken power-laws, see Appendix 2.9.

2.3 Broadband modeling

We use the theoretical framework described in the previous section and the Appendices 2.7, 2.8 and 2.9, to model broadband data from GRB afterglows. There are only a few bursts for which there are well sampled light curves over the whole broadband spectrum, ranging from X-rays down to radio frequencies. Well sampled light curves at various wavelengths are needed to accurately determine the evolution of the characteristic frequencies and the peak flux, from which the blast wave energy E_j, the density of the surrounding medium ρ_0, and the fractions of energy in the electrons and magnetic field, ε_e and ε_B respectively, can be derived. The opening angle θ_0 of the collimated outflow can be determined from these physical parameters and the so-called jet break time t_j, when the blast wave has decelerated down to a Lorentz factor which is equal to the reverse of θ_0 (Rhoads 1997, 1999; Sari et al. 1999). The slope of the light curves at optical and X-ray frequencies gives the power-law index p of the electron energy spectrum and the structure of the surrounding medium, characterised by the power-law index k, adopting $\rho \propto R^{-k}$ for the density of the surrounding medium as a function of radius R (Mészáros et al. 1998).

2.3.1 Circumburst medium

A significant difference between our method and previous broadband modeling efforts is that we treat k as an independent fit parameter. Other authors have modeled GRB afterglows by adopting a certain value for k: $k = 0$ for a homogeneous medium or $k = 2$ for a stellar wind environment. Since long GRBs are associated with the collapse of a massive star and the blast wave resides at 10^{16-18} cm from the center in the afterglow phase, a signature of the massive stellar wind is expected in the afterglow light curves (Chevalier & Li 1999). Interactions of this wind with the direct stellar environment, however, can change the picture dramatically (see e.g. Wijers 2001; Ramirez-Ruiz et al. 2005; Pe'er & Wijers 2006): at the point where the wind meets the interstellar medium a reverse shock going back into the wind is formed, besides a forward shock moving into the interstellar medium. This reverse shock alters the wind medium structure such that it becomes homogeneous; for wind and ISM parameters in plausible ranges, the blast wave may be outside or inside the reverse shock during the period we observe the afterglow. There are, however, some uncertainties in the exact position of the transition between the unshocked stellar wind and the shocked wind, because it depends on the density of the wind and the interstellar medium. Therefore, determining the circumburst medium structure gives important clues on the progenitor and environment of long GRBs.

In some GRB afterglows both the spectral and temporal coverage are good enough to distinguish between a homogeneous and a wind medium. This is usually done by modeling the broadband afterglow for $k = 0$ and $k = 2$, and then choosing the one with the best chi-squared (e.g. Panaitescu & Kumar 2002). In contrast, we treat k as a fitting parameter, determine its value and also the uncertainty in its value, as we do for the other parameters (see Section 2.4). In this way we can obtain values for k which are not 0 or 2, which could well be the case, because we are probing a medium that is probably altered by shock interactions. Furthermore, the value $k = 2$ is only valid for a constant mass-loss rate and wind velocity, which is not always expected for the stellar wind of a Wolf-Rayet star (Ramirez-Ruiz et al. 2001; Van Marle et al. 2006). We note that if there are only optical and X-ray observations of a GRB afterglow, the value of k can also be determined from combining spectral and temporal slopes only, as was done for a sample of 10 GRB afterglows in Starling et al. (2007a), but here we continue by modeling an afterglow which also has good coverage at radio wavelengths.

2.4 Results

We have developed a code in which we can use a broadband data set and fit our theoretical model simultaneously in time and frequency by means of chi-squared fitting. To minimize the chi-squared we use the method of simulated annealing

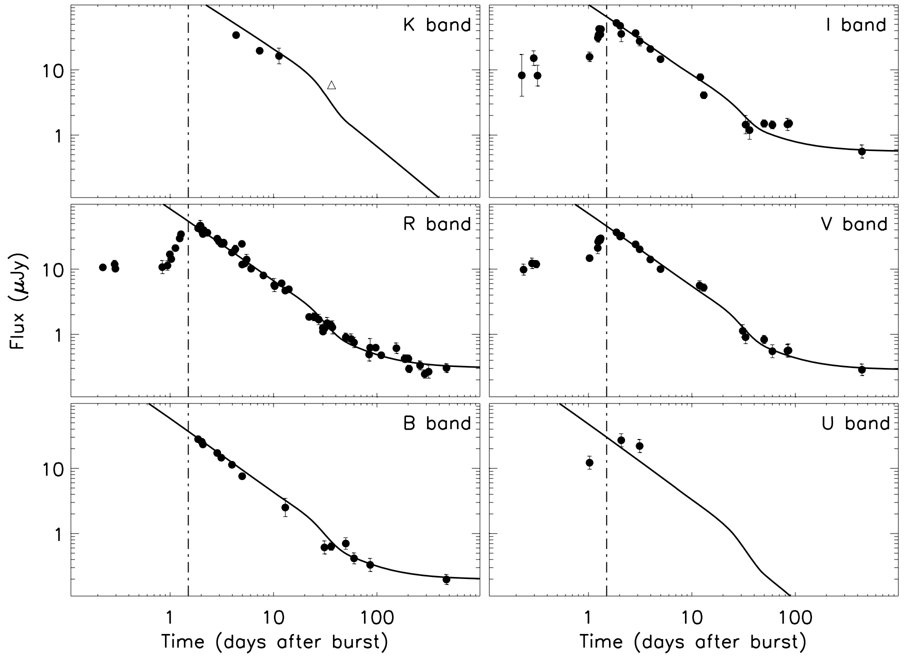

Figure 2.1 — Broadband modeling results for GRB 970508: the UV, optical and near-infrared light curves. The best fit parameters are shown in Table 2.1. The solid line corresponds to the light curve with the best fit parameters; the open symbols are 3σ upper limits. The vertical dotted line at 1.5 days indicates the time after which the data were modeled, see the discussion on the early optical brightening in the text.

in order to find the global minimum, i.e. the best fit parameters. An estimate of the accuracy of the best fit parameters is found by performing Monte Carlo simulations with 10^3 synthetic datasets. These datasets are possible measurements within the measurement uncertainties, generated by taking random numbers from the probability distributions that are defined by the measured fluxes and their uncertainties. We assume that the probability distributions are normal distributions, with the measurement being the mean value and its measurement uncertainty the width of the distribution.

2.4.1 Modeling GRB 970508

As a case study we have modelled GRB 970508. We have used all the published data of this GRB afterglow from radio to X-ray frequencies. Radio observations were done with the Westerbork Synthesis Radio Telescope at 1.4 GHz

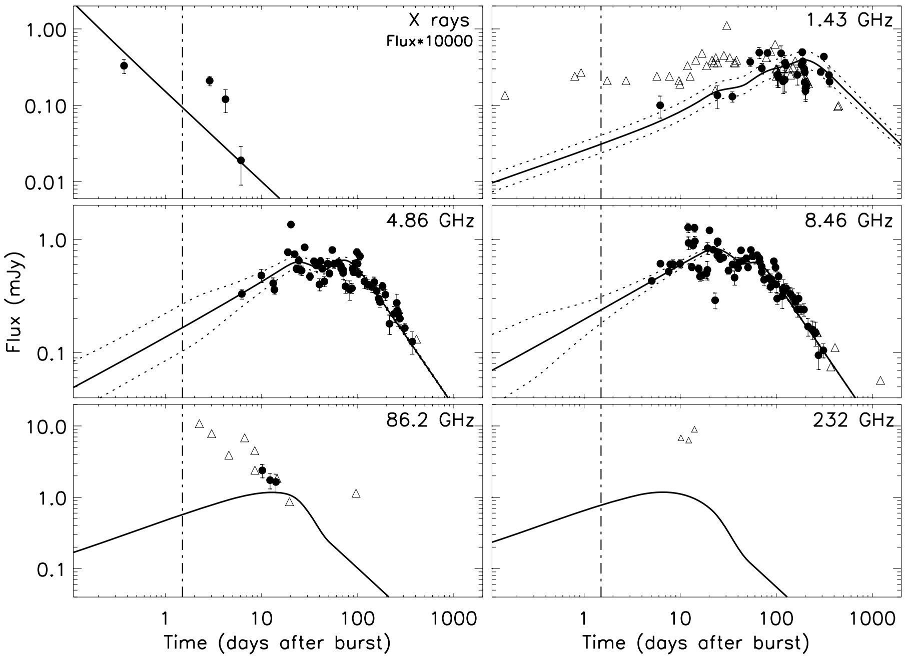

Figure 2.2 — Broadband modeling results for GRB 970508: the radio, millimeter and X-ray light curves. The best fit parameters are shown in Table 2.1. The solid line corresponds to the light curve with the best fit parameters; the dashed line indicates interstellar scintillation effects; the open symbols are 3σ upper limits. The vertical dotted line at 1.5 days indicates the time after which the data was modeled, see the discussion on the early optical brightening in the text.

(Galama et al. 1998c), and with the Very Large Array at 1.43, 4.86 and 8.46 GHz (Frail et al. 2000b). The afterglow was observed at millimeter wavelengths with the Plateau de Bure Interferometer at 86.2 and 232 GHz (Bremer et al. 1998). The Near Infrared Camera of the Keck I telescope was used to do near-infrared imaging of GRB 970508 (Chary et al. 1998). Optical data were taken with the William Herschel Telescope (Galama et al. 1998a), the Special Astrophysical Observatory of the Russian Academy of Science (Sokolov et al. 1998), the Kitt Peak National Observatory (Sahu et al. 1997), and by various other optical telescopes (collected in Garcia et al. 1998). The magnitudes at B, V, R_c and I_c wavelengths of the underlying host galaxy of GRB 970508 are presented in Zharikov & Sokolov (1999). They observed the optical remnant with the Special Astrophysical Observatory of the Russian Academy of Science in July-August 1998 and showed that the remnant has varied little since November 1997. The afterglow was observed in X rays with BeppoSAX (Piro et al. 1998). We have corrected the observed optical magnitudes for galactic extinction and converted them to fluxes; we converted the X-ray count rates to fluxes by assuming a spectral index of -1.1 over the observing band. We add the host galaxy component to our modeling code by taking the host galaxy fluxes from Zharikov & Sokolov (1999).

To carry out the modeling we adopt the following cosmology: $\Omega_M = 0.27$, $\Omega_\Lambda = 0.73$ and the Hubble-parameter $H_0 = 71\,\mathrm{km\,s^{-1}\,Mpc^{-1}}$; so at the redshift of GRB 970508 of $z = 0.835$ (Metzger et al. 1997), the luminosity distance $d_L = 1.635 \cdot 10^{28}\,\mathrm{cm}$. The resulting light curves, including the best broadband fit, are shown in Figures 2.1 (UV, optical and infrared) and 2.2 (radio, millimeter and X rays). The best fit parameters from our broadband modeling, and the physical parameters that can be deduced from these fit parameters, are given in Table 2.1, including their 1σ uncertainties. In Figure 2.3 we show the distributions of the physical parameters we derived in the broadband modeling, or deduced from the best fit parameters, for the Monte Carlo simulations with 10^3 synthetic datasets. For some parameters the distributions are quite symmetric, e.g. p and ε_e, while others are clearly asymmetric, e.g. ε_B. The isotropic equivalent blast wave energy E_{iso} and the jet opening angle θ_0 are also both asymmetrically distributed, resulting in a roughly symmetric distribution for the collimation corrected energy E_{j}. The circumburst medium density and k have some clear outliers in their distributions, which can also be seen in the asymmetric 1σ uncertainties in Table 2.1, especially for the density.

2.4.2 Early optical brightening

In our fit we have excluded the data up to 1.5 days after the burst. The optical light curves show a behaviour that can not be explained within the model presented here: a plateau followed by a brightening, and a turnover of the light curves at ~ 1.5 days, after which we observe the usual behaviour. Various explanations for the unusual early behaviour have been put forward: a refreshed shock from slow shells in the outflow catching up with the decelarating blast wave (Panaitescu et al. 1998; Sari & Mészáros 2000; Nakar et al. 2003), or a sudden change in the circumburst medium that the blast wave ploughs through (Wang & Loeb 2000; Dai & Lu 2002; Nakar et al. 2003). Early time plateau phases and rising optical light curves have been observed now quite often in the Swift era (e.g. Rykoff et al. 2006; Curran et al. 2007), and are often explained by late-time energy injection by the central engine. This is probably not the correct explanation, since this would mean that the energy injection phase ends at ~ 1.5 days, which poses serious challenges on to central engine models.

Fit parameters	Physical parameters
$\nu_{\mathrm{c}}\left(t_{\mathrm{j}}\right) = \left(9.21^{+1.65}_{-0.06}\right) \cdot 10^{13}$ Hz	$\varepsilon_{\mathrm{e}} = 0.155^{+0.003}_{-0.007}$
$\nu_{\mathrm{m}}\left(t_{\mathrm{j}}\right) = \left(4.26^{+0.17}_{-0.34}\right) \cdot 10^{10}$ Hz	$\varepsilon_{\mathrm{B}} = 0.103^{+0.06}_{-0.11}$
$\nu_{\mathrm{a}}\left(t_{\mathrm{j}}\right) = \left(3.09^{+0.19}_{-0.06}\right) \cdot 10^{9}$ Hz	$E_{\mathrm{iso}} = \left(4.35^{+0.05}_{-0.17}\right) \cdot 10^{51}$ erg
$F_{\nu,\mathrm{max}}\left(t_{\mathrm{j}}\right) = 0.756^{+0.005}_{-0.023}$ mJy	$\theta_0 = 14.1^{+0.4}_{-0.1}$ deg
$t_{\mathrm{j}} = 23.3^{+0.5}_{-0.9}$ days	$E_{\mathrm{j}} = \left(1.31^{+0.06}_{-0.03}\right) \cdot 10^{50}$ erg
$t_{\mathrm{nr}} = 44.7^{+0.6}_{-2.5}$ days	$n_0 = 0.019^{+0.067}_{-0.008}$ cm^{-3}
$p = 2.22^{+0.02}_{-0.02}$	
$k = 0.0307^{+0.0305}_{-0.0174}$	
$\chi^2_{\mathrm{red}} = 58$	

Table 2.1 — Results from our broadband modeling of the afterglow of GRB 970508. We modeled all the data after 1.5 days after the burst, because of the unexplained optical rebrightening. The best fit parameters and the deduced physical parameters are shown together with accuracy estimates from Monte Carlo simulations with synthetic data sets. The characteristic frequencies of the synchrotron spectrum and the peak flux are given at the jet break time t_{j}.

2.4.3 Interstellar scintillation

The radio light curves show significant scatter around the best fit light curve, which can be accounted for by interstellar scintillation (ISS; Goodman 1997; Frail et al. 1997a). The radio flux will be modulated when the source size is close to one of the three characteristic angular scales, i.e. for weak, refractive or diffractive ISS. The angular size of the blast wave starts out smaller than the ISS angular scales, resulting in a significant modulation of the flux. Because of the expansion of the blast wave the angular source size exceeds one of the characteristic angular scales at some point in time, and the modulation will begin to quench.

We have calculated the scattering measure from the Cordes & Lazio (2002) model for the galactic distribution of free electrons: $SM = 3.74 \times 10^{-4}\,\mathrm{kpc\,m^{-20/3}}$. From Walker (1998) we calculate the transition frequency between weak and strong ISS, $\nu_0 = 11.66\,\mathrm{GHz}$, and the angular size of the first Fresnel zone, $\theta_{\mathrm{F}_0} = 0.797\,\mu\mathrm{as}$. Our measurements were all performed at frequencies below ν_0, i.e. in the strong ISS regime, which means that only refrac-

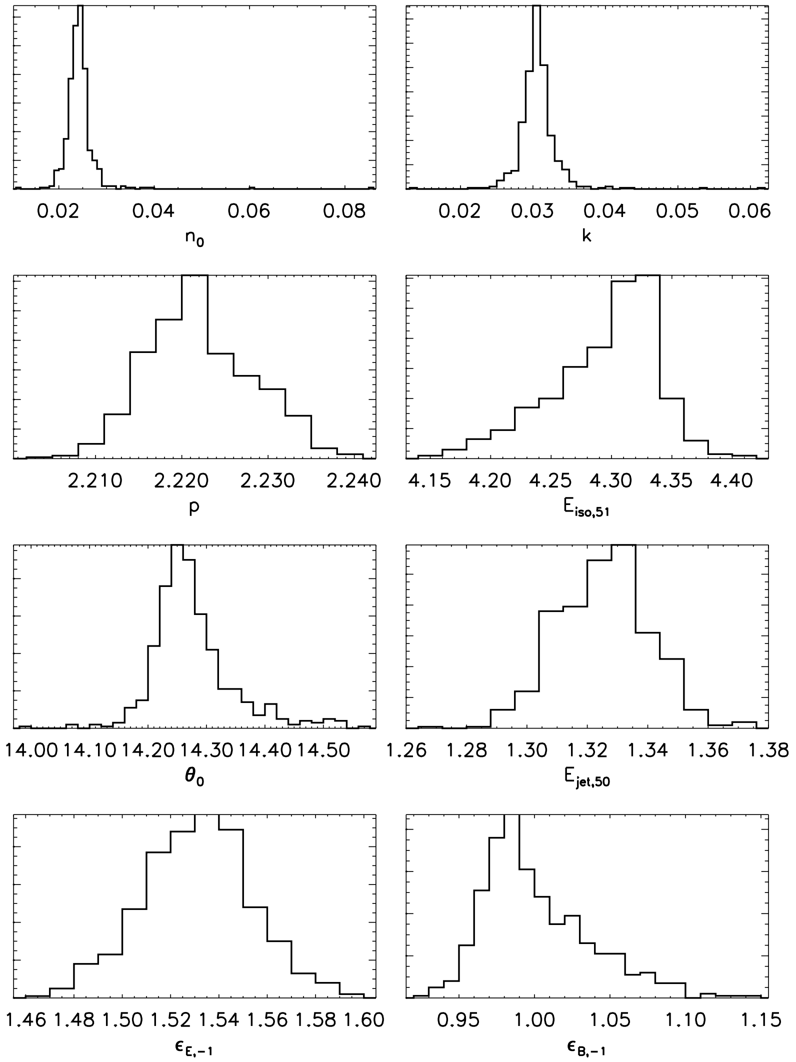

Figure 2.3 — Distributions of the physical parameters derived from broadband modeling of GRB 970508 for Monte Carlo simulations with 10^3 synthetic datasets: the circumburst medium density n_0, the power-law index k of the circumburst medium structure, and the power-law index p of the electron energy distribution; the isotropic equivalent blast wave energy $E_{\rm iso,51}$, the opening angle of the jet θ_0, and the collimation corrected blast wave energy $E_{\rm jet,50}$; and the fractional energies in the electrons and magnetic field, $\varepsilon_{\rm e,-1}$ and $\varepsilon_{\rm B,-1}$ respectively. The best fit parameters and the deduced physical parameters are shown in Table 2.1, together with their 1σ uncertainties.

tive and diffractive ISS modulate the flux significantly. We calculate the evolution of the source size in the extreme relativistic phase ($\theta_s = R/\Gamma$) and after the jet break ($\theta_s = R\theta_j$), and compare this source size with the diffractive angular scale $\theta_d = \theta_{F_0}(\nu_0/\nu)^{-6/5} = 0.418\,\nu_{\rm GHz}^{6/5}\,\mu$as and the refractive angular scale $\theta_r = \theta_{F_0}(\nu_0/\nu)^{11/5} = 177\,\nu_{\rm GHz}^{-11/5}\,\mu$as to calculate the modulation index m_p. In the case of diffractive ISS the modulation index is 1, and in the case of refractive ISS $m_p = (\nu_0/\nu)^{-17/30} = 0.249\,\nu_{\rm GHz}^{17/30}$.

2.5 Discussion

The afterglow of GRB 970508 was only the second afterglow ever observed, and was also the first afterglow for which broadband modeling from radio to X-ray frequencies was performed (see e.g. Wijers & Galama 1999; Granot et al. 1999b). In the first modeling efforts of GRB afterglows, SEDs and light curves were inspected separately to deduce physical parameters. GRB 970508, for instance, was first modeled by Wijers & Galama (1999) by constructing the SED at 12 days and determining the values of the characteristic frequencies and the peak flux at that time. This approach has some drawbacks, e.g. the modeling of light curves and SEDs near the characteristic frequencies is inaccurate, and only a few data points can be used in the broadband fitting, with as a result that the uncertainty in the derived parameters is large. After that various authors (e.g. Chevalier & Li 2000; Panaitescu & Kumar 2002; Yost et al. 2003) have performed broadband modeling, using all the available data, in similar detailed analyses as the one described in this paper. There are, however, some significant differences in the assumptions made by the different authors.

The most striking difference is the fact that we fit the circumburst medium structure, as highlighted in Section 2.3. Chevalier & Li (2000) assume a wind medium in their modeling efforts. Panaitescu & Kumar (2002) explore both possibilities of a homogeneous and a wind medium, and find that a wind-like medium is favoured. Yost et al. (2003) fit the data adopting a homogeneous circumburst medium, and explore the possible influences of increasing and declining density gradients. They conclude that the fits are not very sensitive to increasing density gradients, and that a wind medium is close to a value of k in which the solutions become unphysical (at $k = 2.5$). We show here that the value of k is consistent with a homogeneous medium and has a small uncertainty, in contrast with the findings of Panaitescu & Kumar (2002).

There are more differences between the various authors, e.g. analytical versus numerical calculations of the hydrodynamics and SEDs. One important extra component that is included in the modeling effort of Yost et al. (2003) is interstellar scintillation. They calculate the angular size as a function of time for each set of parameters and compare this to the characteristic angular sizes of ISS. This is then used as an additional uncertainty in the model flux, added in quadrature to the data's uncertainties when estimating the chi-squared. This was not used by Chevalier & Li (2000) and Panaitescu & Kumar (2002), and also not in this paper, because the model of the galactic distribution of free electrons is only accurate for certain sight-lines; especially sight-lines well above or below the galactic mid-plane are very uncertain. This also makes the calculation of the characteristic angular scales and the modulation index very uncertain, which then introduces a larger (systematic) uncertainty in the fit parameters, while the chi-squared is decreasing. Furthermore, the radio light curves of GRB 970508 are well covered temporally, so that an average trend of the light curves can be easily deduced in the broadband modeling.

2.6 Conclusions

We have presented our method of broadband modeling of GRB afterglows. Our calculations of the SEDs and light curves are similar to previous studies, but have some significant differences. We adopt a continuous asymptotic description of the single-electron synchrotron spectrum, and give an analytical description of the complete SED, including synchrotron cooling and self-absorption. To calculate the light curves we assume that the circumburst medium into which the blast wave moves, has a density gradient that is a decreasing power-law as a function of radius, with power-law index k. We give analytical expressions for the characteristic frequencies in the synchrotron spectrum and the peak flux in terms of the physical parameters describing the micro- and macrophysics of the blast wave and its surroundings, i.e. the kinetic energy of the blast wave, the jet opening angle, the energy in electrons and magnetic field, the power-law index of the electron energy distribution, the circumburst medium density, and k.

We have developed a semi-analytical code to perform broadband modeling of GRB afterglows from radio to X-ray frequencies, from hours up to years after the burst. We determine best fit parameters using the simulated annealing method and estimate uncertainties in these parameters by performing Monte Carlo simulations with synthetic datasets. We have modelled the well studied afterglow of GRB 970508 and compared our results with previous studies. An important difference between our method and others is that we treat k as a fitting parameter, instead of adopting either a homogeneous or a stellar wind medium. In the case of GRB 970508 we find a value of $k \simeq 0.03^{+0.03}_{-0.02}$, consistent with a homogeneous medium and with a small uncertainty.

Determining k from broadband modeling is important for our understanding of GRB progenitors. Well sampled afterglows are needed, both spectrally and temporally, to determine all the physical parameters. Well determined values of k for different bursts, using all the available data per burst, are necessary for studying the stellar winds of the massive progenitors, and the interactions these winds have with their surroundings.

2.7 Appendix A: Broadband synchrotron spectra

To produce the synchrotron emission observed, we assume that electrons are accelerated in a relativistic blast wave to a power-law distribution of Lorentz factor γ_e, with minimum Lorentz factor γ_m ($N(\gamma_\mathrm{e})d\gamma_\mathrm{e} \propto \gamma_\mathrm{e}^{-p} d\gamma_\mathrm{e}$, $\gamma_\mathrm{e} \geq \gamma_\mathrm{m}$). The spectral power of one electron received by an observer is given by

$$P_\nu(x) = \sqrt{3}\frac{q_\mathrm{e}^3 B \Gamma_2}{m_\mathrm{e} c^2} x \int_x^\infty K_{\frac{5}{3}}(\xi) d\xi \,, \qquad (2.1)$$

with $K_{\frac{5}{3}}(\xi)$ the modified Bessel function of order $\frac{5}{3}$, $x = \frac{\nu}{\nu_e}$, ν the observing frequency, $\nu_e = \Gamma_2 \gamma_\mathrm{e}^2 q_\mathrm{e} B/(2\pi m_\mathrm{e} c)$ the characteristic synchrotron frequency, B the magnetic field strength, and Γ_2 the Lorentz factor of the shocked medium in the frame of the unshocked medium. Because the exact expression for $P_\nu(x)$ is not so practical for numerical calculations, we approximate $P_\nu(x)$ by (Kaplan & Tsytovich 1973)

$$P_\nu(x) = 3\left(\frac{3}{2}\right)^{\frac{1}{3}} \frac{q_\mathrm{e}^3 B \Gamma_2}{m_\mathrm{e} c^2} x^{\frac{1}{3}} e^{-x} \,. \qquad (2.2)$$

To calculate the total power P_ν, one just integrates the power of one electron over all the possible values of γ_e, given by the distribution function $N(\gamma_\mathrm{e})$. The distribution function is not just a single power-law because of synchrotron cooling: the electrons lose energy by emitting radiation. This results in a break in the distribution function at the cooling Lorentz factor γ_c, i.e. the Lorentz factor for which the cooling timescale is equal to the lifetime of the source. For electrons with $\gamma_\mathrm{e} > \gamma_\mathrm{c}$ the cooling timescale is smaller than the lifetime of the source, which results in a steepening of the distribution function to $N(\gamma_\mathrm{e})d\gamma_\mathrm{e} \propto \gamma_\mathrm{e}^{-p-1} d\gamma_\mathrm{e}$ when $\gamma_\mathrm{c} < \gamma_\mathrm{m} < \gamma_\mathrm{e}$, while in the case of $\gamma_\mathrm{c} < \gamma_\mathrm{e} < \gamma_\mathrm{m}$ the distribution function changes to $N(\gamma_\mathrm{e})d\gamma_\mathrm{e} \propto \gamma_\mathrm{e}^{-2} d\gamma_\mathrm{e}$.

For calculating the total emitted power one has to distinguish between slow cooling and fast cooling. In the latter case $\gamma_\mathrm{m} > \gamma_\mathrm{c}$, so all the electrons have a Lorentz factor $\gamma_\mathrm{e} > \gamma_\mathrm{c}$ and thus all the electrons cool rapidly, i.e. this is the fast cooling regime. If $\gamma_\mathrm{m} < \gamma_\mathrm{c}$ a fraction of the electrons has Lorentz factors $\gamma_\mathrm{e} < \gamma_\mathrm{c}$

and a fraction has $\gamma_{\mathrm{e}} > \gamma_{\mathrm{c}}$. Because of the form of the distribution function and because of the cooling effect, most of the electrons have a Lorentz factor of the order of γ_{m} (provided $p > 2$). At least the largest fraction has $\gamma_{\mathrm{e}} < \gamma_{\mathrm{c}}$, and therefore this case is called slow cooling. The distribution can be normalized by integrating the distribution function $N(\gamma_{\mathrm{e}})$ over γ_{e}, which gives the total electron number density n_{e}. Furthermore, by demanding that the distribution function is continuous at the break, i.e. at γ_{c} in the case of slow cooling and at γ_{m} in the case of fast cooling, the distribution function can be formulated as

$$N(\gamma_{\mathrm{e}})d\gamma_{\mathrm{e}} = n_{\mathrm{e}}(p-1)\left(1-\frac{1}{p}\left(\frac{\gamma_{\mathrm{c}}}{\gamma_{\mathrm{m}}}\right)^{-(p-1)}\right)^{-1}\left(\frac{\gamma_{\mathrm{e}}}{\gamma_{\mathrm{m}}}\right)^{-p} d\left(\frac{\gamma_{\mathrm{e}}}{\gamma_{\mathrm{m}}}\right) \tag{2.3}$$

when $\gamma_{\mathrm{m}} < \gamma_{\mathrm{e}} < \gamma_{\mathrm{c}}$ (slow cooling),

$$N(\gamma_{\mathrm{e}})d\gamma_{\mathrm{e}} = n_{\mathrm{e}}(p-1)\left(1-\frac{1}{p}\left(\frac{\gamma_{\mathrm{c}}}{\gamma_{\mathrm{m}}}\right)^{-(p-1)}\right)^{-1}\left(\frac{\gamma_{\mathrm{c}}}{\gamma_{\mathrm{m}}}\right)^{-(p-1)}\left(\frac{\gamma_{\mathrm{e}}}{\gamma_{\mathrm{c}}}\right)^{-p-1} d\left(\frac{\gamma_{\mathrm{e}}}{\gamma_{\mathrm{c}}}\right) \tag{2.4}$$

when $\gamma_{\mathrm{m}} < \gamma_{\mathrm{c}} < \gamma_{\mathrm{e}}$ (slow cooling),

$$N(\gamma_{\mathrm{e}})d\gamma_{\mathrm{e}} = n_{\mathrm{e}}\left(1-\frac{p-1}{p}\left(\frac{\gamma_{\mathrm{m}}}{\gamma_{\mathrm{c}}}\right)^{-1}\right)^{-1}\left(\frac{\gamma_{\mathrm{e}}}{\gamma_{\mathrm{c}}}\right)^{-2} d\left(\frac{\gamma_{\mathrm{e}}}{\gamma_{\mathrm{c}}}\right) \tag{2.5}$$

when $\gamma_{\mathrm{c}} < \gamma_{\mathrm{e}} < \gamma_{\mathrm{m}}$ (fast cooling), and

$$N(\gamma_{\mathrm{e}})d\gamma_{\mathrm{e}} = n_{\mathrm{e}}\left(1-\frac{p-1}{p}\left(\frac{\gamma_{\mathrm{m}}}{\gamma_{\mathrm{c}}}\right)^{-1}\right)^{-1}\left(\frac{\gamma_{\mathrm{m}}}{\gamma_{\mathrm{c}}}\right)^{-1}\left(\frac{\gamma_{\mathrm{e}}}{\gamma_{\mathrm{m}}}\right)^{-p-1} d\left(\frac{\gamma_{\mathrm{e}}}{\gamma_{\mathrm{m}}}\right), \tag{2.6}$$

when $\gamma_{\mathrm{c}} < \gamma_{\mathrm{m}} < \gamma_{\mathrm{e}}$ (fast cooling). The total power P_ν can now be calculated. First for the slow cooling case:

$$\begin{aligned}
P_\nu \;=\;& n_{\mathrm{e}}(p-1)\left(1-\frac{1}{p}\left(\frac{\gamma_{\mathrm{c}}}{\gamma_{\mathrm{m}}}\right)^{-(p-1)}\right)^{-1}\left[\int_1^{\frac{\gamma_{\mathrm{c}}}{\gamma_{\mathrm{m}}}} P_\nu(\gamma_{\mathrm{e}})\left(\frac{\gamma_{\mathrm{e}}}{\gamma_{\mathrm{m}}}\right)^{-p} d\left(\frac{\gamma_{\mathrm{e}}}{\gamma_{\mathrm{m}}}\right)\right. \\
& \left. + \left(\frac{\gamma_{\mathrm{c}}}{\gamma_{\mathrm{m}}}\right)^{-(p-1)}\int_1^{\infty} P_\nu(\gamma_{\mathrm{e}})\left(\frac{\gamma_{\mathrm{e}}}{\gamma_{\mathrm{c}}}\right)^{-p-1} d\left(\frac{\gamma_{\mathrm{e}}}{\gamma_{\mathrm{c}}}\right)\right] \\
=\;& 3\left(\frac{3}{2}\right)^{\frac{1}{3}}\frac{n_{\mathrm{e}}q_{\mathrm{e}}^3 B\Gamma_2}{m_{\mathrm{e}}c^2}\frac{(p-1)}{2}\left(1-\frac{1}{p}\left(\frac{\nu_{\mathrm{c}}}{\nu_{\mathrm{m}}}\right)^{-\frac{p-1}{2}}\right)^{-1} \\
& \cdot\left\{\left(\frac{\nu}{\nu_{\mathrm{m}}}\right)^{-\frac{p-1}{2}}\left[\Gamma\left(\frac{p}{2}-\frac{1}{6},\frac{\nu}{\nu_{\mathrm{c}}}\right)-\Gamma\left(\frac{p}{2}-\frac{1}{6},\frac{\nu}{\nu_{\mathrm{m}}}\right)\right]\right. \\
& \left. + \left(\frac{\nu_{\mathrm{c}}}{\nu_{\mathrm{m}}}\right)^{-\frac{p-1}{2}}\left(\frac{\nu}{\nu_{\mathrm{c}}}\right)^{-\frac{p}{2}}\left[\Gamma\left(\frac{p}{2}+\frac{1}{3}\right)-\Gamma\left(\frac{p}{2}+\frac{1}{3},\frac{\nu}{\nu_{\mathrm{c}}}\right)\right]\right\},
\end{aligned} \tag{2.7}$$

with equation 2.2 for the single-electron spectrum $P_\nu(x)$. Here $\Gamma(y,a)$ is the incomplete Gamma function:

$$\Gamma(y,a) = \int_a^\infty \frac{x^y e^{-x}}{x} dx\,. \tag{2.8}$$

For $a = 0$ the ordinary Gamma function $\Gamma(y)$ is obtained.

For the fast cooling case we get in a similar way:

$$\begin{aligned} P_\nu &= n_\mathrm{e} \left(1 - \frac{p-1}{p}\left(\frac{\gamma_\mathrm{m}}{\gamma_\mathrm{c}}\right)^{-1}\right)^{-1} \left[\int_1^{\frac{\gamma_\mathrm{m}}{\gamma_\mathrm{c}}} P_\nu(\gamma_\mathrm{e}) \left(\frac{\gamma_\mathrm{e}}{\gamma_\mathrm{c}}\right)^{-2} d\left(\frac{\gamma_\mathrm{e}}{\gamma_\mathrm{c}}\right)\right. \\ &\quad \left. + \left(\frac{\gamma_\mathrm{m}}{\gamma_\mathrm{c}}\right)^{-1} \int_1^\infty P_\nu(\gamma_\mathrm{e}) \left(\frac{\gamma_\mathrm{e}}{\gamma_\mathrm{m}}\right)^{-p-1} d\left(\frac{\gamma_\mathrm{e}}{\gamma_\mathrm{m}}\right)\right] \\ &= 3\left(\frac{3}{2}\right)^{\frac{1}{3}} \frac{n_\mathrm{e} q_\mathrm{e}^3 B \Gamma_2}{m_\mathrm{e} c^2} \frac{1}{2} \left[1 - \frac{p-1}{p}\left(\frac{\nu_\mathrm{m}}{\nu_\mathrm{c}}\right)^{-\frac{1}{2}}\right]^{-1} \\ &\quad \cdot \left\{\left(\frac{\nu}{\nu_\mathrm{c}}\right)^{-\frac{1}{2}} \left[\Gamma\left(\frac{5}{6}, \frac{\nu}{\nu_\mathrm{m}}\right) - \Gamma\left(\frac{5}{6}, \frac{\nu}{\nu_\mathrm{c}}\right)\right]\right. \\ &\quad \left. + \left(\frac{\nu_\mathrm{m}}{\nu_\mathrm{c}}\right)^{-\frac{1}{2}} \left(\frac{\nu}{\nu_\mathrm{m}}\right)^{-\frac{p}{2}} \left[\Gamma\left(\frac{p}{2} + \frac{1}{3}\right) - \Gamma\left(\frac{p}{2} + \frac{1}{3}, \frac{\nu}{\nu_\mathrm{m}}\right)\right]\right\}. \end{aligned} \tag{2.9}$$

Besides synchrotron emission, self-absorption also plays an important role. The processes of absorption and stimulated emission result in the following formula for the absorption coefficient (Ginzburg & Syrovatskii 1965):

$$\alpha_\nu = -\frac{1}{8\pi m_\mathrm{e} \nu^2} \int P_\nu(\gamma_\mathrm{e}) \gamma_\mathrm{e}^2 \frac{d}{d\gamma_\mathrm{e}} \left(\frac{N(\gamma_\mathrm{e})}{\gamma_\mathrm{e}^2}\right) d\gamma_\mathrm{e}\,. \tag{2.10}$$

In the case of slow cooling the absorption coefficient becomes:

$$\begin{aligned} \alpha_\nu &= \frac{n_\mathrm{e}}{8\pi m_\mathrm{e} \nu^2} (p-1) \left(1 - \frac{1}{p}\left(\frac{\nu_\mathrm{c}}{\nu_\mathrm{m}}\right)^{-\frac{p-1}{2}}\right)^{-1} \\ &\quad \cdot \left[(p+2) \int_1^{\frac{\gamma_\mathrm{c}}{\gamma_\mathrm{m}}} P_\nu(\gamma_\mathrm{e}) \left(\frac{\gamma_\mathrm{e}}{\gamma_\mathrm{m}}\right)^{-p} \gamma_\mathrm{e}^{-1} d\left(\frac{\gamma_\mathrm{e}}{\gamma_\mathrm{m}}\right)\right. \\ &\quad \left. + (p+3) \left(\frac{\gamma_\mathrm{c}}{\gamma_\mathrm{m}}\right)^{-(p-1)} \int_1^\infty P_\nu(\gamma_\mathrm{e}) \left(\frac{\gamma_\mathrm{e}}{\gamma_\mathrm{c}}\right)^{-(p-1)} \gamma_\mathrm{e}^{-1} d\left(\frac{\gamma_\mathrm{e}}{\gamma_\mathrm{m}}\right)\right] \\ &= 3\left(\frac{3}{2}\right)^{\frac{1}{3}} \frac{n_\mathrm{e} q_\mathrm{e}^3 B \Gamma_2}{8\pi m_\mathrm{e}^2 c^2 \gamma_\mathrm{m} \nu^2} \frac{p-1}{2} \left(1 - \frac{1}{p}\left(\frac{\nu_\mathrm{c}}{\nu_\mathrm{m}}\right)^{-\frac{p-1}{2}}\right)^{-1} \end{aligned}$$

$$\begin{aligned}
&\cdot\left\{(p+2)\left(\frac{\nu}{\nu_\mathrm{m}}\right)^{-\frac{p}{2}}\left[\Gamma\left(\frac{p}{2}+\frac{1}{3},\frac{\nu}{\nu_\mathrm{c}}\right)-\Gamma\left(\frac{p}{2}+\frac{1}{3},\frac{\nu}{\nu_\mathrm{m}}\right)\right]\right.\\
&\left.+(p+3)\left(\frac{\nu_\mathrm{c}}{\nu_\mathrm{m}}\right)^{-\frac{p}{2}}\left(\frac{\nu}{\nu_\mathrm{c}}\right)^{-\frac{p+1}{2}}\left[\Gamma\left(\frac{p}{2}+\frac{5}{6}\right)-\Gamma\left(\frac{p}{2}+\frac{5}{6},\frac{\nu}{\nu_\mathrm{c}}\right)\right]\right\}. \qquad (2.11)
\end{aligned}$$

In the case of fast cooling the absorption coefficient we get in a similar way:

$$\begin{aligned}
\alpha_\nu &= \frac{n_\mathrm{e}}{8\pi m_\mathrm{e}\gamma_\mathrm{c}\nu^2}\frac{1}{2}\left(1-\frac{p-1}{p}\left(\frac{\nu_\mathrm{m}}{\nu_\mathrm{c}}\right)^{-\frac{1}{2}}\right)^{-1}\left[4\left(\frac{\nu}{\nu_\mathrm{c}}\right)^{-1}\int_{\frac{\nu}{\nu_\mathrm{m}}}^{\frac{\nu}{\nu_\mathrm{c}}}P_\nu(x)dx\right.\\
&\quad\left.+(p+3)\left(\frac{\nu_\mathrm{m}}{\nu_\mathrm{c}}\right)^{-1}\left(\frac{\nu}{\nu_\mathrm{m}}\right)^{-\frac{p+1}{2}}\int_0^{\frac{\nu}{\nu_\mathrm{m}}}P_\nu(x)x^{\frac{p-1}{2}}dx\right]\\
&= 3\left(\frac{3}{2}\right)^{\frac{1}{3}}\frac{n_\mathrm{e}q_\mathrm{e}^3B\Gamma_2}{8\pi m_\mathrm{e}^2c^2\gamma_\mathrm{c}\nu^2}\frac{1}{2}\left(1-\frac{p-1}{p}\left(\frac{\nu_\mathrm{m}}{\nu_\mathrm{c}}\right)^{-\frac{1}{2}}\right)^{-1}\\
&\quad\cdot\left\{4\left(\frac{\nu}{\nu_\mathrm{c}}\right)^{-1}\left[\Gamma\left(\frac{4}{3},\frac{\nu}{\nu_\mathrm{m}}\right)-\Gamma\left(\frac{4}{3},\frac{\nu}{\nu_\mathrm{c}}\right)\right]\right.\\
&\quad\left.+(p+3)\left(\frac{\nu_\mathrm{m}}{\nu_\mathrm{c}}\right)^{-1}\left(\frac{\nu}{\nu_\mathrm{m}}\right)^{-\frac{p+1}{2}}\left[\Gamma\left(\frac{p}{2}+\frac{5}{6}\right)-\Gamma\left(\frac{p}{2}+\frac{5}{6},\frac{\nu}{\nu_\mathrm{m}}\right)\right]\right\}. \qquad (2.12)
\end{aligned}$$

Synchrotron self-absorption only plays a role when the radiating medium is optically thick, i.e. the optical depth $\tau_\nu \geq 1$. The optical depth is given by $\tau_\nu = \int \alpha_\nu ds = \alpha_\nu L$, where the assumption is made that the absorption coefficient is constant across the medium with thickness L. The synchrotron self-absorption frequency ν_a is the frequency at which the medium changes from optically thin to optically thick. Now the optical depth can be written as $\tau_\nu = \alpha_\nu/\alpha_{\nu_\mathrm{a}}$, so $\alpha_{\nu_\mathrm{a}} = L^{-1}$. In the optically thin case (so no self-absorption present) the flux is given by $F_\nu = \frac{4}{3}\pi R^3 P_\nu / \left(4\pi D_\mathrm{L}^2\right)$, with D_L the luminosity distance to the source. In the optically thick case the flux is proportional to the source function, i.e. the emission coefficient divided by the absorption coefficient. Following the solutions of the radiative transfer equation for a homogeneous layer with thickness L in which the emission and absorption coefficient are constant (see e.g. Rybicki & Lightman 1979), the flux for the whole range of τ_ν can be written as

$$F_\nu = \frac{\frac{4}{3}\pi R^3 P_\nu}{4\pi D_\mathrm{L}^2}\left(\frac{\alpha_\nu}{\alpha_{\nu_\mathrm{a}}}\right)^{-1}\left[1-\exp\left(-\frac{\alpha_\nu}{\alpha_{\nu_\mathrm{a}}}\right)\right]. \qquad (2.13)$$

This implies that $F_\nu \propto \nu^2$ in the slow cooling as well as in the fast cooling regime for $\nu < \nu_\mathrm{a} < \nu_\mathrm{m}$, so the spectral flux falls of very steeply at low frequencies. When $\nu_\mathrm{m} < \nu < \nu_\mathrm{a}$ the flux is even proportional to $\nu^{5/2}$.

2.8 Appendix B: Afterglow light curves

The instantaneous synchrotron spectra do not depend on the hydrodynamical evolution of the blast wave. The light curves at a given observing frequency ν, however, depend on the temporal evolution of the characteristic frequencies ν_m, ν_c and ν_a and the factor

$$F_{\nu,\mathrm{max}} \equiv \frac{\frac{4}{3}\pi R^3 n_\mathrm{e} q_\mathrm{e}^3 B \Gamma_2}{4\pi D_\mathrm{L}^2 m_\mathrm{e} c^2} = \frac{1+X}{2} \frac{R^3 \rho q_\mathrm{e}^3 B \Gamma_2}{3 D_\mathrm{L}^2 m_\mathrm{e} m_\mathrm{p} c^2} \,. \tag{2.14}$$

Here we parametrize the ratio of the nucleon to electron number densities, $n = \rho/m_\mathrm{p}$ and n_e respectively, as $2/(1+X)$ with X being the hydrogen mass fraction.

The characteristic frequencies ν_m and ν_c correspond to γ_m and γ_c in the following way (Sari et al. 1998):

$$\nu_\mathrm{m,c} = \Gamma_2 \gamma_\mathrm{m,c}^2 \frac{q_\mathrm{e} B}{2\pi m_\mathrm{e} c} \,. \tag{2.15}$$

As usual we assume that the electron energy density and the magnetic energy density are constant fractions of the nucleon energy density behind the shock, ε_e and ε_B respectively. The minimum electron Lorentz factor γ_m is then given by

$$\gamma_\mathrm{m} = \frac{2}{1+X} \frac{m_\mathrm{p}}{m_\mathrm{e}} \frac{p-2}{p-1} \varepsilon_\mathrm{e} \Gamma_2 \tag{2.16}$$

while the cooling Lorentz factor γ_c can be found to be

$$\gamma_\mathrm{c} = \frac{6\pi m_\mathrm{e} c}{\sigma_\mathrm{T} \Gamma_2 B^2 t} = \frac{9}{128\pi} \frac{m_\mathrm{e}^3 c^3}{q_\mathrm{e}^4 \Gamma_2^3 \varepsilon_\mathrm{B} \rho t} \tag{2.17}$$

with $\sigma_\mathrm{T} = 8\pi q_\mathrm{e}^4/(3 m_\mathrm{e}^2 c^4)$ the Thomson cross-section, and the magnetic field strength

$$B = \Gamma_2 c \sqrt{32\pi\rho\varepsilon_\mathrm{B}} \,. \tag{2.18}$$

So now we have ν_m and ν_c as a function of Γ_2 and R:

$$\nu_\mathrm{m} = 2\sqrt{\frac{2}{\pi}} \left(\frac{1+X}{2}\right)^{-2} \left(\frac{p-2}{p-1}\right)^2 q_\mathrm{e} m_\mathrm{e}^{-3} m_\mathrm{p}^2 \varepsilon_\mathrm{e}^2 \varepsilon_\mathrm{B}^{\frac{1}{2}} \rho^{\frac{1}{2}} \Gamma_2^4 \,. \tag{2.19}$$

$$\nu_\mathrm{c} = \frac{81}{8192} \sqrt{2} \pi^{-\frac{5}{2}} q_\mathrm{e}^{-7} m_\mathrm{e}^5 c^6 \varepsilon_\mathrm{B}^{-\frac{3}{2}} \rho^{-\frac{3}{2}} \Gamma_2^{-4} t^{-2} \,, \tag{2.20}$$

$F_{\nu,\max}$ is given by

$$F_{\nu,\max} = \frac{4}{3}\sqrt{2\pi}\frac{1+X}{2}q_\mathrm{e}^3 m_\mathrm{e}^{-1} m_\mathrm{p}^{-1} c^{-1} \varepsilon_\mathrm{B}^{\frac{1}{2}} \rho^{\frac{3}{2}} D_\mathrm{L}^{-2} \Gamma_2^2 R^3 \,. \tag{2.21}$$

The synchrotron self-absorption frequency ν_a is a function of ν_m and ν_c, and can be found by stating that $\alpha_{\nu'_\mathrm{a}} = L^{-1}$ in the frame of the shocked fluid (the apostrophe denotes variables in the frame of the shocked fluid). The thickness L of the shell that emits the synchrotron radiation is R/Γ_2. When ν'_a is found from $\alpha_{\nu'_\mathrm{a}} = \Gamma_2/R$, it has to be transformed to the observer's frame by multiplying it with a factor of Γ_2. To calculate the dependence of ν_a on the physical parameters, the value of ν_a compared to that of ν_m and ν_c is important. As an example we examine the case of slow cooling with $\nu_\mathrm{a} \ll \nu_\mathrm{m} \ll \nu_\mathrm{c}$, so

$$\alpha_{\nu'_\mathrm{a}} \simeq 3\left(\frac{3}{2}\right)^{\frac{1}{3}} \frac{n_\mathrm{e} q_\mathrm{e}^3 B \Gamma_2}{8\pi m_\mathrm{e}^2 c^2 \gamma_\mathrm{m} \nu_\mathrm{a}^2} \frac{p-1}{p+\frac{2}{3}}(p+2)\left(\frac{\nu'_\mathrm{a}}{\nu'_\mathrm{m}}\right)^{\frac{1}{3}} = \frac{\Gamma_2}{R}\,, \tag{2.22}$$

$$\nu_\mathrm{a}'^{\frac{5}{3}} = 3\left(\frac{3}{2}\right)^{\frac{1}{3}} \frac{1+X}{2} \frac{p-1}{p+\frac{2}{3}}(p+2)\frac{q_\mathrm{e}^3 B R \rho}{8\pi m_\mathrm{e}^2 m_\mathrm{p} c^2 \gamma_\mathrm{m}} \nu_\mathrm{m}'^{-\frac{1}{3}}\,. \tag{2.23}$$

Using $\nu'_\mathrm{m} = \gamma_\mathrm{m}^2 q_\mathrm{e} B/(2\pi m_\mathrm{e} c)$ in the comoving frame in combination with equations 2.16 and 2.18 gives

$$\nu_\mathrm{a}'^{\frac{5}{3}} = 12\left(\frac{3}{2}\right)^{\frac{1}{3}} \pi^{\frac{2}{3}} \left(\frac{1+X}{2}\right)^{\frac{8}{3}} \frac{(p-1)^{\frac{8}{3}}(p+2)}{(p-2)^{\frac{5}{3}}(p+\frac{2}{3})} q_\mathrm{e}^{\frac{8}{3}} m_\mathrm{p}^{-\frac{8}{3}} c^{-1} \varepsilon_\mathrm{e}^{-\frac{5}{3}} \varepsilon_\mathrm{B}^{\frac{1}{3}} \rho^{\frac{4}{3}} \Gamma_2^{-1} R\,, \tag{2.24}$$

so in the frame of the unshocked medium

$$\nu_\mathrm{a} = 2\,(3)^{\frac{4}{5}}\,\pi^{\frac{2}{5}} \left(\frac{1+X}{2}\right)^{\frac{8}{5}} \frac{(p-1)^{\frac{8}{5}}(p+2)^{\frac{3}{5}}}{(p-2)(p+\frac{2}{3})^{\frac{3}{5}}} q_\mathrm{e}^{\frac{8}{5}} m_\mathrm{p}^{-\frac{8}{5}} c^{-\frac{3}{5}} \varepsilon_\mathrm{e}^{-1} \varepsilon_\mathrm{B}^{\frac{1}{5}} \rho^{\frac{4}{5}} \Gamma_2^{\frac{2}{5}} R^{\frac{3}{5}}\,, \tag{2.25}$$

by multiplying ν_a by a factor of Γ_2. In the case of fast cooling with $\nu_\mathrm{a} \ll \nu_\mathrm{c} \ll \nu_\mathrm{m}$ we find in a similar way:

$$\nu_\mathrm{a} = (2)^{\frac{28}{5}}\,(3)^{-\frac{3}{5}}\,\pi^{\frac{4}{5}} \left(\frac{1+X}{2}\right)^{\frac{3}{5}} q_\mathrm{e}^{\frac{28}{5}} m_\mathrm{e}^{-4} m_\mathrm{p}^{-\frac{3}{5}} c^{-\frac{18}{5}} \varepsilon_\mathrm{B}^{\frac{6}{5}} \rho^{\frac{9}{5}} \Gamma_2^{\frac{22}{5}} R^{\frac{3}{5}} t\,. \tag{2.26}$$

In practice there is one other case which is observed, namely slow cooling with $\nu_\mathrm{m} \ll \nu_\mathrm{a} \ll \nu_\mathrm{c}$:

$$\begin{aligned}\nu_\mathrm{a} \;=\; & (2)^{\frac{9p-22}{6(p+4)}}\,(3)^{\frac{8}{3(p+4)}}\,\pi^{-\frac{p+2}{2(p+4)}} \left(\frac{1+X}{2}\right)^{-\frac{2(p+2)}{p+4}} (p-2)^{\frac{2(p-1)}{p+4}} (p+2)^{\frac{2}{p+4}} (p-1)^{-\frac{2(p-2)}{p+4}} \\ & \left(\Gamma\left(\frac{p}{2}+\frac{1}{3}\right)\right)^{\frac{2}{p+4}} q_\mathrm{e}^{\frac{p+6}{p+4}} m_\mathrm{e}^{-\frac{3p+2}{p+4}} m_\mathrm{p}^{\frac{2(p-2)}{p+4}} c^{-\frac{2}{p+4}} \varepsilon_\mathrm{e}^{\frac{2(p-1)}{p+4}} \varepsilon_\mathrm{B}^{\frac{p+2}{2(p+4)}} \rho^{\frac{p+6}{2(p+4)}} \Gamma_2^{\frac{4(p+1)}{p+4}} R^{\frac{2}{p+4}}\end{aligned} \tag{2.27}$$

Now $\nu_{\rm c}$, $\nu_{\rm m}$, $\nu_{\rm a}$ and $F_{\nu,\rm max}$ are functions of Γ_2 and R. The evolution of the shock determines the time-dependence of Γ_2 and R. There are three phases in this evolution: the extreme relativistic phase, the jet-spreading phase, and the non-relativistic phase. In the extreme relativistic phase the shock ploughs through the external medium with an ultra-relativistic velocity in a jet geometry with a constant opening angle θ_0. The shock gradually decelerates until the jet opening angle is approximately equal to Γ_2^{-1}. From this moment on, which is called the jet break time $t_{\rm j}$, the jet starts to spread sideways, i.e. the jet-spreading phase. When the shock has become (almost) spherical, it also becomes non-relativistic, and at this time $t_{\rm nr}$, the evolution enters its non-relativistic phase.

We consider two extreme limits for the hydrodynamical evolution of the shock in the extreme relativistic phase: either fully adiabatic or fully radiative. In the distinction between these two cases an important role is reserved for the following timescales: the cooling timescale $\tau_{\rm cool}$, the lifetime of the source $\tau_{\rm source}$ and the expansion timescale $\tau_{\rm exp}$. In the discussion about slow and fast cooling it was pointed out that $\tau_{\rm cool} < \tau_{\rm source}$ corresponds to fast cooling, while $\tau_{\rm cool} > \tau_{\rm source}$ corresponds to slow cooling. The distinction between adiabatic and radiative evolution is embedded in the ratio between the cooling and the expansion timescale. When $\tau_{\rm cool} < \tau_{\rm exp}$ the energy in the electrons is emitted faster than injection through expansion can supply new electrons, so this corresponds to radiative expansion. When $\tau_{\rm cool} > \tau_{\rm exp}$ the energy is supplied faster than it can be radiated away, so this corresponds to an adiabatic evolution. It is obvious that the expansion timescale $\tau_{\rm exp}$ is always smaller than the lifetime of the source $\tau_{\rm source}$. These relations between the different timescales at hand give rise to the following possibilities for the evolution of the spectrum: radiative fast cooling ($\tau_{\rm cool} < \tau_{\rm exp} < \tau_{\rm source}$), adiabatic fast cooling ($\tau_{\rm exp} < \tau_{\rm cool} < \tau_{\rm source}$), and adiabatic slow cooling ($\tau_{\rm exp} < \tau_{\rm source} < \tau_{\rm cool}$).

To describe the temporal evolution of the spectrum, one needs to determine $R(t)$ and $\Gamma_2(t)$. In the extreme relativistic phase we use the relations between R and Γ_2 from Blandford & McKee (1976):

$$E = \alpha_{\rm ad}\pi\rho c^2\Gamma_2^2 R^3 = \alpha_{\rm ad}\pi\rho_0 c^2\Gamma_2^2 R^{3-k} \quad \text{(adiabatic)}\,, \tag{2.28}$$

$$E_0 = \alpha_{\rm rad}\pi\rho c^2\Gamma_0\Gamma_2 R^3 = \alpha_{\rm rad}\pi\rho_0 c^2\Gamma_0\Gamma_2 R^{3-k} \quad \text{(radiative)}\,, \tag{2.29}$$

in which $\alpha_{\rm ad} = \alpha_{\rm rad} = 16/(17-4k)$. In order to obtain expressions for $R(t)$ and $\Gamma_2(t)$ one needs the following equation:

$$R = \beta_{\rm ad}\Gamma_2^2 ct = \beta_{\rm rad}\Gamma_2^2 ct\,, \tag{2.30}$$

with $\beta_{\rm ad} = \beta_{\rm rad} = 4 - k$. The resulting expressions for $R(t)$ and $\Gamma_2(t)$ are:

$$R = \begin{cases} (\beta_{\rm ad} E t)^{\frac{1}{4-k}} \, (\alpha_{\rm ad} \pi \rho_0 c)^{-\frac{1}{4-k}} & \text{(adiabatic)}\,, \\ \left(\beta_{\rm rad} E_0^2 t\right)^{\frac{1}{7-2k}} \left(\alpha_{\rm rad}^2 \pi^2 \rho_0^2 \Gamma_0^2 c^3\right)^{-\frac{1}{7-2k}} & \text{(radiative)}\,, \end{cases} \tag{2.31}$$

$$\Gamma_2 = \begin{cases} \left(\alpha_{\rm ad} \beta_{\rm ad}^{3-k} \pi c^{5-k} \rho_0 E^{-1} t^{3-k}\right)^{-\frac{1}{2(4-k)}} & \text{(adiabatic)}\,, \\ \left(\alpha_{\rm rad} \beta_{\rm rad}^{3-k} \pi c^{5-k} \rho_0 E_0^{-1} \Gamma_0 t^{3-k}\right)^{-\frac{1}{7-2k}} & \text{(radiative)}\,. \end{cases} \tag{2.32}$$

The results of substituting these expressions in the equations for $\nu_{\rm m}$, $\nu_{\rm c}$, $\nu_{\rm a}$ and $F_{\nu,\rm max}$ are shown in Tables 2.2 to 2.6, for both the radiative and adiabatic evolution. In both tables we have written the exact equations for an arbitrary value for k, as well as the cases that are often studied, i.e. a homogeneous external medium ($k = 0$) and a massive stellar wind ($k = 2$).

The opening angle of the jet θ_0 is given by Γ_2^{-1} at $t = t_{\rm j}$:

$$\theta_0 = \left(\alpha_{\rm ad} \beta_{\rm ad}^{3-k} \pi c^{5-k} \rho_0 E^{-1} t_{\rm j}^{3-k}\right)^{\frac{1}{2(4-k)}} \,, \tag{2.33}$$

so for $k = 0$:

$$\theta_0 = \left(\alpha_{\rm ad} \beta_{\rm ad}^3 \pi m_{\rm p} c^5 n E^{-1} t_{\rm j}^3 (1+z)^{-3}\right)^{\frac{1}{8}} \simeq 0.126 \cdot n_0^{\frac{1}{8}} \, E_{52}^{-\frac{1}{8}} \, t_{\rm j,d}^{\frac{3}{8}} \left(\frac{1+z}{2}\right)^{-\frac{3}{8}} \,, \tag{2.34}$$

and for $k = 2$:

$$\theta_0 = \left(\alpha_{\rm ad} \beta_{\rm ad} \pi c^3 A E^{-1} t_{\rm j} (1+z)^{-1}\right)^{\frac{1}{4}} \simeq 0.160 \cdot A_*^{\frac{1}{4}} \, E_{52}^{-\frac{1}{4}} \, t_{\rm j,d}^{\frac{1}{4}} \left(\frac{1+z}{2}\right)^{-\frac{1}{4}} \,. \tag{2.35}$$

The beaming-corrected energy is $E_j = (1 - \cos(\theta_0))E \simeq \theta_0^2 E/2$.

When the extreme relativistic blast wave has decelerated until $\theta_0 \simeq \Gamma_2^{-1}$, the jet-spreading phase starts. The time-dependence of Γ_2 and R then changes from $R \propto t^{\frac{1}{7-2k}}$, $\Gamma_2 \propto t^{-\frac{3-k}{7-2k}}$ (radiative) or $R \propto t^{\frac{1}{4-k}}$, $\Gamma_2 \propto t^{-\frac{3-k}{2(4-k)}}$ (adiabatic), to $R \propto t^0$, $\Gamma_2 \propto t^{-\frac{1}{2}}$ (Rhoads 1999). After $t_{\rm nr}$ the blast wave becomes non-relativistic, so $\Gamma_2 \sim 1$, and we can apply the Sedov-Taylor solutions $R \propto t^{\frac{2}{5-k}}$, $\beta_2 \propto t^{-\frac{3-k}{5-k}}$, with β_2 the bulk-velocity of the shocked medium in the frame of the unshocked medium divided by the speed of light.

The characteristic frequencies and $F_{\nu,\rm max}$ depend on $R(t)$, $\Gamma_2(t)$, $\beta_2(t)$ and t. We assume that the scalings on $R(t)$ are the same in all three of the phases in the blast wave evolution, and the scalings on $\Gamma_2(t)$ are only applicable to the extreme relativistic and the jet-spreading phase. For the scalings in the non-relativistic phase we use the Rankine-Hugoniot jump conditions: the particle density and nucleon energy density behind the shock are given by $4\rho/m_{\rm p}$ and $2\rho\beta_2^2 c^2$ respectively. This leads to $\gamma_{\rm m} = m_{\rm p}(p-2)\varepsilon_{\rm e}\beta_2^2 / \left[(1+X)m_{\rm e}(p-1)\right]$, $B = 4\beta_2 c\sqrt{\pi\rho\varepsilon_{\rm B}}$ and $\gamma_{\rm c} = 9m_{\rm e}^3 c^3 / \left(64\pi q_{\rm e}^4 \beta_2^2 \varepsilon_{\rm B}\rho t\right)$. Since in the non-relativistic case $\nu_e = \gamma_{\rm e}^2 q_{\rm e} B/(2\pi m_{\rm e} c)$, the cooling frequency $\nu_{\rm c} \propto \Gamma_2\,\gamma_{\rm c}^2\, B \propto R^{\frac{3k}{2}}\,\Gamma_2^{-4}\,\beta_2^{-3}\,t^{-2}$, the peak frequency $\nu_{\rm m} \propto \Gamma_2\,\gamma_{\rm m}^2\, B \propto R^{-\frac{k}{2}}\,\Gamma_2^4\,\beta_2^5$, the peak flux $F_{\nu,\rm max} \propto R^3\,\rho\,\Gamma_2\,B \propto R^{\frac{3(2-k)}{2}}\,\Gamma_2^2\,\beta_2$, and the self-absorption frequency $\nu_{\rm a} \propto R^{\frac{3-4k}{5}}\,\Gamma_2^{\frac{2}{5}}\,\beta_2^{-\frac{8}{5}}$ $(\nu_{\rm a} < \nu_{\rm m} < \nu_{\rm c})$, $\nu_{\rm a} \propto R^{\frac{3(1-3k)}{5}}\,\Gamma_2^{\frac{22}{5}}\,\beta_2^{\frac{12}{5}}\,t$ $(\nu_{\rm a} < \nu_{\rm c} < \nu_{\rm m})$ or $\nu_{\rm a} \propto R^{\frac{4-6k-pk}{2(p+4)}}\,\Gamma_2^{\frac{4(p+1)}{p+4}}\,\beta_2^{\frac{5p-2}{p+4}}$ $(\nu_{\rm m} < \nu_{\rm a} < \nu_{\rm c})$. The scalings of the spectral flux on $R(t)$, $\Gamma_2(t)$, $\beta_2(t)$ and t in different parts of the broadband spectrum are given in Table 2.8.

The spectral flux in all the different parts of the broadband spectrum as a function of time in the three phases of the blast wave evolution can now be determined. The results are shown in the Tables 2.9, 2.10 and 2.11: the radiative extreme relativistic phase (only valid in the case of fast cooling with $\nu_{\rm c} < \nu_{\rm m}$) in Table 2.9; the adiabatic extreme relativistic phase and the jet-spreading phase in Table 2.10, and the non-relativistic phase in Table 2.11. The expressions for an arbitrary value of k are also given for some spectral regimes in the extreme relativistic phase in Yost et al. (2003).

2.9 Appendix C: Modeling light curves

In our method of modeling the afterglow light curves we use the synchrotron SEDs as described in Appendix 2.7 and the aymptotic temporal behaviour of the three break frequencies and the peak flux in the three phases of the blast wave evolution. In practice this means that we describe $F_{\nu,\rm max}$, $\nu_{\rm c}$, $\nu_{\rm m}$ and $\nu_{\rm a}$ as functions $f = f_{\rm n}\cdot b(t, t_{\rm j}, t_{\rm nr})$, with $f_{\rm n}$ functions of the physical parameters, as given in Tables 2.2 to 2.6; and we describe $b(t, t_{\rm j}, t_{\rm nr})$ as a smoothly broken power-law with three slopes. The functional form of the smoothly broken power-laws depends on the relative difference between the three slopes, and these relativive differences for $F_{\nu,\rm max}$, $\nu_{\rm c}$, $\nu_{\rm m}$ and $\nu_{\rm a}$ depend on the values of p and k. Therefore, we give a general discription for the smoothly broken power-laws with three slopes: α_1 for $t < t_{\rm j}$, α_2 for $t_{\rm j} < t < t_{\rm nr}$, and α_3 for $t_{\rm nr} < t$. The three slopes can then be taken from the Tables 2.9, 2.10 and 2.11. The functional forms are:

$$\alpha_1 < \alpha_2 < \alpha_3 \;\Rightarrow\; b = \left\{\left(\frac{t}{t_{\rm j}}\right)^{\alpha_1 s} + \left(\frac{t}{t_{\rm nr}}\right)^{\alpha_2 s} + \left(\frac{t_{\rm j}}{t_{\rm nr}}\right)^{\alpha_2 s}\left(\frac{t}{t_{\rm nr}}\right)^{\alpha_3 s}\right\}^{1/s}, \qquad (2.36)$$

$$\alpha_1 < \alpha_3 < \alpha_2 \;\Rightarrow\; b = \left\{ \left(\frac{t}{t_{\rm j}}\right)^{\alpha_1 s} + \left(\frac{t}{t_{\rm nr}}\right)^{-\alpha_2 s} + \left(\frac{t_{\rm j}}{t_{\rm nr}}\right)^{-\alpha_2 s} \left(\frac{t}{t_{\rm nr}}\right)^{-\alpha_3 s} \right\}^{1/s} , \quad (2.37)$$

$$\alpha_2 < \alpha_1 < \alpha_3 \;\Rightarrow\; b = \left\{ \left[\left(\frac{t}{t_{\rm j}}\right)^{-\alpha_1 s} + \left(\frac{t}{t_{\rm nr}}\right)^{-\alpha_2 s} \right] + \left(\frac{t_{\rm j}}{t_{\rm nr}}\right)^{\alpha_2 s} \left(\frac{t}{t_{\rm nr}}\right)^{\alpha_3 s} \right\}^{1/s} , \quad (2.38)$$

$$\alpha_2 < \alpha_3 < \alpha_1 \;\Rightarrow\; b = \left\{ \left(\frac{t}{t_{\rm j}}\right)^{-\alpha_1 s} + \left[\left(\frac{t}{t_{\rm nr}}\right)^{\alpha_2 s} + \left(\frac{t_{\rm j}}{t_{\rm nr}}\right)^{\alpha_2 s} \left(\frac{t}{t_{\rm nr}}\right)^{\alpha_3 s} \right] \right\}^{-1/s} , \quad (2.39)$$

$$\alpha_3 < \alpha_1 < \alpha_2 \;\Rightarrow\; b = \left\{ \left[\left(\frac{t}{t_{\rm j}}\right)^{\alpha_1 s} + \left(\frac{t}{t_{\rm nr}}\right)^{\alpha_2 s} \right] + \left(\frac{t_{\rm j}}{t_{\rm nr}}\right)^{-\alpha_2 s} \left(\frac{t_{\rm j}}{t_{\rm nr}}\right)^{-\alpha_3 s} \right\}^{-1/s} , \quad (2.40)$$

$$\alpha_3 < \alpha_2 < \alpha_1 \;\Rightarrow\; b = \left\{ \left(\frac{t}{t_{\rm j}}\right)^{-\alpha_1 s} + \left(\frac{t}{t_{\rm nr}}\right)^{-\alpha_2 s} + \left(\frac{t_{\rm j}}{t_{\rm nr}}\right)^{-\alpha_2 s} \left(\frac{t}{t_{\rm nr}}\right)^{-\alpha_3 s} \right\}^{-1/s} . \quad (2.41)$$

The smoothening parameter s can be varied, but in this paper we fix it to $s = 10$ (transitions become sharper when s increases). In the case of $\nu_{\rm a}$ there is actually the possibility that there are four different slopes in the full temporal range of the afterglow, since its temporal behaviour changes when $\nu_{\rm m}$ passes $\nu_{\rm a}$. For this situation we use smoothly broken power-laws with four slopes, constructed in a similar way as the functional forms given above.

Acknowledgements We thank E. Rol and L. Kaper for useful discussions. RAMJW gratefully acknowledges support of NWO under grant 639.043.302. The authors acknowledge benefits from collaboration within the Research Training Network ”Gamma-Ray Bursts: An Enigma and a Tool”, funded by the EU under contract HPRN-CT-2002-00294.

$$
\begin{aligned}
F_{\nu,\mathrm{max}} &= \tfrac{4}{3}\sqrt{2}\alpha_{\mathrm{rad}}^{-\frac{8-3k}{7-2k}}\beta_{\mathrm{rad}}^{-\frac{6-k}{2(7-2k)}}\pi^{-\frac{9-4k}{7-2k}}\left(\tfrac{1+X}{2}\right)q_{\mathrm{e}}^{3}m_{\mathrm{e}}^{-1}m_{\mathrm{p}}^{-1}c^{-\frac{52-17k}{2(7-2k)}}\varepsilon_{\mathrm{B}}^{\frac{1}{2}}\rho_0^{\frac{5}{2(7-2k)}}E_0^{\frac{8-3k}{7-2k}}\Gamma_0^{-\frac{8-3k}{7-2k}}D_{\mathrm{L}}^{-2}t^{-\frac{6-k}{2(7-2k)}}\,(1+z)^{\frac{5(4-k)}{2(7-2k)}}\\
\nu_{\mathrm{c}} &= \tfrac{81}{8192}\sqrt{2}\alpha_{\mathrm{rad}}^{\frac{4-3k}{7-2k}}\beta_{\mathrm{rad}}^{\frac{24-5k}{2(7-2k)}}\pi^{-\frac{27-4k}{7-2k}}q_{\mathrm{e}}^{-7}m_{\mathrm{e}}^{5}c^{\frac{124-41k}{2(7-2k)}}\varepsilon_{\mathrm{B}}^{-\frac{3}{2}}\rho_0^{-\frac{13}{2(7-2k)}}E_0^{-\frac{4-3k}{7-2k}}\Gamma_0^{\frac{4-3k}{7-2k}}t^{-\frac{4-3k}{2(7-2k)}}\,(1+z)^{-\frac{10-k}{2(7-2k)}}\\
\nu_{\mathrm{m}} &= 2\sqrt{2}\alpha_{\mathrm{rad}}^{-\frac{4-k}{7-2k}}\beta_{\mathrm{rad}}^{-\frac{24-7k}{2(7-2k)}}\pi^{-\frac{15-4k}{2(7-2k)}}\left(\tfrac{1+X}{2}\right)^{-2}(p-2)^2\,(p-1)^{-2}\,q_{\mathrm{e}}m_{\mathrm{e}}^{-3}m_{\mathrm{p}}^{2}c^{-\frac{40-11k}{2(7-2k)}}\\
&\quad\cdot\varepsilon_{\mathrm{e}}^{2}\varepsilon_{\mathrm{B}}^{\frac{1}{2}}\rho_0^{-\frac{1}{2(7-2k)}}E_0^{\frac{4-k}{7-2k}}\Gamma_0^{-\frac{4-k}{7-2k}}t^{-\frac{24-7k}{2(7-2k)}}\,(1+z)^{\frac{10-3k}{2(7-2k)}}\\
\nu_{\mathrm{a}} &= (2)^{\frac{28}{5}}\,(3)^{-\frac{3}{5}}\,\alpha_{\mathrm{rad}}^{-\frac{2(14-9k)}{5(7-2k)}}\beta_{\mathrm{rad}}^{-\frac{63-13k}{5(7-2k)}}\pi^{\frac{2k}{7-2k}}\left(\tfrac{1+X}{2}\right)^{\frac{3}{5}}q_{\mathrm{e}}^{\frac{28}{5}}m_{\mathrm{e}}^{-4}m_{\mathrm{p}}^{-\frac{3}{5}}c^{-\frac{49-17k}{7-2k}}\\
&\quad\cdot\varepsilon_{\mathrm{B}}^{\frac{6}{5}}\rho_0^{\frac{7}{7-2k}}E_0^{\frac{2(14-9k)}{5(7-2k)}}\Gamma_0^{-\frac{2(14-9k)}{5(7-2k)}}t^{-\frac{28-3k}{5(7-2k)}}\,(1+z)^{-\frac{7(1-k)}{5(7-2k)}}
\end{aligned}
$$

Table 2.2 — Expressions for $F_{\nu,\mathrm{max}}$, ν_{c}, ν_{m} and ν_{a} in the case of an ultra-relativistic shock moving into an external medium with density $\rho = \rho_0 R^{-k}$, assuming that the evolution is fully radiative, in the situation $\nu_{\mathrm{a}} < \nu_{\mathrm{c}} < \nu_{\mathrm{m}}$. In the case of a homogeneous ($k = 0$) medium $\rho_0 = nm_p$, and in the stellar wind ($k = 2$) case $\rho_0 = A = \dot{M}/(4\pi v_w^2)$, with $\dot{M}$ the mass-loss rate and v_w the wind velocity. We adopt $\alpha_{\mathrm{ad}} = \alpha_{\mathrm{rad}} = 16/(17-4k), \beta_{\mathrm{ad}} = \beta_{\mathrm{rad}} = 4-k$, $X = 0.7$ and $p = 2.2$, and use the notation for variables $Q_x = 10^x Q$, with the exception of A_* which is A for $\dot{M} = 10^{-5}$ solar masses per year and $v_w = 10^3$ km/sec.

$$\begin{aligned}
F_{\nu,\mathrm{max}} &= \tfrac{4}{3}\sqrt{2}\alpha_{\mathrm{rad}}^{-\frac{8}{7}}\beta_{\mathrm{rad}}^{-\frac{3}{7}}\pi^{-\frac{9}{7}}\left(\tfrac{1+X}{2}\right)q_{\mathrm{e}}^{3}m_{\mathrm{e}}^{-1}m_{\mathrm{p}}^{-\frac{9}{14}}c^{-\frac{26}{7}}\varepsilon_{\mathrm{B}}^{\frac{1}{2}}n^{\frac{5}{14}}E_{0}^{\frac{8}{7}}\Gamma_{0}^{-\frac{8}{7}}D_{\mathrm{L}}^{-2}t^{-\frac{3}{7}}\,(1+z)^{\frac{10}{7}} \\
&\simeq 109\cdot\,\varepsilon_{\mathrm{B},-1}^{\frac{1}{2}}\,n_0^{\frac{5}{14}}\,E_{0,54}^{\frac{8}{7}}\,\Gamma_{0,2}^{-\frac{8}{7}}\,d_{L,28}^{-2}\,t_{\mathrm{d}}^{-\frac{3}{7}}\,\left(\tfrac{1+z}{2}\right)^{\frac{10}{7}}\ \mathrm{mJy} \\
\nu_{\mathrm{c}} &= frac818192\,\sqrt{2}\alpha_{\mathrm{rad}}^{\frac{4}{7}}\beta_{\mathrm{rad}}^{\frac{12}{7}}\pi^{-\frac{27}{7}}q_{\mathrm{e}}^{-7}m_{\mathrm{e}}^{5}m_{\mathrm{p}}^{-\frac{13}{14}}c^{\frac{62}{7}}\varepsilon_{\mathrm{B}}^{-\frac{3}{2}}n^{-\frac{13}{14}}E_{0}^{-\frac{4}{7}}\Gamma_{0}^{\frac{4}{7}}t^{-\frac{2}{7}}\,(1+z)^{-\frac{5}{7}} \\
&\simeq 2.01\cdot10^{12}\cdot\,\varepsilon_{\mathrm{B},-1}^{-\frac{3}{2}}\,n_0^{-\frac{13}{14}}\,E_{0,54}^{-\frac{4}{7}}\,\Gamma_{0,2}^{\frac{4}{7}}\,t_{\mathrm{d}}^{-\frac{2}{7}}\left(\tfrac{1+z}{2}\right)^{-\frac{5}{7}}\ \mathrm{Hz} \\
\nu_{\mathrm{m}} &= 2\sqrt{2}\alpha_{\mathrm{rad}}^{-\frac{4}{7}}\beta_{\mathrm{rad}}^{-\frac{12}{7}}\pi^{-\frac{15}{14}}\left(\tfrac{1+X}{2}\right)^{-2}(p-2)^{2}\,(p-1)^{-2}\,q_{\mathrm{e}}m_{\mathrm{e}}^{-3}m_{\mathrm{p}}^{\frac{27}{14}}c^{-\frac{20}{7}}\varepsilon_{\mathrm{e}}^{2}\varepsilon_{\mathrm{B}}^{\frac{1}{2}}n^{-\frac{1}{14}}E_{0}^{\frac{4}{7}}\Gamma_{0}^{-\frac{4}{7}}t^{-\frac{12}{7}}\,(1+z)^{\frac{5}{7}} \\
&\simeq 2.94\cdot10^{12}\cdot\,\varepsilon_{\mathrm{e},-1}^{2}\,\varepsilon_{\mathrm{B},-1}^{\frac{1}{2}}\,n_0^{-\frac{1}{14}}\,E_{0,54}^{\frac{4}{7}}\,\Gamma_{0,2}^{-\frac{4}{7}}\,t_{\mathrm{d}}^{-\frac{12}{7}}\,\left(\tfrac{1+z}{2}\right)^{\frac{5}{7}}\ \mathrm{Hz} \\
\nu_{\mathrm{a}} &= (2)^{\frac{28}{5}}\,(3)^{-\frac{3}{5}}\,\alpha_{\mathrm{rad}}^{-\frac{4}{5}}\beta_{\mathrm{rad}}^{-\frac{9}{5}}\left(\tfrac{1+X}{2}\right)^{\frac{3}{5}}\,q_{\mathrm{e}}^{\frac{28}{5}}\,m_{\mathrm{e}}^{-4}m_{\mathrm{p}}^{\frac{2}{5}}c^{-7}\varepsilon_{\mathrm{B}}^{\frac{6}{5}}nE_{0}^{\frac{4}{5}}\Gamma_{0}^{-\frac{4}{5}}t^{-\frac{4}{5}}\,(1+z)^{-\frac{1}{5}} \\
&\simeq 6.56\cdot10^{9}\cdot\,\varepsilon_{\mathrm{B},-1}^{\frac{6}{5}}\,n_0\,E_{0,54}^{\frac{4}{5}}\,\Gamma_{0,2}^{-\frac{4}{5}}\,t_{\mathrm{d}}^{-\frac{4}{5}}\,\left(\tfrac{1+z}{2}\right)^{-\frac{1}{5}}\ \mathrm{Hz}
\end{aligned}$$

Table 2.3 — Expressions for $F_{\nu,\mathrm{max}}$, ν_{c}, ν_{m} and ν_{a} in the case of an ultra-relativistic shock moving into a homogeneous medium ($k = 0$). Further details can be found in the caption of Table 2.2.

$$\begin{aligned}
F_{\nu,\mathrm{max}} &= \tfrac{4}{3}\sqrt{2}\alpha_{\mathrm{rad}}^{-\frac{2}{3}}\beta_{\mathrm{rad}}^{-\frac{2}{3}}\pi^{-\frac{1}{3}}\left(\tfrac{1+X}{2}\right)q_{\mathrm{e}}^{3}m_{\mathrm{e}}^{-1}m_{\mathrm{p}}^{-1}c^{-3}\varepsilon_{\mathrm{B}}^{\frac{1}{2}}A^{\frac{5}{6}}E_{0}^{\frac{2}{3}}\Gamma_{0}^{-\frac{2}{3}}D_{\mathrm{L}}^{-2}t^{-\frac{2}{3}}\,(1+z)^{\frac{5}{3}} \\
&\simeq 170\cdot\,\varepsilon_{\mathrm{B},-1}^{\frac{1}{2}}\,A_{*}^{\frac{5}{6}}\,E_{0,54}^{\frac{2}{3}}\,\Gamma_{0,2}^{-\frac{2}{3}}\,d_{L,28}^{-2}\,t_{\mathrm{d}}^{-\frac{2}{3}}\,\left(\tfrac{1+z}{2}\right)^{\frac{5}{3}}\ \mathrm{mJy} \\
\nu_{\mathrm{c}} &= \tfrac{81}{8192}\sqrt{2}\alpha_{\mathrm{rad}}^{-\frac{2}{3}}\beta_{\mathrm{rad}}^{\frac{7}{3}}\pi^{-\frac{19}{3}}q_{\mathrm{e}}^{-7}m_{\mathrm{e}}^{5}c^{7}\varepsilon_{\mathrm{B}}^{-\frac{3}{2}}A^{-\frac{13}{6}}E_{0}^{\frac{2}{3}}\Gamma_{0}^{-\frac{2}{3}}t^{\frac{1}{3}}\,(1+z)^{-\frac{4}{3}} \\
&\simeq 9.02\cdot 10^{10}\cdot\,\varepsilon_{\mathrm{B},-1}^{-\frac{3}{2}}\,A_{*}^{-\frac{13}{6}}\,E_{0,54}^{\frac{2}{3}}\,\Gamma_{0,2}^{-\frac{2}{3}}\,t_{\mathrm{d}}^{\frac{1}{3}}\,\left(\tfrac{1+z}{2}\right)^{-\frac{4}{3}}\ \mathrm{Hz} \\
\nu_{\mathrm{m}} &= 2\sqrt{2}\alpha_{\mathrm{rad}}^{-\frac{2}{3}}\beta_{\mathrm{rad}}^{-\frac{5}{3}}\pi^{-\frac{7}{6}}\left(\tfrac{1+X}{2}\right)^{-2}(p-2)^{2}\,(p-1)^{-2}\,q_{\mathrm{e}}m_{\mathrm{e}}^{-3}m_{\mathrm{p}}^{2}c^{-3}\varepsilon_{\mathrm{e}}^{2}\varepsilon_{\mathrm{B}}^{\frac{1}{2}}A^{-\frac{1}{6}}E_{0}^{\frac{2}{3}}\Gamma_{0}^{-\frac{2}{3}}t^{-\frac{5}{3}}\,(1+z)^{\frac{2}{3}} \\
&\simeq 6.27\cdot 10^{12}\cdot\,\varepsilon_{\mathrm{e},-1}^{2}\,\varepsilon_{\mathrm{B},-1}^{\frac{1}{2}}\,A_{*}^{-\frac{1}{6}}\,E_{0,54}^{\frac{2}{3}}\,\Gamma_{0,2}^{-\frac{2}{3}}\,t_{\mathrm{d}}^{-\frac{5}{3}}\,\left(\tfrac{1+z}{2}\right)^{\frac{2}{3}}\ \mathrm{Hz} \\
\nu_{\mathrm{a}} &= (2)^{\frac{28}{5}}\,(3)^{-\frac{3}{5}}\,\alpha_{\mathrm{rad}}^{\frac{8}{15}}\beta_{\mathrm{rad}}^{-\frac{37}{15}}\pi^{\frac{4}{3}}\left(\tfrac{1+X}{2}\right)^{\frac{3}{5}}\,q_{\mathrm{e}}^{\frac{28}{5}}\,m_{\mathrm{e}}^{-4}m_{\mathrm{p}}^{-\frac{3}{5}}c^{-5}\varepsilon_{\mathrm{B}}^{\frac{6}{5}}A^{\frac{7}{3}}E_{0}^{-\frac{8}{15}}\Gamma_{0}^{\frac{8}{15}}t^{-\frac{22}{15}}\,(1+z)^{\frac{7}{15}} \\
&\simeq 3.47\cdot 10^{10}\cdot\,\varepsilon_{\mathrm{B},-1}^{\frac{6}{5}}\,A_{*}^{\frac{7}{3}}\,E_{0,54}^{-\frac{8}{15}}\,\Gamma_{0,2}^{\frac{8}{15}}\,t_{\mathrm{d}}^{-\frac{22}{15}}\,\left(\tfrac{1+z}{2}\right)^{\frac{7}{15}}\ \mathrm{Hz}
\end{aligned}$$

Table 2.4 — Expressions for $F_{\nu,\mathrm{max}}$, ν_{c}, ν_{m} and ν_{a} in the case of an ultra-relativistic shock moving into a stellar wind ($k = 2$). Further details can be found in the caption of Table 2.2.

$$
\begin{aligned}
F_{\nu,\mathrm{max}} &= \tfrac{4}{3}\,\sqrt{2}\alpha_{\mathrm{ad}}^{-\frac{8-3k}{2(4-k)}}\beta_{\mathrm{ad}}^{-\frac{k}{2(4-k)}}\pi^{-\frac{2-k}{4-k}}\left(\tfrac{1+X}{2}\right)q_{\mathrm{e}}^{3}m_{\mathrm{e}}^{-1}m_{\mathrm{p}}^{-1}c^{-\frac{24-7k}{2(4-k)}}\,\varepsilon_{\mathrm{B}}^{\frac{1}{2}}\rho_0^{\frac{2}{4-k}}\,E^{\frac{8-3k}{2(4-k)}}D_{\mathrm{L}}^{-2}t^{-\frac{k}{2(4-k)}}\,(1+z)^{\frac{8-k}{2(4-k)}} \\
\nu_{\mathrm{c}} &= \tfrac{81}{8192}\,\sqrt{2}\alpha_{\mathrm{ad}}^{\frac{4-3k}{2(4-k)}}\beta_{\mathrm{ad}}^{\frac{12-k}{2(4-k)}}\pi^{-\frac{8-k}{4-k}}q_{\mathrm{e}}^{-7}m_{\mathrm{e}}^{5}c^{\frac{68-19k}{2(4-k)}}\,\varepsilon_{\mathrm{B}}^{-\frac{3}{2}}\rho_0^{-\frac{4}{4-k}}E^{-\frac{4-3k}{2(4-k)}}t^{-\frac{4-3k}{2(4-k)}}\,(1+z)^{-\frac{4+k}{2(4-k)}} \\
\nu_{\mathrm{m}} &= 2\,\sqrt{2}\alpha_{\mathrm{ad}}^{-\frac{1}{2}}\beta_{\mathrm{ad}}^{-\frac{3}{2}}\pi^{-1}\left(\tfrac{1+X}{2}\right)^{-2}(p-2)^{2}\,(p-1)^{-2}\,q_{\mathrm{e}}m_{\mathrm{e}}^{-3}m_{\mathrm{p}}^{2}c^{-\frac{5}{2}}\varepsilon_{\mathrm{e}}^{2}\varepsilon_{\mathrm{B}}^{\frac{1}{2}}E^{\frac{1}{2}}t^{-\frac{3}{2}}\,(1+z)^{\frac{1}{2}} \\
\nu_{\mathrm{a}}\ (\nu_{\mathrm{a}}<\nu_{\mathrm{m}}<\nu_{\mathrm{c}}) &= 2\,(3)^{\frac{4}{5}}\,\alpha_{\mathrm{ad}}^{-\frac{4(1-k)}{5(4-k)}}\beta_{\mathrm{ad}}^{-\frac{3k}{5(4-k)}}\pi^{\frac{4+2k}{5(4-k)}}\left(\tfrac{1+X}{2}\right)^{\frac{8}{5}}(p-2)^{-1}\,(p-1)^{\frac{8}{5}}\left(p+\tfrac{2}{3}\right)^{-\frac{3}{5}}(p+2)^{\frac{3}{5}}\,q_{\mathrm{e}}^{\frac{8}{5}}m_{\mathrm{p}}^{-\frac{8}{5}}c^{-\frac{4(5-2k)}{5(4-k)}} \\
&\quad\cdot\varepsilon_{\mathrm{e}}^{-1}\varepsilon_{\mathrm{B}}^{\frac{1}{5}}\rho_0^{\frac{12}{5(4-k)}}E^{\frac{4(1-k)}{5(4-k)}}t^{-\frac{3k}{5(4-k)}}\,(1+z)^{-\frac{4(5-2k)}{5(4-k)}} \\
\nu_{\mathrm{a}}\ (\nu_{\mathrm{a}}<\nu_{\mathrm{c}}<\nu_{\mathrm{m}}) &= (2)^{\frac{28}{5}}\,(3)^{-\frac{3}{5}}\,\alpha_{\mathrm{ad}}^{-\frac{14-9k}{5(4-k)}}\beta_{\mathrm{ad}}^{-\frac{2(15-k)}{5(4-k)}}\pi^{\frac{2+5k}{5(4-k)}}\left(\tfrac{1+X}{2}\right)^{\frac{3}{5}}q_{\mathrm{e}}^{\frac{28}{5}}\,m_{\mathrm{e}}^{-4}m_{\mathrm{p}}^{-\frac{3}{5}}c^{-\frac{2(65-19k)}{5(4-k)}} \\
&\quad\cdot\varepsilon_{\mathrm{B}}^{\frac{6}{5}}\rho_0^{\frac{22}{5(4-k)}}E^{\frac{14-9k}{5(4-k)}}t^{-\frac{10+3k}{5(4-k)}}\,(1+z)^{-\frac{2(5-4k)}{5(4-k)}} \\
\nu_{\mathrm{a}}\ (\nu_{\mathrm{m}}<\nu_{\mathrm{a}}<\nu_{\mathrm{c}}) &= (2)^{\frac{9p-22}{6(p+4)}}\,(3)^{\frac{8}{3(p+4)}}\,\alpha_{\mathrm{ad}}^{-\frac{4(p+2)-k(p+6)}{2(4-k)(p+4)}}\beta_{\mathrm{ad}}^{-\frac{4(3p+2)-k(3p-2)}{2(4-k)(p+4)}}\pi^{-\frac{8(p+2)-2k(p+4)}{2(4-k)(p+4)}}\left(\tfrac{1+X}{2}\right)^{-\frac{2(p+2)}{p+4}}\left[\Gamma\left(\tfrac{p}{2}+\tfrac{1}{3}\right)\right]^{\frac{2}{p+4}} \\
&\quad\cdot(p-2)^{\frac{2(p-1)}{p+4}}(p-1)^{-\frac{2(p-2)}{p+4}}(p+2)^{\frac{2}{p+4}}q_{\mathrm{e}}^{\frac{p+6}{p+4}}m_{\mathrm{e}}^{-\frac{3p+2}{p+4}}m_{\mathrm{p}}^{\frac{2(p-2)}{p+4}}c^{-\frac{4(5p+10)-k(5p+14)}{2(4-k)(p+4)}} \\
&\quad\cdot\varepsilon_{\mathrm{e}}^{\frac{2(p-1)}{p+4}}\varepsilon_{\mathrm{B}}^{\frac{p+2}{2(p+4)}}\rho_0^{\frac{8}{(4-k)(p+4)}}E^{\frac{4(p+2)-k(p+6)}{2(4-k)(p+4)}}t^{-\frac{4(3p+2)-k(3p-2)}{2(4-k)(p+4)}}\,(1+z)^{\frac{4(p-6)-k(p-10)}{2(4-k)(p+4)}}
\end{aligned}
$$

Table 2.5 — Expressions for $F_{\nu,\mathrm{max}}$, ν_{c}, ν_{m}, and ν_{a}, in the case of an ultra-relativistic shock moving adiabatically into an external medium with density $\rho = \rho_0 R^{-k}$. Further details can be found in the caption of Table 2.2.

$$
\begin{aligned}
F_{\nu,\mathrm{max}} \quad & = \tfrac{4}{3}\sqrt{2}\alpha_{\mathrm{ad}}^{-1}\pi^{-\frac{1}{2}}\left(\tfrac{1+X}{2}\right)q_{\mathrm{e}}^{3}m_{\mathrm{e}}^{-1}m_{\mathrm{p}}^{-\frac{1}{2}}c^{-3}\varepsilon_{\mathrm{B}}^{\frac{1}{2}}n^{\frac{1}{2}}ED_{\mathrm{L}}^{-2}\,(1+z) \\
& \simeq 21.3\cdot\varepsilon_{\mathrm{B},-1}^{\frac{1}{2}}\,n_{0}^{\frac{1}{2}}\,E_{52}\,d_{L,28}^{-2}\,\left(\tfrac{1+z}{2}\right)\ \mathrm{mJy} \\
\nu_{\mathrm{c}} \quad & = \tfrac{81}{8192}\sqrt{2}\alpha_{\mathrm{ad}}^{\frac{1}{2}}\beta_{\mathrm{ad}}^{\frac{3}{2}}\pi^{-2}q_{\mathrm{e}}^{-7}m_{\mathrm{e}}^{5}m_{\mathrm{p}}^{-1}c^{\frac{17}{2}}\varepsilon_{\mathrm{B}}^{-\frac{3}{2}}n^{-1}E^{-\frac{1}{2}}t^{-\frac{1}{2}}\,(1+z)^{-\frac{1}{2}} \\
& \simeq 5.98\cdot 10^{13}\cdot\varepsilon_{\mathrm{B},-1}^{-\frac{3}{2}}\,n_{0}^{-1}\,E_{52}^{-\frac{1}{2}}\,t_{\mathrm{d}}^{-\frac{1}{2}}\,\left(\tfrac{1+z}{2}\right)^{-\frac{1}{2}}\ \mathrm{Hz} \\
\nu_{\mathrm{m}} \quad & 2 = \sqrt{2}\alpha_{\mathrm{ad}}^{-\frac{1}{2}}\beta_{\mathrm{ad}}^{-\frac{3}{2}}\pi^{-1}\left(\tfrac{1+X}{2}\right)^{-2}(p-2)^{2}\,(p-1)^{-2}\,q_{\mathrm{e}}m_{\mathrm{e}}^{-3}m_{\mathrm{p}}^{2}c^{-\frac{5}{2}}\varepsilon_{\mathrm{e}}^{2}\varepsilon_{\mathrm{B}}^{\frac{1}{2}}E^{\frac{1}{2}}t^{-\frac{3}{2}}\,(1+z)^{\frac{1}{2}} \\
& \simeq 8.98\cdot 10^{11}\cdot\varepsilon_{\mathrm{e},-1}^{2}\,\varepsilon_{\mathrm{B},-1}^{\frac{1}{2}}\,E_{52}^{\frac{1}{2}}\,t_{\mathrm{d}}^{-\frac{3}{2}}\,\left(\tfrac{1+z}{2}\right)^{\frac{1}{2}}\ \mathrm{Hz} \\
\nu_{\mathrm{a}}\ (\nu_{\mathrm{a}}<\nu_{\mathrm{m}}<\nu_{\mathrm{c}}) \quad & = 2\,(3)^{\frac{4}{5}}\,\alpha_{\mathrm{ad}}^{-\frac{1}{5}}\pi^{\frac{1}{5}}\left(\tfrac{1+X}{2}\right)^{\frac{8}{5}}(p-2)^{-1}\,(p-1)^{\frac{8}{5}}\left(p+\tfrac{2}{3}\right)^{-\frac{3}{5}}(p+2)^{\frac{3}{5}}\,q_{\mathrm{e}}^{\frac{8}{5}}m_{\mathrm{p}}^{-1}c^{-1}\varepsilon_{\mathrm{e}}^{-1}\varepsilon_{\mathrm{B}}^{\frac{1}{5}}n^{\frac{3}{5}}E^{\frac{1}{5}}\,(1+z)^{-1} \\
& \simeq 7.75\cdot 10^{10}\cdot\varepsilon_{\mathrm{e},-1}^{-1}\,\varepsilon_{\mathrm{B},-1}^{\frac{1}{5}}\,n_{0}^{\frac{3}{5}}\,E_{52}^{\frac{1}{5}}\,\left(\tfrac{1+z}{2}\right)^{-1}\ \mathrm{Hz} \\
\nu_{\mathrm{a}}\ (\nu_{\mathrm{a}}<\nu_{\mathrm{c}}<\nu_{\mathrm{m}}) \quad & = (2)^{\frac{28}{5}}\,(3)^{-\frac{3}{5}}\,\alpha_{\mathrm{ad}}^{-\frac{7}{10}}\beta_{\mathrm{ad}}^{-\frac{3}{2}}\pi^{\frac{1}{10}}\left(\tfrac{1+X}{2}\right)^{\frac{3}{5}}q_{\mathrm{e}}^{\frac{28}{5}}\,m_{\mathrm{e}}^{-4}m_{\mathrm{p}}^{\frac{1}{2}}c^{-\frac{13}{2}}\varepsilon_{\mathrm{B}}^{\frac{6}{5}}n^{\frac{11}{10}}E^{\frac{7}{10}}t^{-\frac{1}{2}}\,(1+z)^{-\frac{1}{2}} \\
& \simeq 1.25\cdot 10^{9}\cdot\varepsilon_{\mathrm{B},-1}^{\frac{6}{5}}\,n_{0}^{\frac{11}{10}}\,E_{52}^{\frac{7}{10}}\,t_{\mathrm{d}}^{-\frac{1}{2}}\,\left(\tfrac{1+z}{2}\right)^{-\frac{1}{2}}\ \mathrm{Hz} \\
\nu_{\mathrm{a}}\ (\nu_{\mathrm{m}}<\nu_{\mathrm{a}}<\nu_{\mathrm{c}}) \quad & = (2)^{\frac{9p-22}{6(p+4)}}\,(3)^{\frac{8}{3(p+4)}}\,\alpha_{\mathrm{ad}}^{-\frac{p+2}{2(p+4)}}\beta_{\mathrm{ad}}^{-\frac{3p+2}{2(p+4)}}\pi^{-\frac{p+2}{p+4}}\left(\tfrac{1+X}{2}\right)^{-\frac{2(p+2)}{p+4}}\left[\Gamma\left(\tfrac{p}{2}+\tfrac{1}{3}\right)\right]^{\frac{2}{p+4}}(p-2)^{\frac{2(p-1)}{p+4}}(p-1)^{-\frac{2(p-2)}{p+4}}(p+2)^{\frac{2}{p+4}} \\
& \cdot q_{\mathrm{e}}^{\frac{p+6}{p+4}}m_{\mathrm{e}}^{-\frac{3p+2}{p+4}}m_{\mathrm{p}}^{\frac{2(p-1)}{p+4}}c^{-\frac{5p+10}{2(p+4)}}\varepsilon_{\mathrm{e}}^{\frac{2(p-1)}{p+4}}\varepsilon_{\mathrm{B}}^{\frac{p+2}{2(p+4)}}n^{\frac{2}{p+4}}E^{\frac{p+2}{2(p+4)}}t^{-\frac{3p+2}{2(p+4)}}\,(1+z)^{\frac{p-6}{2(p+4)}} \\
& \simeq 1.13\cdot 10^{11}\cdot\varepsilon_{\mathrm{e},-1}^{0.39}\,\varepsilon_{\mathrm{B},-1}^{0.34}\,n_{0}^{0.32}\,E_{52}^{0.34}\,t_{\mathrm{d}}^{-0.69}\,\left(\tfrac{1+z}{2}\right)^{-0.31}\ \mathrm{Hz}
\end{aligned}
$$

Table 2.6 — Expressions for $F_{\nu,\mathrm{max}}$, ν_{c}, ν_{m}, and ν_{a}, in the case of an ultra-relativistic shock moving adiabatically into a homogeneous medium. Further details can be found in the caption of Table 2.2.

$$
\begin{aligned}
F_{\nu,\mathrm{max}} \quad & = \tfrac{4}{3}\sqrt{2}\alpha_{\mathrm{ad}}^{-\frac{1}{2}}\beta_{\mathrm{ad}}^{-\frac{1}{2}}\left(\tfrac{1+X}{2}\right)q_{\mathrm{e}}^{3}m_{\mathrm{e}}^{-1}m_{\mathrm{p}}^{-1}c^{-\frac{5}{2}}\varepsilon_{\mathrm{B}}^{\frac{1}{2}}AE^{\frac{1}{2}}D_{\mathrm{L}}^{-2}t^{-\frac{1}{2}}\,(1+z)^{\frac{3}{2}} \\
& \simeq 60.8\cdot\,\varepsilon_{\mathrm{B},-1}^{\frac{1}{2}}\,A_{*}\,E_{52}^{\frac{1}{2}}\,d_{L,28}^{-2}\,t_{\mathrm{d}}^{-\frac{1}{2}}\,\left(\tfrac{1+z}{2}\right)^{\frac{3}{2}}\ \mathrm{mJy} \\
\nu_{\mathrm{c}} \quad & = \tfrac{81}{8192}\sqrt{2}\alpha_{\mathrm{ad}}^{-\frac{1}{2}}\beta_{\mathrm{ad}}^{\frac{5}{2}}\pi^{-3}q_{\mathrm{e}}^{-7}m_{\mathrm{e}}^{5}c^{\frac{15}{2}}\varepsilon_{\mathrm{B}}^{-\frac{3}{2}}A^{-2}E^{\frac{1}{2}}t^{\frac{1}{2}}\,(1+z)^{-\frac{3}{2}} \\
& \simeq 9.97\cdot 10^{11}\cdot\,\varepsilon_{\mathrm{B},-1}^{-\frac{3}{2}}\,A_{*}^{-2}\,E_{52}^{\frac{1}{2}}\,t_{\mathrm{d}}^{\frac{1}{2}}\,\left(\tfrac{1+z}{2}\right)^{-\frac{3}{2}}\ \mathrm{Hz} \\
\nu_{\mathrm{m}} \quad & = 2\sqrt{2}\alpha_{\mathrm{ad}}^{-\frac{1}{2}}\beta_{\mathrm{ad}}^{-\frac{3}{2}}\pi^{-1}\left(\tfrac{1+X}{2}\right)^{-2}(p-2)^{2}\,(p-1)^{-2}\,q_{\mathrm{e}}m_{\mathrm{e}}^{-3}m_{\mathrm{p}}^{2}c^{-\frac{5}{2}}\varepsilon_{\mathrm{e}}^{2}\varepsilon_{\mathrm{B}}^{\frac{1}{2}}E^{\frac{1}{2}}t^{-\frac{3}{2}}\,(1+z)^{\frac{1}{2}} \\
& \simeq 1.85\cdot 10^{12}\cdot\,\varepsilon_{\mathrm{e},-1}^{2}\,\varepsilon_{\mathrm{B},-1}^{\frac{1}{2}}\,E_{52}^{\frac{1}{2}}\,t_{\mathrm{d}}^{-\frac{3}{2}}\,\left(\tfrac{1+z}{2}\right)^{\frac{1}{2}}\ \mathrm{Hz} \\
\nu_{\mathrm{a}}\ (\nu_{\mathrm{a}}<\nu_{\mathrm{m}}<\nu_{\mathrm{c}}) \quad & = 2\,(3)^{\frac{4}{5}}\,\alpha_{\mathrm{ad}}^{\frac{2}{5}}\beta_{\mathrm{ad}}^{-\frac{3}{5}}\pi^{\frac{4}{5}}\left(\tfrac{1+X}{2}\right)^{\frac{8}{5}}(p-2)^{-1}\,(p-1)^{\frac{8}{5}}\left(p+\tfrac{2}{3}\right)^{-\frac{3}{5}}(p+2)^{\frac{3}{5}}\,q_{\mathrm{e}}^{\frac{8}{5}}m_{\mathrm{p}}^{-\frac{8}{5}}c^{-\frac{2}{5}}\varepsilon_{\mathrm{e}}^{-1}\varepsilon_{\mathrm{B}}^{\frac{1}{5}}A^{\frac{6}{5}}E^{-\frac{2}{5}}t^{-\frac{3}{5}}\,(1+z)^{-\frac{2}{5}} \\
& \simeq 5.16\cdot 10^{11}\cdot\,\varepsilon_{\mathrm{e},-1}^{-1}\,\varepsilon_{\mathrm{B},-1}^{\frac{1}{5}}\,A_{*}^{\frac{6}{5}}\,E_{52}^{-\frac{2}{5}}\,t_{\mathrm{d}}^{-\frac{3}{5}}\,\left(\tfrac{1+z}{2}\right)^{-\frac{2}{5}}\ \mathrm{Hz} \\
\nu_{\mathrm{a}}\ (\nu_{\mathrm{a}}<\nu_{\mathrm{c}}<\nu_{\mathrm{m}}) \quad & = (2)^{\frac{28}{5}}\,(3)^{-\frac{3}{5}}\,\alpha_{\mathrm{ad}}^{\frac{2}{5}}\beta_{\mathrm{ad}}^{-\frac{13}{5}}\pi^{\frac{6}{5}}\left(\tfrac{1+X}{2}\right)^{\frac{3}{5}}\,q_{\mathrm{e}}^{\frac{28}{5}}\,m_{\mathrm{e}}^{-4}m_{\mathrm{p}}^{-\frac{3}{5}}c^{-\frac{27}{5}}\varepsilon_{\mathrm{B}}^{\frac{6}{5}}A^{\frac{11}{5}}E^{-\frac{2}{5}}t^{-\frac{8}{5}}\,(1+z)^{\frac{3}{5}} \\
& \simeq 9.23\cdot 10^{10}\cdot\,\varepsilon_{\mathrm{B},-1}^{\frac{6}{5}}\,A_{*}^{\frac{11}{5}}\,E_{52}^{-\frac{2}{5}}\,t_{\mathrm{d}}^{-\frac{8}{5}}\,\left(\tfrac{1+z}{2}\right)^{\frac{3}{5}}\ \mathrm{Hz} \\
\nu_{\mathrm{a}}\ (\nu_{\mathrm{m}}<\nu_{\mathrm{a}}<\nu_{\mathrm{c}}) \quad & = (2)^{\frac{9p-22}{6(p+4)}}\,(3)^{\frac{8}{3(p+4)}}\,\alpha_{\mathrm{ad}}^{-\frac{p-2}{2(p+4)}}\beta_{\mathrm{ad}}^{-\frac{3(p+2)}{2(p+4)}}\pi^{-\frac{p}{p+4}}\left(\tfrac{1+X}{2}\right)^{-\frac{2(p+2)}{p+4}}\left[\Gamma\left(\tfrac{p}{2}+\tfrac{1}{3}\right)\right]^{\frac{2}{p+4}}(p-2)^{\frac{2(p-1)}{p+4}}(p-1)^{-\frac{2(p-2)}{p+4}}(p+2)^{\frac{2}{p+4}} \\
& \quad \cdot q_{\mathrm{e}}^{\frac{p+6}{p+4}}m_{\mathrm{e}}^{-\frac{3p+2}{p+4}}m_{\mathrm{p}}^{\frac{2(p-2)}{p+4}}c^{-\frac{5p+6}{2(p+4)}}\varepsilon_{\mathrm{e}}^{\frac{2(p-1)}{p+4}}\varepsilon_{\mathrm{B}}^{\frac{p+2}{2(p+4)}}A^{\frac{4}{p+4}}E^{\frac{p-2}{2(p+4)}}t^{-\frac{3(p+2)}{2(p+4)}}\,(1+z)^{\frac{p-2}{2(p+4)}} \\
& \simeq 4.38\cdot 10^{11}\cdot\,\varepsilon_{\mathrm{e},-1}^{0.39}\,\varepsilon_{\mathrm{B},-1}^{0.34}\,A_{*}^{0.65}\,E_{52}^{0.016}\,t_{\mathrm{d}}^{-1.02}\,\left(\tfrac{1+z}{2}\right)^{0.016}\ \mathrm{Hz}
\end{aligned}
$$

Table 2.7 — Expressions for $F_{\nu,\mathrm{max}}$, ν_{c}, ν_{m}, and ν_{a}, in the case of an ultra-relativistic shock moving adiabatically into a stellar wind. Further details can be found in the caption of Table 2.2.

	Fast cooling with $\nu_{\mathrm{a}} < \nu_{\mathrm{c}} < \nu_{\mathrm{m}}$
$\nu < \nu_{\mathrm{a}} < \nu_{\mathrm{c}} < \nu_{\mathrm{m}}$	$F_{\nu,\max}\left(\frac{\nu}{\nu_{\mathrm{a}}}\right)^{2}\left(\frac{\nu_{\mathrm{a}}}{\nu_{\mathrm{c}}}\right)^{\frac{1}{3}} \propto \nu^{2} R^{2+k}\,\Gamma_2^{-4}\beta_2^{-2}\,t^{-1}$
$\nu_{\mathrm{a}} < \nu < \nu_{\mathrm{c}} < \nu_{\mathrm{m}}$	$F_{\nu,\max}\left(\frac{\nu}{\nu_{\mathrm{c}}}\right)^{\frac{1}{3}} \propto \nu^{\frac{1}{3}} R^{3-2k}\,\Gamma_2^{\frac{10}{3}}\,\beta_2^{2}\,t^{\frac{2}{3}}$
$\nu_{\mathrm{a}} < \nu_{\mathrm{c}} < \nu < \nu_{\mathrm{m}}$	$F_{\nu,\max}\left(\frac{\nu}{\nu_{\mathrm{c}}}\right)^{-\frac{1}{2}} \propto \nu^{-\frac{1}{2}} R^{\frac{3(4-k)}{4}}\,\beta_2^{-\frac{1}{2}}\,t^{-1}$
$\nu_{\mathrm{a}} < \nu_{\mathrm{c}} < \nu_{\mathrm{m}} < \nu$	$F_{\nu,\max}\left(\frac{\nu_{\mathrm{m}}}{\nu_{\mathrm{c}}}\right)^{-\frac{1}{2}}\left(\frac{\nu}{\nu_{\mathrm{m}}}\right)^{-\frac{p}{2}} \propto \nu^{-\frac{p}{2}} R^{\frac{12-2k-pk}{4}}\,\Gamma_2^{2(p-1)}\beta_2^{\frac{5p-6}{2}}\,t^{-1}$
	Slow cooling with $\nu_{\mathrm{a}} < \nu_{\mathrm{m}} < \nu_{\mathrm{c}}$
$\nu < \nu_{\mathrm{a}} < \nu_{\mathrm{m}} < \nu_{\mathrm{c}}$	$F_{\nu,\max}\left(\frac{\nu}{\nu_{\mathrm{a}}}\right)^{2}\left(\frac{\nu_{\mathrm{a}}}{\nu_{\mathrm{m}}}\right)^{\frac{1}{3}} \propto \nu^{2} R^{2}\beta_2^{2}$
$\nu_{\mathrm{a}} < \nu < \nu_{\mathrm{m}} < \nu_{\mathrm{c}}$	$F_{\nu,\max}\left(\frac{\nu}{\nu_{\mathrm{m}}}\right)^{\frac{1}{3}} \propto \nu^{\frac{1}{3}} R^{\frac{9-4k}{3}}\,\Gamma_2^{\frac{2}{3}}\beta_2^{-\frac{2}{3}}$
$\nu_{\mathrm{a}} < \nu_{\mathrm{m}} < \nu < \nu_{\mathrm{c}}$	$F_{\nu,\max}\left(\frac{\nu}{\nu_{\mathrm{m}}}\right)^{-\frac{p-1}{2}} \propto \nu^{-\frac{p-1}{2}} R^{\frac{12-5k-pk}{4}}\,\Gamma_2^{2p}\beta_2^{\frac{5p-3}{2}}$
$\nu_{\mathrm{a}} < \nu_{\mathrm{m}} < \nu_{\mathrm{c}} < \nu$	$F_{\nu,\max}\left(\frac{\nu_{\mathrm{c}}}{\nu_{\mathrm{m}}}\right)^{-\frac{p-1}{2}}\left(\frac{\nu}{\nu_{\mathrm{c}}}\right)^{-\frac{p}{2}} \propto \nu^{-\frac{p}{2}} R^{\frac{12-2k-pk}{4}}\,\Gamma_2^{2(p-1)}\beta_2^{\frac{5p-6}{2}}\,t^{-1}$
	Slow cooling with $\nu_{\mathrm{m}} < \nu_{\mathrm{a}} < \nu_{\mathrm{c}}$
$\nu < \nu_{\mathrm{m}} < \nu_{\mathrm{a}} < \nu_{\mathrm{c}}$	$F_{\nu,\max}\left(\frac{\nu}{\nu_{\mathrm{m}}}\right)^{2}\left(\frac{\nu_{\mathrm{m}}}{\nu_{\mathrm{a}}}\right)^{\frac{p+4}{2}} \propto \nu^{2} R^{2}\beta_2^{2}$
$\nu_{\mathrm{m}} < \nu < \nu_{\mathrm{a}} < \nu_{\mathrm{c}}$	$F_{\nu,\max}\left(\frac{\nu}{\nu_{\mathrm{a}}}\right)^{\frac{5}{2}}\left(\frac{\nu_{\mathrm{m}}}{\nu_{\mathrm{a}}}\right)^{\frac{p-1}{2}} \propto \nu^{\frac{5}{2}} R^{\frac{8+k}{4}}\,\Gamma_2^{-2}\beta_2^{-\frac{1}{2}}$
$\nu_{\mathrm{m}} < \nu_{\mathrm{a}} < \nu < \nu_{\mathrm{c}}$	$F_{\nu,\max}\left(\frac{\nu}{\nu_{\mathrm{m}}}\right)^{-\frac{p-1}{2}} \propto \nu^{-\frac{p-1}{2}} R^{\frac{12-5k-pk}{4}}\,\Gamma_2^{2p}\beta_2^{\frac{5p-3}{2}}$
$\nu_{\mathrm{m}} < \nu_{\mathrm{a}} < \nu_{\mathrm{c}} < \nu$	$F_{\nu,\max}\left(\frac{\nu}{\nu_{\mathrm{c}}}\right)^{-\frac{p}{2}}\left(\frac{\nu_{\mathrm{c}}}{\nu_{\mathrm{m}}}\right)^{-\frac{p-1}{2}} \propto \nu^{-\frac{p}{2}} R^{\frac{12-2k-pk}{4}}\,\Gamma_2^{2(p-1)}\beta_2^{\frac{5p-6}{2}}\,t^{-1}$

Table 2.8 — The flux in different parts of the broadband spectrum as a function of observing frequency ν, blast wave radius $R(t)$, Lorentz factor of the shocked medium $\Gamma_2(t)$, velocity of the shocked medium (divided by the speed of light) $\beta_2(t)$ and t, in the case of a blast wave moving into an external medium with density $\rho = \rho_0 R^{-k}$.

	Radiative	$k = 0$	$k = 2$
$F_{\nu,\mathrm{max}}$	$-\frac{6-k}{2(7-2k)}$	$-\frac{3}{7}$	$-\frac{2}{3}$
ν_c	$-\frac{4-3k}{2(7-2k)}$	$-\frac{2}{7}$	$\frac{1}{3}$
ν_m	$-\frac{24-7k}{2(7-2k)}$	$-\frac{12}{7}$	$-\frac{5}{3}$
ν_a $(\nu_\mathrm{a} < \nu_\mathrm{c} < \nu_\mathrm{m})$	$-\frac{28-3k}{5(7-2k)}$	$-\frac{4}{5}$	$-\frac{22}{15}$
$\nu < \nu_\mathrm{a} < \nu_\mathrm{c} < \nu_\mathrm{m}$	$\frac{7+k}{7-2k}$	1	$\frac{5}{3}$
$\nu_\mathrm{a} < \nu < \nu_\mathrm{c} < \nu_\mathrm{m}$	$-\frac{7}{3(7-2k)}$	$-\frac{1}{3}$	$-\frac{7}{9}$
$\nu_\mathrm{a} < \nu_\mathrm{c} < \nu < \nu_\mathrm{m}$	$-\frac{16-5k}{4(7-2k)}$	$-\frac{4}{7}$	$-\frac{1}{2}$
$\nu_\mathrm{a} < \nu_\mathrm{c} < \nu_\mathrm{m} < \nu$	$-\frac{24p-8-7pk+2k}{4(7-2k)}$	$-\frac{2(3p-1)}{7}$	$-\frac{5p-2}{6}$

Table 2.9 — $F_{\nu,\mathrm{max}}$, ν_c, ν_m and ν_a as a function of time, and the time-dependence of the flux in different parts of the broadband spectrum, in the case of an ultra-relativistic blast wave moving into an external medium with density $\rho = \rho_0 R^{-k}$, assuming that the evolution is fully radiative. The scalings for $k = 0$ correspond to a homogeneous external medium, while $k = 2$ corresponds to a massive stellar wind.

	Adiabatic	$k = 0$	$k = 2$	Jet
$F_{\nu,\mathrm{max}}$	$-\frac{k}{2(4-k)}$	0	$-\frac{1}{2}$	-1
ν_c	$-\frac{4-3k}{2(4-k)}$	$-\frac{1}{2}$	$\frac{1}{2}$	0
ν_m	$-\frac{3}{2}$	$-\frac{3}{2}$	$-\frac{3}{2}$	-2
ν_a ($\nu_\mathrm{a} < \nu_\mathrm{c} < \nu_\mathrm{m}$)	$-\frac{10+3k}{5(4-k)}$	$-\frac{1}{2}$	$-\frac{8}{5}$	$-\frac{6}{5}$
ν_a ($\nu_\mathrm{a} < \nu_\mathrm{m} < \nu_\mathrm{c}$)	$-\frac{3k}{5(4-k)}$	0	$-\frac{3}{5}$	$-\frac{1}{5}$
ν_a ($\nu_\mathrm{m} < \nu_\mathrm{a} < \nu_\mathrm{c}$)	$-\frac{12p+8-3pk+2k}{2(4-k)(p+4)}$	$-\frac{3p+2}{2(p+4)}$	$-\frac{3(p+2)}{2(p+4)}$	$-\frac{2(p+1)}{p+4}$
$\nu < \nu_\mathrm{a} < \nu_\mathrm{c} < \nu_\mathrm{m}$	$\frac{4}{4-k}$	1	2	1
$\nu_\mathrm{a} < \nu < \nu_\mathrm{c} < \nu_\mathrm{m}$	$\frac{2-3k}{3(4-k)}$	$\frac{1}{6}$	$-\frac{2}{3}$	-1
$\nu_\mathrm{a} < \nu_\mathrm{c} < \nu < \nu_\mathrm{m}$	$-\frac{1}{4}$	$-\frac{1}{4}$	$-\frac{1}{4}$	-1
$\nu_\mathrm{a} < \nu_\mathrm{c} < \nu_\mathrm{m} < \nu$	$-\frac{3p-2}{4}$	$-\frac{3p-2}{4}$	$-\frac{3p-2}{4}$	$-p$
$\nu < \nu_\mathrm{a} < \nu_\mathrm{m} < \nu_\mathrm{c}$	$\frac{2}{4-k}$	$\frac{1}{2}$	1	0
$\nu_\mathrm{a} < \nu < \nu_\mathrm{m} < \nu_\mathrm{c}$	$\frac{2-k}{4-k}$	$\frac{1}{2}$	0	$-\frac{1}{3}$
$\nu_\mathrm{a} < \nu_\mathrm{m} < \nu < \nu_\mathrm{c}$	$-\frac{12p-12-3pk+5k}{4(4-k)}$	$-\frac{3(p-1)}{4}$	$-\frac{3p-1}{4}$	$-p$
$\nu_\mathrm{a} < \nu_\mathrm{m} < \nu_\mathrm{c} < \nu$	$-\frac{3p-2}{4}$	$-\frac{3p-2}{4}$	$-\frac{3p-2}{4}$	$-p$
$\nu < \nu_\mathrm{m} < \nu_\mathrm{a} < \nu_\mathrm{c}$	$\frac{2}{4-k}$	$\frac{1}{2}$	1	0
$\nu_\mathrm{m} < \nu < \nu_\mathrm{a} < \nu_\mathrm{c}$	$\frac{20-3k}{4(4-k)}$	$\frac{5}{4}$	$\frac{7}{4}$	1
$\nu_\mathrm{m} < \nu_\mathrm{a} < \nu < \nu_\mathrm{c}$	$-\frac{12p-12-3pk+5k}{4(4-k)}$	$-\frac{3(p-1)}{4}$	$-\frac{3p-1}{4}$	$-p$
$\nu_\mathrm{m} < \nu_\mathrm{a} < \nu_\mathrm{c} < \nu$	$-\frac{3p-2}{4}$	$-\frac{3p-2}{4}$	$-\frac{3p-2}{4}$	$-p$

Table 2.10— $F_{\nu,\mathrm{max}}$, ν_c, ν_m and ν_a as a function of time, and the time-dependence of the flux in different parts of the broadband spectrum, in the case of a blast wave moving into an external medium with density $\rho = \rho_0 R^{-k}$, in the adiabatic extreme relativistic phase and the jet-spreading phase. The scalings for $k = 0$ correspond to a homogeneous external medium, while $k = 2$ corresponds to a massive stellar wind.

	Non-rel.	$k = 0$	$k = 2$
$F_{\nu,\mathrm{max}}$	$\frac{3-2k}{5-k}$	$\frac{3}{5}$	$-\frac{1}{3}$
ν_c	$-\frac{1-2k}{5-k}$	$-\frac{1}{5}$	1
ν_m	$-\frac{15-4k}{5-k}$	-3	$-\frac{7}{3}$
ν_a ($\nu_\mathrm{a} < \nu_\mathrm{c} < \nu_\mathrm{m}$)	$-\frac{5-11k}{5(5-k)}$	$-\frac{1}{5}$	$\frac{17}{15}$
ν_a ($\nu_\mathrm{a} < \nu_\mathrm{m} < \nu_\mathrm{c}$)	$\frac{2(15-8k)}{5(5-k)}$	$\frac{6}{5}$	$-\frac{2}{15}$
ν_a ($\nu_\mathrm{m} < \nu_\mathrm{a} < \nu_\mathrm{c}$)	$-\frac{15p-10-4pk+8k}{(5-k)(p+4)}$	$-\frac{3p-2}{p+4}$	$-\frac{7p+6}{3(p+4)}$
$\nu < \nu_\mathrm{a} < \nu_\mathrm{c} < \nu_\mathrm{m}$	-1	-1	-1
$\nu_\mathrm{a} < \nu < \nu_\mathrm{c} < \nu_\mathrm{m}$	$\frac{2(5-4k)}{3(5-k)}$	$\frac{2}{3}$	$-\frac{2}{3}$
$\nu_\mathrm{a} < \nu_\mathrm{c} < \nu < \nu_\mathrm{m}$	$\frac{5-2k}{2(5-k)}$	$\frac{1}{2}$	$\frac{1}{6}$
$\nu_\mathrm{a} < \nu_\mathrm{c} < \nu_\mathrm{m} < \nu$	$-\frac{15p-20-4pk+6k}{2(5-k)}$	$-\frac{3p-4}{2}$	$-\frac{7p-8}{6}$
$\nu < \nu_\mathrm{a} < \nu_\mathrm{m} < \nu_\mathrm{c}$	$-\frac{2(1-k)}{5-k}$	$-\frac{2}{5}$	$\frac{2}{3}$
$\nu_\mathrm{a} < \nu < \nu_\mathrm{m} < \nu_\mathrm{c}$	$\frac{2(12-5k)}{3(5-k)}$	$\frac{8}{5}$	$\frac{4}{9}$
$\nu_\mathrm{a} < \nu_\mathrm{m} < \nu < \nu_\mathrm{c}$	$-\frac{15p-21-4pk+8k}{2(5-k)}$	$-\frac{3(5p-7)}{10}$	$-\frac{7p-5}{6}$
$\nu_\mathrm{a} < \nu_\mathrm{m} < \nu_\mathrm{c} < \nu$	$-\frac{15p-20-4pk+6k}{2(5-k)}$	$-\frac{3p-4}{2}$	$-\frac{7p-8}{6}$
$\nu < \nu_\mathrm{m} < \nu_\mathrm{a} < \nu_\mathrm{c}$	$-\frac{2(1-k)}{5-k}$	$-\frac{2}{5}$	$\frac{2}{3}$
$\nu_\mathrm{m} < \nu < \nu_\mathrm{a} < \nu_\mathrm{c}$	$\frac{11}{2(5-k)}$	$\frac{11}{10}$	$\frac{11}{6}$
$\nu_\mathrm{m} < \nu_\mathrm{a} < \nu < \nu_\mathrm{c}$	$-\frac{15p-21-4pk+8k}{2(5-k)}$	$-\frac{3(5p-7)}{10}$	$-\frac{7p-5}{6}$
$\nu_\mathrm{m} < \nu_\mathrm{a} < \nu_\mathrm{c} < \nu$	$-\frac{15p-20-4pk+6k}{2(5-k)}$	$-\frac{3p-4}{2}$	$-\frac{7p-8}{6}$

Table 2.11 — $F_{\nu,\mathrm{max}}$, ν_c, ν_m and ν_a as a function of time, and the time-dependence of the flux in different parts of the broadband spectrum, in the case of a blast wave moving into an external medium with density $\rho = \rho_0 R^{-k}$, in the non-relativistic phase. The scalings for $k = 0$ correspond to a homogeneous external medium, while $k = 2$ corresponds to a massive stellar wind.

3

Gamma-Ray Burst Afterglows as Probes of Environment and Blast Wave Physics II: the Distribution of p and Structure of the Circumburst Medium

R.L.C. Starling, A.J. van der Horst, E. Rol, R.A.M.J. Wijers, C. Kouveliotou, K. Wiersema, P.A. Curran & P. Weltevrede

Submitted to Astrophysical Journal

Abstract We constrain blast wave parameters and the circumburst media of a subsample of *BeppoSAX* Gamma-Ray Bursts. For this sample we derive the values of the injected electron energy distribution index, p, and the density structure index of the circumburst medium, k, from simultaneous spectral fits to their X-ray, optical and nIR afterglow data. The spectral fits have been done in count space and include the effects of metallicity, and are compared with the previously reported optical and X-ray temporal behavior. Assuming the fireball model, on-axis viewing and standard jet structure, we can find a mean value of p for the sample as a whole of $2.04^{+0.02}_{-0.03}$. A statistical analysis of the distribution demonstrates that the p values in this sample are inconsistent with a single universal value for p at the 3σ level or greater, which has significant implications for particle acceleration models. This approach provides us with a measured distribution of circumburst density structures rather than considering only the cases of $k = 0$ (homogeneous) and $k = 2$ (wind-like). We find five GRBs for which k can be well constrained, and in four of these cases the circumburst medium is clearly wind-like. The fifth source has a value of $0 \le k \le 1$, consistent with a homogeneous circumburst medium.

3.1 Introduction

Since the discovery of GRB afterglows in 1997 (Costa et al. 1997; Van Paradijs et al. 1997; Frail et al. 1997a), their relatively longer duration and broader wavelength coverage compared with the prompt emission has made them the most accessible and arguably the most profitable area for observational GRB studies. Their non-thermal spectra and lightcurves can generally be well described by the fireball model (Cavallo & Rees 1978; Rees & Mészáros 1992; Mészáros & Rees 1997; Wijers et al. 1997) which describes a decelerating, highly relativistic outflow, the so-called blast wave, interacting with a surrounding external medium. Adaptations have been made to accommodate a non-uniform external medium (Mészáros et al. 1998; Chevalier & Li 1999) and the fact that the outflow is collimated (Rhoads 1997, 1999; Sari et al. 1999). The evidence for collimation comes from energy considerations, and directly from observations of an achromatic break in afterglow lightcurves, the so-called jet break. The jet break is an indication of the time at which sideways spreading of the jet begins to become important, combined with the fact that the effect of relativistic beaming starts to be noticeable within the jet. For the long-duration GRBs, which most probably originate in the core-collapse of a massive star (Woosley 1993; MacFadyen et al. 2001; Woosley et al. 2002; Hjorth et al. 2003), a $n(r) \propto r^{-2}$ density profile from a stellar wind would not be unexpected for the external medium. Its density can be probed through the temporal decays of the afterglow and, contrary to expectations given their stellar progenitors, long GRBs studied thus far do not all require a wind-like $n(r) \propto r^{-2}$ density profile in the local external medium (e.g. Panaitescu & Kumar 2002).

The synchrotron nature of the blast wave radiation produces spectra and lightcurves comprising of a set of power laws with characteristic slopes and frequencies. Accurate measurements of these observed quantities allow the underlying parameters of the blast wave to be determined (e.g. Wijers & Galama 1999; Panaitescu & Kumar 2001). Optical through X-ray spectra provide the opportunity to measure the index of the input power law energy distribution of electrons, p, potentially the index k of the density profile of the circumburst medium, $n(r) \propto r^{-k}$, and in some cases also the cooling break frequency ν_c — the frequency of electrons whose radiative cooling time is equal to the dynamical timescale of the blast wave.

If the microphysics of all GRBs is assumed to be the same, the range of values of the input electron energy distribution indices should be narrow. However, the directly measurable data that lead to the parameter p, such as the break frequencies and power-law slopes of the spectra and lightcurves, are dependent on various other factors, like the circumburst density, the fraction of energy in electrons (ϵ_e) and magnetic fields (ϵ_B), and simply the total amount of energy, making it more difficult to obtain a consistent value for p. Further, determination of these parameters so far works most successfully for the later-time afterglow considered here: before approximately 0.1 days the observed lightcurves and spectra are likely some mixture of the prompt emission (attributed to internally colliding shocks) and afterglow (the external shock), see e.g., Nousek et al. (2006) and O'Brien et al. (2006). These authors discuss the 'canonical' X-ray lightcurve for *Swift* bursts, which has three phases, the final phase beginning between 0.01 and 0.12 days after trigger (Nousek et al. 2006) and showing the type of steady decay seen in the pre-*Swift* era. The advantage of this is, though, that we can reliably restrict ourselves to the slow cooling regime in modeling the blast wave, where the injection frequency of the electrons is well below their cooling frequency. The measurements we perform in this study are at late enough epochs (see Table 1 in Starling et al. 2007b, hereafter Paper I), that they should not be affected by any prompt emission components.

A potential problem is that occasionally values of p below 2 have been found (e.g. for GRB 010222, Masetti et al. 2001; Stanek et al. 2001). This requires a cut-off at the high-energy end of the distribution of the electrons, and adaptations have been made for such cases (Bhattacharya 2001; Panaitescu & Kumar 2001). The details of these adaptations, however, are still under debate, since the evolution of the high-energy cutoff is not well constrained. Since the lowest values for p we find are ~ 2, we do not take any adaptations for this effect into account.

For several bursts studied here the underlying parameter set has been measured independently. Determinations for sets of GRBs have been made by e.g.Wijers & Galama (1999); Panaitescu & Kumar (2001); Yost et al. (2003); Gendre & Boër (2005); Granot et al. (2006). Unfortunately, only a small fraction of GRBs have measurements in all wavebands, most notably GRB 970508 (e.g. Wijers & Galama 1999; Panaitescu & Kumar 2002; Yost et al. 2003, ; Van der Horst, Wijers & Van den Horn, submitted to A&A) and GRB 030329 (e.g. Berger et al. 2003b; Willingale et al. 2004; Frail et al. 2005). In the Swift era such studies are generally limited to part of the parameter set, since they often use only one waveband, and therefore lack the possibility of finding the charactersitic break frequencies in the broadband spectrum.

Here, we fit the broadband spectral energy distributions (SEDs, from nIR through X-ray) of a subsample of the *BeppoSAX* sample of GRB afterglows. We constrain a subset of the blast wave parameters: the index of the power law energy distribution of electrons, p, the density profile parameter of the circumburst medium, k, and for some bursts the position of the cooling break, ν_c. Because of the paucity of radio data for most bursts in our sample, we have not included these, ensuring a more homogeneous approach. Radio data are not needed to determine p and k, since this is possible from only the nIR through X-ray SEDs.

We make use of simultaneous fits in count space to obtain the most accurate possible measurements. In Paper I we provide details of the observations, data reduction and fitting method, summarized here in Sections 2 and 3 together with the description of the model used. In Section 4 we present the results of our p- and k-value and cooling break analysis, both for the sample and for individual sources. We compare these results to those of previous studies of this kind in Section 5, and perform statistical modeling of the p-value dataset. Here we discuss our findings in the context of the fireball model and long GRB progenitors. We conclude by summarizing our results in Section 6.

3.2 Observations and Spectral Fitting Method

X-ray observations were made with the narrow field instruments on-board *BeppoSAX* (Paper I, Table 2), and here we have combined data from the MECS2 and MECS3 instruments (except in the case of GRB 970228, where we use the MECS3 instrument only).

Optical and nIR photometric points were taken from the literature (Paper I, Table 3) and from our own observations of GRB 990510 (Curran et al. in preparation). Temporal decay slopes were again taken from the literature (see Paper I, Table 1): the temporal optical slopes from Zeh et al. (2006) and the X-ray temporal slopes from Gendre & Boër (2005); in 't Zand et al. (1998); Nicastro et al. (1999). We have transformed the time of the optical and nIR photometry to the log of the midpoint of the combined X-ray observations. We avoid using data taken before 0.1 days after the GRB, hence we assume no complex and flaring behavior occurs in the lightcurves and we restrict ourselves to the slow cooling regime. All data are transformed to count space for fitting purposes, in order that no model need be assumed *a priori* for the X-ray spectrum, and fitted within the ISIS spectral fitting package (Houck & Denicola 2000). Models consist of either a single or a broken power law, to allow for a possible cooling break in between the optical and X-rays. In the broken power law model we fix the difference in spectral slope to 0.5, as expected in the case of such a cooling break. Both Galactic and intrinsic absorption are components in the models, allowing for either Milky Way, Large Magellanic Cloud (LMC) or Small Magellanic Cloud (SMC) extinction laws for the GRB host galaxy, at either Solar ($Z_\odot$), LMC (Z=1/3 $Z_\odot$) or SMC (Z=1/8 $Z_\odot$) metallicity. All details of the observations, reduction and analysis are given in Paper I.

	k	$k=0$	$k=2$	Jet
$F_{\nu,max}$	$-\frac{k}{2(4-k)}$	0	$-\frac{1}{2}$	-1
ν_c	$-\frac{4-3k}{2(4-k)}$	$-\frac{1}{2}$	$\frac{1}{2}$	0
ν_m	$-\frac{3}{2}$	$-\frac{3}{2}$	$-\frac{3}{2}$	-2

Table 3.1 — The temporal power-law indices of the peak flux $F_{\nu,max}$, the cooling frequency ν_c and the peak frequency ν_m, as a function of the circumburst density profile index k for pre- (columns 2–4) and post- jet break (column 5).

3.3 Theoretical Modeling

We assume that the ambient medium density as a function of radius can be described as a power law with index k, i.e. $n(r) \propto r^{-k}$, so that a homogeneous medium is given by $k = 0$ and a stellar wind environment by $k = 2$ — the two most likely scenarios. For the purpose of looking at optical and X-ray data at ~ 1 day, we need to derive the time dependency of the peak flux $F_{\nu,max}$ and the cooling frequency ν_c as a function of k, and the peak frequency ν_m (which has no dependence on k), assuming the afterglows are in the slow cooling regime. After the jet break all of these parameters have no dependence on k; in this region we know we are dealing with a jet geometry hence we label this case 'Jet' or$_j$ (Table 3.1).

If one assumes that the flux is a power law in frequency and time with β (or Γ) the spectral slope and α the temporal slope, using the conventions $F_\nu \propto \nu^{-\beta} t^{-\alpha} \propto \nu^{-(\Gamma-1)} t^{-\alpha}$, with power law photon index $\Gamma = \beta + 1$, one can derive these slopes as a function of k and the power-law index p of the electron energy distribution. These values for α, β and Γ are given in Table 3.2 for two different situations: the observing frequency in between ν_m and ν_c, and the observing frequency above both frequencies. Also shown in this table are the closure relations between α and β.

One can invert all these relations to obtain p from α and β, and even determine k from these observables:

$$k = \frac{4(3\beta - 2\alpha)}{3\beta - 2\alpha - 1} = \frac{4[3(\Gamma - 1) - 2\alpha]}{3\Gamma - 2\alpha - 4}. \tag{3.1}$$

From Table 3.2 it is clear that when the observing frequency is higher than

	$\nu_m < \nu < \nu_c$				$\nu_m < \nu_c < \nu$	
	k	$k = 0$	$k = 2$	Jet	k	Jet
$\beta(p)$	$\frac{p-1}{2}$	$\frac{p-1}{2}$	$\frac{p-1}{2}$	$\frac{p-1}{2}$	$\frac{p}{2}$	$\frac{p}{2}$
$\Gamma(p)$	$\frac{p+1}{2}$	$\frac{p+1}{2}$	$\frac{p+1}{2}$	$\frac{p+1}{2}$	$\frac{p+2}{2}$	$\frac{p+2}{2}$
$\alpha(p,k)$	$\frac{12(p-1)-k(3p-5)}{4(4-k)}$	$\frac{3(p-1)}{4}$	$\frac{3p-1}{4}$	p	$\frac{3p-2}{4}$	p
$\alpha(\beta,k)$	$\frac{6\beta(4-k)+2k}{4(4-k)}$	$\frac{3\beta}{2}$	$\frac{3\beta+1}{2}$	$2\beta + 1$	$\frac{3\beta-1}{2}$	2β
$\alpha(\Gamma,k)$	$\frac{6\Gamma(4-k)-8(3-k)}{4(4-k)}$	$\frac{3(\Gamma-1)}{2}$	$\frac{3\Gamma-2}{2}$	$2\Gamma - 1$	$\frac{3\Gamma-4}{2}$	$2(\Gamma - 1)$
$p(\beta)$	$2\beta + 1$	$2\beta + 1$	$2\beta + 1$	$2\beta + 1$	2β	2β
$p(\Gamma)$	$2\Gamma - 1$	$2\Gamma - 1$	$2\Gamma - 1$	$2\Gamma - 1$	$2(\Gamma - 1)$	$2(\Gamma - 1)$
$p(\alpha,k)$	$\frac{4\alpha(4-k)+12-5k}{3(4-k)}$	$\frac{4\alpha+3}{3}$	$\frac{4\alpha+1}{3}$	α	$\frac{2(2\alpha+1)}{3}$	α

Table 3.2 — The temporal and spectral slopes of the flux, α and β (or Γ, where $\Gamma = \beta + 1$) respectively, the closure relations between α and β (or Γ), and p as a function of α, β and Γ.

ν_m and ν_c, both α and β only depend on p, and do not depend on k. In the situation where the observing frequency is situated in between ν_m and ν_c, the spectral slope only depends on p, but the temporal slope depends on both p and k. So the structure of the ambient medium can only be determined in the latter case ($\nu_m < \nu < \nu_c$), although having more accurate information on p from the situation with $\nu_m < \nu_c < \nu$ is useful to get a better handle on k.

3.4 Results

The results of fits to the SEDs for all GRBs in the sample are given in both Table 4 and Fig. 2 of Paper I. For derivation of the blast wave parameter p we adopt the best-fitting models as listed in Paper I and in particular cases additional models were included. SMC-like absorption was the preferred extinction model in all cases except for GRB 000926 where LMC-like absorption is preferred. We calculate the values for p and k for two cases: the cooling frequency in between the optical and X-rays, and the cooling frequency above both. We have checked whether the cooling frequency could lie below the optical band using the relations of the fireball model, but this turns out not to be the case for these GRBs. The cooling frequency, ν_c, is obtained directly from the SED fits for 3 bursts: GRBs 990123, 990510 and 010222, with $\nu_{\rm c}$ = $(1.3^{+4.5}_{-0.9})\times10^{17}$, $(4.3 \pm 0.5)\times10^{15}$, and $(4.1^{+15.2}_{-4.1})\times10^{15}$ Hz at 1.245, 1.067 and 1.511 days since burst respectively. Applying the fireball model we find that another two sources, GRBs 980329 and 980703, may require a break within their SEDs, at $\sim 2.6 \times 10^{17}$ and $\sim 8 \times 10^{17}$ Hz, at 1.148 and 1.333 days (the logarithmic midpoint of the X-ray spectrum), respectively.

The resulting values for p can be found in Tables 3.6 and 3.5, and for k in Table 3.3. All errors are given at the 90% confidence level for one interesting parameter, unless otherwise stated. α_1 and α_2 refer to the pre- and post-break optical lightcurve slopes given in Paper I; we allowed for the possibility that these breaks are not jet breaks by considering that α_2 is both pre- (columns 6 and 7) and post- (column 8) jet break. This has also been done for the X-ray temporal slopes.

3.4.1 Results: Individual Sources

GRB 970228

We find $p = 2.44^{+0.18}_{-0.06}$ and $k = 1.73^{+0.56}_{-1.69}$, with $\nu_{\rm X} < \nu_{\rm c}$ at 0.52 days. A cooling break between optical and X-ray bands is not required at the time of our SED (0.52 days) according to the F-test: the F-test probability, the probability that the result is obtained by chance, is 2.1×10^{-2}, which is quite high; so adding one free extra parameter is not a significant improvement. Using the best fitting model of a single power law plus SMC-like extinction, in the regime $\nu_{\rm X} < \nu_{\rm c}$, we find that the data can be fit by both a homogeneous and a wind-like circumburst medium; the value of k is best constrained by the optical temporal slope.

GRB 970508

We find $p = 2.56^{+0.10}_{-0.46}$ and $k = 0.49^{+1.36}_{-0.67}$, with $\nu_{\rm X} < \nu_{\rm c}$ at 1.68 days. Using the single power law with LMC extinction (rather than SMC to obtain the more conservative errors on the spectral slope) and optical to X-ray offset free, in the regime $\nu_{\rm X} < \nu_{\rm c}$, we find the data are best fit by a homogeneous medium; the value k is best constrained by the optical temporal slope. Broadband modeling

GRB	$k\ (\alpha_1,\Gamma)$	$k\ (\alpha_2,\Gamma)$	$k\ (\alpha_x,\Gamma)$	$k\ (\alpha_1,\Gamma)$	$k\ (\alpha_2,\Gamma)$
	$\nu_X < \nu_c$	$\nu_X < \nu_c$	$\nu_X < \nu_c$	$\nu_c < \nu_X$	$\nu_c < \nu_X$
970228	$\mathbf{1.73}^{+0.56}_{-1.69}$	...	$\mathbf{1.22}^{+0.93}_{-4.77}$	$2.21^{+0.36}_{-1.95}$	...
970508	$\mathbf{0.49}^{+1.36}_{-0.67}$	...	$\mathbf{-0.65}^{+2.51}_{-5.61}$	$1.44^{+0.94}_{-1.05}$	...
971214	$\mathbf{2.17}^{+0.25}_{-0.35}$	...	$\mathbf{2.33}^{+0.24}_{-0.34}$	$2.31^{+0.38}_{-0.49}$	...
980329	$\mathit{-12.67}^{+31.82}_{-43.94}$	...	$\mathit{1.40}^{+0.92}_{-2.53}$	$\mathbf{-4.89}^{+25.98}_{-1.40}$	...
980519	$\mathbf{0.23}^{+1.22}_{-3.05}$	$2.46^{+0.12}_{-0.12}$	$\mathbf{1.67}^{+0.90}_{-3.64}$	$0.69^{+1.19}_{-3.19}$	$2.55^{+0.18}_{-0.18}$
980703	$\mathit{70.67}^{+65.16}_{-68.24}$	$\mathit{1.40}^{+184.42}_{-22.72}$	$\mathit{-96.00}^{+107.84}_{-93.22}$	$\mathbf{-40.44}^{+46.57}_{-42.92}$	$\mathbf{1.63}^{+1.34}_{-56.46}$
990123	$1.58^{+0.29}_{-0.38}$	$2.34^{+0.29}_{-0.45}$	$2.78^{+0.55}_{-5.41}$	$\mathbf{2.00}^{+0.26}_{-0.21}$	$\mathbf{2.55}^{+0.25}_{-0.31}$
990510	$-10.55^{+3.71}_{-6.51}$	$2.48^{+0.12}_{-0.13}$	$0.76^{+0.72}_{-1.24}$	$\mathbf{0.80}^{+0.22}_{-0.90}$	$\mathbf{2.89}^{+0.06}_{-0.14}$
000926	$\mathbf{2.16}^{+0.17}_{-0.30}$	$2.89^{+0.08}_{-0.13}$	$\mathbf{2.09}^{+0.86}_{-12.37}$	$2.21^{+0.53}_{-0.32}$	$2.90^{+0.24}_{-0.13}$
010222	$\mathit{14.53}^{+224.77}_{-5.12}$	$\mathit{0.92}^{+0.30}_{-0.36}$	$\mathit{0.30}^{+0.59}_{-0.84}$	$\mathbf{-2.25}^{+2.54}_{-42.53}$	$\mathbf{2.28}^{+0.15}_{-0.29}$

Table 3.3 — Values for k. Bold type highlights consistent results (at 90% level). In cases where the best-fitting spectral model to the SED (from Paper I) is inconsistent with the model fits, we show the results for this original best-fitting model in italics.

by Van der Horst, Wijers & Van den Horn (submitted to A&A) with k as a free parameter gives very tight constraints on k: a value of 0.02 ± 0.03 is derived, i.e. a homogeneous medium.

Previous works put the cooling break at optical frequencies, $\nu_c = 1.6 \times 10^{14}$ Hz, at 12.1 days since burst, between the B and V bands (e.g. Wijers & Galama 1999). We, however, find that the cooling break is likely to lie above the X-rays at 1.68 days. We note in this context the uncertain extrapolation of the optical data used in the SED, owing to an irregular shaped lightcurve at early times, which we have attempted to account for in allowing the optical to X-ray offset to go free. This is a particularly difficult case given that the X-ray data cover the time period immediately following an optical flare when the optical lightcurve appears to have flattened before breaking to a typical and well defined power law.

GRB 971214

We find $p = 2.20 \pm 0.06$ and $k = 2.17^{+0.25}_{-0.35}$, with $\nu_\mathrm{X} < \nu_\mathrm{c}$ at 1.36 days. Using the best-fitting model of a power law plus SMC extinction, in the regime $\nu_\mathrm{X} < \nu_\mathrm{c}$, the data are best fit by a wind medium: from the optical temporal slope we find $k = 2.17^{+0.25}_{-0.35}$, whilst from the X-ray temporal slope $k = 2.33^{+0.24}_{-0.34}$. A broken power law does not provide a significant improvement in the fit compared to a single power law, i.e. the F-test probability is high (4.1×10^{-2}). A spectral break is claimed for this burst in the IR (~1 micron) at 0.58 days ($\nu_\mathrm{c} \sim 3 \times 10^{14}$ Hz, Ramaprakash et al. 1998). This is not the cooling break, but the peak of the SED moving to lower frequencies, so there is no conflict with our results for ν_c.

GRB 980329

We find $p = 2.50^{+0.20}_{-0.62}$ and $k = -4.89^{+25.98}_{-1.40}$, with $\nu_\mathrm{c} < \nu_\mathrm{X}$ at 1.15 days. The spectral fit obtained with a single power law plus SMC extinction is inconsistent with the optical temporal slopes. A spectral break in the power law does not provide a significant improvement of the fit according to the F-test (probability of 7.2×10^{-2}), but this spectral break model provides agreement between the spectral slopes and the optical and X-ray temporal slopes. In this regime, $\nu_\mathrm{c} < \nu_\mathrm{X}$, k cannot be well constrained though the centroid of the fit to the optical data is that of a homogeneous medium. We note that when omitting the I band point from the SED, which may be overestimated (see Yost et al. 2002, and Paper I), our results do not change.

GRB 980519

We find $p = 2.96^{+0.06}_{-0.08}$ and $k = 0.23^{+1.22}_{-3.05}$, with $\nu_\mathrm{X} < \nu_\mathrm{c}$ at 0.93 days. Using the power law plus SMC extinction model for the SED, in the regime $\nu_\mathrm{X} < \nu_\mathrm{c}$, the optical data are best fit by a homogeneous medium, and the X-ray temporal slopes can be fitted by both a homogeneous and a wind medium; k is therefore best constrained by the optical temporal slope. In contrast, Chevalier & Li (1999) found that the radio emission of the afterglow of GRB 980519 measured between 7.2 hours and 63 days since the burst is consistent with an external wind instead of a homogeneous medium. Frail et al. (2000a) note, however, that the interstellar scintillation present in the radio data does not allow to draw firm conclusions on this.

The optical temporal break at 0.48 ± 0.03 days (Zeh et al. 2006) cannot be explained by passage through the optical bands of ν_c, since the derived value for p from the temporal slope is too high in that case ($p = 3.69 \pm 0.06$) compared to the p-value from the joint spectral slope. It also cannot be explained by a jet break, since p is too low in that case ($p = 2.27 \pm 0.05$). It appears that the fireball model is a good explanation for the first temporal slope and the spectrum used here, but the post-break optical slope has either been incorrectly measured or we do not yet have the correct model for this afterglow. We note that this afterglow showed a very steep temporal decay compared to other GRBs (Halpern et al. 1999). This is somewhat reminiscent of the very early-time decays of many *Swift* bursts which occur at $\lesssim$500 s after trigger (Nousek et al. 2006) and likely have a significant prompt emission component.

GRB 980703

We find $p = 2.74^{+0.10}_{-0.48}$ and $k = 1.63^{+1.34}_{-56.46}$, with $\nu_c < \nu_X$ at 1.33 days. The spectral fit obtained with a single power law plus SMC extinction is inconsistent with the X-ray temporal slopes. A spectral break in the power law does not provide a significant improvement of the fit according to the F-test (probability of 7.2×10^{-2}), but this spectral break model provides agreement between the spectral slopes and the optical and X-ray temporal slopes. Hence we use the broken power law plus SMC extinction model in the regime $\nu_c < \nu_X$. The nature of the optical temporal break at 1.35 ± 0.94 days cannot be determined because of large uncertainties in the optical temporal slopes, which are also the reason why k cannot be constrained.

Two publications have postulated a position for the cooling break in past studies. Vreeswijk et al. (1999) propose $\nu_o < \nu_X < \nu_c$ at 1.2 days after the burst, Bloom et al. (1998) propose $\nu_o < \nu_c < \nu_X$ at 5.3 days, and our SED study at 1.33 days, when compared with the optical temporal slope, is inconclusive since both $\nu_X < \nu_c$ and $\nu_X > \nu_c$ can be accommodated. It may be that the cooling break has moved into our observed bands during accumulation of the X-ray spectrum (possibly indicated by the inability of the fireball model to fit the data when a single power law is assumed for the spectrum). If we require consistency with these previous results, the cooling break must be moving to lower energies and lies approximately at X-ray frequencies in our data. This would mean that the circumburst medium is homogeneous, since the ν_c is expected to move as $t^{-1/2}$ in this case, while ν_c will increase in time as $t^{1/2}$ in the wind case.

The host galaxy of GRB 980703 appears to have a high and possibly variable optical extinction along the line of sight to the GRB (see Paper I). The different (and formally inconsistent) values of A_V may be due to different methods for measuring the extinction, probing of different regions of the host galaxy, or may indicate that the environment in which the burst occurred is changing with time. We have used the Vreeswijk et al. (1999) optical data and scaled it from 1.2 days to 1.33 days after trigger. Combining the optical and X-ray data when fitting provides us with a different estimate for the extinction than was obtained by Vreeswijk et al. (1999) for the optical alone. Any change in optical extinction will have an effect upon the measured spectral slope and hence the derived value of p.

GRB 990123

We find $p = 1.99^{+0.00}_{-0.07}$ and $k = 2.00^{+0.26}_{-0.21}$, with $\nu_{\rm c} < \nu_{\rm X}$ at 1.25 days. With this best fitting SED model of a broken power law plus SMC extinction, in the regime $\nu_{\rm c} < \nu_{\rm X}$, the optical temporal decay is best fit by a wind medium. The optical temporal break at 2.06 ± 0.83 days is marginally consistent with a jet break: the p-value derived from the post-break temporal slope is consistent with the one derived from the pre-break optical temporal slope, but inconsistent with the spectral slope. The uncertainties in the X-ray temporal slope are too large to determine the phase of blast wave evolution (i.e. before or after jet break) from the X-ray data alone.

For GRB 990123 the temporal slope difference between optical and X-ray of 0.25 also agrees with the spectral analysis where a broken power law model is the best fit, indicating a cooling break between the optical and X-ray bands at 1.25 days post-burst. The value we derive for p is consistent with that derived from the X-ray spectrum alone of $p = 2.0 \pm 0.1$ (Stratta et al. 2004) and lower than a previous estimate via broadband modeling of $p = 2.28 \pm 0.05$ (Panaitescu & Kumar 2002) (we note that the latter uncertainty is $1\,\sigma$ and not the 90% error used in the rest of our paper).

GRB 990510

We find $p = 2.06^{+0.14}_{-0.02}$ and $k = 0.80^{+0.22}_{-0.90}$, with $\nu_{\rm c} < \nu_{\rm X}$ at 1.07 days. The best fitting model to the SED is clearly a broken power law with negligible extinction, in the regime $\nu_{\rm c} < \nu_{\rm X}$. There is considerable improvement in the χ^2 when allowing for this break in the power law, noted by previous authors, which we find is located at 0.016 - 0.020 keV at $\sim$1.07 days since burst (consistent with the value given by Pian et al. 2001). The slope change is as expected for a cooling break in the slow cooling regime when leaving both power law slopes free.

The optical data are best fit by the values for p and k mentioned above. In this case, however, the X-ray temporal slope is not consistent with the spectral slope nor the optical temporal slope at the 90% ($\sim 1.6\sigma$) level, but does agree within $3\,\sigma$. The optical temporal break at 1.31 ± 0.07 days is marginally consistent with a jet break. The derived value of p is consistent with the value derived from the *BeppoSAX* X-ray spectrum alone of $p \sim 2.1$, by Kuulkers et al. (2000), and rules out the value of $p = 2.6 \pm 0.2$ also derived from the *BeppoSAX* X-ray spectrum by Stratta et al. (2004); that same X-ray data is used here, but is combined with nIR and optical data to obtain our limits on p.

GRB 000926

We find $p = 2.54^{+0.14}_{-0.08}$ and $k = 2.16^{+0.17}_{-0.30}$, with $\nu_{\rm X} < \nu_{\rm c}$ at 2.23 days. With the power law plus LMC extinction model, in the regime $\nu_{\rm X} < \nu_{\rm c}$, the optical temporal decay is best fit by a wind-like medium. Large uncertainties in the X-ray temporal slope prevent determination of the circumburst medium structure and blast wave evolution phase from X-ray data alone; the optical temporal break at 2.10 ± 0.15 days is consistent with a jet break.

GRB 010222

We do not find a consistent solution for this afterglow taking 90% uncertainties, but we do find one taking 3σ uncertainties: $p = 2.04^{+0.18}_{-0.10}$ and $k = 2.28^{+0.15}_{-0.29}$, with $\nu_{\rm c} < \nu_{\rm X}$ at 1.51 days. Adopting the single power law model with LMC extinction, in the regime $\nu_{\rm X} < \nu_{\rm c}$, the optical slopes are not consistent with the spectral slope nor the X-ray temporal slopes, both at the 90% and 3σ levels. Using a broken power law plus SMC extinction, in the regime $\nu_{\rm c} < \nu_{\rm X}$, for which the F-test indicates a marginal improvement (probability of 1×10^{-4}), the X-ray temporal slope is not consistent with the spectral slope nor the optical temporal slope at the 90% level, but they are consistent at 3σ. In the first case we obtain $p = 2.72^{+0.05}_{-0.05}$ and $k = 0.30^{+0.59}_{-0.84}$; in the latter case $p = 2.04^{+0.18}_{-0.10}$ and $k = -2.25^{+2.54}_{-43}$, which is derived from the pre-break optical temporal slope, or $k = 2.28^{+0.15}_{-0.29}$, derived from the post-break optical temporal slope. Since the temporal break happens quite early, 0.64 ± 0.09 days after the burst (Zeh et al. 2006), and the post-break optical slopes are inconsistent with a jet-interpretation, the early temporal slope is probably influenced by late-time energy injection and a medium with $k = 2.28^{+0.15}_{-0.29}$ the correct interpretation.

Panaitescu & Kumar (2002) find the cooling break to lie at optical wavelengths or longer, in agreement with our results. However, they derive a low value for p of 1.35, and find significant reddening of the optical spectrum which they say explains the second steepening observed in the optical after 6 days by Fruchter et al. (2001a). Bhattacharya & Resmi (2004) obtain good fits by adopting a two-slope electron energy distribution with p-values of 1.3 and 2.1, below and above a so-called injection break, respectively. This injection break is located in the X-ray regime at $\sim$ 1 days after the burst. In their model the optical temporal break is a jet break and the circumburst medium is homogeneous. Björnsson et al. (2002) argue that the unusually slow decay of this afterglow and positive detection of linear polarization can be explained by a jet model with continuous energy injection. Such slow decays are seen in the 'canonical' *Swift* X-ray lightcurves (e.g. Nousek et al. 2006), termed the plateau phase, and typically begin a few hundred seconds after the GRB trigger. The electron energy distribution then has $p = 2.49 \pm 0.05$, which is inconsistent with our result for p from the spectral fits.

3.5 Discussion

The parameters that can be derived from broadband modeling of afterglow lightcurves describe the micro- and macrophysics of the relativistic jet and its surrounding medium. To obtain the full set of parameters the spectral energy distribution has to be covered from X-ray to radio wavelengths. Two of these parameters can be deduced from just the spectral and temporal slopes in the optical and X-rays, i.e. the electron energy distribution index p and the circumburst medium profile parameter k. These two parameters have been determined in this paper for a selection of 10 GRBs, for which the final results are shown in Table 3.4 and Fig. 3.1. For completeness the values for ν_c are also listed in Table 3.4; half of the GRBs in this sample have a value $\nu_c \leq \nu_X \sim 8 \times 10^{17}$ Hz.

3.5.1 The Distribution of p

Some theoretical studies of particle acceleration by ultra-relativistic shocks indicate that there is a nearly universal value of p of $2.2 - 2.3$ (e.g. Kirk et al. 2000; Achterberg et al. 2001), while other studies indicate that there is a large range of possible values for p of $1.5 - 4$ (e.g. Baring 2004). From the results presented in this paper and from broadband modeling of individual bursts, quite a large range of values for p have been found, which could indicate that there is a large intrinsic scatter in the value of p. Here we test the null-hypothesis namely that the observed distribution of p can be obtained from a parent distribution with a single central value of p, by performing a statistical log-likelihood analysis on the obtained values of p.

We first determine the most likely value of p for our sample, by minimizing the log-likelihood of our 10 measured values of p. In order to do this, we

GRB	p	k	Medium	ν_c (Time of SED)
970228	$2.44^{+0.18}_{-0.06}$	$1.73^{+0.56}_{-1.69}$	wind/homog.	$> \nu_\mathrm{X} \sim 8 \times 10^{17}$ (0.52 days)
970508[a]	$2.56^{+0.10}_{-0.46}$	$0.49^{+1.36}_{-0.67}$	homogeneous	$> \nu_\mathrm{X}$ (1.68 days)
971214	$2.20^{+0.06}_{-0.06}$	$2.17^{+0.25}_{-0.35}$	wind	$> \nu_\mathrm{X}$ (1.36 days)
980329[b]	$2.50^{+0.20}_{-0.62}$	$-4.89^{+25.98}_{-1.40}$	wind/homog.	$\sim 2.6 \times 10^{17}$ (1.15 days)
980519[c]	$2.96^{+0.06}_{-0.08}$	$0.23^{+1.22}_{-3.05}$	homogeneous	$> \nu_\mathrm{X}$ (0.93 days)
980703[d]	$2.74^{+0.10}_{-0.48}$	$1.63^{+1.34}_{-56.46}$	wind/homog.	$\sim \nu_\mathrm{X}$ (1.33 days)
990123	$1.99^{+0.00}_{-0.07}$	$2.00^{+0.26}_{-0.21}$	wind	$1.3^{+4.5}_{-0.9} \times 10^{17}$ (1.25 days)
990510[e]	$2.06^{+0.14}_{-0.02}$	$0.80^{+0.22}_{-0.90}$	homogeneous	$4.3 \pm 0.5 \times 10^{15}$ (1.07 days)
000926[f]	$2.54^{+0.14}_{-0.08}$	$2.16^{+0.17}_{-0.30}$	wind	$> \nu_\mathrm{X}$ (2.23 days)
010222[g]	$2.04^{+0.18}_{-0.10}$	$2.28^{+0.15}_{-0.29}$	wind	$4.1^{+15.2}_{-4.1} \times 10^{15}$ (1.51 days)

Table 3.4 — Final results for p, k and ν_c for all ten bursts in the sample.

---

[a] Optical data extrapolation is uncertain.

[b] Broken power-law better than single power-law in SED.

[c] This solution is consistent with all measurements except the post-break optical temporal slope.

[d] Broken power-law better than single power-law in SED. Large uncertainties in the optical temporal slopes.

[e] X-ray temporal slope only consistent at 3σ level.

[f] X-ray temporal slopes have large uncertainties.

[g] Break in the optical lightcurve at 0.6 days is not a jet break. X-ray temporal slope only consistent at 3σ level.

describe the measured values of p and their uncertainties as probability distributions, in which we take asymmetric measurement uncertainties into account. These probability distributions are given as two halves of normal distributions with different widths that are set by the measured uncertainties. The two halves of the probability distributions are normalized such that they are connected as a continuous function and have a total integral equal to 1. This results in distribu-

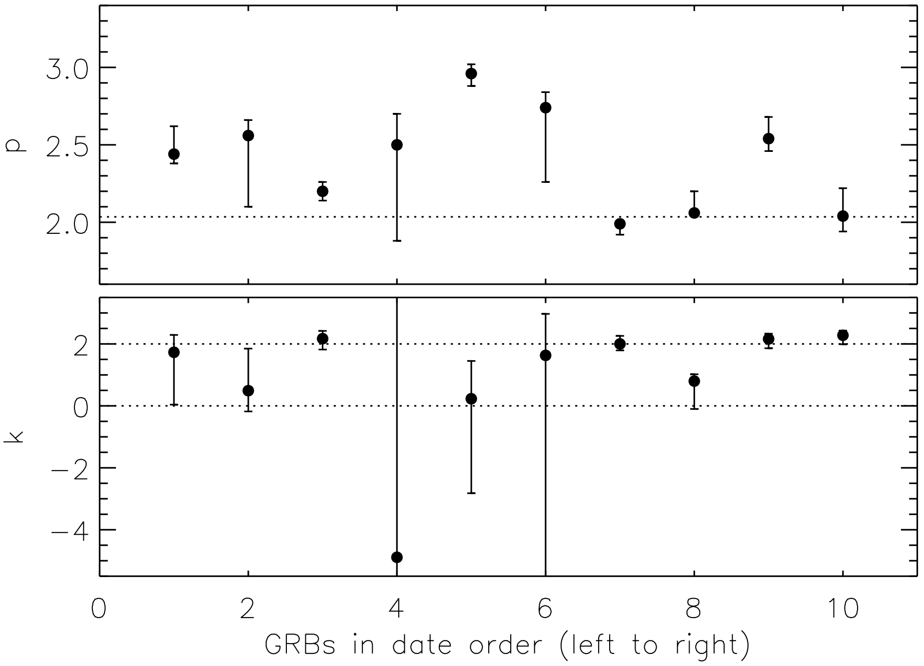

Figure 3.1 — Derived values of p (top panel) and k (lower panel) for each individual afterglow (see Table 3.4): the horizontal axes represent the GRBs in date order left to right and errors are 90 % confidence. In the top panel the dotted line indicates the most likely value of $p = 2.04$; in the lower panel the dotted lines indicate $k = 0$ (homogeneous medium) and $k = 2$ (stellar wind).

tion functions which are given by

$$P(p, p_{\rm meas}, \sigma_1, \sigma_2) \;=\; \frac{\sqrt{2}}{\sqrt{\pi}(\sigma_1 + \sigma_2)} \cdot \begin{cases} e^{-(p-p_{\rm meas})^2/2\sigma_1^2} & (p < p_{\rm meas}) \\ e^{-(p-p_{\rm meas})^2/2\sigma_2^2} & (p > p_{\rm meas}) \end{cases} , \quad (3.2)$$

with σ_1 and σ_2 the lower and upper $1\,\sigma$ uncertainties in the measured value of p (indicated as $p_{\rm meas}$) respectively. This probability function describes how likely a value of p is given the measurement ($p_{\rm meas}$,σ_1,σ_2). To convert the 90 % confidence limits in Table 3.4 to $1\,\sigma$ uncertainties, we divided those by a factor of 1.6. The log-likelihood for these probability distributions is given by

$$-2\log\left(\prod_{i=1}^{N} P_i\right) \;=\; \sum_{i=1}^{N}(-2\log P_i)$$

$$= N \log(2\pi) + \sum_{i=1}^{N} \left[\log\left(\frac{\sigma_{1,i} + \sigma_{2,i}}{2}\right)^2 + \left(\frac{p - p_{\mathrm{meas},i}}{\sigma_{1/2,i}}\right)^2 \right] \quad (3.3)$$

in which in the last term $\sigma_{1,i}$ is used for $p < p_{\mathrm{meas},i}$ and $\sigma_{2,i}$ for $p > p_{\mathrm{meas},i}$. N is the number of measurements, i.e. in this case $N = 10$.

The log-likelihood is a function of p and we determine the most probable p-value by minimizing this function for our 10 bursts. We find the most likely value of $p = 2.04^{+0.02}_{-0.03}$, with a log-likelihood of 613.6. We have derived the uncertainties in this most likely p-value by generating 10^5 synthetic datasets for the 10 bursts in our sample. These datasets are possible measurements within the measurement uncertainties, generated by taking random numbers from the probability distributions that are defined by the measured p-values and their uncertainties. For each possible dataset we determine the most likely p-value, and from the resulting distribution of most likely p-values we obtain the $1\,\sigma$ uncertainties in the value of $p = 2.04$.

To test our null-hypothesis that the observed distribution of p can be obtained from a parent distribution with a single central value of p, we generate 10^5 different synthetic datasets for p for the 10 bursts in our sample by taking random numbers from probability distributions that are described by the most likely value of $p = 2.04$ and the $1\,\sigma$ uncertainties in the 10 values of p. We then take 10 values of p coming from these synthetic datasets (one random number for each measurement), calculate the most likely value of p and the accompanying log-likelihood. The resulting distribution of log-likelihood values is plotted in Fig. 3.2, together with the minimal log-likelihood of 613.6 coming from the measurements. We find that in 99.92 % of the cases the log-likelihood of the synthetic data is smaller than the one coming from the measured p-values. *This leads to the conclusion that the hypothesis, that the distribution of p from our sample can be obtained from a parent distribution with a single central value of p, is rejected at the* $3\,\sigma$*-level.*

This result challenges the theoretical studies of particle acceleration which claim that there is one universal value of p (e.g. Kirk et al. 2000; Achterberg et al. 2001), and is consistent with similar findings by Shen et al. (2006) from fits to the prompt emission of a sample of Burst And Transient Source Experiment GRBs. Baring (2004) shows that this often quoted value of $p = 2.23$ is a special case, with particular assumptions on hydrodynamic quantities, like the compression ratio of the upstream and downstream velocities, on the influence of the magnetic field on the dynamics, and on electron scattering angles. He claims that there is a large range of possible values for p of $1.5 - 4$. We derive constraints on the width of the distribution of p-values below.

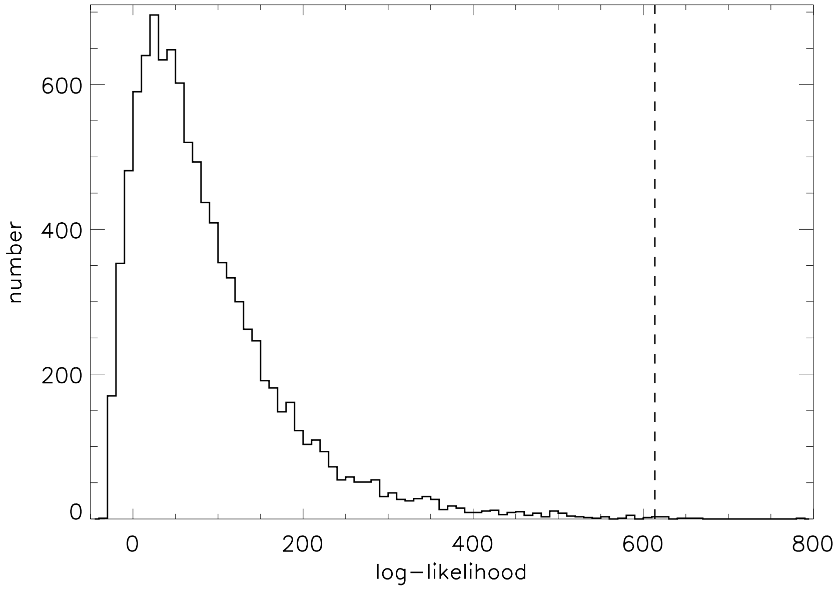

Figure 3.2 — The log-likelihood distribution coming from the 10^5 synthetic datasets generated from one single value of p (solid line); the dashed vertical line indicates the log-likelihood for the real data. In 99.92 % of the cases the log-likelihood of the synthetic data is smaller than the one coming from our measured sample.

From Table 3.4 and Fig. 3.1 it can be seen that the log-likelihood is dominated by the value for p of GRB 990123, and after that by GRB 980519. In fact, just the two p-values of GRB 990123 and GRB 980519 are different by $12\,\sigma$, and thus they alone refute the constant p hypothesis. We also examined the strength of the evidence against the constant p from samples excluding one of the 10 bursts in our sample. Only in cases where either GRB 990123 or GRB 980519 are excluded is the significance less than $3\,\sigma$, but even then the hypothesis can be rejected at the $\sim 2\,\sigma$-level.

Since we now know that the measured values of p from our sample are not coming from a parent distribution with a single central value of p, we can put constraints on the width of the parent distribution of p-values. We do this by introducing an intrinsic scatter on the most likely value of $p = 2.04$: we generate 10^5 synthetic datasets by first taking random numbers from normal distributions with a central value of $p = 2.04$ and a certain scattering $\sigma_{\rm scat}$; we then take random numbers from the probability distributions that are centered at these scattered p-values and have a width given by the measurement uncertainties. Performing the same log-likelihood analysis as described above for varying $\sigma_{\rm scat}$, we find that the $3\,\sigma$ result holds for $\sigma_{\rm scat} > 0.03$; at the $1\,\sigma$ level this is $\sigma_{\rm scat} > 0.24$. We can also constrain the upper limit on the scatter in the parent distribution of p-values from our sample. This can be derived by determining for which $\sigma_{\rm scat}$ the log-likelihood of the measured p-values is smaller than the one from the synthetic dataset analysis in 99.73 % of the 10^5 cases. This upper limit for $\sigma_{\rm scat}$ is 1.40 at the $3\,\sigma$ level; at the $1\,\sigma$ level this is $\sigma_{\rm scat} < 0.45$. In summary, from our sample we constrain the intrinsic width of the parent distribution of p-values to be $0.24 < \sigma_{\rm scat} < 0.45$ at the $1\,\sigma$ level and $0.03 < \sigma_{\rm scat} < 1.40$ at the $3\,\sigma$ level

Values of $p = 2.2$ have been widely quoted as a typical number and the deviations from this interpreted as due to the external environment or further energy injections from the source (e.g. Berger et al. 2003a). Mészáros et al. (1998) showed that for a single value of p, variations in the jet energy per solid angle, i.e. structured jets, could lead to a range of lightcurve decays; which can also be produced if a set of intrinsically similar, structured jets are viewed at various off-axis angles (Rossi et al. 2002). The study of such structure in the jet and viewing angle dependence is, however, beyond the scope of this work.

Jóhannesson et al. (2006) claim that from broken power law fits the value of p is overestimated from the pre-break lightcurve slope while being underestimated from the post-break slope, if the temporal coverage is limited. The results presented in that paper were only for a homogeneous ambient medium; they claim that in a wind medium the p value from the pre-break lightcurve slope does not show a systematic deviation.

More recently, breaks in lightcurves, both optical and X-ray, which would generally have been attributed to jet breaks, have been found to be chromatic, in sharp contrast to the picture of a jet break which should be achromatic. As such, several previously claimed jet breaks may have to be revised; unfortunately, there is no relevant data to confirm or reject these claimed jet breaks, since these have been found only in one waveband (mostly the optical, owing to the lack of dense monitoring in X-rays in the pre-*Swift* era). As such, the mention of jet breaks in this paper has been taken at face value, but with the caveat mentioned here.

If we compare the values for p calculated here with those calculated from the X-ray spectra alone (Stratta et al. 2004), we find they agree within the 90% errors except for the bursts GRB 970508 and GRB 990510. With this method we reduce the average 90% error on p from ± 0.58 (Stratta et al. 2004) to $^{+0.12}_{-0.20}$, and the values obtained are also likely to be more robust given that consistency between the nIR, optical, UV and X-ray is required.

Shen et al. (2006) have measured the minimum possible width of the electron energy index distribution for X-ray afterglows of BeppoSAX bursts taken from de Pasquale et al. (2006), by fitting single absorbed power laws to the spectra and deriving p. They found that the narrowest possible distribution is consistent with a delta function within the 1σ errors, in contradiction to their findings from a *Swift* sample of X-ray afterglows and from the prompt emission of a BATSE GRB sample. They comment that the relatively larger errors on the X-ray slopes of the *BeppoSAX* sample compared with the Swift sample are likely allowing for an apparently narrower distribution. They calculate that the distribution of p for the *Swift* sample of X-ray afterglows (O'Brien et al. 2006) has a width of 0.34 ± 0.07. We note that Shen et al. (2006) have derived distributions of p from X-ray afterglows only, which makes it impossible to know whether the cooling frequency lies above or below the X-ray regime, and can only be determined if there are accompanying optical measurements.

Panaitescu & Kumar (2002) calculated jet parameters for a sample of 10 GRBs including several studied here, using broadband observations including radio data when possible. In their model, based also on the fireball model, they assume uniform jets (no structure across the jet) and the the energy parameters ϵ_e and ϵ_B are constant, and finally they assume the observer is located on the jet symmetry axis. Our spectrally-derived values are consistent with theirs at the 3σ level or better for GRBs 970508, 980519, 990510 and 000926. There is no agreement for GRB 990123. They found a spread in p values as do we, but with half the values lying below 2, and a mean value of $p = 1.92^{+0.28}_{-0.26}$ (2σ).

Chevalier & Li (2000) carried out a similar study of broadband afterglow data, and their estimates for p are in agreement with ours for the GRBs 970228, 970508, 980519 and 990510, and disagree for GRB 990123 (they do not quote errors per source but estimate errors to be ~ 0.1). They conclude that their sample shows a range in the values of p which is not consistent with a single value.

3.5.2 The Circumburst Medium

The profile of the circumburst medium is a particularly important parameter in studying the progenitors of GRBs. In the case of long-soft bursts the progenitor is a massive star that is expected to have had a massive stellar wind in earlier phases of its evolution, and one would expect to see a signature of that wind in the afterglow lightcurves. Evidence for a stellar wind in the form of fast outflowing absorption lines within restframe UV spectra has been seen in a small number of cases, the best example being GRB 021004 (e.g. Schaefer et al. 2003; Starling et al. 2005). This does not mean, however, that a density profile with $n \propto r^{-2}$ is always expected, since this assumes a constant mass-loss rate and a constant wind velocity. Changes in mass-loss rate and also interactions of the wind with the interstellar medium can alter the ambient medium profile (e.g. Ramirez-Ruiz et al. 2005; Van Marle et al. 2006).

In the first broadband modeling attempts the ambient medium was assumed to be the homogeneous interstellar medium, which was consistent with the derived particle densities. However, since the progenitors of at least a fraction of all GRBs are now known to be massive stars and the blast wave is situated at $\sim 10^{17}$ cm at ~ 1 day after the burst, a massive stellar wind profile is expected. Nonetheless, the medium that the blast wave is probing could still be homogeneous, because of the emergence of a reverse shock in the wind when the wind meets the interstellar medium (see e.g. Wijers 2001; Ramirez-Ruiz et al. 2005). This shocked wind turns out to become homogeneous and, for typical physical parameters derived from afterglow modeling, the blast wave encounters the transition from the stellar wind to this homogeneous shocked medium at ~ 1 day (see e.g. Pe'er & Wijers 2006). The actual time of the transition, which would be detectable in the afterglow lightcurves, depends for instance on the mass-loss rate and the density of the interstellar medium, which are both not really well constrained for most GRBs. In our sample we do not see this kind of transition in the optical lightcurves in which there is a break. It has been claimed for some bursts, for instance GRB 030329 (Pe'er & Wijers 2006), that this transition is observed, but the often complex structure of the lightcurves confuses the determination of such a transition.

Another way to obtain a constant density from a massive stellar wind is in the region after the wind termination shock. The distance to the termination shock can be very large, but recent observations of two Wolf-Rayet binaries has suggested that this distance could be several times smaller if the wind is asymmetric. Eldridge (2007) shows that wind asymmetry probably exists in two systems, that can be caused for example by rotation, which is expected for GRB progenitors in the framework of the collapsar model in order to retain enough angular momentum. If the asymmetry exists for the entire stellar lifetime, then a closer termination shock and asymmetric supernova may be expected, increasing the chances of observing an afterglow traversing a constant density medium.

In our sample of 10 GRBs there are four sources that are consistent with an r^{-2} wind medium, with relatively small uncertainties, namely GRBs 971214, 990123, 000926, and 010222. There are three GRBs which are not consistent at a 90 % confidence level with a wind medium, GRBs 970508, 980519, and 990510, although for GRB 970508 caution is warranted with the interpretation of the lightcurves; and for the other four bursts the uncertainties are too large to constrain the ambient medium profile. We contrast our findings with Panaitescu & Kumar (2002), who, in broadband fits to the data of 10 bursts, found that a wind-like medium was preferred over a homogeneous medium in only one case: GRB 970508. For this particular burst our analysis provides a value of p which is an equally good fit to wind or uniform medium predictions for $\nu < \nu_c$ from the spectra and lightcurves, but the closure relations are obeyed (at the 2σ level for both cases) if $\nu > \nu_c$. They find circumburst densities of order 0.1–100 cm^{-3} for most sources, which they argue demonstrates the surrounding medium does not have, in general, the r^{-2} profile expected for the unperturbed wind of a massive GRB progenitor.

The association of long-soft GRBs with Ib/c supernovae was first suggested for GRB 980425 / SN 1998bw by Galama et al. (1998b), and confirmed by the discovery of GRB 030329 / SN 2003dh (e.g. Hjorth et al. 2003). Therefore, it is useful to compare the circumburst medium characteristics derived from GRB afterglows and from radio observations of supernovae, which also trace the density profile of the surroundings of these massive stars. Around radio supernovae r^{-2} density profiles have been found, but also in some cases significantly flatter behavior of $\sim r^{-1.5}$ in SN 1993J and SN 1979C (for a review on radio supernovae see Weiler et al. 2004, and references therein for individual supernovae). In the latter case a transition from r^{-2} to $r^{-1.4}$ was even observed. This flatter density profile can be attributed to changes in the mass-loss rate of the massive star in some phases of its evolution. The three sources in our sample of GRBs with a density profile flatter than r^{-2} are possible examples of the relativistic blast wave ploughing its way through a region of the circumburst medium which is affected by changing mass-loss rates. So although in Table 3.4 we have described them as GRBs with a homogeneous ambient medium, this is not necessarily the case. Especially for GRBs 970508 and 980519 this is a possibility, but the uncertainties on k are too large to distinguish a homogeneous from a flattened wind medium. GRB 990510 has smaller uncertainties and seems to be more consistent with a homogeneous medium, especially since the upper limit on k is ~ 1.0, which is much flatter than what is observed in radio supernovae.

The *Swift* satellite now provides us with substantially greater coverage of a large number of X-ray afterglows (~100 per year) and often with high quality data from which to measure the spectral and temporal slopes. However, few of these also have substantial optical follow-up. The combination of X-ray and optical data helps determine the position of the cooling break and obtain accurate spectral slopes which provide the value of p. For the derivation of k in this study, we have found the optical temporal data most constraining. For this reason, and for the confirmation of achromatic jet breaks it is essential that such late-time optical data be obtained for as many well sampled *Swift* X-ray afterglows as possible.

3.6 Conclusions

We have measured the injected electron energy distribution index, p, and the density profile of the circumburst medium, $n(r) \propto r^{-k}$, from simultaneous spectral fits to the X-ray, optical and nIR afterglow data of 10 *BeppoSAX* GRB afterglows. A statistical analysis demonstrates that the distribution of p values in this sample is inconsistent with a single value for p at the $3\,\sigma$ certainty, which is at variance with many theoretical studies of relativistic particle acceleration. We constrain the width of the parent distribution of p values and find it to be of the order of a few tenths, with $p = 2.04^{+0.02}_{-0.03}$ as the most likely p-value in our sample.

We measure the distribution of the local density parameter k, generally only assumed to be 0 or 2, and we find that the majority of GRBs for which we can constrain k well are consistent with a wind-like circumburst medium. One source (GRB 990510) is clearly, i.e. $> 3\,\sigma$ certainty, inconsistent with this picture and fits instead a homogeneous medium. These results are consistent with the expectations of at least a subset of GRBs originating from massive stars, which have a lot of mass-loss in the form of a surrounding stellar wind. We have discussed the possibility of values of $k < 2$ within the stellar wind framework.

The method presented here provides a way to study the distribution of blast wave parameters for a sample of GRBs, and allows estimates to be derived when insufficient data are available for a full time-dependent solution. In the current *Swift* era the method is equally well applicable, although one would have to ensure that the data are in the afterglow domain, i.e. not contaminated by prompt emission or late-time energy-injection. A decent sampling of the optical SED and lightcurve, more difficult with the average fainter *Swift* afterglow sample, is crucial to constrain the temporal slopes and cooling break frequency, which in turn are necessary to determine p and k.

Acknowledgements We thank Dipankar Bhattacharya for useful discussions. We thank Mike Nowak for his assistance with ISIS, Nanda Rea for assistance with the *BeppoSAX* data reduction and Martin Heemskerk for his help with the running of both ISIS and SAXDAS. This research has made use of SAXDAS linearized and cleaned event files produced at the *BeppoSAX* Science Data Center. The authors acknowledge benefits from collaboration within the Research Training Network ‘Gamma-Ray Bursts: An Enigma and a Tool’, funded by the EU under contract HPRN-CT-2002-00294. RLCS and ER acknowledge support from PPARC. RAMJW, PAC and KW thank NWO for support under grant 639.043.302.

	Spectral	Optical Temporal					X-ray Temporal	
GRB	p (Γ)	p ($\alpha_1, 0$)	p ($\alpha_1, 2$)	p ($\alpha_2, 0$)	p ($\alpha_2, 2$)	p (α_2, j)	p (α_x)	p (α_x, j)
970228	$2.12^{+0.46}_{-0.06}$	**2.95 ± 0.32**	**2.28 ± 0.32**	...	...	...	2.40 ± 0.43	1.30 ± 0.32
970508	$2.28^{+0.28}_{-0.58}$	**2.65 ± 0.02**	1.99 ± 0.02	...	...	...	2.13 ± 0.21	1.10 ± 0.16
971214	$2.08^{+0.18}_{-0.28}$	2.99 ± 0.17	**2.32 ± 0.17**	...	...	...	2.80 ± 0.21	1.60 ± 0.16
980329	**2.50**$^{+0.20}_{-0.62}$	**2.13 ± 0.26**	1.47 ± 0.26	...	...	...	**2.67 ± 0.43**	1.50 ± 0.32
980519	$2.86^{+0.14}_{-0.20}$	**3.00 ± 0.26**	2.33 ± 0.26	4.03 ± 0.06	3.36 ± 0.06	2.27 ± 0.05	3.11 ± 0.64	1.83 ± 0.48
980703	**2.74**$^{+0.10}_{-0.48}$	**2.13 ± 1.79**	**1.47 ± 1.79**	**3.20 ± 0.98**	**2.53 ± 0.98**	**1.65 ± 0.74**	**1.87 ± 0.43**	0.90 ± 0.32
990123	**1.99**$^{+0.00}_{-0.07}$	2.65 ± 0.13	**1.99 ± 0.13**	3.16 ± 0.32	2.49 ± 0.32	**1.62 ± 0.24**	**3.41 ± 1.77**	**2.06 ± 1.33**
990510	**2.06**$^{+0.14}_{-0.02}$	**2.23 ± 0.04**	1.56 ± 0.04	3.80 ± 0.13	3.13 ± 0.13	**2.10 ± 0.10**	2.53 ± 0.21	1.40 ± 0.16
000926	$2.50^{+0.16}_{-0.56}$	3.32 ± 0.06	**2.65 ± 0.06**	4.27 ± 0.11	3.60 ± 0.11	**2.45 ± 0.08**	2.93 ± 1.07	1.70 ± 0.80
010222	**2.04**$^{+0.18}_{-0.10}$	**1.80 ± 0.19**	1.13 ± 0.19	2.92 ± 0.04	**2.25 ± 0.04**	1.44 ± 0.03	2.44 ± 0.09	1.33 ± 0.06

Table 3.5 — Values for p in the case of $\nu_{\rm opt} < \nu_{\rm c} < \nu_{\rm X}$. We calculate the results for the cases $k = 0$ and $k = 2$. Bold type highlights consistent results (at 90% level). In cases where the best-fitting spectral model to the SED (from Paper I) is inconsistent with the model fits, we show the results for this original best-fitting model in italics.

	Spectral	Optical Temporal					X-ray Temporal		
GRB	p (Γ)	p ($\alpha_1, 0$)	p ($\alpha_1, 2$)	p ($\alpha_2, 0$)	p ($\alpha_2, 2$)	p (α_2, j)	p ($\alpha_x, 0$)	p ($\alpha_x, 2$)	p (α_x, j)
970228	$\mathbf{2.44}^{+0.18}_{-0.06}$	**2.95 ± 0.32**	**2.28 ± 0.32**	...	...	...	**2.73 ± 0.43**	**2.07 ± 0.43**	1.30 ± 0.32
970508	$\mathbf{2.56}^{+0.10}_{-0.46}$	**2.65 ± 0.02**	1.99 ± 0.02	...	...	...	**2.47 ± 0.21**	1.80 ± 0.21	1.10 ± 0.16
971214	$\mathbf{2.20}^{+0.06}_{-0.06}$	2.99 ± 0.17	**2.32 ± 0.17**	...	...	...	3.13 ± 0.21	**2.47 ± 0.21**	1.60 ± 0.16
980329	$\mathit{2.64}^{+0.08}_{-0.14}$	**2.13 ± 0.26**	1.47 ± 0.26	...	...	...	*3.00 ± 0.43*	*2.33 ± 0.43*	1.50 ± 0.32
980519	$\mathbf{2.96}^{+0.06}_{-0.08}$	**3.00 ± 0.26**	2.33 ± 0.26	4.03 ± 0.06	3.36 ± 0.06	2.27 ± 0.05	**3.44 ± 0.64**	**2.77 ± 0.64**	1.83 ± 0.48
980703	$\mathit{2.84}^{+0.06}_{-0.06}$	**2.13 ± 1.79**	**1.47 ± 1.79**	**3.20 ± 0.98**	**2.53 ± 0.98**	**1.65 ± 0.74**	2.20 ± 0.43	1.53 ± 0.43	0.90 ± 0.32
990123	$2.22^{+0.02}_{-0.02}$	2.65 ± 0.13	**1.99 ± 0.13**	3.16 ± 0.32	2.49 ± 0.32	**1.62 ± 0.24**	3.75 ± 1.77	3.08 ± 1.77	2.06 ± 1.33
990510	$2.71^{+0.01}_{-0.02}$	**2.23 ± 0.04**	1.56 ± 0.04	3.80 ± 0.13	3.13 ± 0.13	**2.10 ± 0.10**	2.87 ± 0.21	2.20 ± 0.21	1.40 ± 0.16
000926	$\mathbf{2.54}^{+0.14}_{-0.08}$	3.32 ± 0.06	**2.65 ± 0.06**	4.27 ± 0.11	3.60 ± 0.11	**2.45 ± 0.08**	**3.27 ± 1.07**	**2.60 ± 1.07**	**1.70 ± 0.80**
010222	$\mathit{2.72}^{+0.05}_{-0.05}$	**1.80 ± 0.19**	1.13 ± 0.19	2.92 ± 0.04	**2.25 ± 0.04**	1.44 ± 0.03	*2.77 ± 0.09*	2.11 ± 0.09	1.33 ± 0.06

Table 3.6 — Values for p in the case of $\nu_{\rm opt} < \nu_{\rm X} < \nu_{\rm c}$. We calculate the results for the cases $k = 0$ and $k = 2$. Bold type highlights consistent results (at 90% level). In cases where the best-fitting spectral model to the SED (from Paper I) is inconsistent with the model fits, we show the results for this original best-fitting model in italics.

4

The radio afterglow of GRB 030329 at centimeter wavelengths: evidence for a structured jet or non-relativistic expansion

A.J. van der Horst, E. Rol, R.A.M.J. Wijers, R. Strom, L. Kaper
& C. Kouveliotou

Astrophysical Journal 634, 1166 (2005)

Abstract We present our centimeter wavelength (1.4, 2.3 and 4.8 GHz) light curves of the afterglow of GRB 030329, which were obtained with the Westerbork Synthesis Radio Telescope. Modeling the data according to a collimated afterglow results in a jet break time of 10 days. This is in accordance with earlier results obtained at higher radio frequencies. However, with respect to the afterglow model, some additional flux at the lower frequencies is present when these light curves reach their maximum after 40-80 days. We show that this additional flux can be modeled with two or more components with progressively later jet breaks. From these results we infer that the jet is in fact a structured or a layered jet, where the ejecta with lower Lorentz factors produce additional flux that becomes visible at late times in the lowest frequency bands. We show that a transition to non-relativistic expansion of the fireball at late times can also account for the observed flux excess, except for the lowest frequency (1.4 GHz) data.

4.1 Introduction

Since the discovery of afterglow emission of gamma-ray bursts (GRBs) at X-ray, optical and radio wavelengths (Costa et al. 1997; Van Paradijs et al. 1997; Frail et al. 1997a), it has become clear that broad-band observations are needed to determine the physical processes producing the afterglow emission in the context of the available models, the most popular being the fireball model (e.g., Rees & Mészáros 1992; Mészáros & Rees 1997). Obtaining the overall shape of the energy distribution and the time evolution of the GRB afterglow provides information about the intrinsic energy, both in electrons and in magnetic fields, as well as about the matter into which the GRB blasted its ejecta (see, e.g., Wijers & Galama 1999). Although optical observations alone can constrain the value of some of these physical parameters, observations covering the radio to X-ray wavelength regions are required to determine all of them.

The self-absorption frequency, ν_a, of the afterglow broad-band spectrum can often be constrained by radio observations at centimeter wavelengths (e.g., Wijers & Galama 1999). As the afterglow spectrum evolves, the two other characteristic break frequencies in its broad-band spectrum (the frequency at the peak flux, ν_m, and the cooling frequency, ν_c) enter the radio regime as well, although in practice the flux level at ν_c is below the detection limit of current radio telescopes. The latter frequency can usually be determined from the available optical and X-ray data, which span the frequency range where the cooling frequency is found during the first days of the afterglow. These break frequencies and their time evolution uniquely determine the parameters that make up the fireball model and its evolution.

GRB 030329 is the closest gamma-ray burst discovered so far for which an afterglow has been found[1]. At a redshift of $z = 0.1685$ (Greiner et al. 2003), its afterglow was discovered in $R = 12.4$ magnitude, just 67 minutes after the GRB itself (Sato et al. 2003), about 100 times brighter than the average GRB afterglow. The brightness of the afterglow made it possible to study its evolution for a long time and in detail over a broad range of frequencies, from X-ray to centimeter wavelengths. Furthermore, its proximity provided an excellent opportunity to look for a supernova signature in both the light curve and the spectrum, as predicted by the collapsar model (Woosley 1993; MacFadyen & Woosley 1999), the currently favored progenitor model for long duration gamma-ray bursts. The resemblance between the supernova spectrum distilled from the GRB 030329 afterglow and that of the energetic type Ic supernova SN1998bw (associated with GRB 980425, Galama et al. 1998b) provides strong support for the core collapse

---

[1] GRB 980425/SN 1998bw at $z = 0.0085$ was closer, but no afterglow was found

of massive stars as the cause for GRBs (Hjorth et al. 2003; Stanek et al. 2003).

Several authors have modeled the broad-band afterglow behavior with a standard fireball model for the afterglow. A first approximation shows excess flux (on top of the already bumpy light curve) after the first few days, most noticeable at the lower frequencies. Willingale et al. (2004) attribute the excess flux to the underlying supernova, but most authors (e.g. Berger et al. (2003b); Sheth et al. (2003); Tiengo et al. (2004)) prefer a two-component jet model, where a slower jet is responsible for the extra emission appearing at optical wavelengths around 10 days after the burst. Even later time observations show a likely transition to the non-relativistic regime, estimated around 40 - 50 days after the burst (Tiengo et al. (2004); Frail et al. (2005)).

Here we describe our radio monitoring campaign of this extraordinarily bright afterglow with the Westerbork Synthesis Radio Telescope (WSRT) in the centimeter waveband. In Section 4.2 we describe the data we obtained. In Section 4.3 we apply an afterglow model to the data, and in Section 4.4 we compare our results with radio data obtained by other groups. Finally, in Section 4.5, we summarize our findings and draw our conclusions.

4.2 Data reduction and analysis

Data were obtained with the WSRT, at 1.4, 2.3 and 4.8 GHz. We used the Multi Frequency Front Ends (Tan 1991) in combination with the IVC+DZB backend[2] in continuum mode, with a bandwidth of 8x20 MHz. Gain and phase calibrations were performed with the calibrator 3C286, though sometimes 3C147 or 3C48 were used. Table 4.3 lists the log of the observations, all done in 2003. VLBI observations prevented us from using the WSRT in the second half of May, and observations were resumed in June, mostly at 4.8 GHz. At 2.3 and 1.4 GHz the observations suffered from confusion from nearby bright sources, causing the noise to be at least a factor of two above the theoretical limit.

We checked our results for consistency by measuring the flux of several nearby point sources, which were assumed to be constant. In a few observations, we found these sources to be systematically dimmer, as indicated in the observation log; we therefore suspect that the flux derived in these observations for the afterglow is also below its real value. Although we could in principle scale these fluxes upward, we decided to ignore these observations in our analysis, as the cause of these low flux levels is not clear.

The 1.4, 2.3 and 4.8 GHz light curves are presented in Figure 4.1. The

---

[2] See sect. 5.2 at http://www.astron.nl/wsrt/wsrtGuide/node6.html

general trend of the light curves is that expected for the low-frequency part of a GRB afterglow: as long as the self-absorption frequency, ν_a, is higher than the observed frequency interval, the light curve rises since the frequency of the minimum electron injection energy ν_m moves toward lower frequencies. When both ν_a and ν_m pass the observed frequency interval (not necessarily at the same time), a turn-over in the light curve occurs and the flux falls off steeply. We have listed the precise temporal dependencies of ν_a, ν_m, ν_c and the peak flux $F_{\nu,\max}$ in Table 4.1, for a homogeneous circumburst medium as well as for a massive stellar wind, in which the external density ρ depends on distance r to the center as $\rho \propto r^{-2}$. The evolution in time of ν_a, ν_m and $F_{\nu,\max}$ is plotted in Figure 4.2. Table 4.2 lists the dependencies of the flux on ν and t (note the change in the spectral index when ν_m becomes less than ν_a).

4.3 Applying the fireball model to the data

We have modeled the data simultaneously in time and frequency, using a general broad-band afterglow model which includes a jet break and a transition to non-relativistic expansion of the fireball. The several power-law segments of the broad-band spectrum were connected smoothly in a way described in Appendix 4.6. Because $F_{\nu,\max}$, ν_a, ν_m and ν_c are functions of time, we need to quote them at some fixed moment, for which we choose the jet break time. At earlier and later times the characteristic frequencies and the peak flux evolve in time according to Table 4.1. The resulting light curves are given in Table 4.2. The transitions between the different regimes, marked by the jet break time t_j and the time t_{nr} at which the fireball becomes non-relativistic, are treated as smoothly broken power-laws as described in Appendix 4.6.

Since our data show a large scatter, especially at early times due to scintillation, where they do not follow a smooth curve, we did not apply a χ^2 fit, but merely tried to obtain a best fit by eye. This ignores the scintillation, and it will also put some more emphasis on the 1.4 GHz light curve: a χ^2 fit tends to follow the 4.8 GHz data points since they are more numerous, and will hence ignore the global trend seen in the 1.4 GHz light curve. The result of such an eye-ball broad-band fit is shown in Figure 4.1. Note that the scintillation amplitude is largest in the first few days, after which it quickly declines (the large decrease in the 2.3 GHz light curve around 20 days could be an artifact in the data, since it does not show up in the other light curves).

In this way, we obtained a value of 35 GHz for the electron injection frequency, ν_m, and a value of 13 GHz for the self absorption frequency, ν_a, at 10 days after the burst, which is the jet break time. The flux at ν_m is about 61 mJy

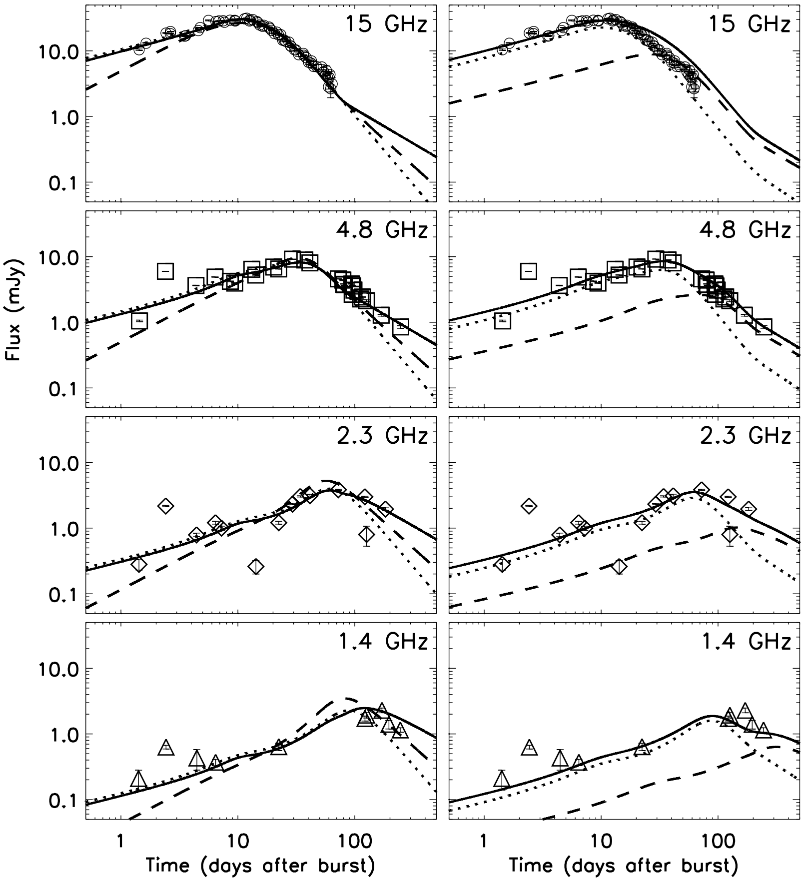

Figure 4.1 — Eyeball fits to the 4.8, 2.3 and 1.4 GHz WSRT data simultaneously, with 15 GHz VLA/ATCA/RT observations from Berger et al. (2003b) for comparison. Note the large scatter around the model light curves during the first days. **Left:** The lines represent models with $\nu_\mathrm{m} \simeq 35$ GHz, $\nu_\mathrm{a} \simeq 13$ GHz and $F_{\nu,\mathrm{max}} \simeq 61$ mJy at $t_\mathrm{j} = 10$ days. The solid line corresponds to a model in which the fireball expands into a homogeneous medium and the non-relativistic phase of the fireball evolution starts after 80 days; the dotted line corresponds to the same model but without a non-relativistic phase, so it deviates from the solid line after 50 days; the dashed line corresponds to a model with a non-relativistic phase after 80 days and expansion of the fireball into a massive stellar wind. The peak frequency falls below the self absorption frequency at 17 days. From then on, the maximum of a light curve at a given wavelength marks the passing of the self absorption frequency. **Right:** A two-component fit to the data. The first component (dotted line, with a jet break time of 10 days) is responsible for the light curves until 50 days, while the second component (dashed line, with $t_\mathrm{j} \simeq 30$ days) accounts for the later peak in the light curves. The combined light curve is shown as the solid line.

	ν_a	ν_a	ν_m	ν_c	$F_{\nu,\mathrm{max}}$
	$(\nu_\mathrm{a} < \nu_\mathrm{m})$	$(\nu_\mathrm{m} < \nu_\mathrm{a})$			
$t < t_\mathrm{j} < t_\mathrm{nr}$ (homog.)	t^{0}	$t^{-(3p+2)/2(p+4)}$	$t^{-3/2}$	$t^{-1/2}$	t^{0}
$t < t_\mathrm{j} < t_\mathrm{nr}$ (wind)	$t^{-3/5}$	$t^{-3(p+2)/2(p+4)}$	$t^{-3/2}$	$t^{1/2}$	$t^{-1/2}$
$t_\mathrm{j} < t < t_\mathrm{nr}$	$t^{-1/5}$	$t^{-2(p+1)/(p+4)}$	t^{-2}	t^{0}	t^{-1}
$t_\mathrm{j} < t_\mathrm{nr} < t$ (homog.)	$t^{6/5}$	$t^{-(3p-2)/(p+4)}$	t^{-3}	$t^{-1/5}$	$t^{3/5}$
$t_\mathrm{j} < t_\mathrm{nr} < t$ (wind)	$t^{-2/15}$	$t^{-(7p+6)/3(p+4)}$	$t^{-7/3}$	t^{1}	$t^{-1/3}$

Table 4.1 — The various temporal dependencies of the break frequencies and peak flux of the afterglow broad band spectrum. Before the jet break time t_j and after the non-relativistic timescale t_nr different scalings arise from a homogeneous circumburst medium or a stellar wind, when the external density ρ depends on distance r to the center as $\rho \propto r^{-2}$. Between t_j and t_nr the external density profile does not influence the scalings.

at that time. We find the electron index to be $p = 2.1$. The value of ν_c can only be determined with observations at higher frequencies; our dataset indicates that $\nu_\mathrm{c} \geq 10^{12}$ Hz, which is in agreement with the findings by Smith et al. (2005), who find that the rapid fall in their 350 GHz light curve can be attributed to the cooling frequency passing through their observing band. These results are somewhat at odds with the findings by Berger et al. (2003b). They obtain higher values for the characteristic frequencies ν_a (19 GHz) and ν_m (43 GHz), and the peak flux $F_{\nu,\mathrm{max}}$ (96 mJy) at the jet break time $t_\mathrm{j} \simeq 9.8$ days. To investigate this further, we performed a fit which includes their data, as well as radio data from Sheth et al. (2003). This fit gives similar results to those obtained from our previous fit.

From the obtained characteristic frequencies and the peak flux we find an isotropic energy $E_\mathrm{iso} \simeq 4.0 \cdot 10^{51} \nu_{\mathrm{c},13}^{1/4}$ erg, a circumburst density $n \simeq 0.56 \nu_{\mathrm{c},13}^{3/4}$ cm^{-3}, and the fractions of energy in the electrons ε_e and magnetic field ε_B of $0.25 \nu_{\mathrm{c},13}^{1/4}$ and $0.49 \nu_{\mathrm{c},13}^{-5/4}$ respectively. The cooling frequency can not be determined from the radio observations at centimeter wavelengths, but we take $\nu_\mathrm{c} \equiv 10^{13} \nu_{\mathrm{c},13}$ to compare our results with Berger et al. (2003b). The opening angle of the jet can be found to be $\theta_\mathrm{j} \simeq 0.38 \nu_{\mathrm{c},13}^{-1/2}$ rad (22°) from the jet break time of 10 days, which gives a beaming-corrected energy of $E_\mathrm{cor} \simeq 2.9 \cdot 10^{50} \nu_{\mathrm{c},13}^{-3/4}$ erg. This energy is comparable to Berger et al. (2003b), the circumburst medium density we find is smaller, but ε_e and ε_B are larger.

$\nu_a < \nu_m < \nu_c$	F ($\nu < \nu_a$)	F ($\nu_a < \nu < \nu_m$)	F ($\nu_m < \nu < \nu_c$)	F ($\nu_c < \nu$)
$t < t_j < t_{nr}$ (homogeneous)	$\nu^2 \cdot t^{1/2}$	$\nu^{1/3} \cdot t^{1/2}$	$\nu^{-(p-1)/2} \cdot t^{-3(p-1)/4}$	$\nu^{-p/2} \cdot t^{-(3p-2)/4}$
$t < t_j < t_{nr}$ (stellar wind)	$\nu^2 \cdot t^1$	$\nu^{1/3} \cdot t^0$	$\nu^{-(p-1)/2} \cdot t^{-(3p-1)/4}$	$\nu^{-p/2} \cdot t^{-(3p-2)/4}$
$t_j < t < t_{nr}$	$\nu^2 \cdot t^0$	$\nu^{1/3} \cdot t^{-1/3}$	$\nu^{-(p-1)/2} \cdot t^{-p}$	$\nu^{-p/2} \cdot t^{-p}$
$t_j < t_{nr} < t$ (homogeneous)	$\nu^2 \cdot t^{-2/5}$	$\nu^{1/3} \cdot t^{8/5}$	$\nu^{-(p-1)/2} \cdot t^{-3(5p-7)/10}$	$\nu^{-p/2} \cdot t^{-(3p-4)/2}$
$t_j < t_{nr} < t$ (stellar wind)	$\nu^2 \cdot t^{2/3}$	$\nu^{1/3} \cdot t^{4/9}$	$\nu^{-(p-1)/2} \cdot t^{-(7p-5)/6}$	$\nu^{-p/2} \cdot t^{-(7p-8)/6}$
$\nu_m < \nu_a < \nu_c$	F ($\nu < \nu_m$)	F ($\nu_m < \nu < \nu_a$)	F ($\nu_m < \nu < \nu_c$)	F ($\nu_c < \nu$)
$t < t_j < t_{nr}$ (homogeneous)	$\nu^2 \cdot t^{1/2}$	$\nu^{5/2} \cdot t^{5/4}$	$\nu^{-(p-1)/2} \cdot t^{-3(p-1)/4}$	$\nu^{-p/2} \cdot t^{-(3p-2)/4}$
$t < t_j < t_{nr}$ (stellar wind)	$\nu^2 \cdot t^1$	$\nu^{5/2} \cdot t^{7/4}$	$\nu^{-(p-1)/2} \cdot t^{-(3p-1)/4}$	$\nu^{-p/2} \cdot t^{-(3p-2)/4}$
$t_j < t < t_{nr}$	$\nu^2 \cdot t^0$	$\nu^{5/2} \cdot t^1$	$\nu^{-(p-1)/2} \cdot t^{-p}$	$\nu^{-p/2} \cdot t^{-p}$
$t_j < t_{nr} < t$ (homogeneous)	$\nu^2 \cdot t^{-2/5}$	$\nu^{5/2} \cdot t^{11/10}$	$\nu^{-(p-1)/2} \cdot t^{-3(5p-7)/10}$	$\nu^{-p/2} \cdot t^{-(3p-4)/2}$
$t_j < t_{nr} < t$ (stellar wind)	$\nu^2 \cdot t^{2/3}$	$\nu^{5/2} \cdot t^{11/6}$	$\nu^{-(p-1)/2} \cdot t^{-(7p-5)/6}$	$\nu^{-p/2} \cdot t^{-(7p-8)/6}$

Table 4.2 — The spectral and temporal flux dependencies in the different regimes of the broad-band afterglow spectrum.

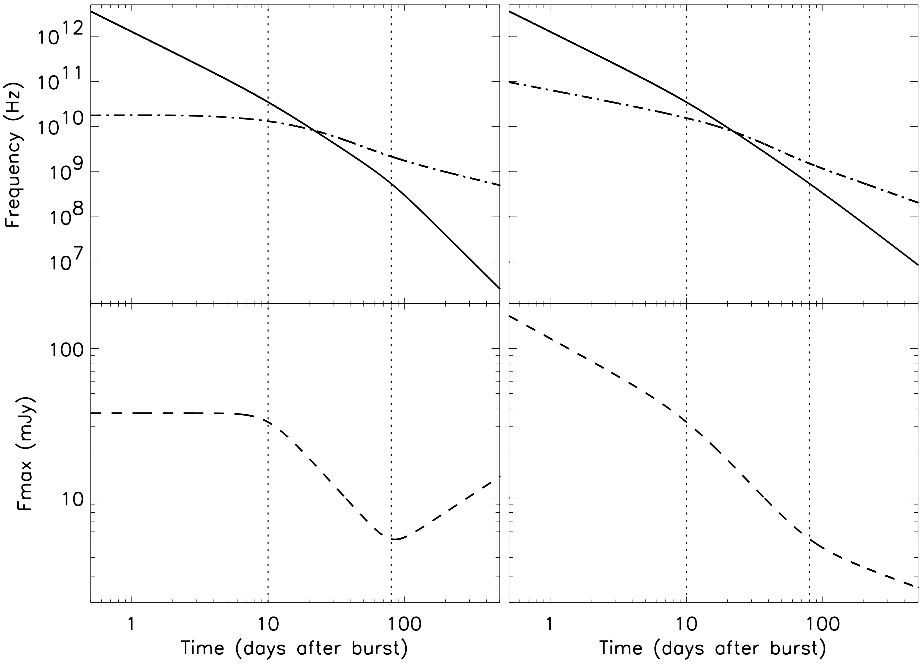

Figure 4.2 — The temporal evolution of the electron injection frequency, ν_{m}, the self absorption frequency, ν_{a}, and the peak flux, $F_{\nu,\mathrm{max}}$. The upper panels show the evolution of ν_{m} (solid line) and ν_{a} (dash-dotted line), the lower panels the evolution of $F_{\nu,\mathrm{max}}$. The left panels show a model in which the fireball expands into a homogeneous medium, with a jet break time $t_{\mathrm{j}} = 10$ days, and the non-relativistic phase of the fireball evolution starts after $t_{\mathrm{nr}} = 80$ days. The right panels show a model in which the fireball expands into a massive stellar wind, with a jet break time $t_{\mathrm{j}} = 10$ days, and the non-relativistic phase of the fireball evolution starts after $t_{\mathrm{nr}} = 80$ days. The dotted lines show where the breaks in the temporal behavior of the parameters occur at t_{j} and t_{nr}.

At the turnover in the late-time light curves at 1.4, 2.3 and 4.8 GHz we find an excess in flux compared to the model. We present two possible explanations for this behavior. The first one is a non-relativistic phase after $t_{\mathrm{nr}} \simeq 80$ days. Table 4.2 shows that the light curves flatten in the transition to a non-relativistic phase. In Figure 4.1 one can see that this extension of the model fits the data at 2.3 and 4.8 GHz well when one assumes a homogeneous external medium. However, the flux at 1.4 GHz is overestimated at the latest times in this case (note that the symbols are larger than the error bars). The model with an external density gradient and a non-relativistic phase gives a better result at 1.4 GHz, but underestimates the flux at higher frequencies.

The second explanation of the late-time flux excess is an extra component, which consists of an afterglow with a jet break time later than 10 days. The resultant fit is also shown in Figure 4.1. For the first component, which produces the main flux at higher frequencies, the parameters are set as before except for $F_{\nu,\mathrm{max}} \simeq 48$ mJy. The second component has $t_{\mathrm{j}} \simeq 30$ days, $\nu_{\mathrm{m}} \simeq 20$ GHz, $\nu_{\mathrm{a}} \simeq 10$ GHz and $F_{\nu,\mathrm{max}} \simeq 16$ mJy at the jet break time; so at $t = 10$ days the second component has $\nu_{\mathrm{m}} \simeq 35$ GHz, $\nu_{\mathrm{a}} \simeq 13$ GHz and $F_{\nu,\mathrm{max}} \simeq 48$ mJy. The electron index $p \simeq 2.2$ for both jets. The physical parameters we derive from these characteristic frequencies and peak flux are $n \simeq 0.82\nu_{\mathrm{c},13}^{3/4}\,\mathrm{cm}^{-3}$, $\varepsilon_{\mathrm{e}} \simeq 0.28\nu_{\mathrm{c},13}^{1/4}$ and $\varepsilon_{\mathrm{B}} \simeq 0.43\nu_{\mathrm{c},13}^{-5/4}$ for both components; for the first component we find $E_{\mathrm{iso}} \simeq 4.0 \cdot 10^{51}\nu_{\mathrm{c},13}^{1/4}$ erg, $\theta_{\mathrm{j}} \simeq 0.42\nu_{\mathrm{c},13}^{-1/2}$ rad (24°) and $E_{\mathrm{cor}} \simeq 2.4 \cdot 10^{50}\nu_{\mathrm{c},13}^{-3/4}$ erg, while for the second component $E_{\mathrm{iso}} \simeq 9.1 \cdot 10^{50}\nu_{\mathrm{c},13}^{1/4}$ erg, $\theta_{\mathrm{j}} \simeq 0.73\nu_{\mathrm{c},13}^{-1/2}$ rad (42°) and $E_{\mathrm{cor}} \simeq 2.4 \cdot 10^{50}\nu_{\mathrm{c},13}^{-3/4}$ erg. The data are well fitted by this two-component jet model. However, data at higher radio frequencies from Berger et al. (2003b) can not be fitted well in this model.

4.4 Discussion

A similar procedure of fitting two components with different jet breaks was applied by Berger et al. (2003b) to explain the break in the early-time optical (and X-ray) light curve. The underlying mechanism involves two jetted outflows, one with a small opening angle and a high Lorentz factor that produces the early-time light curve (with $t_{\mathrm{j}} \simeq 0.5$ days), and a jet with a larger opening angle and lower Lorentz factor that carries the bulk of the energy and produces the later-time light curve (with $t_{\mathrm{j}} \simeq 10$ days). The WSRT observations at 2.4 days after the burst have values for the flux that are well above the theoretical curves (see Figure 4.1). We investigated the possibility that these are signatures of the jet that produces the early-time optical light curve. However, with the constraints on the parameters from the optical and X-ray observations, it is not possible to fit the early radio observations with this jet with a jet break time of 0.5 days. A better explanation for these observations is scintillation.

From the result of our two-component model fit, we can conclude that, besides the jets with $t_{\mathrm{j}} \simeq 0.5$ and $t_{\mathrm{j}} \simeq 10$, another jet is present with even larger opening angle, that powers the late-time ($t > 50$ days) light curve and is therefore best visible at the very low frequencies observed here. However, it may be that the total jet (which possibly includes the first narrow jet as well) is structured (e.g. Mészáros et al. 1998; Rossi et al. 2002) and that the Lorentz factor Γ decreases toward the edge of the jet-cone. Alternatively, the outflow consists of a layered jet, where shocks with lower Γ follow the faster ones as they run into the surrounding medium. In both cases, one expects that the low Lorentz factors dominate at low frequencies and late times, and that the jet break occurs later at progressively lower frequencies.

The multiple component model is certainly not satisfactory: it does not give a good fit to the data at radio frequencies above 4.8 GHz at late times. Our model in which a transition to a non-relativistic phase of the fireball occurs after 80 days gives a better broadband radio fit except for the data at 1.4 GHz. This transition to a non-relativistic phase is also seen in VLA radio observations by Frail et al. (2005) and at X-ray frequencies by Tiengo et al. (2004), although their estimate for the time at which this transition occurs is lower than ours, i.e. $\sim$ 50 and $\sim$ 44 days respectively. Our low frequency radio data can not be fitted well by applying this low value for the non-relativistic transition.

Although the model in which a transition to a non-relativistic phase of the fireball occurs, gives the best broadband radio fit, the value of $t_{\rm nr}$ we find is much lower than theoretical estimates done by Granot et al. (2005) and Oren et al. (2004), based on determinations of the evolution of the image size of GRB 030329 (Taylor et al. (2005)). We estimate $t_{\rm nr} \simeq 209(\frac{E_{\rm cor}}{10^{51}n})^{1/3} \simeq 168\nu_{\rm c,13}^{-1/6}$ days, which is a factor of 2 higher than the 80 days we get from modeling the centimeter light curves. This discrepancy could be solved by fitting the broadband afterglow light curves of GRB 030329 simultaneously with the evolution of its image size.

4.5 Summary and conclusions

Our data confirm the picture of a second jet in the afterglow of GRB 030329, that manifests itself around $t_{\rm j} = 10$ days. However, the flux level around the time when the low frequency light curves peak is higher than that predicted by the two-component afterglow model (cf. Berger et al. 2003b). Adding a third component with a later $t_{\rm j}$, we can account for this excess flux. Taking into account the early jet break, seen most clearly at optical wavelengths, we suggest that one is actually seeing the result of several blast waves with a range in Lorentz factors (Rees & Mészáros 1998; Granot et al. 2003), something which comes quite naturally in the collapsar model for GRBs (MacFadyen et al. 2001; Ramirez-Ruiz et al. 2002; Zhang et al. 2003), and was already suggested by Sheth et al. (2003). However, their high frequency data was unable to distinguish jet breaks at later times. Our later time low frequency radio data show such a late-time jet break, corresponding to a lower Lorentz factor, and therefore support a layered or structured jet for the afterglow of GRB 030329.

An alternative explanation is the transition to a non-relativistic phase of the fireball. This model gives a good fit to the data at 2.3 and 4.8 GHz, but overestimates the flux at 1.4 GHz. This overestimation can be caused by the method of smoothly broken power-laws as described in Appendix 4.6. We did not take into account the jet that is pointing away from us, and this can possibly give extra flux at late times when the jet becomes non-relativistic and spherical. Continuation of observations at late times at low radio frequencies and more detailed physical models can diagnose the cause of this discrepancy more closely.

4.6 Appendix A: Broadband spectrum and light curve modeling

The dominating radiation mechanism for GRB afterglows is synchrotron emission. The broadband synchrotron spectrum is determined by the peak flux and three break frequencies, namely the synchrotron self-absorption frequency, ν_a, the frequency that corresponds to the minimal energy in the electron energy distribution, ν_m, and the cooling frequency, ν_c, that corresponds to electrons that lose their energy quickly by radiation. The time evolution of these four parameters gives the evolution of the spectrum and thus light curves at all observing frequencies.

The relativistic electrons emitting the synchrotron radiation are accelerated at the shock front to a power-law distribution of energies, $N(\gamma_e)d\gamma_e \propto \gamma_e^{-p}d\gamma_e$ for $\gamma_e \geq \gamma_m$. For electrons that cool on a timescale smaller than the dynamical timescale, the energy distribution is steeper, $N(\gamma_e)d\gamma_e \propto \gamma_e^{-p-1}d\gamma_e$. The broadband energy spectrum is found by connecting these two energy distributions at the cooling Lorentz factor γ_c, and then integrating the single-electron synchrotron spectrum over the distribution function. Synchrotron self-absorption is taken into account by calculating the flux F_ν as follows:

$$F_\nu = \frac{j_\nu}{D^2}(\frac{\alpha_\nu}{\alpha_{\nu_a}})^{-1}[1 - \exp(-\frac{\alpha_\nu}{\alpha_{\nu_a}})]\,, \tag{4.1}$$

with j_ν the emission coefficient, α_ν the absorption coefficient, and D the distance. A detailed description of our modeling is presented in Van der Horst, Wijers & Van den Horn (submitted to A&A).

The evolution of the characteristic frequencies and the peak flux is given in Table 4.1. We assume that after the jet break time the jet spreads sideways (Rhoads (1999)), until it becomes spherical approximately at the same time the fireball becomes non-relativistic and enters the Sedov-Von Neumann-Taylor phase of the evolution. The transitions between the different regimes, marked by the jet break time t_{j} and the time t_{nr} at which the fireball becomes non-relativistic, are treated as smoothly broken power-laws. We introduce a smoothening parameter s and take ν_{m} and ν_{c} as examples:

$$\nu_{\mathrm{m}}(t) = \nu_{\mathrm{m}}(t_{\mathrm{j}}) \cdot \left[\left(\frac{t}{t_{\mathrm{j}}}\right)^{3/2 \cdot s} + \left(\frac{t}{t_{\mathrm{j}}}\right)^{2 \cdot s} + \left(\frac{t_{\mathrm{nr}}}{t_{\mathrm{j}}}\right)^{2 \cdot s} \cdot \left(\frac{t}{t_{\mathrm{nr}}}\right)^{3 \cdot s} \right]^{-1/s} , \tag{4.2}$$

$$\nu_{\mathrm{c}}(t) = \nu_{\mathrm{c}}(t_{\mathrm{j}}) \cdot \left[\left(\frac{t}{t_{\mathrm{j}}}\right)^{-1/2 \cdot s} + \left(1 + \left(\frac{t}{t_{\mathrm{nr}}}\right)^{1/5 \cdot s}\right)^{-1} \right]^{1/s} . \tag{4.3}$$

Expressions for ν_{a} and $F_{\nu,\mathrm{max}}$ are similar.

We choose to have a smoothening parameter of $s = 5$ for every transition. However, these transitions will probably be different and this can only be accounted for in detailed hydrodynamical modeling of the fireball. So this smoothening parameter gives a an uncertainty which may account for the discrepancy seen at 1.4 GHz in the case of one jet with a transition to the non-relativistic phase at $t_{\mathrm{nr}} \simeq 80$ days.

Acknowledgements We greatly appreciate the support from the WSRT staff in their help with scheduling these observations as efficiently as possible. We thank Ed van den Heuvel for useful discussions. ER acknowledges support from NWO grant nr. 614-51-003. ER would like to thank the hospitality of the observatory of Padua. The authors acknowledge benefits from collaboration within the Research Training Network "Gamma-Ray Bursts: An Enigma and a Tool", funded by the EU under contract HPRN-CT-2002-00294.

Observing dates	Δt[3] (days)	Int. time (hours)	Frequency (GHz)	Flux (mJy)	Error (mJy)
Mar 30.658 - 31.138	1.414	3.3	1.4	0.21	0.07
Mar 30.674 - 31.148	1.427	3.6	2.3	0.28	0.05
Mar 30.691 - 31.157	1.440	3.6	4.8	1.05	0.03
Mar 31.655 - Apr 1.110	2.399	3.6	4.8	5.98	0.03
Mar 31.672 - Apr 1.126	2.415	3.6	2.3	2.17	0.05
Mar 31.688 - Apr 1.142	2.431	3.3	1.4	0.63	0.04
Apr 2.650 - 3.088	4.385	4.0	4.8	3.64	0.04
Apr 2.694 - 3.132	4.429	4.0	2.3	0.79	0.05
Apr 2.738 - 3.149	4.459	3.3	1.4	0.43	0.15
Apr 4.644 - 5.083	6.380	4.0	4.8	4.89	0.04
Apr 4.688 - 5.127	6.424	4.0	2.3	1.21	0.06
Apr 4.732 - 5.143	6.454	3.3	1.4	0.37	0.04
Apr 5.641 - 5.818	7.246	4.2	2.3	1.00	0.07
Apr 7.072 - 7.138	8.621	1.6	4.8	4.21	0.06
Apr 7.636 - 8.135	9.401	12.0	4.8	3.96	0.04
Apr 11.625 - 11.693	13.175	1.6	4.8	6.42	0.05
Apr 12.622 - 12.806	14.230	2.5	4.8	5.25	0.05
Apr 12.659 - 12.843	14.267	2.5	2.3	0.26	0.06
Apr 18.606 - 18.908	20.273	7.0	4.8	6.96	0.05
Apr 20.600 - 21.055	22.344	3.3	4.8	6.50	0.04
Apr 20.617 - 21.072	22.360	3.3	2.3	1.21	0.06
Apr 20.633 - 21.087	22.376	3.3	1.4	0.64	0.08
Apr 27.583 - 28.062	29.338	3.9	4.8	9.17	0.04
Apr 27.606 - 28.078	29.357	5.5	2.3	2.32	0.04
May 2.568 - 2.816	34.208	6.0	2.3	3.04	0.06
May 3.732 - 3.955	37.360	5.3	4.8	8.90	0.04
May 9.783 - 9.811	41.313	0.7	4.8	8.05	0.10
May 9.813 - 9.841	41.343	0.7	2.3	3.11	0.18
Jun 9.714 - 9.963	72.354	2.5	4.8	4.59	0.04
Jun 9.737 - 9.944	72.356	2.5	2.3	3.84	0.07
Jun 16.567 - 16.645	79.122	1.9	4.8	4.39[4]	0.08
Jun 17.750 - 17.792	80.287	1.0	4.8	3.79	0.08
Jun 18.777 - 18.819	81.314	1.0	4.8	3.74	0.10

---

[3] In days after the burst. The indicated time is the logarithmic average of the start and end of the integration.

[4] The flux of surrounding point sources is consistently lower compared to other observations.

Jun 30.430 - 30.440	92.951	0.3	4.8	2.34	0.18
Jul 1.652 - 1.743	94.214	1.0	4.8	3.82	0.10
Jul 2.488 - 2.524	95.022	0.9	4.8	2.67[4]	0.08
Jul 3.548 - 3.587	96.084	1.6	4.8	3.57	0.07
Jul 5.892 - 5.933	98.429	1.0	4.8	3.09	0.04
Jul 19.580 - 19.854	112.233	6.6	4.8	2.27	0.05
Jul 23.673 - 23.843	116.274	4.1	4.8	2.43	0.05
Jul 29.519 - 29.644	122.097	3.0	2.3	3.00	0.06
Jul 29.675 - 29.800	122.254	3.0	1.4	1.72	0.15
Aug 2.546 - 2.595	126.086	1.2	4.8	2.13	0.07
Aug 2.619 - 2.668	126.159	1.2	2.3	0.80[4]	0.27
Aug 2.692 - 2.740	126.232	1.2	1.4	1.93	0.18
Sep 13.535 - 13.701	168.134	4.0	4.8	1.28	0.04
Sep 16.196 - 16.250	170.739	1.3	1.4	2.29	0.19
Sep 28.161 - 28.285	182.739	3.0	2.3	1.95	0.09
Oct 11.291 - 11.458	195.891	4.0	1.4	1.40	0.21
Nov 29.248 - 29.491	244.885	5.8	1.4	1.15	0.09
Dec 1.128 - 1.288	246.724	3.8	4.8	0.85	0.04

Table 4.3: Log of the WSRT observations of GRB030329 in 2003

5

Detailed study of the GRB 030329 radio afterglow deep into the non-relativistic phase

A.J. van der Horst, A. Kamble, L. Resmi, R.A.M.J. Wijers, D. Bhattacharya,
B. Scheers, E. Rol, R. Strom, C. Kouveliotou, T. Oosterloo
& C.H. Ishwara-Chandra

Submitted to Astronomy & Astrophysics

Abstract We explore the physics behind one of the brightest radio afterglows ever, GRB 030329, at late times when the jet is non-relativistic. We determine the physical parameters of the blastwave and its surroundings, in particular the index of the electron energy distribution, the energy of the blastwave and the density (structure) of the circumburst medium; and compare our results with results from image size measurements. We observed the GRB 030329 radio afterglow with the Westerbork Synthesis Radio Telescope and the Giant Metrewave Radio Telescope at frequencies from 325 MHz to 8.4 GHz, spanning a time range of 268-1128 days after the burst. We modeled all the available radio data and derived the physical parameters. The index of the electron energy distribution is $p = 2.1$, the circumburst medium is homogeneous, and the transition to the non-relativistic phase happens at $t_{\rm NR} \sim 80$ days. The energy of the blastwave and density of the surrounding medium are comparable to previous findings. Our findings indicate that the blastwave is roughly spherical at $t_{\rm NR}$, and they are in agreement with the implications from the VLBI studies of the image size evolution. It is not clear from the presented dataset whether we have seen emission from the counter jet or not. We predict that the Low Frequency Array will be able to observe the afterglow of GRB 030329 and many other radio afterglows, constraining the physics of the blastwave during its non-relativistic phase even further.

5.1 Introduction

GRB 030329 has been a very distinctive event in many respects. Residing at a redshift of 0.1685 (Greiner et al. 2003), i.e. at a luminosity distance of 802 Mpc (adopting a flat universe with $\Omega_M = 0.27$, $\Omega_\Lambda = 0.73$ and $H_0 = 71 \mathrm{kms}^{-1}\mathrm{Mpc}^{-1}$), it is one of the nearest GRBs for which an afterglow has been observed (GRB 980425 at z = 0.0085 remains the nearest of the GRBs). GRB 030329 displayed one of the brightest afterglows ever, enabling the study of its evolution for a long time and in detail over a broad range of frequencies, from X-ray to centimetre wavelengths. The afterglow of this GRB is one with the longest follow ups ever, still visible in radio waves three years after the burst trigger. It was also the first GRB to have provided unambiguous evidence of the long suspected (e.g. Galama et al. 1998b) association between GRBs and supernovae (Hjorth et al. 2003; Stanek et al. 2003).

GRB 030329 was detected and localised by the HETE-II satellite (Vanderspek et al. 2003) on 29th March 2003, at UT 11:37:14.7 and lasted more than 100 s. The measured fluence for this burst was 5.5×10^{-5} erg cm^{-2} in the 7-30 keV band, and 1.1×10^{-4} erg cm^{-2} in the 30-400 keV band. The burst was followed by an extremely bright X-ray afterglow, 1.4×10^{-10} erg cm^{-2} s^{-1} in the 2-10 keV band, detected by RXTE $\sim$ 5 h after the burst (Marshall & Swank 2003). The optical afterglow was detected, 67 minutes after the burst, in R band at 12.4 mag (Sato et al. 2003). A bright radio afterglow of 3.5 mJy at 8.46 GHz was detected by the Very Large Array (VLA) on 2003 March 30.06 UT (Berger et al. 2003b). Around 7 days after the burst the optical spectrum showed the signature of underlying supernova emission, SN 2003dh (Hjorth et al. 2003; Stanek et al. 2003). The afterglow was subsequently followed at X-ray, optical, millimeter and radio wavelengths, providing the extremely rich temporal coverage of the transient in all wavebands (e.g. Tiengo et al. 2004; Lipkin et al. 2004; Gorosabel et al. 2006; Sheth et al. 2003; Kuno et al. 2004; Berger et al. 2003b). The proximity of the GRB and its exceptional radio brightness made it possible to resolve the afterglow image with a Very Long Baseline Interferometry (VLBI) campaign from 8 days (Taylor et al. 2004) up to 806 days (Pihlström et al. 2007) after the burst.

Extensive radio follow up of the afterglow has been reported earlier by (Berger et al. 2003b), Frail et al. (2005), Van der Horst et al. (2005b) and Resmi et al. (2005). These reports cover a period of up to 1 year post burst. In this paper, we report further extension of the low frequency radio follow up of the GRB 030329 afterglow, up to 1128 days after the burst, using the Westerbork Synthesis Radio Telescope (WSRT) and the Giant Metrewave Radio Telescope (GMRT). GRB 030329 is the first afterglow to be detected below an observing frequency of 1 GHz, and even as low as 610 MHz. In Section 5.2 we describe the observations and data analysis. In Section 5.3 we present the results from modeling the light curves of all the available radio data of the GRB 030329 afterglow, focusing on the blastwave physics in the non-relativistic phase of its evolution. In Section 5.4 we compare our modeling results with previous light curve studies and with the VLBI image size evolution. Furthermore, we put constraints on the emission of the counter jet, and we show model predictions for radio afterglow observations with the Low Frequency Array (LOFAR). Section 5.5 summarizes our results.

5.2 Observations & Analysis

GRB 030329 was observed with the WSRT and GMRT from 325 MHz to 8.46 GHz, spanning a time range of 268-1128 days after the burst. The afterglow was clearly detected at all frequencies except for 325 MHz, where we only obtained upper limits. GRB 030329 is the first afterglow to be detected at frequencies less than 1 GHz: at 840 GHz with WSRT and even as low as 610 MHz with GMRT. Here we describe the data reduction and analysis of our observations; the observational results are summarised in Table 5.1 and Table 5.2, for WSRT and GMRT respectively.

5.2.1 WSRT Observations

The first observations of GRB 030329 with WSRT were carried out at ~ 1.4 days after the burst, at 1.4, 2.3 and 4.8 GHz. After the clear detections of the afterglow, we started an intensive monitoring campaign at these three frequencies, of which the first results were presented in Van der Horst et al. (2005b). Here we present the results of follow up measurements up to 1128 days after the burst in a wider frequency range, adding detections at 840 MHz and 8.4 GHz, and upper limits at 350 MHz. We used the Multi Frequency Front Ends (Tan 1991) in combination with the IVC+DZB backend[1] in continuum mode, with a bandwidth of 8x20 MHz. Gain and phase calibrations were performed with the calibrator 3C286, though sometimes 3C147 or 3C48 were used. The observations were analysed using the Multichannel Image Reconstruction Image Analysis and Display (MIRIAD) software package; except for the 350 MHz observations, which were analysed using the Astronomical Image Processing System (AIPS). Table 5.1 lists the observations log, spanning a time range of 268-1128 days after the burst. We checked our results for consistency by measuring the flux of several

---

[1] See Section 5.2 at http://www.astron.nl/wsrt/wsrtGuide/node6.html

point sources in the primary beam, which were assumed to be constant in time. We found no significant correlated flux-variations between the various epochs.

5.2.2 GMRT Observations

The radio afterglow of GRB 030329 was first detected by GMRT at 1280 MHz on the 31st of March 2003, 2.3 days after the burst (Rao et al. 2003) with a flux of 0.25 mJy. The afterglow was observed since then at 1280 MHz, 610 MHz and 325 MHz. We observed the afterglow at a total of 27 epochs (12 epochs at 1280 MHz, 13 epochs at 610 MHz and 2 epochs at 325 MHz), excluding the first year observations reported in Resmi et al. (2005) (9 epochs at 1280 MHz). We have used a bandwidth of 32 MHz for all these observations. One of the three possible flux calibrators, 3C48, 3C147 or 3C286, was observed at the beginning and end of each observing session for about 15 minutes, as a primary flux calibrator to which the flux scale was set. Radio sources 1125+261 and 1021+219 were used as phase calibrators at 1280 MHz and 610 MHz, respectively. The phase calibrator was observed for about 6 minutes before and after an observing scan of about 30 to 45 minutes on GRB 030329. The data thus recorded were then converted to FITS format and analysed using AIPS. Fluxes of the individual sources were measured using the task 'jmfit' in AIPS.

We found some flux variation in sources in the fiel of GRB 030329, i.e. in the primary beam, with an rms of which the maximum is 20 % and the minumum is 10 %. A maximum of 15 % of this variation appears to be correlated, i.e. all the sources varying in the same sense from one frame to another. The correlated variation can be attributed to calibration uncertainties. To correct for this variation we followed the following procedure. For calibration of each frame observed at 1280 MHz we used a frame of the same field from the VLA FIRST Survey (White et al. 1997) as a reference frame. For calibration of the field at 610 MHz we used one of our own observations, dated September 2 2005, as a reference frame. We selected four sources in the field within $5'$ of the GRB 030329 position and measured their fluxes. Ratios of these measured fluxes to those sources in the reference frame were computed and averaged for each frame. The flux of the afterglow measured in each frame was then calibrated using this average of the flux ratios. The final fluxes are presented in Table 5.2.

5.3 Modeling Results

We have modeled the light curves obtained together with previously reported fluxes from WSRT (Van der Horst et al. 2005b), GMRT (Resmi et al. 2005), and

Table 5.1 — Log of WSRT observations of GRB 030329.

Observing Dates	ΔT[a] (days)	Int. time (hours)	Frequency (GHz)	Flux[b] (μJy)
2003 Dec 22.926 - 23.196	268.577	6.5	2.3	1618 ± 31
2003 Dec 25.005 - 25.188	270.612	4.4	1.4	2502 ± 139
2004 Jan 25.833 - 26.333	302.599	12.0	0.35	< 951 (3σ) [c]
2004 Jan 29.822 - 29.961	306.408	3.3	1.4	1552 ± 111
2004 Jan 29.995 - 30.134	306.580	3.3	4.8	< 648 (3σ) [d]
2004 Jan 30.168 - 30.307	306.753	3.3	2.3	1389 ± 67
2004 Jan 31.012 - 31.137	307.591	3.0	8.4	815 ± 225
2004 Feb 10.790 - 11.289	318.555	12.0	0.84	2332 ± 288
2004 Mar 26.667 - 26.934	363.816	6.4	4.8	597 ± 27
2004 Mar 27.664 - 28.152	364.424	11.7	1.4	1318 ± 104
2004 Mar 28.862 - 29.153	365.524	7.0	2.3	871 ± 29
2004 Apr 11.623 - 11.880	379.267	6.2	0.84	1525 ± 389
2004 May 2.566 - 3.065	400.331	12.0	0.35	< 1305 (3σ) [c]
2004 May 19.634 - 20.018	417.342	9.2	1.4	1824 ± 100
2004 May 22.511 - 22.794	420.168	6.8	2.3	933 ± 34
2004 Jul 3.396 - 3.729	462.078	8.0	2.3	707 ± 39
2004 Jul 4.394 - 4.726	463.076	8.0	4.8	329 ± 27
2004 Aug 1.317 - 1.598	490.974	6.7	1.4	622 ± 95
2004 Sep 25.328 - 25.667	546.013	8.1	4.8	274 ± 34
2004 Nov 2.063 - 2.271	583.683	5.0	2.3	543 ± 46
2004 Nov 11.039 - 11.371	592.721	8.0	1.4	1162 ± 63
2004 Nov 12.036 - 12.536	593.802	12.0	0.84	1306 ± 366
2004 Nov 20.014 - 20.486	601.766	11.3	0.35	< 2124 (3σ) [c]
2005 Mar 24.673 - 25.172	726.439	12.0	0.84	1199 ± 238
2005 Mar 26.667 - 27.167	728.433	12.0	0.35	< 996 (3σ) [c]
2005 Apr 9.629 - 10.129	742.395	12.0	1.4	1078 ± 72
2005 Apr 10.627 - 11.126	743.892	12.0	2.3	504 ± 48
2005 May 14.534 - 14.919	777.242	9.2	4.8	409 ± 27
2005 May 15.531 - 15.883	778.223	8.1	8.4	< 309 (3σ) [e]
2005 Nov 27.993 - 28.493	974.759	12.0	4.8	150 ± 19
2005 Dec 7.004 - 8.292	984.163	13.8	2.3	318 ± 58
2005 Dec 9.000 - 10.233	986.132	12.5	1.4	842 ± 127
2006 Apr 9.637 - 10.129	1107.399	11.8	0.84	817 ± 392
2006 Apr 30.573 - May 1.072	1128.338	12.0	4.8	157 ± 22

---

[a] The indicated time is the logarithmic average of the start and end of the integration.

[b] The measurement uncertainties are given at 1σ level.

[c] A meaningful formal flux measurement at the GRB position cannot be determined because of confusion by a very nearby, bright source.

[d] Formal flux measurement at the GRB position gives 1 ± 216 μJy.

[e] Formal flux measurement at the GRB position gives −69 ± 103 μJy.

Table 5.2 — Log of GMRT observations of GRB 030329.

Observing Dates	ΔT (days)	Frequency (MHz)	Flux[a] (mJy)
2004 Jan 4.97	281.49	610	0.90 ± 0.20
2004 Feb 26.63	334.15	610	1.14 ± 0.25
2004 Apr 10.49	378.01	610	0.61 ± 0.11
2004 Jun 27.28	455.80	610	1.01 ± 0.18
2004 Jun 28.28	456.80	1280	0.97 ± 0.14
2004 Jul 18.31	476.83	1280	0.90 ± 0.10
2004 Jul 20.28	478.80	610	0.84 ± 0.17
2004 Aug 20.04	509.56	1280	0.90 ± 0.10
2004 Sep 06.00	526.52	610	0.98 ± 0.15
2004 Sep 17.96	538.48	1280	0.42 ± 0.09
2004 Dec 3.00	614.52	610	1.08 ± 0.35
2004 Dec 10.30	621.82	1280	0.54 ± 0.09
2005 Jan 6.82	649.34	610	0.50 ± 0.11
2005 Feb 8.81	682.33	325	$< 1.5(3\sigma)$[b]
2005 Feb 13.84	687.34	1280	0.85 ± 0.13
2005 Feb 21.71	695.23	610	0.47 ± 0.13
2005 Mar 10.77	712.29	1280	0.63 ± 0.06
2005 Mar 18.66	720.18	610	0.69 ± 0.13
2005 Jun 17.54	811.06	610	$< 1.1(3\sigma)$[c]
2005 Jun 28.59	702.11	325	$< 1.8(3\sigma)$[b]
2005 Jul 1.19	824.71	1280	0.46 ± 0.08
2005 Sep 2.99	888.51	610	0.68 ± 0.13
2005 Oct 8.20	923.72	1280	0.43 ± 0.08

---

[a] The measurement uncertainties are given at 1σ level.

[b] A meaningful formal flux measurement at the GRB position cannot be determined because of confusion by a very nearby, bright source.

[c] Formal flux measurement at the GRB position gives 0.74 ± 0.36 mJy.

VLA, ATCA & Ryle Telescope (Berger et al. 2003b; Frail et al. 2005; Pihlström et al. 2007), see Figure 5.1. The light curves show the characteristics that are expected for the low-frequency part of a GRB afterglow. Since both the peak frequency $\nu_{\rm m}$ of the spectral energy distribution and the synchrotron self-absorption frequency $\nu_{\rm a}$ are situated above the radio regime at early times and they both decrease in time, the light curves rise. When the peak of the broadband synchrotron spectrum, either $\nu_{\rm m}$ or $\nu_{\rm a}$, has moved through the observing band, the light curves turn over and decline steeply.

According to the blastwave model (Rees & Mészáros 1992; Mészáros & Rees 1997; Wijers et al. 1997) the afterglow of a GRB is due to non-thermal

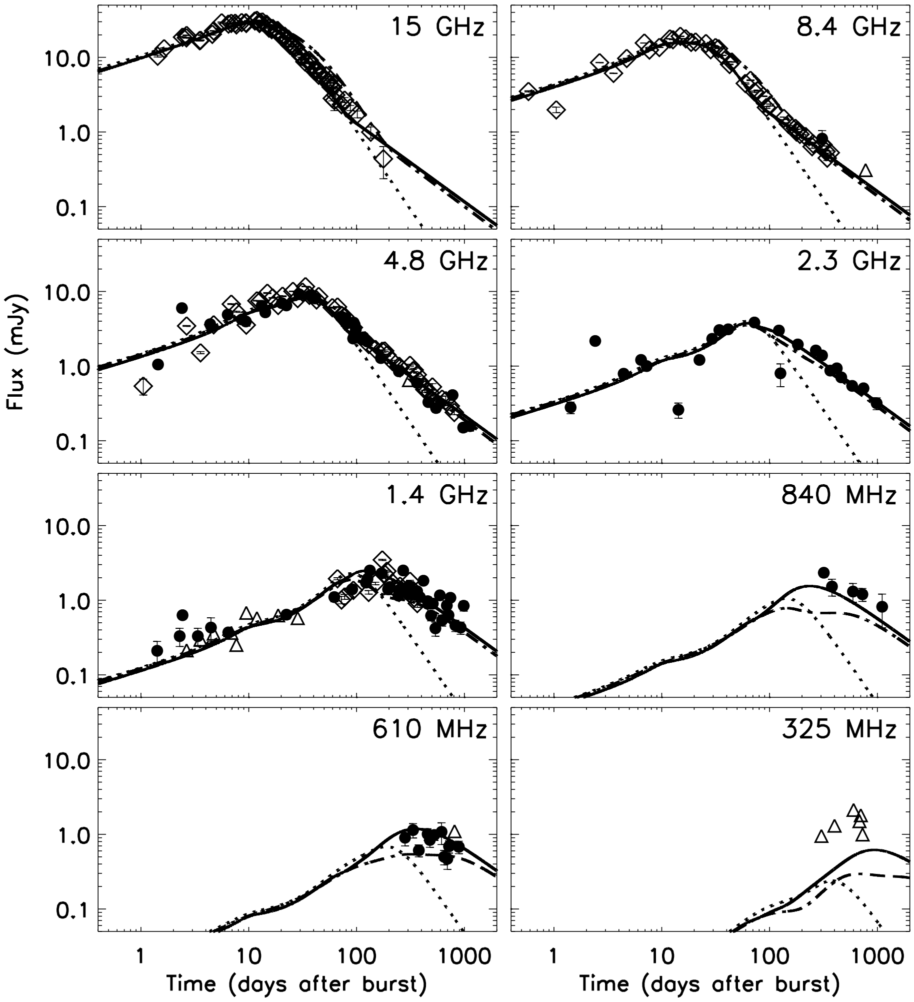

Figure 5.1 — Modeling results of the afterglow of GRB 030329 at centimetre wavelengths. Our light curves obtained with WSRT and GMRT are shown together with previously reported fluxes from WSRT and GMRT (filled circles), and VLA, ATCA and Ryle Telescope (open diamonds); the open triangles are 3σ upper limits. Three fits to the data are shown: the dotted line represents a fit to the first 100 days of radio observations with a wide jet expanding in a homogeneous medium; the solid line corresponds to a model in which the blastwave becomes non-relativistic after 80 days; the dash-dotted line corresponds to a model in which a third jet-component with an even wider opening angle is present. The latter model is excluded by the observations below 1 GHz, which leaves the model with the non-relativistic phase after 80 days as the preferred model for the late-time behaviour of the blastwave.

synchrotron radiation emitted by shock accelerated electrons. The large amount of energy released during the burst, with a collimated outflow to start with, drives a powerful relativistic blastwave. As the blastwave propagates into the circumburst medium, the electrons in the medium are accelerated to a power-law distribution of Lorentz factors with power-law index p. These relativistic electrons gyrate in the post-shock magnetic field and emit synchrotron radiation which is seen as the afterglow of the GRB. The power-law distribution of the electrons results in a power-law spectrum of the afterglow. Meanwhile the shock wave decelerates as it propagates into the circumburst medium. Assuming mass-energy conservation across the shock front, it has been shown that the Lorentz factor of the blastwave falls off as a power-law with its radius.

It is expected that the decelerating shock wave becomes non-relativistic after a few weeks. Somewhat earlier, the sideways expansion of the initially tightly collimated outflow would become important, and by the time of the non-relativistic transition the shock wave becomes nearly spherical. In the non-relativistic phase the evolution of the shock wave can be described using the Sedov-Taylor self similar solutions. A detailed description of this phase can be found in Frail et al. (2000b) (hereafter FWK00). Observations of the broadband afterglow during this phase can be used to estimate various physical parameters related to the explosion, such as the amount of energy released during the explosion, fractional amount of energy in the accelerated electrons and in the post-shock magnetic field, and the density and structure of the circumburst medium. These parameters can also be estimated, independently, by modeling the evolution of the afterglow in the relativistic phase, but this suffers from uncertainties related to collimation geometry and relative orientation of the observer, problems that do not plague the non-relativistic phase.

The broadband afterglow of GRB 030329, from radio to X-ray frequencies, can be modeled by the standard relativistic blastwave model, assuming either a ‘double jet model’ (Berger et al. 2003b) or a ‘refreshed jet model’ (Resmi et al. 2005). In both the models, the early-time optical and X-ray light curves are explained by a jet with a small opening angle of $\sim 5^\circ$. The double jet model assumes a co-aligned wider jet component ($\sim 20^\circ$) that carries the bulk of the energy and produces the later time light curves. In the refreshed jet model, the initial jet is re-energised by the central engine during its lateral expansion, re-collimating it to a wider opening angle. This refreshed jet then produces the late-time emission. Unfortunately, we cannot distinguish between the two models with all the available data, including the data presented in this paper.

After 80 days the observed radio light curves flatten, which can be explained by a transition into the non-relativistic phase of the blastwave (Van der Horst et al. 2005b; Resmi et al. 2005; Frail et al. 2005). It was suggested in Van der Horst et al. (2005b) that this late-time behaviour could also be explained by a third jet-component with an even wider opening angle than the first two. The latter model, however, is excluded by the observations below 1 GHz (see Figure 5.1), which leaves the model with the non-relativistic phase after 80 days as the preferred model for the late-time behaviour of the blastwave. The precise value of the time of the transition into the non-relativistic phase varies between 60 to 80 days because of the different modeling methods applied by various authors. The transition into the non-relativistic phase is also observed at X-ray frequencies by Tiengo et al. (2004), who estimate a transition time of ~ 44 days. The X-ray light curve, however, is less well sampled than the radio light curves at centimetre wavelengths, which makes the determination of the transition time uncertain.

Because most of the GRBs occur at cosmological distances, they are not bright enough to be observed at late times, and in fact most of them fade below the detection limits much before the start of the non-relativistic phase. GRB 030329, being one of the closest GRBs, provides us with a unique example of late time observations deep into the non-relativistic phase. Since the first months of the radio afterglow have been extensively discussed in the literature, we will focus on the late-time behaviour of the light curves. Here we present a detailed analysis of the non-relativistic phase of the afterglow.

5.3.1 Spectral & Temporal Slopes

We investigate the spectral and temporal slopes in the non-relativistic phase by performing a joint temporal and spectral power-law fit of $F_\nu = F_{\rm n} \cdot (\nu_{\rm GHz}/4.86)^{-\beta} \cdot (t_{\rm days}/100)^{-\alpha}$. Because of the uncertainty in the exact transition time into the non-relativistic phase, $t_{\rm NR}$, and because the value for the temporal slope could be altered by the smoothness of the transition, we use all the available data after 100 days at 2.3, 4.8, 8.4, 15 and 22.5 GHz. At 1.28 & 1.4 GHz we use all the data after 300 days, as the light curve at these frequencies peaks around 100 days. We find $\alpha = 1.08 \pm 0.03, \beta = 0.54 \pm 0.02$ and $F_{\rm n} = 2.69 \pm 0.06$ mJy.

After 100 days the peak frequency and synchrotron self-absorption frequency have passed through the observing bands we used for this fit, and we do not find any evidence for a chromatic break, caused by the so-called cooling break, up to 1128 days. So in this case the spectral slope β is given by $(p-1)/2$, and the temporal slope α is given by $3(5p-7)/10$ or $(7p-5)/6$, for a homogeneous and wind circumburst medium respectively. The power-law index p of the electron energy distribution is thus given by $2\beta + 1$, and $(10\alpha + 21)/15$ (homogeneous medium) or $(6\alpha + 5)/7$ (wind medium). For our fitted values we find

$p = 2.09 \pm 0.03$ from the spectral slope, and $p = 2.12 \pm 0.02$ (homogeneous) or $p = 1.64 \pm 0.02$ (wind) from the temporal slope. This indicates that the circumburst medium is homogeneous in the non-relativistic phase of the blastwave evolution, and that a wind medium is completely rejected in this phase. If one assumes that the circumburst medium density is a power-law of the radius r with index k, i.e. proportional to r^{-k}, the value of k and its uncertainty can actually be calculated directly from α and β: $k = (5\alpha - 15\beta + 3)/(\alpha - 4\beta + 2)$. For our fitted values we get $k = 0.33^{+0.34}_{-0.41}$, consistent with a homogeneous medium ($k = 0$); and this value is inconsistent with a wind medium ($k = 2$) at the 5σ level.

The value of $p = 2.1$ is in agreement with values found by other authors, although it does matter which data one includes, i.e. whether one takes only the data after 100 days or also earlier data. Including earlier data gives higher values for α and β, and as a result a higher value for p, with a significantly higher reduced chi-squared. This indicates that if one includes part of the data before 100 days, a steeper decay phase is also sampled, i.e. the jet-spreading phase. And thus our choice of fitting the data after 100 days is a valid assumption.

5.3.2 Physical Parameters

We have used 1128 days of broadband radio observations (610 MHz to 43.3 GHz) of the afterglow of GRB 030329 to model the dynamical evolution of the afterglow as well as to constrain the explosion energy. In Figure 5.1 we compare our model predictions with the observations. The model presented in Van der Horst et al. (2005b), which fitted the data up to eight months, perfectly fits the data up to more than three years after the burst. In Van der Horst et al. (2005b) values for the peak frequency $\nu_{\rm m}$ of 35 GHz and for the self-absorption frequency $\nu_{\rm a}$ of 13 GHz were found, both measured at the jet-break time of 10 days; the flux at $\nu_{\rm m}$ at that time was 61 mJy. After about 80 days the afterglow shows a flattening of the light curve, which is the start of the non-relativistic phase of the explosion: $t_{\rm NR}$.

The fitted spectral parameters may now be used to derive the physical parameters of the explosion. The break frequencies and the peak flux, estimated deep in the non-relativistic phase, i.e. at a reference time $t_0 \gg t_{\rm NR}$, can be used to yield an estimate of the blastwave energy $E_{\rm ST}$ and the ambient baryon density n_i, using the Sedov-Taylor solution for the blastwave, in the manner adopted by FWK00 for GRB970508. Two other physical parameters that determine the evolution of the radiation are the fraction of total energy in relativistic electrons ($\epsilon_{\rm e}$) and in the post-shock magnetic field ($\epsilon_{\rm B}$). In order to determine these four quantities, one requires the measurement of four spectral parameters, traditionally the three break frequencies and the flux normalisation. In the late phase, however, direct determination of the cooling frequency is difficult, since the afterglow is not detectable at frequencies above radio bands. We therefore express the physical parameters as a function of the ratio $\varepsilon_{\rm r} \equiv \varepsilon_{\rm e}/\varepsilon_{\rm B}$; $\varepsilon_{\rm r} = 1$ would signify an equipartition of energy between the magnetic field and the relativistic particles.

Following Eq. (5) of FWK00, we may then write the post-shock electron number density as

$$n = \varepsilon_{\rm r} \left(\frac{p-2}{p-1}\right) \frac{B_0^2}{8\pi\gamma_0 m_e c^2} \tag{5.1}$$

We insert this in Eq. (A12) of FWK00, and invert their Eqs. (A10) to (A12) while making use of the relations (A6) to (A8). This yields the following set of expressions for the FWK00 model parameters:

$$\begin{aligned}\gamma_0 \;&=\; 88.3\, d_{28}^{2/17} \left(\frac{\varepsilon_{\rm r}}{\eta_{10}}\right)^{2/17} \left(\frac{f_2^3}{f_3}\right)^{1/17} \\ &\cdot \left[(p-2)^2(p+2)^3\right]^{1/17} \left(\frac{\nu_{\rm m0,GHz}}{\nu_{\rm a0,GHz}}\right)^{3(p+4)/34} F_{\rm m0,mJy}^{1/17}\end{aligned} \tag{5.2}$$

$$\begin{aligned}r_0 \;&=\; 1.407\times10^{18}\ {\rm cm}\, \frac{d_{28}^{16/17}}{(1+z)} \left(\frac{\eta_{10}}{\varepsilon_{\rm r}}\right)^{1/17} \left(\frac{f_2^7}{f_3^8}\right)^{1/17} \\ &\cdot \left[\frac{(p+2)^7}{(p-2)}\right]^{1/17} \nu_{\rm m0,GHz}^{(7p-6)/34} \nu_{\rm a0,GHz}^{-7(p+4)/34} F_{\rm m0,mJy}^{8/17}\end{aligned} \tag{5.3}$$

$$\begin{aligned}B_0 \;&=\; 4.58\times10^{-2}\ {\rm G}\, \frac{(1+z)}{d_{28}^{4/17}} \left(\frac{\eta_{10}}{\varepsilon_{\rm r}}\right)^{4/17} \left(\frac{f_3}{f_2^3}\right)^{2/17} \\ &\cdot \left[(p-2)^4(p+2)^6\right]^{-1/17} \nu_{\rm m0,GHz}^{(5-3p)/17} \nu_{\rm a0,GHz}^{3(p+4)/17} F_{\rm m0,mJy}^{-2/17}\end{aligned} \tag{5.4}$$

$$\begin{aligned}n_i \;&=\; \frac{0.69\ {\rm cm}^{-3}}{1+X_{\rm H}} \frac{(1+z)^2}{d_{28}^{10/17}} \left(\frac{\varepsilon_{\rm r}}{\eta_{10}}\right)^{7/17} \left(\frac{f_3}{f_2^3}\right)^{5/17} \\ &\cdot \frac{1}{(p-1)} \left[\frac{(p-2)^7}{(p+2)^{15}}\right]^{1/17} \nu_{\rm m0,GHz}^{(8-15p)/34} \nu_{\rm a0,GHz}^{15(p+4)/34} F_{\rm m0,mJy}^{-5/17}\end{aligned} \tag{5.5}$$

In the above, r_0 is the radius of the blastwave, B_0 is the post-shock magnetic field, and γ_0 is the lower cutoff of the power-law distribution of relativistic electron

Lorentz factors, all at the reference time t_0. From these, the blastwave energy may be computed as:

$$\begin{aligned} E_{\rm ST} &= n_i m_p \left(\frac{1+z}{t_0}\right)^2 \left(\frac{r_0}{\xi}\right)^5 && (5.6)\\ &= \frac{8.576\times10^{56}\ \text{erg}}{(1+X_{\rm H})\xi^5 t_{0,\rm d}^2}\,\frac{d_{28}^{70/17}}{(1+z)}\left(\frac{\varepsilon_{\rm r}}{\eta_{10}}\right)^{2/17}\left(\frac{f_2^{20}}{f_3^{35}}\right)^{1/17}\frac{(p+2)}{(p-1)}\\ &\quad \cdot\left[(p-2)^2(p+2)^3\right]^{1/17}\nu_{\rm m0,GHz}^{(10p-11)/17}\nu_{\rm a0,GHz}^{-10(p+4)/17}F_{\rm m0,mJy}^{35/17} && (5.7)\end{aligned}$$

In Eq. (5.2) through (5.7), $\nu_{\rm a0,GHz}$ and $\nu_{\rm m0,GHz}$ are the two break frequencies, in GHz units, at the reference time $t_0 = t_{0,\rm d}$ days. The expressions assume that $\nu_{\rm a0,GHz} > \nu_{\rm m0,GHz}$, which is indeed the case in GRB030329 at these late times. $F_{\rm m0,mJy}$ is the normalisation of the flux at an observing frequency $\nu \gg \nu_{\rm a}, \nu_{\rm m}$, expressed as

$$F_\nu(t=t_0)\ \text{mJy} = F_{\rm m0,mJy}\left(\frac{\nu}{\nu_{\rm m0}}\right)^{-(p-1)/2} \qquad (5.8)$$

z is the redshift of the burst and d_{28} the corresponding luminosity distance. The thickness of the post-shock emitting region at any time is assumed to be r/η, where r is the radius of the blastwave and $\eta = 10\eta_{10}$. f_2 and f_3 are integrals over the synchrotron function defined in FWK00; both are functions of p. The quantity ξ, close to unity, is an equation of state-dependent normalisation factor for the blastwave radius (FWK00). $X_{\rm H}$ represents the mass fraction of hydrogen in the circumburst medium, and may nominally taken to be 0.75.

Evaluating spectral parameters from the fitted model, one finds, at a reference time $t_0 = 500$ days: $\nu_{\rm m0,GHz} = 2.56\times10^{-3}$, $\nu_{\rm a0,GHz} = 0.498$ and $F_{\rm m0,mJy} = 28.4$. Using $z = 0.1685$ for GRB030329 and the fitted value of $p = 2.1$, one then estimates

$$\begin{aligned} E_{\rm ST} &= 2.6\times10^{51}\ \text{erg}\left(\frac{\varepsilon_{\rm r}}{\eta_{10}}\right)^{0.12} && (5.9)\\ n_i &= 0.35\ \text{cm}^{-3}\left(\frac{\varepsilon_{\rm r}}{\eta_{10}}\right)^{0.41} && (5.10)\end{aligned}$$

The blastwave radius at 500 days works out to be $r_0 = 0.49(\varepsilon_{\rm r}/\eta_{10})^{-0.06}$ pc. The corresponding post-shock magnetic field is $B_0 = 0.036(\varepsilon_{\rm r}/\eta_{10})^{-0.24}$ G, and the lower cutoff of the electron Lorentz factor distribution at that time is $\gamma_0 = 5.5(\varepsilon_{\rm r}/\eta_{10})^{0.12}$. These yield $\varepsilon_{\rm e} = \varepsilon_{\rm r}\varepsilon_{\rm B} = 0.085(\varepsilon_{\rm r}/\eta_{10})^{0.24}$.

5.4 Discussion

The data presented in this paper give an unprecedented view of the non-relativistic evolution phase of a GRB blastwave, because of the wide range covered in both frequency and time. This gives us the opportunity to compare the physical parameters that we have derived from the very late-time data with the physical parameters derived from the early-time data, when the blastwave was still extremely relativistic. From the emerging physical picture we put constraints on the emission from the counter jet, and we compare our findings with the results from VLBI measurements of the source size evolution.

5.4.1 Relativistic versus Non-Relativistic

In Section 5.3.2 we calculated the total energy in the blastwave $E_{\rm ST}$ and the density of the circumburst medium n_i as functions of the ratio $\varepsilon_{\rm r} \equiv \varepsilon_{\rm e}/\varepsilon_{\rm B}$, assuming that the blastwave was in its non-relativistic phase. These parameters are determined in Van der Horst et al. (2005b) in the relativistic phase as functions of the cooling frequency, adopting $\nu_{\rm c} = 10^{13}$ Hz. We calculate the energy and density in the relativistic phase as functions of $\varepsilon_{\rm r}$, a better way to compare the parameters in the two different phases. Since the values of $\varepsilon_{\rm e} = 0.25\nu_{\rm c,13}^{1/4}$ and $\varepsilon_{\rm B} = 0.49\nu_{\rm c,13}^{-5/4}$ in Van der Horst et al. (2005b) indicate near-equipartition, the values for the density and energy do not differ much from the values obtained there: $n_{\rm r} = 0.78 \times \varepsilon_{\rm r}^{1/2}\,{\rm cm}^{-3}$, $E_{\rm r,iso} = 2.6 \times 10^{51} \times \varepsilon_{\rm r}^{1/6}$ erg and $E_{\rm r,cor} = 3.4 \times 10^{50} \times \varepsilon_{\rm r}^{1/4}$ erg, the latter being the beaming-corrected energy. The cooling frequency can be found to be $\nu_{\rm c} = 1.6 \times 10^{13} \times \varepsilon_{\rm r}^{2/3}$ Hz, validating the assumptions in previous studies on $\nu_{\rm c}$ being $\sim 10^{13}$ Hz at 10 days.

We find that the density derived in the non-relativistic phase is a factor of two smaller than the density derived in the relativistic phase. The beaming-corrected energy $E_{\rm r,cor}$, however, is a factor of ~ 7 times smaller than the total energy $E_{\rm ST}$ in the blastwave derived from the non-relativistic evolution. Frail et al. (2005) modeled the first year of observations with the VLA and ATCA, and found a total kinetic energy of 9.0×10^{50} ergs; using only the data before 64 days they derive an energy of 6.7×10^{50} ergs (see also Berger et al. 2003b), a factor of ~ 2 larger than our $E_{\rm r,cor}$; and using only the data after 50 days, to obtain an estimate for $E_{\rm ST}$, they find an energy of 7.8×10^{50} ergs, a factor of ~ 4 smaller than our value for $E_{\rm ST}$. In these models the range for the circumburst density is $\sim 1 - 3\,{\rm cm}^{-3}$, a bit larger than our values. Granot et al. (2005) also determine the energy and density with their models, and find a similar value for the collimation corrected energy as we do. Their value for the density is, however, an order of magnitude larger, but they note that this can be attributed to the fact that the density depends strongly on the precise value of ν_a and ν_m.

Given the differences in the methods used by different authors and the uncertainties in the assumptions made to estimate these numbers, they can all be considered to be comparable. It is not possible to make any definite statements about significant differences in energies derived from the relativistic and non-relativistic phase. If, however, the somewhat larger estimate of the total energy in the non-relativistic phase is indeed true, then two possible explanations may be advanced for this: either the beaming correction in the relativistic phase is too strong, giving a too small value for the beaming corrected energy; or E_ST is over-estimated because of non-isotropy in the emission coming from the blastwave in the non-relativistic phase. In the latter case it could be that the blastwave is not completely spherical yet, but still the evolution is well described by the Sedov-Taylor solution; or that the blastwave is spherical, but the emission is not coming from the blastwave isotropically. In both situations the value of E_ST that we derived would be an over-estimate of the true value.

The energies that we and Frail et al. (2005) derive indicate that our estimate of the relativistic beaming and the assumption that the blastwave becomes spherical at $t \simeq t_\mathrm{NR}$ are valid. The latter is important for testing the models that describe the lateral spreading of the collimated outflow after the jet-break time, when the Lorentz factor drops below the inverse of the half-opening angle of the jet. Some (semi-analytical) models (e.g. Rhoads 1999) assume a very rapid sideways expansion of the jet with a lateral expansion velocity of the order of the velocity of light, resulting in an exponential growth of the jet half-opening angle with radius. Hydrodynamical simulations, however, show a very modest degree of lateral expansion as long as the jet is relativistic (for an extensive review, see Granot 2007). In the latter model the outflow is still strongly collimated when the blastwave becomes non-relativistic, while the first model predicts that the blastwave is (almost) spherical at $t \simeq t_\mathrm{NR}$, which is favoured by our analysis, since there is no significant change in temporal slopes well after t_NR.

5.4.2 Counter Jet Emission

It is expected that there are two collimated outflows formed at the collapse of a massive star: two jets pointed away from each other. When the counter jet becomes non-relativistic, the emission is no longer strongly beamed away from us. Granot & Loeb (2003) predicted a re-brightening in the radio light curves when that occurs, although it would be difficult to detect in the case of GRB 030329. Li & Song (2004) calculated that the observed time at which the counter jet becomes non-relativistic is 5 times larger than t_NR, because of light travel time effects. They claim that the observed flux coming from the counter jet at that time is comparable to the flux of the jet coming towards us at $t_{\rm NR}$. This results in a rapid increase in flux with a peak at $5 \times t_{\rm NR}$, and after the peak the light curve declines steeper than before the rapid increase until it relaxes to the original light curve behaviour. Li & Song (2004) predicted such a feature in the radio light curves of GRB 030329 at ~ 1.7 years after the burst. From Figure 5.1, however, it is clear that this is not observed up to 3 years after the burst (which was also noted, with observations up to 2 years after the burst, by Pihlström et al. 2007).

The apparent discrepancy between the predictions for the counter jet and the observed light curves can be explained by looking carefully at the assumptions. The calculations by Li & Song (2004) are valid for those observing frequencies at which the light curve peaks when the blastwave is still ultra-relativistic and narrowly collimated. This means that it can only be applied to the light curves at 8.4 GHz and higher frequencies. Adopting our value for $t_{\rm NR}$ of 60-80 days, this would mean that the 8.4 GHz light curve has to rapidly increase to a peak of 1-2 mJy at 300-400 days ($5 \times t_{\rm NR}$). This is not observed, although it is hard to make definite statements about this, since there are only observations up to 360 days.

The light curves at 2.3 GHz and lower frequencies are not expected to show this kind of re-brightening, because they peak at or after $t_{\rm NR}$. This results in a flattening of the peak to a width of $2 \times t_{\rm NR}$. Looking at the low frequency light curves this could be the case, although the scatter in the data is too large to make any quantitative statements about this.

The best constraints on the counter jet could come from the 4.8 GHz light curve. Following Li & Song (2004) the flux at 300-400 days has to increase to 4-6 mJy, while the measured flux at that time is $0.6 - 0.8$ mJy. This means that the observed flux coming from the counter jet is suppressed by a factor of ~ 8, while at 8.4 GHz the limit was a factor of ~ 4. The flux from the counter jet, however, is probably lower than that predicted by Li & Song (2004), because, especially at 4.8 GHz, the light curve peaks later than the jet-break time. This means that the two jets, which already have quite a large opening angle of $\sim 20^\circ$ to start with, cannot be treated as two narrowly collimated outflows anymore because of lateral spreading of the jet.

Concluding, we cannot say, from the light curves presented here, whether we have seen emission from the counter jet or not. The fact that we do not see a late-time re-brightening at high radio frequencies could be due to the fact that the outflow is not very narrowly collimated. A flattening of the peak of the light curves at low radio frequencies, caused by the emission coming from the counter jet, could be present, but the scatter in the data prevents us from drawing any firm conclusion regarding this.

5.4.3 Source Size Evolution

VLBI observations of GRB 030329 make it possible to study the image size of the afterglow. The full set of VLBI measurements up to 806 days after the burst has been presented in Pihlström et al. (2007). Granot et al. (2005) have discussed the implications of the measured image sizes up to 83 days after the burst, which have mainly remained the same after including the latest measurements. They conclude that a homogeneous medium gives a better fit to the image size evolution than a stellar wind environment, although it is hard to rule out the latter due to the measurement uncertainties. Furthermore, they try to constrain the amount of lateral spreading, i.e. whether the lateral expansion velocity is of the order of the velocity of light, or that there is hardly any lateral spreading until the blastwave becomes sub- or non-relativistic. This is, however, hard to constrain, again because of the uncertainties in these source size measurements.

An important parameter that comes out of the VLBI studies is $t_{\rm NR}$. Granot et al. (2005) and Pihlström et al. (2007) claim that $t_{\rm NR} \sim 1$ year from looking at the evolution of the apparent expansion velocity, and from theoretical model fits to the source size evolution. The models in which there is rapid lateral expansion, their model 1, $t_{\rm NR} \sim 1$ year is indeed obtained, but the jet-break time in that case is found to be ~ 1 month instead of 10 days (e.g., see Figure 4 of Pihlström et al. 2007). Since the jet-break time is quite well determined from the light curves, the value of $t_{\rm NR}$ in this model 1 is rather uncertain. The models in which there is no lateral expansion until the blastwave becomes non-relativistic, their model 2, the non-relativistic transition actually happens at 60-80 days after the burst; the blastwave then becomes spherical on a time scale of 1-3 years. So the fits of model 2 do indeed indicate a value of $t_{\rm NR} \sim 60 - 80$ days.

From the evolution of the average apparent expansion velocity the value of $t_{\rm NR}$ can also be deduced. The uncertainties and correction factors in deriving the average velocity are discussed thoroughly in Pihlström et al. (2007). From their Figure 3 it seems that the transition happens at $\sim 100 - 200$ days, when the average apparent expansion velocity is ~ 2 times the speed of light. The uncertainties in the correction factors applied, however, make it hard to state that this is significantly higher than the value of $t_{\rm NR}$ that is deduced from the light curves. The issue that still remains, is that the value of $t_{\rm NR}$ that various authors have estimated from energy considerations is a factor of a few higher than 60-80 days (e.g. Granot et al. 2005; Van der Horst et al. 2005b). This is, however, a very rough estimate, and a discrepancy within a small factor should not be regarded as disturbing. In conclusion, the value of $t_{\rm NR}$ determined from the VLBI source size measurements is not at significant odds with the value of $t_{\rm NR}$ derived from light curve studies.

5.4.4 Low Frequency Array

From our analysis of the broadband radio afterglow of GRB 030329 we can calculate predicted light curves for future radio telescopes operating in the metre wavelength regime. As an example we explore the possibilities for the Low Frequency Array (LOFAR) to detect the GRB 030329 afterglow and other GRB afterglows.

LOFAR will be a major new multi-element, interferometric, imaging telescope designed for the 30-240 MHz frequency range. LOFAR will use an array of simple omni-directional antennas, whose electronic signals are digitised, transported to a central digital processor, and combined in software to emulate a conventional antenna. LOFAR will have unprecedented sensitivity and resolution at metre wavelengths, and will be the first of a new generation of radio telescopes to become fully operational, i.e. in early 2009. This sensitivity and resolution will give the GRB community the opportunity to study bright afterglows on even longer timescales than with observations at centimetre wavelengths. For a concise description of LOFAR and the Transients Key Project, in which GRBs are among the prime targets, see Röttgering et al. (2006) and Fender et al. (2006a).

The fact that our early-time model calculations from Van der Horst et al. (2005b) gave such good predictions for the late-time behaviour, in particular at observing frequencies below 1 GHz, gives us confidence to extrapolate the modeling results of the radio afterglow of GRB 030329 to the LOFAR observing range, see Figure 5.2. The predicted light curves show that GRB 030329 will be observable in the high band of LOFAR (120-240 MHz), but not in the low band (30-80 MHz). The light curves are expected to peak in 2009, when LOFAR will be fully operational, and even later going down from 240 to 120 MHz; the expected peak flux is $\sim 0.3 - 0.4$ mJy in the LOFAR high band. We also calculated light curves for GRB 030329 if it were situated at a redshift of 1 instead of 0.16. The resulting fainter afterglow can also be detected, although with longer integration times, i.e. on the order of a day instead of an hour.

5.5 Conclusions

We have presented a detailed study of the late-time radio afterglow of GRB 030329. We have obtained measurements with the WSRT and GMRT, spanning a spectral range of 325 MHz-8.4 GHz and a temporal range of 268-1128 days after the burst. Combined with all the already published radio observations of this afterglow, from WSRT, GMRT and other large radio telescopes,

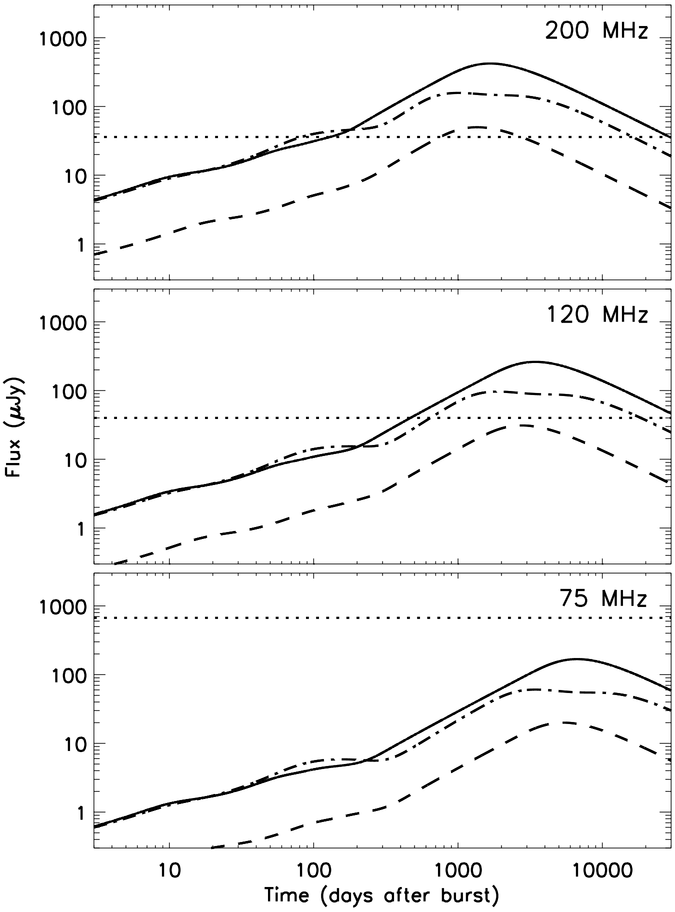

Figure 5.2 — The predicted light curves of GRB 030329 at three frequencies within the LOFAR observing range. The solid line and dash-dotted line correspond to the two models shown in Figure 5.1; the dashed line shows the predicted light curve of GRB 030329 when situated at a redshift of 1 instead of 0.16. The horizontal dotted lines are the sensitivity limits after 4 hours of observing. It shows that GRB afterglows similar in brightness to that of GRB 030329 can easily be detected with LOFAR on timescales of months to decades; and that fainter afterglows can also be detected after long integration times.

we have studied the physics of the blastwave in the non-relativistic phase and compared these results with those from studies of the relativistic phase. The well-sampled late-time light curves made it possible to determine the index of the electron energy distribution accurately, and to confirm that the circumburst medium is homogeneous.

The energy of the blastwave and density of the circumburst medium, determined from the non-relativistic evolution of the blastwave, are comparable to findings by several studies based on earlier time observations. We have shown that the blastwave is spherical, or almost spherical at least, at the time that the blastwave becomes non-relativistic: $t_{\rm NR} \sim 80$ days. In contrast with some predictions, a radio re-brightening due to the counter jet becoming non-relativistic, is not observed. The existence of a counter jet cannot be ruled out, since it is possible that the peaks of the light curves at low radio frequencies are flattened due to this counter jet. We have also shown that the high-resolution VLBI measurements of the afterglow image size are in agreement with our light curve studies. In particular, the value of $t_{\rm NR}$ derived from modeling the image size evolution does not differ from our findings significantly within the measurement and modeling uncertainties.

The afterglow of GRB 030329 will be followed-up at radio frequencies for many years to come. The current brightness and the fact that the flux drops logarithmically, make it possible to continue studying this afterglow for the next decade at least. VLBI capabilities will increase significantly in the coming years, so the image size evolution can also be observed. A new generation of radio telescopes will also be able to observe this afterglow. The first one of this new generation to come on-line is LOFAR, which will be able to detect GRB 030329 at metre wavelengths. Besides this extremely bright afterglow, LOFAR will also be able to study many afterglows at frequencies and on timescales that so far have been unexplored.

Acknowledgements We greatly appreciate the support from the WSRT and GMRT staff in their help with scheduling these observations. The Westerbork Synthesis Radio Telescope is operated by ASTRON (Netherlands Foundation for Research in Astronomy) with support from the Netherlands Foundation for Scientific Research (NWO). The Giant Metrewave Radio Telescope is operated by the National Center for Radio Astrophysics of the Tata Institute of Fundamental Research. RAMJW gratefully acknowledges the support of NWO under grant 639.043.302. ER gratefully acknowledges support from PPARC. DB thanks the Astronomical Institute 'Anton Pannekoek' for hospitality during a part of this work.

6

GRB 051022: physical parameters and extinction of a prototype dark burst

E. Rol, A.J. van der Horst, K. Wiersema, S.K. Patel, A. Levan, M. Nysewander, C. Kouveliotou, R.A.M.J. Wijers, N. Tanvir, D. Reichart, A.S. Fruchter, J. Graham, R.L.C. Starling, P.T. O'Brien, J. Hjorth, J. Fynbo, P. Jonker, W. van Ham, D.N. Burrows, J.-E. Ovaldsen, A.O. Jaunsen & R. Strom

Accepted for Publication, Astrophysical Journal

Abstract GRB 051022 was undetected to deep limits in early optical observations, but precise astrometry from radio and X-ray showed that it most likely originated in a galaxy at $z \approx 0.8$. We report radio, optical, near infra-red and X-ray observations of GRB 051022. Using the available X-ray and radio data, we model the afterglow and calculate the energetics of the afterglow, finding it to be an order of magnitude lower than that of the prompt emission. The broad-band modeling also allows us to precisely define various other physical parameters and the minimum required amount of extinction, to explain the absence of an optical afterglow. Our observations suggest a high extinction, at least 2.3 magnitudes in the infrared (J) and at least 5.4 magnitudes in the optical (U) in the host-galaxy restframe. Such high extinctions are unusual for GRBs, and likely indicate a geometry where our line of sight to the burst passes through a dusty region in the host that is not directly co-located with the burst itself.

6.1 Introduction

Dark gamma-ray bursts (GRBs) — at the most basic level those without optical afterglows — are a long-standing issue in GRB observations. Although in many cases the non-detection of an afterglow at optical wavelengths may simply be due to an insufficiently deep search, or one which takes place at late times (e.g. Fynbo et al. 2001), a subset of GRBs with bright X-ray afterglows remains undetected despite prompt and deep optical searches (e.g. Groot et al. 1998) and directly implies suppression of the optical light.

There are several plausible explanations for this, the most likely being that the burst is at high redshift, such that the Ly-alpha break has crossed the passband in question, or that there is high extinction in the direction of the GRB. Examples of both have been found, with a small number of GRBs at $z > 5$ appearing as *V* and *R* band dropouts (e.g. Jakobsson et al. 2006b; Haislip et al. 2006) and some GRB afterglows appearing very red at lower redshift, due to effects of extinction (e.g. Levan et al. 2006; Rol et al. 2007).

Identification of GRBs at very high redshifts is the key to using them as cosmological probes. The proportion of bursts exhibiting high dust extinction is also interesting from the point of view of estimating the proportion of star formation that is dust enshrouded, as well as understanding the environments which favor GRB production (Trentham et al. 2002; Tanvir et al. 2004).

The detection and follow-up of dark bursts at other wavelengths is essential, as it enables 1) the modeling of the afterglow, deriving estimates of the extinction and energies involved, potentially providing information about the direct burst environment, 2) pinpointing the burst position in the host, to enable late-time high resolution imaging and the detection of dust enhanced regions in the host, and 3) determination of the properties of the GRB host itself, such as the SFR and average host-galaxy extinction.

The High Energy Transient Explorer 2 mission (HETE-2; Ricker et al. 2003) detected and located an unusually bright gamma-ray burst (Olive et al. 2005) with its three main instruments, the French Gamma Telescope (FREGATE), the Wide field X-ray monitor (WXM) and the Soft X-ray Camera, (SXC), on October 22, 2005. A 2.5 arcminute localization was sent out within minutes, enabling prompt follow-up observations (e.g. Torii 2005; Schaefer 2005); a target-of-opportunity observation was also performed with *Swift*. Details of the HETE-2 observations can be found in Nakagawa et al. (2006).

The *Swift* observations resulted in the detection of a single fading point source inside the SXC error region, which was consequently identified as the X-ray afterglow of GRB 051022 (Racusin et al. 2005a). However, optical and near infra-red (nIR) observations failed to reveal any afterglow to deep limits, while radio and millimeter observations with the Very Large Array (VLA), the Westerbork Synthesis Radio Telescope (WSRT) and the Plateau de Bure Interferometer detected the radio counterpart (Cameron & Frail 2005; Van der Horst et al. 2005a; Bremer et al. 2005). The position coincides with its likely host galaxy (Berger & Wyatt 2005) at a redshift of $z = 0.8$ (Gal-Yam et al. 2005).

In this paper, we describe our X-ray, optical, nIR and radio observations of GRB 051022. The outline of the paper is as follows: in Section 6.2 we describe our observations, data reduction and initial results. In Section 6.3, we analyze these results and form our afterglow picture, which is discussed in Section 6.4. Our findings are summarized in Section 6.5.

In the following, we have used $F \propto \nu^{-\beta} t^{-\alpha}$ in our definition of α and β. We assume a cosmology with $H_0 = 71\,\mathrm{km s^{-1} Mpc^{-1}}$, $\Omega_M = 0.27$ and $\Omega_\Lambda = 0.73$. All quoted errors in this paper are 1 sigma (68%) errors.

6.2 Observations and data reduction

6.2.1 X-ray observations

X-ray observations were performed with the *Swift* X-Ray Telescope (XRT) and the Chandra X-ray Observatory (CXO).

The XRT started observing the afterglow of GRB 051022 3.46 hours after the HETE-2 trigger, for a total effective integration time of 137 ks between October 22 and November 6.

Observations were performed in Photon Counting (PC) mode, the most sensitive observing mode. We reduced the data using the *Swift* software version 2.6 in the HEAsoft package version 6.2.0. Data were obtained from the quick-look site and processed from level 1 to level 2 FITS files using the xrtpipeline tool in its standard configuration. The first two orbits (until 2.1×10^4 seconds post burst) show pile-up and were therefore extracted with an annular rather than circular region, with an inner radius of 19 and $12''$ for orbits 1 and 2, respectively, and an outer radius of $71''$. Orbits 3 – 7 (2.4×10^4 – 4.9×10^4 seconds) were extracted with a circular region of $71''$ radius, and later orbits were extracted using a $47''$ radius circle instead. The data for the light curve were extracted between channels 100 and 1000, corresponding to 1 and 10 keV, respectively; while the commonly used range is 0.3 – 10 keV, the large absorption prevents the detection of any data from the source below 1 keV. Otherwise, the procedure is similar to that described in Evans et al. (2007).

Observations with the CXO started on October 25, 2005, 21:14:20, 3.34 days after the HETE trigger, for a total integration time of 20 ks (Patel et al. 2005). Data were reduced in a standard fashion with the CIAO package.

We performed astrometry by matching X-ray sources with an optical R-band image that was astrometrically calibrated to the 2MASS catalog. Our CXO position is RA, Dec = 23:56:04.115, +19:36:24.04 (J2000), with positional errors of $0.33''$ and $0.12''$ for the Right Ascension and Declination, respectively. This puts the afterglow within $0.5''$ of the center of its host galaxy.

We modeled the XRT spectra with an absorbed power law in XSpec (Arnaud 1996), using data from the first seven orbits. A good fit (χ^2/d.o.f. = 87.2/99) was obtained with a resulting spectral energy index of $\beta = 1.00 \pm 0.12$ and excess absorption (at $z = 0.8$ and for assumed Galactic abundances) of $N_{\mathrm{H}} = (2.82 \pm 0.46) \times 10^{22}$ cm^{-2} on top of the estimated Galactic absorption at this position ($N_{\mathrm{H}} = 4.06 \times 10^{20}$ cm^{-2}, Dickey & Lockman 1990). The CXO data are fully in agreement with these values, showing no change in the spectrum over time between 0.3 and 3.3 days after the burst. The absorption measured is far less than that measured by the HETE team in their prompt data, $N_{\mathrm{H}} = (8.8^{+1.9}_{-1.8}) \times 10^{22}$ cm^{-2} (Nakagawa et al. 2006). This could indicate a change in absorption between the early (prompt) measurements and those at the time of the XRT observations. For the prompt emission spectrum, however, the values found by Konus-Wind (Golenetskii et al. 2005) are rather different than those found by HETE-2, and may be the result of the lower energy cut-off for FREGATE compared to Konus-wind. Alternatively, the fact that these spectra are an average over the whole emission period may also result in incorrect model parameters. In the two last cases, the N_{H} in the prompt emission could be as low as the XRT value and still produce an equally well fit, but with slightly different model parameters.

For the XRT data, Butler et al. (2005a) and Nakagawa et al. (2006) find a value somewhat higher than our value (4.9×10^{22} cm^{-2} and 5.3×10^{22} cm^{-2} respectively, when scaled by $(1 + z)^3$, Gunn & Peterson 1965). This difference could be explained by a different count-binning or an updated XRT calibration used in our modeling.

The XRT light curve count rates have been converted to 1–10 keV fluxes using the results from our spectral modeling and calculating the ratio of the flux and count rate at the logarithmic center of the orbits. The 1 – 10 keV CXO flux was derived using the actual spectral fit.

A broken power law fit to the X-ray light curve results in $\alpha_1 = 1.16 \pm 0.06$, $\alpha_2 = 2.14 \pm 0.17$ and a break time of 110^{+21}_{-23} ks, or around 1.27 days. The difference between α_1 and α_2, and the fact that the spectral slope does not change across the break (the CXO measurement is past the break), are highly indicative that the observed break in the light curve is a jet break. In Section 6.3.1, we perform full modeling of the afterglow using the fireball model, indeed resulting in a jet break time t_j that agrees reasonably well with the break time as determined from only the X-rays. We point out that our value for t_j is different than that cited in Racusin et al. (2005b), largely because their measurement of t_j was based on a preliminary XRT light curve.

6.2.2 Optical and near infra-red observations

Observations were obtained in Z and R-band with the William Herschel Telescope (WHT) using the Auxiliary Port and the Prime Focus Imaging Camera, respectively, in $r'i'z'$ with the Gemini South telescope using the GMOS instrument, in JHK_s with the Wide Field Camera on the United Kingdom InfraRed Telescope (UKIRT), in $BVRI$ with the DFOSC instrument on the Danish 1.54m telescope and in J and K_s with the Southern Astrophysical Research (SOAR) telescope using OSIRIS. The optical data were reduced in a standard fashion using the `ccdproc` package within the IRAF software (Tody 1986), whereas the SOAR data were reduced using the `cirred` package within IRAF. The UKIRT data were reduced using the standard pipeline reduction for WFCAM.

Photometric calibration was done using the calibration provided by Henden (2005) for Johnson-Cousins filters. For the $r'i'z'$ GMOS filters, we converted the magnitudes of the calibration stars provided by Henden to the Sloan filter system using the transformations provided by Jester et al. (2005), and verified by the published GMOS zero points. The WHT Z-band was calibrated using the spectroscopic standard star SP2323+157. Calibration of the infrared JHK magnitudes was done using the 2MASS catalog (Skrutskie et al. 2006).

No variable optical source was found at the position of the X-ray and radio afterglow. For the early epoch images ($<$ 1 day post burst), we estimated a limiting magnitude by performing image subtraction between this and a later image using the ISIS image subtraction package (Alard 2000). To this end, artificial low signal-to-noise sources were added onto the images, with a Gaussian PSF matched in size to the seeing (some artificial sources were added on top of existing sources, e.g. galaxies, some on the background sky). We determined our upper limit to be the point where we could retrieve 50% of the artificial sources in the subtracted image. This assumes that the change in brightness of any point source on top of the host galaxy is sufficient to be seen in such a subtracted image. With the difference in time between the epochs, this seems a reasonable assumption (for example, for a source fading with a shallow power law like slope of $F \propto t^{-0.5}$, the magnitude difference between the two WHT Z-band observations is ≈ 0.6 magnitudes).

Table 6.1 — Limiting magnitudes

Filter	Limiting magnitude[1]	ΔT (average) days	Frequency Hz	Flux[2] μJy
K_s	> 20.0	0.5035	$3.403 \cdot 10^{14}$	< 6.82
J	> 20.3	0.4800	$2.403 \cdot 10^{14}$	< 12.3
Z	> 22.9	0.4443	$3.434 \cdot 10^{14}$	< 2.66
r'	> 25.3	0.5288	$4.762 \cdot 10^{14}$	< 0.305
z'	> 23.5	0.5426	$3.359 \cdot 10^{14}$	< 1.53

Photometry of the host galaxy has been performed using aperture photometry, with an aperture 1.5 times the seeing for each image, estimated from the measured FWHM of the PSF for point sources in the images.

Table 6.6 shows the log of our optical/nIR observations, while Table 6.1 shows the upper limits for any optical/nIR afterglow.

6.2.3 Radio observations

Radio observations were performed with the WSRT at 8.4 GHz, 4.9 GHz and 1.4 GHz. We used the Multi Frequency Front Ends (Tan 1991) in combination with the IVC+DZB back end[3] in continuum mode, with a bandwidth of 8x20 MHz. Gain and phase calibrations were performed with the calibrators 3C 286 and 3C 48, although at one 8.4 GHz measurement 3C 147 was used. Reduction and analysis were performed using the MIRIAD software package[4]. The observations are detailed in Table 6.2. In our modeling described in section 6.3.1 we have also used the VLA radio detection at 8.5 GHz from Cameron & Frail (2005).

6.3 Analysis

6.3.1 Broadband modeling

We have performed broadband modeling of the X-ray and radio measurements, using the methods presented in Van der Horst, Wijers & Van der Horn (submitted to A&A). In our modeling we assume a purely synchrotron radiation mechanism.

The relativistic blast wave causing the afterglow accelerates electrons to relativistic velocities, which gives rise to a broadband spectrum with three character-

---

[3] See sect. 5.2 at http://www.astron.nl/wsrt/wsrtGuide/node6.html

[4] http://www.atnf.csiro.au/computing/software/miriad

Table 6.2 — Overview of WSRT radio observations

Start date	$\Delta T_{\rm aver}$ (days)	Int. time (hours)	Frequency (GHz)	Flux (μJy)
2005-11-04T18:14:24	13.37	4.0	8.5	38 ± 132
2005-11-08T14:19:41	17.19	7.0	8.5	28 ± 97
2005-10-23T15:20:10	1.19	5.0	4.9	281 ± 32
2005-10-24T15:17:17	2.22	6.2	4.9	342 ± 34
2005-10-25T15:12:58	3.30	5.4	4.9	143 ± 30
2005-10-28T18:33:08	6.40	8.5	4.9	91 ± 28
2005-10-30T18:00:00	8.32	5.8	4.9	138 ± 28
2005-11-01T18:00:00	10.38	8.9	4.9	169 ± 28
2005-11-04T17:31:12	13.37	4.6	4.9	70 ± 34
2005-10-25T15:56:10	3.33	5.4	1.4	8 ± 78

istic frequencies: the peak frequency $\nu_{\rm m}$, corresponding to the minimum energy of the relativistic electrons that are accelerated by the blast wave, the cooling frequency $\nu_{\rm c}$, corresponding to the electron energy at which electrons lose a significant fraction of their energy by radiation on a timescale that is smaller than the dynamical timescale, and the self-absorption frequency $\nu_{\rm a}$, below which synchrotron self-absorption produces significant attenuation. The broadband spectrum is further characterized by the specific peak flux $F_{\nu,\rm max}$ and the slope p of the electron energy distribution.

The dynamics of the relativistic blast wave determine the temporal behavior of the broadband synchrotron spectrum, i.e. the light curves at given frequencies. At first the blast wave is extremely relativistic, but is decelerated by the surrounding medium. When the Lorentz factor Γ of the blast wave becomes comparable to $\theta_{\rm j}^{-1}$, where $\theta_{\rm j}$ is the opening angle of the jet, the jet starts to spread sideways. At that time, $t_{\rm j}$, the temporal behavior of the broadband spectrum changes (see e.g. Rhoads 1997).

We fit our data to six parameters: $\nu_{\rm c}$, $\nu_{\rm m}$, $\nu_{\rm a}$, $F_{\nu,\rm max}$, p and $t_{\rm j}$. From these parameters and the redshift of the burst, $z = 0.8$, we can find the physical parameters governing the blast wave and its surroundings: the blast wave isotropic equivalent energy $E_{\rm iso}$, the jet opening angle $\theta_{\rm j}$, the collimation corrected blast wave energy $E_{\rm jet}$, the fractional energy densities behind the relativistic shock in electrons and in the magnetic field, $\varepsilon_{\rm e}$ and $\varepsilon_{\rm B}$ respectively, and the density of the surrounding medium. The meaning of the latter parameter depends on the density profile of the surrounding medium. For a homogeneous circumburst medium, we simply determine the density n. For a massive stellar wind, where the density is proportional to R^{-2} with R the distance to the GRB explosion center, we obtain the parameter A_*, which is the ratio of the mass-loss rate over the terminal wind velocity of the GRB progenitor.

Our modeling results are shown in Table 6.3, for both the homogeneous external medium and the stellar wind environment. The light curves for the best fit parameters are shown in Figure 6.1. We have performed Monte Carlo simulations with synthetic data sets in order to derive accuracy estimates of the best fit parameters, which are also given in the table. It is evident from the results that our six fit parameters are reasonably well constrained in both cases for the circumburst medium. The derived physical parameters are also well constrained, except for ε_e and ε_B. The values we find for both the isotropic and the collimation corrected energy, are similar to those found for other bursts; this is also true for p. See e.g. Panaitescu & Kumar (2001) and Yost et al. (2003). The jet opening angle and the density of the surrounding medium are quite small, but both not unprecedented. The jet break time t_j is somewhat smaller than estimated in Section 6.2.1, but both estimates have relatively large errors, likely because of the lack of (X-ray) data around the jet break time.

With the absence of optical light curves, it is not possible to discriminate between the two different circumburst media. This is mainly due to the fact that the X-ray band lies above both ν_m and ν_c, in which case the slopes of the light curves do not depend on the density profile of the circumburst medium (even at 0.15 days, back-extrapolating ν_c from Table 2.1 results in its value being below the X-ray band). The χ^2_red is somewhat better for the stellar wind case, but the homogeneous case cannot be excluded. From the X-ray light curve, however, one can conclude that the density profile of the medium does not change between approximately 0.15 and 12 days after the burst. If there were a transition from a stellar wind to a homogeneous medium, the X-ray flux has to rise or drop significantly, unless the densities are the fine-tuned at the transition point (Pe'er & Wijers 2006). From the fact that the medium does not change during the X-ray observations, one can draw conclusions on the distance of the wind termination shock of the massive star: if one assumes that the medium is already homogeneous at $\approx$ 0.15 days, the wind termination shock position is at $R_\mathrm{w} \lesssim 9.8 \cdot 10^{17}$ cm (0.32 pc); if the circumburst medium is a stellar wind up to $\approx$ 12 days after the burst, $R_\mathrm{w} \gtrsim 1.1 \cdot 10^{19}$ cm (3.7 pc).

6.3.2 The non-detection of the optical afterglow

It is quickly seen that GRB 051022 falls into the category of the so-called "dark bursts". Using, for example, the quick criterion proposed by Jakobsson et al. (2004), we find $\beta_{OX} < -0.05$ at 12.7 hours after the burst using the Gemini r'

Table 6.3 — Results of broadband modeling for both a homogeneous external medium and a massive stellar wind. The best fit parameters are shown together with accuracy estimates from Monte Carlo simulations with synthetic data sets. The characteristic frequencies of the synchrotron spectrum and the peak flux are given at t_j.

Parameter	Homogeneous	Stellar wind
$\nu_\mathrm{c}(t_\mathrm{j})$	$(1.45^{+1.12}_{-0.23}) \cdot 10^{17}$ Hz	$(2.84^{+0.32}_{-1.30}) \cdot 10^{17}$ Hz
$\nu_\mathrm{m}(t_\mathrm{j})$	$(3.50^{+2.26}_{-1.47}) \cdot 10^{11}$ Hz	$(2.90^{+2.03}_{-1.15}) \cdot 10^{11}$ Hz
$\nu_\mathrm{a}(t_\mathrm{j})$	$(4.56^{+2.85}_{-3.08}) \cdot 10^{9}$ Hz	$(2.68^{+2.17}_{-1.60}) \cdot 10^{9}$ Hz
$F_{\nu,\mathrm{max}}(t_\mathrm{j})$	888^{+52}_{-109} μJy	694^{+30}_{-240} μJy
p	$2.06^{+0.19}_{-0.05}$	$2.10^{+0.08}_{-0.09}$
t_j	$0.96^{+0.40}_{-0.28}$ days	$1.06^{+0.41}_{-0.11}$ days
θ_j	$3.39^{+2.02}_{-2.27}$ deg	$2.30^{+1.09}_{-0.85}$ deg
E_iso	$(5.23^{+1.13}_{-1.69}) \cdot 10^{52}$ erg	$(28.2^{+31.0}_{-10.4}) \cdot 10^{52}$ erg
E_jet	$(0.917^{+0.655}_{-0.512}) \cdot 10^{50}$ erg	$(2.27^{+2.25}_{-0.79}) \cdot 10^{50}$ erg
ε_e	$0.247^{+1.396}_{-0.212}$	$0.0681^{+0.3951}_{-0.0348}$
ε_B	$(7.63^{+42.57}_{-6.30}) \cdot 10^{-3}$	$(8.02^{+28.18}_{-7.17}) \cdot 10^{-3}$
n	$(1.06^{+9.47}_{-1.04}) \cdot 10^{-2}$ cm^{-3}	...
A_*[5]	...	$(2.94^{+6.98}_{-2.11}) \cdot 10^{-2}$
χ^2_red	1.9	1.5

band observation, well below the proposed limit of $\beta_{OX} < 0.5$. A more precise criterion would combine the available spectral and temporal parameters of the X-ray afterglow, allow all valid combinations, and from that infer the range of possible optical magnitudes from the X-rays (see e.g. Rol et al. 2005). This is, in fact implied in our previous modeling: the modeled specific fluxes corresponding to the band and epoch of our optical and nIR upper limits are listed in Table 6.4 (see also Table 6.1).

While the values in this table are given for local extinction, not K-corrected to $z = 0.8$, it is immediately obvious that our K-band observations put a stringent constraint on the required extinction directly surrounding the burst.

To estimate the amount of local extinction in the host galaxy, we have mod-

Table 6.4 — Upper limits compared to model flux calculations. The inferred lower limits on the extinction are given in the observers frame. The E_{B-V} values are given for a Galactic extinction curve ($R_V = 3.08$), and are for illustrative purposes; see the comments at the end of Section 6.3.2.

Filter	Upper limit	homogeneous density profile			stellar wind density profile		
		Modeled flux	Extinction	E_{B-V}	Modeled flux	Extinction	E_{B-V}
	(μJy)	(μJy)	(mag)		(μJy)	(mag)	
K_s	< 6.82	93.1	> 2.84	> 7.74	57.2	> 2.31	> 6.29
J	< 12.3	117	> 2.44	> 2.71	74.1	> 1.95	> 2.16
Z	< 2.66	103	> 3.97	> 2.58	67.8	> 3.52	> 2.29
r'	< 0.305	74.5	> 5.97	> 2.17	44.4	> 5.41	> 1.97
z'	< 1.53	87.7	> 4.40	> 2.97	51.9	> 3.83	> 2.59

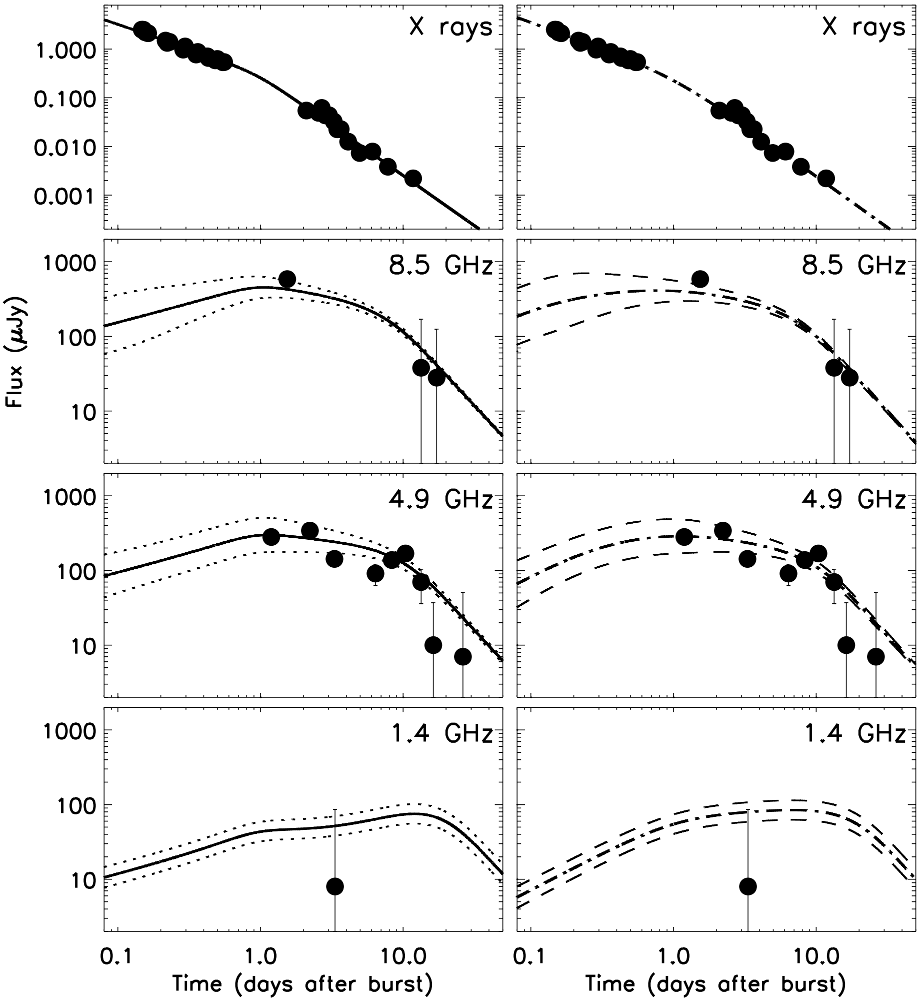

Figure 6.1 — Fit results for a homogeneous circumburst medium (left panel) and a massive stellar wind (right panel). The solid and dash-dotted lines are the best model fits, and the dotted and dashed lines indicate the predicted rms scatter due to insterstellar scintillation; see the appendix for further details. Also included in the figure (and modeling) is the reported VLA 8.5 GHz detection (Cameron & Frail 2005, left-most point in the 8.5 GHz subplot).

eled the nIR to X-ray spectrum around 0.5 days after the burst, considering 3 different extinction curves: those of the Milky Way (MW), the Large Magellanic Cloud (LMC) and the Small Magellanic Cloud (SMC), from Pei (1992), with R_V of 3.08, 3.16 and 2.93, respectively.

For this, we used the unabsorbed XRT flux obtained from the spectral fit to orbits 3 – 7 (which do not contain piled-up data), and fixed the energy spectral slope in the X-rays at $\beta = 1$ (also from the X-ray spectral fit). The optical specific fluxes were scaled to the logarithmic mid-observation time of the X-ray observations with an assumed $\alpha = 1.16$ decline. This estimated optical decay is derived from the pre-break X-ray decay value, allowing for the cooling break between the two wavelength regions, and averaging the two possible values for $\alpha_X - \alpha_{\rm opt}$ (-0.25 and 0.25). We can further put the most stringent constraint on the broken power law spectral shape, by setting the spectral break just below the X-rays, at 1.8×10^{17} Hz, which follows from our previous broad-band modeling. Our results indicate that, for the aforementioned extinction curves, a local extinction of $E_{B-V} \approx 7$ (for all three extinction curves) is necessary to explain the K-band upper limit.

We can relate the resulting $N_{\rm H}$ from our X-ray spectral fits to any local E_{B-V}, using the relations found in Predehl & Schmitt (1995), Fitzpatrick (1985) and Martin et al. (1989) for $N(HI)/E_{B-V}$, and adjusting the metallicity in our X-ray absorption model accordingly. We obtain $E_{B-V} = 7.5, 1.54$ and 0.84 for a MW, LMC and SMC extinction curve respectively, with the MW value showing the best agreement with our findings for optical extinction (both Nakagawa et al. 2006 and Butler et al. 2005b find E_{B-V} values roughly twice as high here, for a MW extinction curve only, since their $N_{\rm H}$ estimate is larger than ours). This, obviously, depends on the assumption that the MW (or otherwise, LMC or SMC) extinction curves are valid models to compare with our observed data here. Since these data happen to originate from just one sight line in a galaxy, this may very well not be the case. Further, even if the extinction curve is correct, the actual value of R_V may be rather different for the host galaxy. Finally, the $E_{B-V} - N_{\rm H}$ relations show a rather large scatter, especially at higher column densities, nor is the $N_{\rm H}$ always derived using X-ray spectroscopy. Our above results are therefore approximations, which are useful to compare with other (GRB host) studies, but should be taken with the necessary caution.

6.3.3 The host galaxy of GRB 051022

Using the optical data described above, we fit the SED of the host of GRB 051022 using the HyperZ program[8] developed by Bolzonella et al. (2000). The photometry of the host has been performed using apphot within IRAF, in an aperture 1.5 times the estimated seeing in the different exposures. The results are reported in Table 6.5 (see also Ovaldsen et al. 2007). The range of photometric

---

[8] See http://webast.ast.obs-mip.fr/hyperz

Table 6.5 — Measured host galaxy magnitudes

Filter	Magnitude	Magnitude error
K	18.40	0.04
K_s	18.36	0.09
H	19.42	0.09
J	19.92	0.05
Z[6]	21.41	0.05
z'	21.30	0.04
i'	21.77	0.01
r'	22.04	0.01
R	21.84	0.09
V	22.30	0.04
B	22.75	0.02
U	> 21.3[7]	...

magnitudes reported in this paper provides one of the most complete broadband optical datasets of a GRB host galaxy to date. We fit using the eight synthetic galaxy templates provided within HyperZ at the redshift of the host, and find that the host galaxy is a blue compact galaxy of type irregular, with a dominant stellar population age of $\approx$ 20 Myr, similar to other long GRB hosts (Christensen et al. 2005). A moderate amount of extinction of $A_V \approx 1$ mag is required to fit the SED, with an SMC-type extinction curve providing a best fit, and the luminosity of the host is approximately 1.5 L_* (assuming $M_{*,B} = -21$); these findings are in full agreement with Castro-Tirado et al. (2006). The amount of extinction in the line of sight towards the GRB required to suppress the optical light of the afterglow to the observed limits is clearly higher than the A_V value found from the host SED: $A_V = 4.4$ magnitudes towards the GRB, estimated from blueshifting our measured (observer frame) z' band extinction to $z = 0.8$. The host galaxy SED extinction is, however, an average value derived from the integrated colors of the host.

The host of GRB 051022 is located in a field crowded with galaxies of various Hubble types. We perform photometry on several galaxies close to the GRB host (within 1 arcminute) to investigate the possibility that the high star formation rate seen in the optical (Castro-Tirado et al. 2006 report an SFR of $\approx 20 \mathrm{M}_\odot \mathrm{yr}^{-1}$) is induced by a recent interaction with one of the neighboring galaxies. As formation of high mass stars has also been observed to occur in dusty regions in merging systems (see e.g. Lin et al. 2007), this could help to explain the excess optical extinction towards GRB 051022. We performed HyperZ fits to these galaxies, and find that none of them is well fit by a photometric redshift of $z \approx 0.8$. Particularly the two galaxies closest to the GRB host galaxy are not compatible with a redshift 0.8, and show best fits with photometric redshifts of $z \approx 0.2 - 0.25$. Out of the sample of six galaxies close to the GRB host we find that four have best-fit photometric redshifts in the range 0.20 – 0.25, making it unlikely that a possible overdensity of galaxies near the host galaxy is due to a cluster or galaxy group at the host redshift.

6.4 Discussion

The issue of non-detected ("dark") GRB afterglows has received significant interest ever since the discovery of the first GRB afterglow, starting with the non-detection of GRB 970828 to very deep limits (Groot et al. 1998; Odewahn et al. 1997). For this particular afterglow, its non-detection has been attributed to a dust-lane in its host galaxy (Djorgovski et al. 2001). Dust extinction as the cause of the non-detection of the optical afterglow has been inferred in the case of several other GRBs, notably those with a precise X-ray or radio position, where one can pinpoint the afterglow position on top of its host galaxy (e.g. GRB 000210, Piro et al. 2002).

Optical drop-outs due to high redshift will also result in dark bursts, but are harder to confirm, since it would require at least one detection in a red band, to detect the Lyα break. Otherwise, it becomes indistinguishable from dust extinction.

Other explanations of afterglow non-detections include the intrinsic faintness of the afterglow. For HETE-2 detected GRBs, this has been inferred for e.g. GRB 020819 (Jakobsson et al. 2005). For Swift bursts, where rapid and accurate X-ray positions are often available, this is a major cause of non-detections (Berger et al. 2005a), largely attributed to a higher average redshift.

In our case here, the host galaxy has been detected at a relatively modest redshift, which almost automatically points to the dust extinction scenario. The radio and X-ray detections even allow us to model the necessary amount of extinction between us and the GRB.

6.4.1 The burst environment

The issue of the role of dust extinction in the lines of sight towards GRBs is still very much an open one. While clear signs of dust depletion are seen in several afterglow spectra, the A_V values that are predicted from these depletion measures are generally much higher than the observed ones, that can be found from the continuum shape (Savaglio & Fall 2004). Recently, selected samples of GRB afterglows were homogeneously analyzed for X-ray and optical extinction, showing dust to gas ratios different from Galactic and Magellanic cloud values (Starling et al. 2007b; Schady et al. 2007). Galama & Wijers (2001) and Stratta et al. (2004) had already found dust (optical) to gas (X-ray) ratios to be lower than the Galactic value (in all cases, however, there is a bias in these samples to optically and X-ray detected afterglows). Comparison of neutral hydrogen columns and metallicities of afterglow lines of sight with X-ray extinction values (Watson et al. 2007) showed that the absorption probed by these two wavelength regimes is generally located at different positions in the host. In all these cases there may be significant biases against bursts with low apparent magnitudes, preventing optical spectroscopy, which are hard to quantify.

In the case of GRB 051022, there is a significant discrepancy between the extinction for the host as a whole and that along the line of sight to the burst, or at least along our line of sight towards the burst. This is perhaps not too surprising if one assumes, for example, that the burst occurred inside a Giant Molecular Cloud (GMC). Jakobsson et al. (2006a) compared the GRB N(HI) distribution to that of modeled GRBs located inside Galactic-like GMCs. They found that the two distributions are incompatible, and possibly GRBs are more likely to occur inside clouds with a lower N(HI), or alternatively, outside the actual GMC. (Note that their study concentrates on bursts with $z > 2$, where the Ly-α absorption is visible in the optical wavebands; it is also biased towards optically detected afterglows). A GMC could therefore actually be positioned in front of the GRB, where the required optical and X-ray extinction is easily achieved. This agrees with the findings by Prochaska et al. (2007), who analyzed several GRB-Damped Lyman Alpha spectra and from observed depletion levels infer that the gas is not located directly near the GRB (e.g. its molecular cloud) but further out. The specific case of GRB 060418 confirmed this through time-resolved high resolution spectroscopy, showing that the observed metal lines originate past 1.7 kpc from the burst itself (Vreeswijk et al. 2007). In fact, X-ray radiation from the burst could easily destroy grains out to 100 pc (Waxman & Draine 2000; Fruchter et al. 2001b; Draine & Hao 2002) and permit the afterglow radiation to penetrate the surrounding molecular cloud. Dust extinction is therefore likely to occur further out, perhaps to several kiloparsecs.

It is interesting to find a non-SMC type of extinction curve from the combination of X-ray and optical absorption (though not completely ruled out): in most cases modeled, an SMC extinction curve fits the optical–X-ray spectra best (Starling et al. 2007b; Schady et al. 2007), presumably attributable to the absence of the 2175 Å feature (Savage & Mathis 1979) and the low dust to gas ratio. Our findings indicate that the extinction along the line of sight to the GRB can be different than one of the three assumed extinction curves. Local small scale density variations in clouds, such as found by from infrared studies in the Taurus region and from simulations (Padoan et al. 2006), could cause this fairly easily.

6.4.2 Energetics

Our modeling provides us with a detailed set of parameters of the afterglow energetics, including $E_{\rm jet}$, the energy of the afterglow. For the prompt emission energy, we use the data from the Konus-Wind measurements (Golenetskii et al. 2005). We calculate a prompt isotropic energy of $4.39^{+0.29}_{-0.18} \times 10^{53}$ erg in the 20 keV – 20 MeV observer frame, and, by applying a K-correction (as in e.g. Bloom et al. 2001), $E_{\rm p,iso} = 10.4^{+0.7}_{-0.4} \times 10^{53}$ erg in the 1 – 10^5 keV rest frame. The collimation corrected energy depends on the assumed density profile of the surrounding medium: for a homogeneous medium, we obtain $E_{\rm p,jet} = 18.2 \times 10^{50}$ erg, and for a wind-like medium, $E_{\rm p,jet} = 8.38 \times 10^{50}$ erg. With $E_{\rm peak} = 918^{+66}_{-59}$ keV in the burst rest frame, we find that the $E_{\rm peak} - E_{\rm p,jet}$ relation (Ghirlanda et al. 2004) somewhat underestimates the $E_{\rm peak}$ when calculated from $E_{\rm p,jet}$: $E_{\rm peak} \approx$ 740 keV for a homogeneous medium, and $\approx$ 430 keV for a wind medium (the difference between our chosen cosmology and that used by Ghirlanda et al. 2004 amounts to only a 0.3% difference in $E_{\rm iso}$). These estimates, however, come with a few caveats: *1)* the $E_{\rm peak}$ from the Konus-Wind data is calculated using an exponential cut-off model, not the Band function (Band et al. 1993). Since the Band function includes the case of an exponential cut-off model (with $\beta = -\infty$, this should, however, pose no problem in estimating the actual $E_{\rm peak}$), *2)* our break time, and therefore the jet-opening angle, are calculated from the full modeling of the afterglow, which effectively means derived from the available X-ray and radio data. Further, the original Ghirlanda relation was derived using optical break times. Recent efforts show that estimating jet break times from X-ray light curves may not lead to the same results (e.g. Panaitescu et al. 2006), and *3)* the relatively large error on the jet opening angle estimate allows for a relatively large range in collimation corrected energies. We have simply used here our best value, but an $E_{\rm peak}$ value of 1498 keV derived from $E_{\rm jet}$ can still be accommodated within our errors. (We note that, with a different $E_{\rm peak}$ estimate and an incorrect value for the jet break time, Nakagawa et al. 2006 still found their results to lie on the Ghirlanda relation). The break time problem can be avoided by looking only at the $E_{\rm peak} - E_{\rm p,iso}$ relation (Amati et al. 2002; Amati 2006). From this, we estimate $E_{\rm peak} \approx$ 924 keV, nicely in agreement with the value found directly from the spectra fit.

Comparing the prompt emission energy ($E_{\rm p,jet}$) and afterglow blast wave kinetic energy ($E_{\rm jet}$), we find their ratio to be $E_{\rm p,jet}/E_{\rm jet} = 3.7$ in the case of a wind-like circumburst medium, while for a homogeneous medium, $E_{\rm p,jet}/E_{\rm jet} = 20$. These ratios are similar to those found for other bursts (e.g. Berger et al. 2003b, Figure 3).

GRB 051022 is also one of the brightest bursts observed by HETE, with a prompt 30–400 keV fluence of $S = 1.31 \times 10^{-4}$ erg cm^{-2} (Nakagawa et al. 2006). In fact, compared to the sample of 35 FREGATE bursts analyzed by Barraud et al. (2003), GRB 051022 has the largest fluence, even topping the relatively close-by GRB 030329 (Vanderspek et al. 2004, $S = 1.2 \times 10^{-4}$ erg cm^{-2}; note that for GRB 051022, its redshift is close to the median redshift of HETE-2 detected GRBs and therefore distance effects will play a very minor role). Rol et al. (2005) noted this potential correlation of fluence with the non-detection of a GRB afterglow for the small subset of genuinely dark bursts in their sample: the truly dark bursts all have a much higher than average fluence (although this is for a relatively small sample only). Potentially, this could point to an external origin for the prompt emission, instead of being due to internal shocks: a large amount of dust may result in more matter that will radiate, while at the same time the radiation will be suppressed at UV and optical wavelengths. This would indicate an origin of the extinction quite close to the burst instead, in contrast to previous findings for other bursts, as discussed in Section 6.4.1. These latter bursts, however, were all optically selected to obtain spectroscopy, and may therefore show different surroundings than GRB 051022. Unfortunately, with the small sample size of genuine dark bursts a firm conclusion on this correlation is not possible, but remains something to watch for in future dark bursts.

6.5 Conclusions

GRB 051022 is a prototypical dark burst, with the local extinction exceeding 2.3 magnitudes in J and 5.4 magnitudes in U, in the host-galaxy restframe, with the exact limits depending on the circumburst density profile. The extinction curve derived from an X-ray – optical spectral fit points towards a Galactic type of extinction curve, although it is likely that this is more or less a coincidence: the host galaxy itself is best modeled with an SMC-like extinction curve, with a modest amount of extinction, $A_V \approx 1$ mag. The large optical absorption towards the afterglow of GRB 051022 is therefore probably the effect of an unfortunate position in the host where the line of sight crosses dense regions within the host.

The X-ray and radio afterglow data allow for a full solution of the blast wave model, although we unfortunately cannot distinguish between the density profile (homogeneous or wind-like) of the circumburst medium. We estimate a collimation-corrected energy in the afterglow emission of 0.92 – 2.3 $\times 10^{50}$ erg, while the energy in prompt emission (1 – 10^5 keV rest frame) is 8.4 – 18 $\times 10^{50}$ erg. Aside from the large optical extinction, the afterglow otherwise appears as an average afterglow, with no outstanding properties. The potentially interesting point here is that the 30-400 keV fluence of the prompt emission is one of the largest ever detected in the HETE-2 sample.

In the era of Swift GRBs, dust-extincted bursts can actually be found in optical/nIR thanks to the rapid availability of precise positions: examples are found where the burst is relatively bright early on at optical/nIR wavelengths, while the afterglow proper (post few hours) often can go undetected (e.g. Oates et al. 2006; Perley et al. 2007). This allows targeted follow-up of such dark bursts, i.e. determining the host galaxy (and the bursts precise position therein) and a redshift measurement. In our case, a precise CXO and radio position pinpointed the host galaxy, but such data may not always be available. High resolution late-time observations of the host, at the location of the GRB, may then reveal whether the burst indeed occurred inside a dense host region.

6.6 Appendix A: Interstellar scintillation in the radio modeling

The 4.9 GHz measurements show scatter around the best fit light curve, which can be accounted for by interstellar scintillation (ISS). In Figure 6.1 we have indicated the predicted rms scatter due to ISS. We have calculated the scattering measure from the Cordes & Lazio (2002) model for the Galactic distribution of free electrons: $SM = 2.04 \cdot 10^{-4}\,\mathrm{kpc}\,/\mathrm{m}^{-20/3}$. The radio specific flux will be modulated when the source size is close to one of the three characteristic angular scales, i.e. for weak, refractive or diffractive ISS. From Walker (1998), we calculate the transition frequency between weak and strong ISS, $\nu_0 = 9.12\,\mathrm{GHz}$, and the angular size of the first Fresnel zone, $\theta_{\mathrm{F}_0} = 0.994\,\mu\mathrm{as}$. Our measurements were all performed at frequencies below ν_0, i.e. in the strong ISS regime, which means that only refractive and diffractive ISS modulate the specific flux significantly. We calculate the evolution of the source size in the extreme relativistic phase ($\theta_\mathrm{s} = R/\Gamma$) and after the jet break ($\theta_\mathrm{s} = R\theta_\mathrm{j}$), and compare this source size with the diffractive angular scale $\theta_\mathrm{d} = \theta_{\mathrm{F}_0}(\nu_0/\nu)^{-6/5} = 0.0701 \cdot \nu_\mathrm{GHz}^{6/5}\,\mu\mathrm{as}$ and the refractive angular scale $\theta_\mathrm{r} = \theta_{\mathrm{F}_0}(\nu_0/\nu)^{11/5} = 128 \cdot \nu_\mathrm{GHz}^{-11/5}\,\mu\mathrm{as}$ to calculate the modulation index m_p. In the case of diffractive ISS the modulation index is 1, and in the case of refractive ISS $m_\mathrm{p} = (\nu_0/\nu)^{-17/30} = 0.286 \cdot \nu_\mathrm{GHz}^{17/30}$. Because of the expansion of the blast wave the angular source size exceeds one of the characteristic angular scales at some point in time. Then the modulation will begin to quench as $m_{\rm p}(\theta_{\rm d}/\theta_{\rm s})$ in the case of diffractive ISS, and as $m_{\rm p}(\theta_{\rm r}/\theta_{\rm s})^{7/6}$ in the case of refractive ISS.

Acknowledgements We thank the referee for a careful reading of the manuscript and constructive comments. We thank Kim Page and Andy Beardmore for useful discussions regarding the XRT data analysis. ER and RLCS acknowledge support from PPARC. KW and RAMJW acknowledge support of NWO under grant 639.043.302. The authors acknowledge funding for the Swift mission in the UK by STFC, in the USA by NASA and in Italy by ASI. The Dark Cosmology Centre is funded by the Danish National Research Foundation. The William Herschel Telescope is operated on the island of La Palma by the Isaac Newton Group in the Spanish Observatorio del Roque de los Muchachos of the Instituto de Astrofísica de Canarias. The United Kingdom Infrared Telescope is operated by the Joint Astronomy Centre on behalf of the U.K. Particle Physics and Astronomy Research Council. The data reported here were obtained as part of the UKIRT Service Programme. The Westerbork Synthesis Radio Telescope is operated by ASTRON (Netherlands Foundation for Research in Astronomy) with support from the Netherlands Foundation for Scientific Research (NWO). Support for this work was provided by the National Aeronautics and Space Administration through Chandra Award Number 1736937 issued by the Chandra X-ray Observatory Center, which is operated by the Smithsonian Astrophysical Observatory for and on behalf of the National Aeronautics Space Administration under contract NAS8-03060. This publication makes use of data products from the Two Micron All Sky Survey, which is a joint project of the University of Massachusetts and the Infrared Processing and Analysis Center/California Institute of Technology, funded by the National Aeronautics and Space Administration and the National Science Foundation. This research has made use of data obtained from the High Energy Astrophysics Science Archive Research Center (HEASARC), provided by NASA's Goddard Space Flight Center.

Table 6.6 — Overview of optical observations

Start date	ΔT_{aver} (days)	Exposure (seconds)	Filter	Seeing (arcsec)	Telescope & instrument
2005-10-22T23:25:14	0.4287	1800	Z	0.8	WHT + API
2005-10-23T00:22:33	0.4684	1620	J	1.2	SOAR + OSIRIS
2005-10-23T00:56:00	0.4917	1620	K_s	1.3	SOAR + OSIRIS
2005-10-23T00:48:03	0.5144	1920	i'	0.6	Gemini S. + GMOS
2005-10-23T01:07:53	0.5288	1920	r'	0.6	Gemini S. + GMOS
2005-10-23T01:27:46	0.5426	1920	z'	0.5	Gemini S. + GMOS
2005-10-23T06:31:03	0.7525	720	J	1.4	UKIRT + WFCAM
2005-10-23T06:36:39	0.7526	360	H	1.3	UKIRT + WFCAM
2005-10-23T06:47:59	0.7604	360	K	1.3	UKIRT + WFCAM
2005-10-23T21:15:57	1.3389	1200	Z	1.0	WHT + API
2005-10-24T09:35:10	1.8467	720	K	0.3	UKIRT + WFCAM
2005-10-25T01:34:03	2.5181	1602	K_s	1.3	SOAR + OSIRIS
2005-10-25T02:13:18	2.5454	720	J	1.2	SOAR + OSIRIS
2005-10-25T02:22:02	2.5698	1920	r'	1.1	Gemini S. + GMOS
2005-10-25T02:39:59	2.5792	1440	z'	1.2	Gemini S. + GMOS
2005-10-26T00:36:58	3.4785	1800	R	1.4	WHT+PFIP
2005-10-26T02:48:06	3.5695	600	Gunn i	1.4	DK1.54m + DFOSC
2005-10-26T03:23:35	3.5942	600	R	1.9	DK1.54m + DFOSC
2005-10-27T01:01:04	4.4952	600	B	2.3	DK1.54m + DFOSC
2005-10-27T02:59:20	4.5773	600	R	1.6	DK1.54m + DFOSC
2005-10-27T02:00:48	4.5367	600	V	1.8	DK1.54m + DFOSC
2005-10-28T02:18:38	5.5491	600	i	1.4	DK1.54m + DFOSC
2005-10-30T02:32:59	7.5590	600	B	1.8	DK1.54m + DFOSC
2005-10-30T04:18:30	7.6323	600	U	1.8	DK1.54m + DFOSC
2005-10-30T01:33:57	7.5180	600	V	1.4	DK1.54m + DFOSC
2005-10-31T03:19:05	8.5910	600	B	1.0	DK1.54m + DFOSC
2005-10-31T01:03:40	8.4970	600	R	1.0	DK1.54m + DFOSC
2005-10-31T02:10:02	8.5431	600	V	1.0	DK1.54m + DFOSC
2005-11-01T01:52:57	9.5312	600	R	0.9	DK1.54m + DFOSC
2005-11-02T02:04:47	10.539	600	V	1.2	DK1.54m + DFOSC
2005-11-03T01:10:34	11.502	600	B	1.2	DK1.54m + DFOSC
2005-11-07T01:25:30	15.512	600	Gunn i	1.4	DK1.54m + DFOSC
2005-11-08T01:40:48	16.523	600	Gunn i	1.4	DK1.54m + DFOSC

7

GRB 060206 and the quandary of achromatic breaks in afterglow light curves

P.A. Curran, A.J. van der Horst, R.A.M.J. Wijers, R.L.C. Starling, A.J. Castro-Tirado, J.P.U. Fynbo, J. Gorosabel, A.S. Järvinen, D. Malesani, E. Rol, N.R. Tanvir, K. Wiersema, M.R. Burleigh, S.L. Casewell, P.D. Dobbie, S. Guziy, P. Jakobsson, M. Jelínek, P. Laursen, A.J. Levan, C.G. Mundell, J. Näränen & S. Piranomonte

Accepted for Publication, Monthly Notices of the Royal Astronomical Society

Abstract

Gamma-ray burst afterglow observations in the *Swift* era have a perceived lack of achromatic jet breaks compared to the *BeppoSAX* era. We present our multi-wavelength analysis of GRB 060206 as an illustrative example of how inferences of jet breaks from optical and X-ray data might differ. The results of temporal and spectral analyses are compared, and attempts are made to fit the data within the context of the standard blast wave model. We find that while the break appears more pronounced in the optical and evidence for it from the X-ray alone is weak, the data are actually consistent with an achromatic break at about 16 hours. This break and the light curves fit standard blast wave models, either as a jet break or as an injection break. As the pre-*Swift* sample of afterglows are dominated by optical observations, and in the *Swift* era most well sampled light curves are in the X-ray, caution is needed when making a direct comparison between the two samples, and when making definite statements on the absence of achromatic breaks.

7.1 Introduction

Gamma-Ray Bursts (GRBs) are well described by the blast wave, or fireball, model (Rees & Mészáros 1992; Mészáros et al. 1998), which details their temporal and spectral behaviour. In this model GRB afterglow emission is created by shocks when a collimated ultra-relativistic jet ploughs into the circumburst medium, driving a blast wave ahead of it. This causes a non-thermal spectrum widely accepted to be synchrotron emission, with characteristic power-law slopes and spectral break frequencies. The signature of the collimation is an achromatic temporal steepening or 'jet break' at ~ 1 day in an otherwise decaying, power-law light curve. The level of collimation, or jet opening angle, has important implications for the energetics of the underlying physical process.

Since the launch of the *Swift* satellite (Gehrels et al. 2004), this standard picture has been called into question by the rich and novel phenomena discovered in the both the early and late light curves (e.g., Nousek et al. 2006). Here we focus on the perceived lack of achromatic temporal breaks in the *Swift* era, up to weeks in some bursts (e.g., Panaitescu et al. 2006; Burrows & Racusin 2007), which calls into question the effects of collimation and therefore the energy requirements of progenitor models. Some bursts show no evidence for breaks in either optical or X-ray, while others show clear breaks in one regime without any apparent accompanying break in the other. Even in those bursts where an achromatic break is observed, they may not be consistent with a jet break as predicted by the blast wave model (e.g., GRB 060124, Curran et al. 2006). We should note that our expectations of the observable signature of a jet break, including the fact that it ought to be perfectly achromatic, is based on highly simplified models, notably those of Rhoads (1997, 1999) and Sari et al. (1999), and break observations, pre-*Swift*, that were based predominately in one regime (i.e., optical). So apart from well sampled multi-regime observations, more realistic models and simulations of the light curves, beyond the scope of this Letter, will also be required to settle this issue.

As the apparent lack of observed achromatic breaks is an important issue in the *Swift* era, we will discuss the perceived presence and absence of these achromatic breaks, using the long burst GRB 060206 as an illustrative example. We present our multi-wavelength analysis of the well sampled afterglow from X-ray to optical wavelengths. In §7.2 we introduce our observations while in §7.3 we present the results of our temporal and spectral analyses. In §7.4 we discuss these results in the overall context of the blast wave model of GRBs and we summarise our findings in §7.5.

7.2 Observations

Throughout, we use the convention that a power-law flux is given as $F_\nu \propto t^{-\alpha}\nu^{-\beta}$ where α is the temporal decay index and β is the spectral index. All errors and uncertainties are quoted at the 1σ confidence level.

Optical observations in B, V, R and I bands were obtained at the 2.5 m Nordic Optical Telescope (NOT), 2.5 m Isaac Newton Telescope (INT) and 3.6 m Telescopio Nazionale Galileo (TNG) on La Palma, the 1.5 m Observatorio de Sierra Nevada (OSN) in Granada, Spain, the 1.8 m Astrophysical Observatory of Asiago, Italy, and the 2.0 m Faulkes Telescope North (FTN) at Haleakala, Hawaii (Table 7.1). The optical counterpart was identified in initial R band frames. No counterpart was detected in the B band frames, in agreement with the significant level of line blanketing associated with the Lyman forest at a redshift of $z = 4.048$ (Fynbo et al. 2006a): the fluxes of the B, V and R bands are reduced to 8, 50 and 88 per cent, respectively, of their true values (Madau 1995). The field was calibrated via a standard Landolt (1992) field taken by the OSN on a photometric night. Differential photometry was carried out relative to a number of stars within $\sim 5'$ of the burst, with resulting deviations less than the individual errors. The photometric calibration error is included in error estimates. We combine our R band data with that already published from the RAPTOR & MDM telescopes (Woźniak et al. 2006; Stanek et al. 2007; where MDM was shifted +0.22 magnitudes as in Monfardini et al. 2006) to extend the optical light curve past 1×10^6 s since trigger.

The X-ray event data from the *Swift* X-Ray Telescope (XRT; Burrows et al. 2005) were initially processed with the FTOOL, `xrtpipeline` (v0.9.9). Source and background spectra from 0.3 – 10.0 keV in Windowed Timing (WT) and Photon Counting (PC) mode were extracted for analysis with `Xspec`. The pre-reduced XRT light curve was downloaded from the on-line repository (Evans et al. 2007).

7.3 Results

7.3.1 Light curves

Visual inspection of the optical light curve (Figure 7.1) clearly shows significant re-brightening at ~ 4000 s and a "bump" at $\sim 1.7 \times 10^4$ s, after which there is a smooth decay with a break at $\sim 5 \times 10^4$ s (Woźniak et al. 2006; Monfardini et al. 2006; Stanek et al. 2007). Fitting a broken power-law to the data after the "bump" gives $\alpha_1 = 1.138 \pm 0.005$, $\alpha_2 = 1.70 \pm 0.06$ and places the break at $t_{\rm break} =$

Table 7.1 — Optical observations of GRB 060206. Magnitudes are given with 1σ errors or as 3σ upper limits.

$T_{\rm mid}$ (sec)	$T_{\rm exp}$ (sec)	Band	Mag
78373	1200	OSN *B*	> 22.7
81977	300	OSN *V*	20.96 ± 0.18
816	60	INT *R*	17.28 ± 0.13
981	180	INT *R*	17.31 ± 0.14
1074	300	NOT *R*	17.45 ± 0.09
1391	600	INT *R*	17.44 ± 0.12
1468	300	NOT *R*	17.43 ± 0.08
1853	180	INT *R*	17.49 ± 0.12
1862	300	NOT *R*	17.55 ± 0.09
5363	120	OSN *R*	16.62 ± 0.09
8300	300	INT *R*	17.03 ± 0.14
18360	1200	FTN *R*	17.90 ± 0.04
29940	1050	FTN *R*	18.50 ± 0.02
68235	1200	Asiago *R*	19.64 ± 0.04
75990	180	OSN *R*	19.87 ± 0.15
80917	180	OSN *R*	19.87 ± 0.09
82225	180	OSN *R*	19.91 ± 0.07
160557	1200	Asiago *R*	20.92 ± 0.07
209760	960	FTN *R*	21.23 ± 0.10
248617	1500	OSN *R*	21.81 ± 0.28
382560	960	FTN *R*	> 21.9
687323	120	TNG *R*	23.19 ± 0.25
1121271	600	NOT *R*	24.66 ± 0.41
2160836	600	NOT *R*	> 23.6
5529	120	OSN *I*	15.77 ± 0.12
82424	180	OSN *I*	19.18 ± 0.15

$5.9 \pm 0.5 \times 10^4$ s ($\chi^2_\nu = 0.77$, 71 degrees of freedom, d.o.f.). It is plausible that the late data suffer from contamination due to the host galaxy which is estimated as $R \sim 24.6$ (Thöne et al. in prep.) and therefore we have included this in our model.

The X-ray light curve also displays a re-brightening at ~ 4000 s (e.g., Monfardini et al. 2006) and a flattening after ~ 10^6 s which has been attributed to a nearby contaminating X-ray source (Stanek et al. 2007). We use the count rate

Table 7.2 — The temporal decay indices in X-ray and optical for a single power-law, α, and a smoothly broken power-law, α_1 & α_2, with a break time, $t_{\rm break}$. Also the spectral indices for X-ray, optical and combined X-ray/optical fits (Section 7.3).

	X-ray	optical	combined
α	1.28 ± 0.02	–	–
α_1	1.04 ± 0.10	1.148 ± 0.005	–
α_2	1.40 ± 0.07	1.70 ± 0.06	–
$t_{\rm break} \times 10^4$ s	$2.2\,^{+2.0}_{-0.8}$	4.9 ± 0.5	–
$\beta_{\rm pre-break}$	1.26 ± 0.09	0.84 ± 0.08	0.93 ± 0.01
$\beta_{\rm post-break}$	0.92 ± 0.14	1.4 ± 1.0	1.00 ± 0.10

light curve since, as we will show in Section 7.3.2, the X-ray data are best described by a single, unchanging spectral index, so converting to flux only adds uncertainties. The X-ray data from 4000 – 10^6 s are well fit by a single power-law decay with $\alpha = 1.28 \pm 0.02$ ($\chi^2_\nu = 1.0$, 65 d.o.f.). However, we also fit a broken power-law with $\alpha_1 = 1.04 \pm 0.10$, $\alpha_2 = 1.40 \pm 0.7$ and a break time of $t_{\rm break} = 2.2^{+2.0}_{-0.8} \times 10^4$ s ($\chi^2_\nu = 0.79$, 63 d.o.f.), giving a marginal improvement. To test whether the X-ray is indeed consistent with the optical, we fix the temporal slopes and break time to those of the optical and fit the X-ray data. We find that these parameters well describe the X-ray data ($\chi^2_\nu = 0.94$, 66 d.o.f.; Figure 7.1). The results of our temporal fits are summarised in Table 7.2.

7.3.2 Spectral analysis

The XRT spectra were fit with an absorbed power-law and in both the WT and PC mode data, a significant amount of absorption over the Galactic value was required. This excess extinction may be explained by host extinction in the rest frame of the burst. For the WT mode data (i.e., pre-break), a spectral index of $\beta_X = 1.26 \pm 0.06$ was found ($\chi^2_\nu = 1.10$, 94 d.o.f.) while the PC mode data (i.e., post-break) was found to have a spectral index of $\beta_X = 0.92 \pm 0.09$ ($\chi^2_\nu = 0.93$, 59 d.o.f.).

Two optical spectral indices are found by fitting the optical spectral energy distributions (SEDs) at $\sim 1.0 \times 10^4$ s and $\sim 8.2 \times 10^4$ s (i.e., pre- and post-break). For the pre-break analysis we use the near-infrared data (JHK_S) of Alatalo et al. (2006) and the shifted R band data, at that time, of Stanek et al. (2007). For the post-break SED we use our V, R and I band data. All data were converted to fluxes and corrected for Galactic extinction of $E_{(B-V)} = 0.013$ (Schlegel et al. 1998) and line blanketing due to the Lyman forest. We find optical spectral indices of $\beta_{\rm opt} = 0.84 \pm 0.05$ and $\beta_{\rm opt} = 1.4 \pm 0.6$ for pre- and post-break,

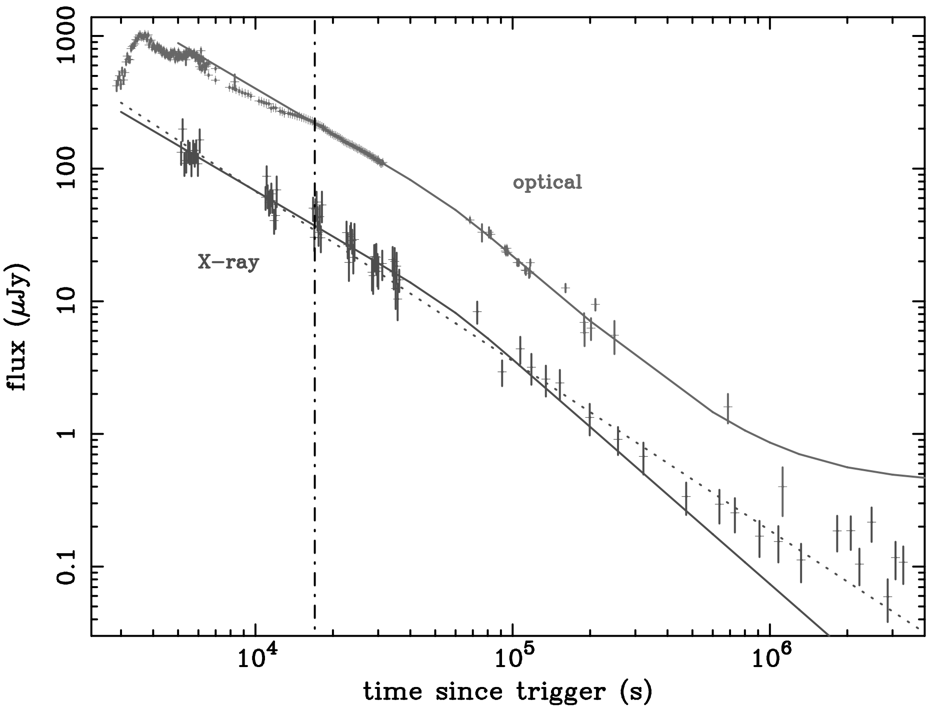

Figure 7.1 — Optical (*R*-band, upper light curve) and X-ray count rate (×200, lower light curve) light curves of GRB 060206. The solid lines show the smoothly broken power-law (with host correction) fit to the optical data to the right of the vertical dot-dash line, and those same parameters scaled to the X-ray. The dotted line shows a single power-law fit to the X-ray.

respectively.

To constrain these values further we use the simultaneous X-ray and optical fitting detailed in Starling et al. (2007b). In this method, the optical to X-ray SED is fit in count-space, incorporating the measured metallicity (Fynbo et al. 2006a) and including the effect host galaxy extinction. The above optical data points were augmented by X-ray data at the given times: the pre-break SED by one orbit of XRT data and the post-break SED by ~ 3×10^4 seconds of data. From this we find that both epochs are well described by a single spectral power-law with $\beta = 0.93 \pm 0.01$ and $\beta = 1.00 \pm 0.06$, respectively, in agreement with each other and with our previous values of $\beta_{\rm opt}$ and $\beta_{\rm X}$ but inconsistent with the interpretation of a possible spectral change in the optical between the two epochs. These results are shown in Table 7.2 and agree, within errors, with those of Monfardini et al. (2006).

7.4 Discussion

We have shown that the well sampled X-ray afterglow can be described by a single power-law decay, though a broken power-law, which gives temporal indices and a break time similar to those in the optical, is as good a fit. While it is difficult to accommodate the single power-law decay in the framework of the blast wave model, an achromatic broken power-law decay can be interpreted in terms of a jet break or an energy injection break, which we will now discuss in the context of the blast wave model (for a review and mathematical relations see, e.g., Zhang & Mészáros 2004).

The spectral indices of the optical to X-ray spectrum are constant before and after the optical break, i.e., at ~ 2.9 and ~ 23 hours with the break at ~ 16 hours (~ 3 hours in the rest frame) after the burst. This indicates that the temporal break is not caused by the passage of a break frequency through the optical regime in the broadband spectrum. The conclusion one can draw from this is that the break is caused by a change in the dynamics of the jet, e.g., the cessation of the energy injection phase or the beginning of the jet-spreading phase (the jet break interpretation). Assuming that the optical and X-ray emission is caused by the same mechanism, the X-ray light curve is expected to show a break at the same time as the optical.

We note that Monfardini et al. (2006) ascribe the dynamical change of the blast wave to a change in the circumburst density profile, the blast wave breaking out of a homogeneous medium into a stellar wind like environment. This model agrees with the observed spectral and temporal slopes but is not expected from the immediate environment models of GRB progenitors which predicts a transition from a wind like to a homogeneous medium, and not the converse (e.g., Wijers 2001; Ramirez-Ruiz et al. 2005). In the following we explore the two possible explanations we propose for the SEDs and light curves of the afterglow of this burst, a jet break and an energy injection break.

7.4.1 Jet break versus energy injection

From the SED spectral indices the power-law index of the electron energy distribution, p, can be determined. For both possible explanations the interpretation of the SEDs is the same, in that the single power-law SED from optical to X-rays is either in between the peak frequency, $\nu_{\rm m}$ and the cooling frequency, $\nu_{\rm c}$, or above both frequencies. In the first case $p = 3.00 \pm 0.12$, while in the latter case $p = 2.00 \pm 0.12$, using the spectral slopes from the optical to X-ray fit in count-space at 23 hours after the burst.

In the jet break interpretation of the achromatic break, the blast wave is moving ultra-relativistically, but decelerating, before the break. When the Lorentz factor of the blast wave drops below the inverse half opening angle of the jet, the observer starts to see the whole jet and the jet begins to spread sideways, giving rise to the so-called jet break. If both the X-ray and optical regimes are situated between $\nu_{\rm m}$ and $\nu_{\rm c}$, the temporal slope before the break, given the value of p derived from the SED, is $\alpha = 3(p-1)/4 = 1.50 \pm 0.09$ or $\alpha = (3p-1)/4 = 2.00 \pm 0.09$, for a homogeneous or a stellar wind environment, respectively. The post-break slope would then be $\alpha = p = 3.00 \pm 0.12$. All these slopes are too steep compared to the observed temporal slopes. If, however, both observing regimes are above $\nu_{\rm m}$ and $\nu_{\rm c}$, the pre-break slope is $\alpha = (3p-2)/4 = 1.00 \pm 0.09$, while the post-break slope is $\alpha = p = 2.00 \pm 0.12$. The pre-break slope in this case is consistent with the observed slopes. The observed post-break slopes are slightly shallower than expected, but they are consistent within 3σ, though further steepening to an asymptotic value of $\alpha = p$ cannot be ruled out. To conclude, in the jet break interpretation we find that $p = 2.00 \pm 0.12$ and $\nu_{\rm m,c} < \nu_{\rm opt,X}$, but we cannot say anything about the structure of the circumburst medium, i.e., homogeneous or wind, since that requires that the observing frequencies are below $\nu_{\rm c}$.

If the achromatic break is interpreted as the cessation of an extended energy injection phase, the post-break slopes are given by the expressions for an ultra-relativistic blast wave. In this case, if both observing frequencies are situated in between $\nu_{\rm m}$ and $\nu_{\rm c}$, the temporal slopes after the break are $\alpha = 3(p-1)/4 = 1.50 \pm 0.09$ (homogeneous medium) or $\alpha = (3p-1)/4 = 2.00 \pm 0.09$ (stellar wind). If both observing frequencies are situated above the spectral break frequencies, the temporal slope is $\alpha = (3p-2)/4 = 1.00 \pm 0.09$, regardless of the circumburst medium structure. Comparing these numbers with the observed post-break slopes, the observations are best fit when $\nu_{\rm m} < \nu_{\rm opt,X} < \nu_{\rm c}$ and hence $p = 3.00 \pm 0.12$, and the ambient medium is homogeneous. Assuming that the energy injection can be described as $E \propto t^q$, the flattening of the light curves before the break is given by $\Delta\alpha = (p+3)/4 \times q \simeq 1.5 \times q$, which gives $q \sim 0.3$ from the observed average flattening of $\Delta\alpha \sim 0.4$.

7.4.2 Energetics

In general, the jet break time is related to the half opening angle of the jet, from which the isotropic equivalent energy can be converted into the collimation corrected energy. If we interpret the achromatic break at $\sim$ 16 hours as a jet break, the half opening angle of the jet is found to be $\theta_0 = 0.075 \times (E_{52}/n_0)^{-1/8} \sim 4^\circ$ or $\theta_0 = 0.11 \times (E_{52}/A_*)^{-1/4} \sim 7^\circ$, for a homogeneous medium or a stellar wind environment, respectively (Panaitescu & Kumar 2002). If we adopt the energy injection interpretation, the observations indicate that there has not been a jet break up to 10 days after the burst, which results in a lower limit on the jet half opening angle of $\theta_0 > 0.22 \times (E_{52}/n_0)^{-1/8} \sim 13^\circ$. In all these expressions for the opening angle, E_{52} is the isotropic equivalent blast wave energy in units of 10^{52} ergs; n_0 is the homogeneous circumburst medium density in cm^{-3}; and $A_* = \dot{M}/(4\pi v_w^2)$, with $\dot{M}$ the mass-loss rate in 10^{-5} $\mathrm{M}_\odot$ per year and v_w the stellar wind velocity in 10^3 km s^{-1}. These typical values for the energy and density (Panaitescu & Kumar 2002) are in agreement with the constraints on the values for ν_m and ν_c compared to the observing frequencies. Also the fractional energies of radiating electrons and magnetic field, ε_e and ε_B respectively, have typical values of ~ 0.1, although in the energy injection interpretation $\varepsilon_\mathrm{B} \sim 10^{-3.5}$, which has been found for other bursts. With these opening angles we can convert the isotropic equivalent gamma-ray energy of 6×10^{52} ergs (Palmer et al. 2006) into collimation corrected energies of $2 - 4 \times 10^{50}$ erg for the jet break interpretation and $> 10^{51}$ ergs for the energy injection interpretation, consistent with the energy distribution of other bursts (Frail et al. 2001).

7.4.3 Implications

Many previously studied jet breaks do not display sharp changes in the temporal decay index, but a shallow roll-over from asymptotic values which is described by a smoothly broken power-law. The prototypical example of such a break is GRB 990510 for which well sampled *B*, *V*, *R* and *I* band light curves display an achromatic break (e.g., Stanek et al. 1999). This is accepted as a jet break even though the X-ray light curve as measured by *BeppoSAX* (Kuulkers et al. 2000) is satisfactorily described by a single power-law. A break at X-ray frequencies at the same time as the optical break is however, not ruled out and the temporal slopes before and after that break are similar in the optical and X-rays. In the analysis of GRB 060206 we are seeing the same phenomenon: the optical light curve displays a break, while the X-ray is satisfactorily described by a single power-law fit, though a broken power-law is not ruled out. However, an X-ray break is necessary to explain the afterglow when interpreting it in the context of the standard blast wave model. A similar issue has been addressed in SED fits by Starling et al. (2007a), where adding a cooling break to some SEDs gives only a marginal improvement according to the statistical F-test, but is necessitated by considerations of the physical model. This has significant implications for the analysis of the myriad of X-ray light curves that the *Swift* satellite has afforded us. For those X-ray light curves extending up to $\sim$ 1 day or longer, for which we do not have well sampled optical light curves, caution is required when making claims about the absence of breaks in isolation, without considering physical interpretations. This is particularly important when performing statistical analyses on a large sample of temporal and spectral slopes, for making collimation corrected energy estimates, and for using GRBs as standard candles.

7.5 Conclusion

We identify a possible achromatic break in the X-ray and optical light curves of GRB 060206 at ~ 16 hours, which is most successfully explained by a change in the dynamics of the jet: either as a jet break or a break due to the cessation of energy injection. Neither is favoured as both are consistent with the blast wave model and the distribution of collimation corrected energies. The presence of a weak constant source near the afterglow in both X-rays and optical precludes, in this case, an examination of the light curves later than $\sim 10^6$ s. GRB 060206 was, up to now, assumed to have a chromatic break (i.e., a break only in the optical) since the X-ray data alone does not require a break. However, examining all X-ray and optical data until late times, we find that the optical and X-ray light curves are consistent with having the same break time and pre- and post-break temporal slopes. There is also no evidence of chromaticity from a comparison of pre- and post-break SEDs that encompass optical and X-ray data.

We should therefore be cautious in ruling out breaks as being achromatic from comparing the nominal fitted slopes. This issue is important for determining true GRB energies, but also has a strong bearing on recent attempts to use GRBs for determining the geometry of the distant Universe. That said, there does seem to be a tendency, if not yet strongly significant, for the X-ray light curves to have less pronounced breaks. Both 060206 and 990510, the achromatic break 'poster child', are examples of this. It would therefore be worthwhile to extend the sample of *Swift* bursts that have well sampled late-time optical light curves, which would be helped by finding more afterglows in the anti-Sun direction. Also, more detailed theoretical models of jet breaks (likely involving numerical simulations of the jet dynamics) should be preformed to clarify whether jet breaks could vary somewhat between wavebands.

Acknowledgements We thank the referee for constructive comments. PAC, RAMJW and KW gratefully acknowledge support of NWO under grant 639.043.302. MRB, ER and RLCS gratefully acknowledge support from PPARC. DM acknowledges the Instrument Center for Danish Astrophysics. ASJ acknowledges Wihuri foundation, Finland. Partially supported by Spanish research programmes ESP2002-04124-C03-01 & AYA2004-01515. NOT operated by Denmark, Finland, Iceland, Norway, & Sweden, in Observatorio del Roque de los Muchachos of the Instituto de Astrofisica de Canarias, Spain.D The Dark Cosmology Centre is funded by the Danish National Research Foundation. We acknowledge benefits from collaboration within the EU FP5 Research Training Network “Gamma-Ray Bursts: An Enigma and a Tool” (HPRN-CT-2002-00294). This work made use of data supplied by the UK Swift Science Data Centre at the University of Leicester and the High Energy Astrophysics Science Archive Research Center Online Service, provided by the NASA/GSFC.

8

The prompt to late-time multiwavelength analysis of GRB 060210

P.A. Curran, A.J. van der Horst, A.P. Beardmore, K.L. Page, E. Rol,
A. Melandri, I.A. Steele, C.G. Mundell, A. Gomboc, P.T. O'Brien, D.F. Bersier,
M.F. Bode, D. Carter, C. Guidorzi, J.E. Hill, C.P. Hurkett, S. Kobayashi,
A. Monfardini, C.J. Mottram, R.J. Smith, R.A.M.J. Wijers & R. Willingale
Astronomy & Astrophysics 467, 1049 (2007)

Abstract We present our analysis of the multiwavelength photometric & spectroscopic observations of GRB 060210 and discuss the results in the overall context of current GRB models. All available optical data underwent a simultaneous temporal fit, while X-ray and γ-ray observations were analysed temporally & spectrally. The results were compared to each other and to possible GRB models. The X-ray afterglow is best described by a smoothly broken power-law with a break at 7.4 hours. The late optical afterglow has a well constrained single power-law index which has a value between the two X-ray indices, though it does agree with a single power-law fit to the X-ray. An evolution of the hardness of the high-energy emission is demonstrated and we imply a minimum host extinction from a comparison of the extrapolated X-ray flux to that measured in the optical. We find that the flaring γ-ray and X-ray emission is likely due to internal shocks while the flat optical light curve at that time is due to the external shock. The late afterglow is best explained by a cooling break between the optical and X-rays and continued central engine activity up to the time of the break. The required collimation corrected energy of $\sim 2 \times 10^{52}$ erg, while at the high end of the known energy distribution, is not unprecedented.

8.1 Introduction

Since the launch of the *Swift* satellite (Gehrels et al. 2004) we have been allowed observations of Gamma Ray Bursts (GRBs) at very early times, occasionally observing in X-rays and optical light even as the prompt γ-ray emission is ongoing. Gradually, evidence has emerged for a fairly canonical behaviour of γ-ray and X-ray light curves in which the X-rays decay fairly rapidly after the prompt emission and then decay more slowly for a while before becoming steeper again (Nousek et al. 2006). This behaviour is seen in many of the bursts, but a significant minority decay more gradually from early times. These differences may be due to the different relative strengths of emission components due to internal and external processes (O'Brien et al. 2006). Similar complexity is seen in the optical, where some bursts show optical behaviour which does not exactly mimic the X-ray, again suggesting a contribution from several emission components. Here we present multiwavelength observations of GRB 060210, covering the early to late-time emission and compare the data to the expected canonical behaviour and the blast wave afterglow model (e.g. Zhang & Mészáros (2004)).

GRB 060210 is a long burst, detected by the Burst Alert Telescope (BAT) on board *Swift* (Barthelmy et al. 2005) on February 10th, 2006 at 04:58:50 UT. The X-Ray Telescope (XRT; Burrows et al. (2005)), which started observing the region 95 seconds after the BAT trigger, identified the X-ray counterpart position to within an error of $5.4''$ (Beardmore et al. 2006). While the Ultraviolet/Optical Telescope (UVOT; Roming et al. (2005)) was unable to identify an optical counterpart, the robotic Palomar 60" telescope observed the R-band counterpart at approximately 5.5 min post trigger (Fox & Cenko 2006). The redshift was estimated as $z = 3.91$ (Cucchiara et al. 2006) and a host galaxy has been proposed based on near infrared observations (Hearty et al. 2006). No radio emission has been observed down to a 3σ limit of $72\,\mu$Jy at 8.64 GHz (Frail 2006).

In this paper we present our multi-wavelength analysis of the burst from γ-ray, through X-ray to optical wavelengths. Throughout, we use the convention that a power-law flux is given as $F_\nu \propto t^{-\alpha}\nu^{-\beta}$ where α is the temporal decay index and β is the spectral index. The power-law of spectra is given as $\mathrm{d}N/\mathrm{d}E \propto E^{-\Gamma}$ where Γ is the photon index and is related to spectral index as $\Gamma = \beta + 1$. In §8.2 we introduce our observations and reduction methods of each wavelength regime. In §8.3 we present the results of our spectral and temporal analysis, while in §8.4 we discuss these results in the overall context of the burst.

8.2 Observations

8.2.1 γ-ray

The *Swift*-BAT triggered and localised GRB 060210 at T_0 = 04:58:50 UT and promptly distributed the coordinates via the Gamma-ray burst Coordinates Network (GCN). Data for the burst were obtained in event mode, covering $T_0 - 300$ s to $T_0 + 300$ s, giving spectral coverage from 15 – 350 keV and time resolution of 64 ms.

BAT event data were reduced and analysed within FTOOLS v6.0.4. Light Curves and spectra were extracted by the standard methods, and standard corrections applied (O'Brien et al. 2006). From the light curve (figure 8.1) the main period of activity is identified as being from $T_0 - 75$ s to $T_0 + 20$ s with the brightest peak at T_0. However significant emission was recorded from T_0 – 230 s to the last peak at T_0 + 200 s, which represents a significant fraction of the total recorded event data. The T_{90} in the BAT range (15-350 keV) is calculated as 220 ± 70 s, covering the period from $\sim T_0$ – 149 s to $\sim T_0$ + 70 s.

8.2.2 X-ray

The XRT started observing at 05:00:25 UT, 95 seconds after the initial BAT trigger, and found an uncatalogued, variable X-ray source which was identified as the afterglow. XRT observed up to March 3, or approximately 2×10^6 seconds post-burst, by which time only an upper limit detection was obtainable from the data. Data were initially collected in Windowed Timing (WT) mode (Hill et al. 2004, 2005), which gives no positional information but high temporal resolution. After the initial $\sim$ 500 s of WT mode, data were collected in Photon Counting (PC) mode.

The XRT data were initially processed with the FTOOL, `xrtpipeline` (v0.9.9) with `wtbiasdiff` applied to correct for potential WT bias-row subtraction problems, caused by bright Earth or CCD temperature variations. Background subtracted 0.3-10keV light curves were extracted from the cleaned event lists with a minimum of 20 counts/bin. Likewise, source and background spectra were extracted for analysis with `Xspec`. The first orbit of PC mode data were corrected for pile-up as detailed in Vaughan et al. (2006). A correction was also made, using `xrtexpomap`, for fractional exposure loss due to bad columns on the CCD, which arose after damage caused by a micrometeroid strike (Abbey et al. 2006).

Spectral fits are used to convert count rates of both WT & PC mode data to fluxes, and to extrapolate the BAT light curve to the XRT energy range (O'Brien

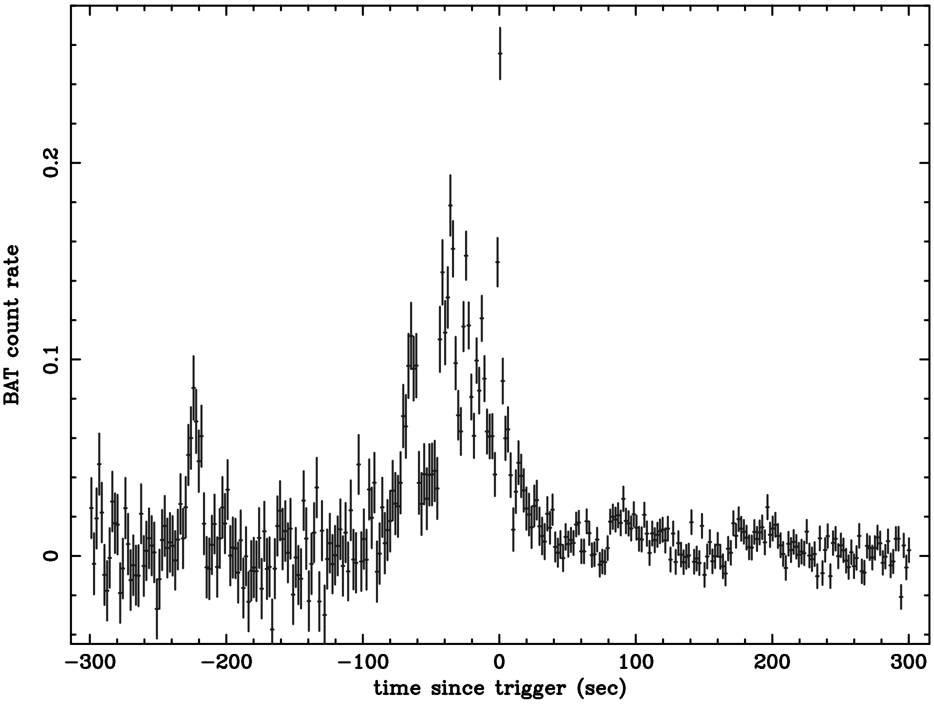

Figure 8.1 — Full BAT light curve (15 – 350 keV) of GRB 060210, clearly showing the main peak and post-trigger activity, as well as the pre-trigger activity at $\sim T_0 - 230$ s.

et al. (2006); figure 8.2). Initial analysis of the early time part of this light curve shows two strong flares at ~200 s and ~380 s, after an initial decay that seems to be a continuation of a flare at ~100 s as observed in γ-rays.

8.2.3 Optical

Optical observations in B, R and i′ bands were obtained by the robotic, 2.0 m Faulkes Telescope North (FTN) at Haleakala on Maui, Hawaii; FTN is the sister instrument of The Liverpool Telescope (Guidorzi et al. 2006). At 05:04:36 UT, approximately 5.8 min post-burst, the telescope triggered its automatic 1 hour-sequence and to ensure good time coverage of the light curve, a second 1 hour sequence was manually triggered at 06:05:27 UT, 66 min post-burst. The previously reported optical transient (Fox & Cenko 2006) was clearly visible in R and i′ but not in B (Table 8.1). This is not unexpected, as the high redshift of the burst and the associated extinction due the Lyman forest causes significant dimming in the B-band while i′ remains unaffected.

Table 8.1 — FTN optical observations of GRB 060210 calibrated to the Cousins photometric system, uncorrected for Galactic extinction of $E_{(B-V)}$ = 0.093. Magnitude errors are at 1σ level.

$T_{\rm mid} - T_0$ (min)	$T_{\rm exp}$ (min)	Band	Mag
65.58	31.33	B	22.10[a]
5.85	0.1667	R	18.50 ± 0.20
6.20	0.1667	R	18.36 ± 0.15
6.55	0.1667	R	18.36 ± 0.15
11.85	0.5	R	18.51 ± 0.12
16.35	1.0	R	18.87 ± 0.10
23.20	2.0	R	19.43 ± 0.10
33.04	3.0	R	19.74 ± 0.10
43.25	2.0	R	20.14 ± 0.15
53.18	3.0	R	19.98 ± 0.15
72.00	2.0	R	20.57 ± 0.20
88.84	5.0	R	20.8 ± 0.4
115.26	9.0	R	21.2 ± 0.3
167.0	30.0	R	22.4 ± 0.5
9.43	0.1667	I	16.94 ± 0.08
13.19	0.5	I	17.20 ± 0.05
18.11	1.0	I	17.66 ± 0.05
25.95	2.0	I	18.25 ± 0.06
36.98	3.0	I	18.56 ± 0.06
46.00	2.0	I	18.80 ± 0.08
57.10	3.0	I	19.18 ± 0.08
70.12	0.1667	I	19.35 ± 0.25
73.73	0.5	I	19.43 ± 0.20
78.73	1.0	I	19.55 ± 0.20
86.41	2.0	I	19.85 ± 0.30
97.26	3.0	I	20.0 ± 0.3
106.13	2.0	I	20.2 ± 0.3
116.97	3.0	I	20.3 ± 0.3

[a] 3σ upper limit

The data were analysed using the IRAF package[1], wherein reduction & differential photometry were carried out. Landolt photometric standards taken on the night were used to calibrate the magnitude of the optical counterpart. The i′ magnitudes were converted to the corresponding I-band magnitudes using the observed filter transformations of Smith et al. (2002), which for normal colours are in agreement with those of Fukugita et al. (1996). The magnitudes are uncorrected for Galactic extinction of $E_{(B-V)} = 0.093$ (Schlegel et al. 1998). Astrometric calibration was carried out with respect to the NOMAD catalogue[2] to refine the position of the burst to within 0.2″ to be 03:50:57.36, +27:01:34.4 (J2000).

8.3 Results

We have split our discussion of the emission into two phases, covering what we refer to as the *early emission* and the *late afterglow*. We take the early emission as being the γ-ray and the flaring X-ray emission at times $\lesssim 600$ seconds, which follows from the X-ray light curve (figure 8.2). We also include up to ~ 600 seconds of optical observations, those not displaying a power-law decay, as being early emission. The late afterglow, we take as the smooth X-ray and optical light curves, obeying power-law decay. All uncertainties of light curve analysis, spectral fits and other are quoted at the 90% confidence level.

8.3.1 Early high-energy emission

The prompt emission as measured by BAT shows a main peak which decays smoothly until ~10 s (figure 8.2). From ~10 s to ~600 s, GRB 060210 is observed to display flaring in both the γ-rays and X-rays. One flare, at ~100 s, is observed by both BAT & XRT. This flaring behaviour seems to be superimposed on an underlying power-law decay due to the afterglow. The time-averaged BAT spectrum (15 – 150 keV) over T_{90} was fit with an unabsorbed power-law in `Xspec` and a photon index, $\Gamma = 1.55 \pm 0.09$ was found ($\chi^2_\nu = 0.84$, 56 d.o.f.). This spectral fit corresponds to a fluence of $(6.0^{+0.1}_{-0.7}) \times 10^{-6}$ erg cm^{-2}.

When the XRT WT-mode spectrum, from 103 s – 614 s is fit with an absorbed power-law, we find a photon index of $\Gamma = 2.09 \pm 0.04$ and a column density of $N_{\rm H} = (16 \pm 1) \times 10^{20}$ cm^{-2} ($\chi^2_\nu = 1.020$, 316 d.o.f.). This is significantly

---

[1] IRAF is distributed by the National Optical Astronomy Observatories, which are operated by the Association of Universities for Research in Astronomy, Inc., under cooperative agreement with the National Science Foundation.

[2] http://www.nofs.navy.mil/nomad/

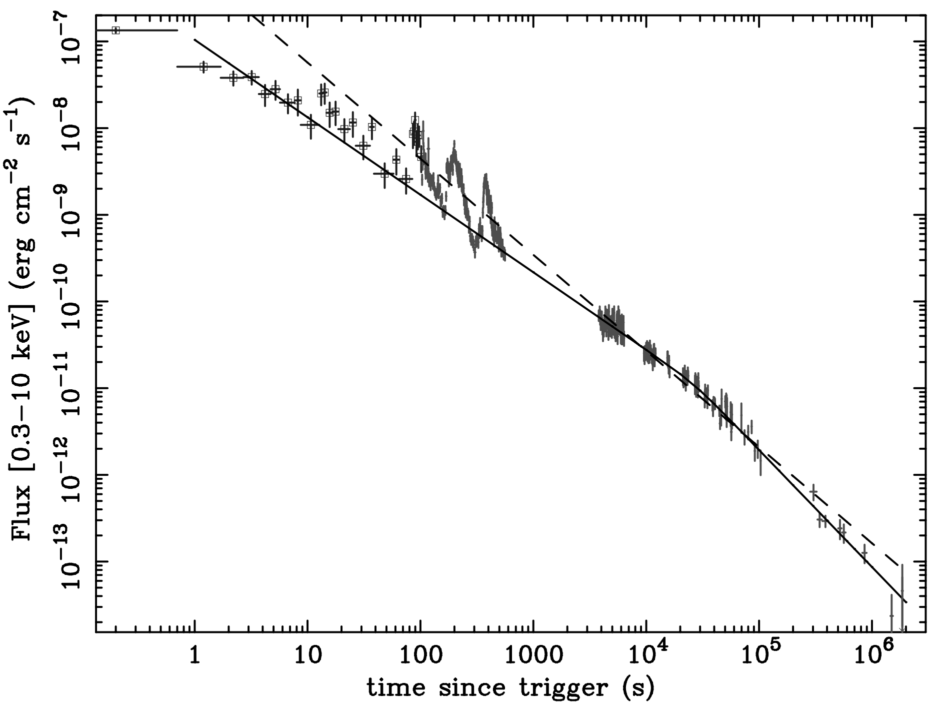

Figure 8.2 — High-energy light curve of GRB 060210 composed of the XRT data (after $\sim 10^2$ seconds) and the BAT data (up to $\sim 10^2$ seconds) extrapolated to the XRT energy range. The dashed line shows a single power-law fit to the late afterglow with $\alpha = 1.11 \pm 0.02$, but the solid line showing a smoothly broken power-law with indices $\alpha_1 = 0.89 \pm 0.05$ & $\alpha_2 = 1.35 \pm 0.06$ is a significantly better fit.

higher than the Galactic value of $N_{\rm H} = 8.5 \times 10^{20}\,{\rm cm}^{-2}$ (Dickey & Lockman 1990). This excess extinction may be explained either by rest frame extinction or by a broken power-law. Fitting an absorbed broken power-law gives a column density consistent with that of the Galactic value, so we fix the parameter to be the Galactic value. This leads to a photon index of $\Gamma = 1.96 \pm 0.03$ above a break energy, $E_{\rm break} = 0.71 \pm 0.07$ keV and an index of $\Gamma = 0.6 \pm 0.3$ ($\chi^2_\nu = 0.923$, 315 d.o.f.) below the break. Alternatively, assuming solar abundances, a rest frame column density of $N_{\rm H} = (2.3 \pm 0.3) \times 10^{22}\,{\rm cm}^{-2}$ in combination with the Galactic value gives an equally good fit ($\chi^2_\nu = 0.936$, 316 d.o.f.) and implies a photon index, $\Gamma = 2.03 \pm 0.03$. Assuming LMC and SMC abundances (Pei 1992) in the host implies $N_{\rm H} = (5.7 \pm 0.7) \times 10^{22}\,{\rm cm}^{-2}$ ($\chi^2_\nu = 0.948$, 316 d.o.f.) and $N_{\rm H} = (10.3 \pm 1.2) \times 10^{22}\,{\rm cm}^{-2}$ ($\chi^2_\nu = 0.950$, 316 d.o.f.) respectively, while leaving the photon index unchanged within uncertainties.Though it is not possible to favour one model over the other, we see that the photon index, $\Gamma \sim 2.0$ is marginally

Table 8.2 — Rest frame column densities as found in combination with Galactic extinction.

	N_H ($\times 10^{22}$ cm^{-2})
SMC	10.3 ± 1.2
LMC	5.7 ± 0.7
Galactic	2.3 ± 0.3

different to that of the earlier γ-ray spectrum. A hardness ratio (1-10 keV/0.3-1 keV) plot of the X-ray emission (figure 8.3) confirms spectral evolution, though the γ-rays are too faint to obtain a similar plot. This evolution is similar to that observed in the γ-rays for a number of BATSE bursts (Bhat et al. 1994).

Using the average photon index of the BAT & XRT spectra, we get a conversion from BAT count rate to unabsorbed flux in the 0.3 – 10 keV range of 4.38×10^{-7} erg cm^{-2} cts^{-1}. Using the same fit of the XRT spectrum, yields a conversion of 4.83×10^{-11} erg cm^{-2} cts^{-1} which we apply to the WT mode data.

8.3.2 Late X-ray afterglow

The late X-ray afterglow was observed from ~1 hour to ~23 days, at which stage only an upper limit determination was possible. The light curve for this period is quite smooth, with no obvious signs of flares or bumps, and a hardness ratio plot of the afterglow shows no signs of evolution. The spectrum gives results comparable with the prompt spectrum (§8.3.1), including an excess extinction over that of the Galactic value. A broken power-law with Galactic absorption suggests a photon index of $\Gamma = 2.13 \pm 0.06$ above a break at $E_{\rm break} = 1.04 \pm 0.15$ keV and an index of $\Gamma = 1.4 \pm 0.2$ ($\chi^2_\nu = 1.021$, 225 d.o.f.) below the break. Assuming a single power-law with Galactic absorption, the rest frame absorption assuming solar abundances is consistent with that found during the prompt emission and hence is fixed at that value. The photon index is then $\Gamma = 2.14 \pm 0.03$ ($\chi^2_\nu = 1.015$, 227 d.o.f.). It is not possible to favour one model over the other but we can assume a corresponding spectral index, $\beta = 1.14 \pm 0.03$, at least at energies $\gtrsim 1.0$ keV. Using the single power-law fit with rest frame absorption yields a PC mode, count rate to flux conversion of 5.12×10^{-11} erg cm^{-2} cts^{-1}.

Fitting a power-law to the temporal decay we find $\alpha = 1.11 \pm 0.02$ ($\chi^2_\nu = 1.69$, 144 d.o.f.), though an F-Test shows that a smoothly broken power-law with $\alpha_1 = 0.89 \pm 0.05$, $\alpha_2 = 1.35 \pm 0.06$ and a break at $t_{\rm break} = 7.4^{+2.1}_{-1.6}$ hr ($\chi^2_\nu = 0.954$, 142 d.o.f.) is a significantly better fit, in agreement with the analysis of Dai & Stanek

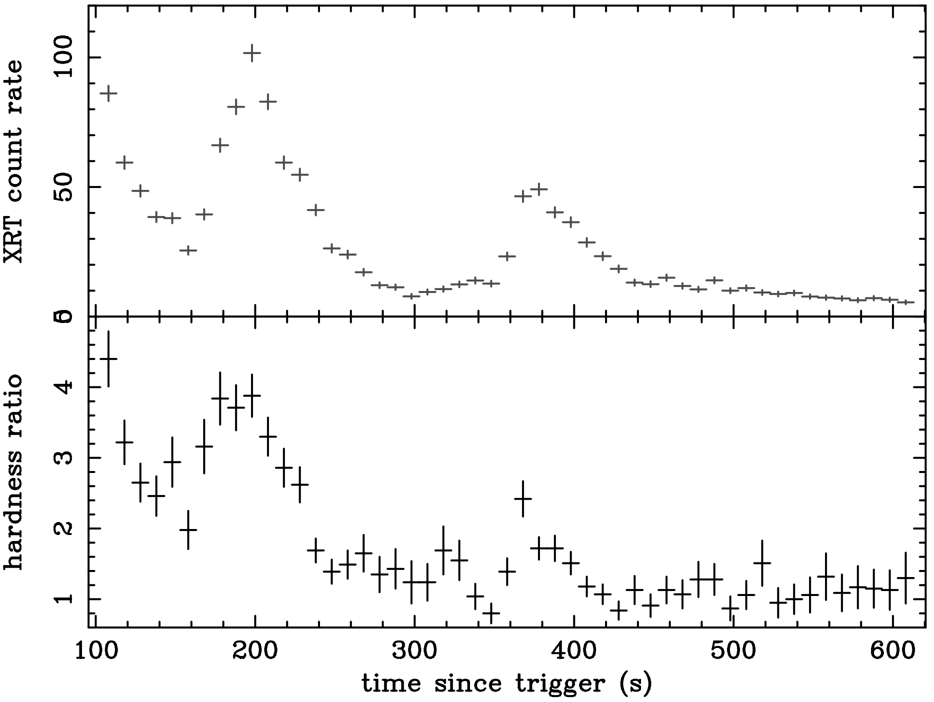

Figure 8.3 — *(top)* Light Curve of the Windowed Timing mode data of GRB 060210 and *(bottom)* the hardness ratio (1-10 keV/0.3-1 keV) plot which clearly displays an evolution coupled to the count rate.

(2006). Extrapolating the power-law fit to early times, we see that it does not match the early emission, which implies a break at $\sim 10^3$ s. Doing likewise for the broken power-law fit, we see that it matches quite well with the troughs of the flares and the extrapolated BAT emission (figure 8.2). To investigate any possible spectral difference, we split the spectrum into pre- and post-break sections but the resultant fits were consistent with each other and the combined fit. This implies that any difference in spectral indices must be smaller than the errors, $\delta\beta \lesssim 0.05$.

8.3.3 Optical emission

Fitting our optical light curves of the late afterglow ($T \gtrsim 500$ s) with a single power-law, we find $\alpha_{\mathrm{R}} = 1.07 \pm 0.11$ ($\chi^2_\nu = 1.07$) and $\alpha_{\mathrm{I}} = 1.19 \pm 0.05$ ($\chi^2_\nu = 0.86$). To make full use of the available data we simultaneously fit our data and previously publised data, at times > 540 s, over 5 bands: FTN R, FTN I, MDM R, KAIT I, & KAIT unfiltered (Li (2006); Stanek et al. (2007)). To do this we assume that each has the same temporal decay but we make no assumptions regarding the relative offsets – thus eliminating any error in absolute magnitude estimates. This fit uses the *simulated annealing* method (§ 10.9 of Press et al. (1992), and references therein) to minimise the combined χ^2 of the data sets and hence find the best fit parameters, while a Monte Carlo analysis with synthetic data sets is carried out to estimate the errors. From this we find an optical temporal decay, $\alpha_{\rm opt} = 1.15 \pm 0.04$ ($\chi^2_\nu = 1.12$, 38 d.o.f.) and magnitude offsets, which are the model magnitudes evaluated at 1 second, as detailed in table 8.3. This decay is shallower than the $\alpha \sim 1.3$ found by Stanek et al. (2007).

Table 8.3 — Simultaneous temporal fit of optical data, where Mag is the model magnitude evaluated at 1 second. The common temporal decay index, $\alpha_{\rm opt}$ is fit as 1.15 ± 0.04.

Band	Mag
FTN R	10.22 ± 0.34
FTN I	8.92 ± 0.30
KAIT I	9.28 ± 0.30
KAIT unfiltered	9.81 ± 0.30
MDM R	10.11 ± 0.34

Shifting all the data to the FTN R magnitude offset confirms that there is no structure above noise in the optical light curve (figure 8.4). It is possible that the light curve is breaking at $\sim$ 5000 seconds, but there are not enough data to support this. Fitting a smoothly broken power-law with three indices to this shifted data, we find that the two break times are at 310 ± 8 s and 540 ± 6 s and the indices are $\alpha_1 = 0.10 \pm 0.10$, $\alpha_2 = -0.90 \pm 0.35$, $\alpha_3 = 1.175 \pm 0.016$ ($\chi^2_\nu = 0.89$, 47 d.o.f.).

8.4 Discussion

It has been claimed (Stanek et al. 2007) that this burst closely resembles GRB 050801 (Rykoff et al. 2006) which is true insofar as both display an initially flat optical light curve. However GRB 060210 displays a peak before decaying as a power-law, while GRB 050801 shows no such peak. Furthermore, the X-ray behaviour of GRB 050801 seems to be consistent with the optical, but in GRB 060210 they seem to be unconnected. This suggests that in GRB 050801 the X-ray and optical emission is originating in the same region, while this is not true for GRB 060210. In the case of GRB 060210 the early flaring X-ray & γ-ray emission implies internal shocks, indicative of prolonged engine activity

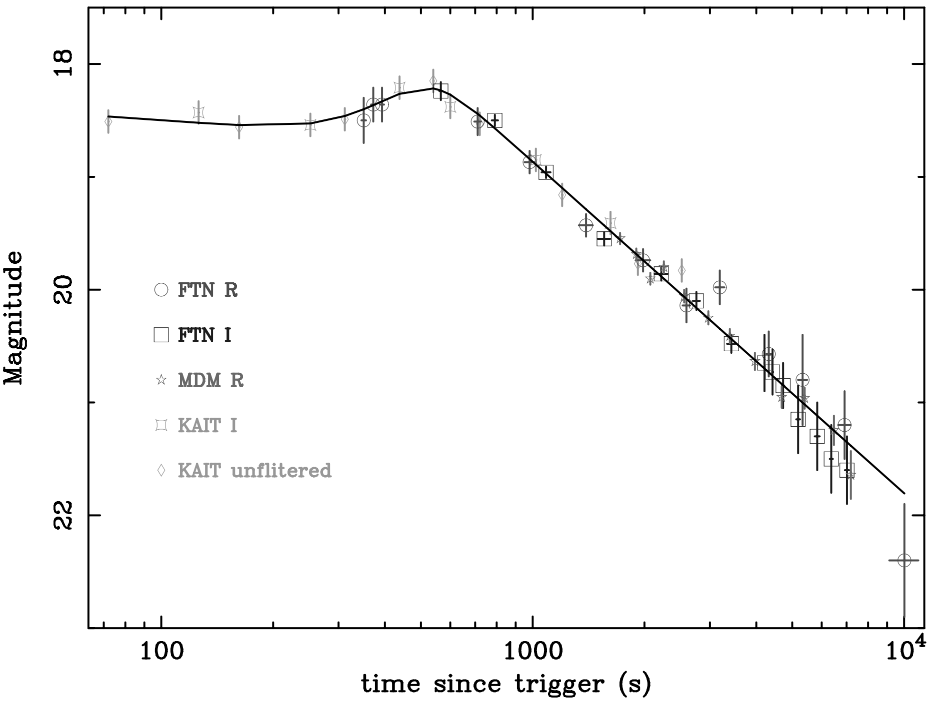

Figure 8.4 — Faulkes Telescope North R and I band light curves, supplemented by previously published data, shifted to the FTN R-band offset. Fit shown is a 3-index smoothly broken power-law.

(King et al. 2005). The optical emission, on the other hand, is consistent with an external shock afterglow.

8.4.1 X-ray flares

The spectral evolution exhibited in the hardness ratio plot (figure 8.3) supports internal shocks as the source of the flaring X-ray emission as suggested for GRB 050607 by Pagani et al. (2006). Though in this case the spectral index of the flaring period is similar to that of the late afterglow, the afterglow is softer, following the trend exhibited by the hardness ratio plot. It should be noted also, that the spectral index of the flaring period is an average over that period. The difference between the two values and the lack of spectral evolution in the late afterglow certainly suggests two distinct origins for energy emission. Combined with the overlap of the last γ-ray and first X-ray flare, it seems likely that these two would share internal shocks as the common emission mechanism.

Liang et al. (2006) show that X-ray flares can be modeled by the curvature effect (Kumar & Panaitescu 2000) which causes a decay of $F \propto (t - t_{\rm ej})^{-(2+\beta)}$ superimposed on the regular afterglow decay of $F \propto t^{-\alpha}$, where $t_{\rm ej}$ is the energy injection time of that flare. We tested the flaring X-ray data against the curvature effect, using the average spectral index over that period and find ejection times for the 3 main X-ray flares at ~ 100 s, 200 s & 380 s of 72 ± 6 s, 155 ± 16 s & 310 ± 16 s respectively. These are consistent with Liang et al. (2006) – insofar as the energy ejection times are at the the start of the rising segment of the flare – supporting the claim that the flares are indeed due to internal shocks.

8.4.2 Spectral indices & host extinction

From the fitted flux of the FTN optical data points at 5000 s, corrected for galactic extinction and extinction due to Lyman absorption (Madau 1995), we find an optical spectral index of $\beta_{\rm opt} = 3.1 \pm 0.4$. Converting the X-ray flux at the same time to mJy using the X-ray spectral index $\beta_{\rm X} = 1.14$, gives a flux $F_{1.732\,{\rm keV}} = 3.27 \times 10^{-3}$ mJy. These fluxes correspond to an optical to X-ray spectral index, $\beta_{\rm opt-X} = 0.3 \pm 0.1$, confirming the optical to X-ray flux ratio of $F_{\nu,{\rm opt}}/F_{\nu,{\rm X}} \sim 10$ of Stanek et al. (2007).

The large differences between $\beta_{\rm opt}$, $\beta_{\rm X}$ and $\beta_{\rm opt-X}$ imply that there could be an amount of host extinction that we have failed to take into account. To estimate this host extinction, we extrapolate the X-ray flux to optical magnitudes to measure the optical extinction, $A_{\nu(1+z)}$ above that of Galactic. From this we can calculate the corresponding value of $E_{\rm B-V}$ assuming SMC, LMC and Galactic extinction curves (Pei 1992) in the host galaxy (Table 8.4). We do this in the limits that the cooling break is below the optical ($\beta_{\rm opt-X} = \beta_{\rm X} = 1.14$) and that the cooling break is far above the optical but below the X-ray region ($\beta_{\rm opt-X} = \beta_{\rm X} - 0.5 = 0.64$ below 10^{17} Hz; Zhang & Mészáros (2004)). The R & I band values of $E_{\rm B-V}$ are consistent with each other at the 2σ level in all cases, so one case cannot be favoured over the other. In the limit where the cooling break is just below the X-ray region, we have lower limits on the host extinction.

Using the host column densities found for the various extinction curves (Table 8.2) we calculate the ratio of column density to optical extinction ($N_{\rm H}/E_{\rm B-V}$, Table 8.4) in the host and compare to the values of the SMC, LMC and Galaxy (Pei 1992). The expected ratios are 4.5, 2.4 & 0.48 $\times 10^{22}\,{\rm cm}^{-2}$ respectively, clearly well below the measured values. This is in agreement with previous work (Galama & Wijers 2001) suggesting dust destruction in the circumburst environment.

Table 8.4 — Host extinction and column density to extinction ratio assuming SMC, LMC & Galactic extinction curves in the host as discussed in §8.4.2. In the case where $\nu < \nu_c$, $\nu_c = 10^{17}$ Hz.

			SMC		LMC		Galactic	
	Band	$A_{\nu(1+z)}$	E_{B-V}	N_H/E_{B-V} $\times 10^{22}$ cm^{-2}	E_{B-V}	N_H/E_{B-V} $\times 10^{22}$ cm^{-2}	E_{B-V}	N_H/E_{B-V} $\times 10^{22}$ cm^{-2}
$\nu_c < \nu$	R	6.7 ± 0.6	0.45 ± 0.04	23 ± 5	0.55 ± 0.05	10 ± 2	0.78 ± 0.08	2.9 ± 0.7
	I	6.1 ± 0.6	0.57 ± 0.06	18 ± 4	0.65 ± 0.06	9 ± 2	0.81 ± 0.08	2.8 ± 0.7
$\nu < \nu_c$	R	3.9 ± 0.7	0.26 ± 0.04	40 ± 10	0.32 ± 0.05	18 ± 5	0.45 ± 0.08	5.0 ± 1.6
	I	3.0 ± 0.7	0.28 ± 0.06	37 ± 12	0.32 ± 0.07	18 ± 6	0.40 ± 0.09	5.8 ± 2.0

8.4.3 Early optical emission

Stanek et al. (2007) suggest that the optical peak at $\sim$ 540 s is the onset of the external shock – i.e. the deceleration time, when the jet has swept up enough of the circumburst medium so that the afterglow dominates emission – however if this was the case we would expect the X-ray to exhibit a peak at the same time. While the X-ray light curve at that time is highly obscured by flares, it does seem that the flares are superimposed on the already decaying X-ray afterglow.

Since early time data has become more common due to the rapid dissemination of burst information from *Swift*, there has been much discussion regarding the reference time, t_0, for the onset of the power-law decay of the afterglow. Most commonly it is taken as the trigger time T_0 of the instrument which detected the burst, which is clearly instrument dependent. We expect that the light curve will evolve as $F \propto (t - t_0)^{-\alpha}$, and that it will exhibit a break if it has been assigned the incorrect reference time (Quimby et al. 2006).

To test whether this is a plausible scenario, we fit the optical light curve at times $\gtrsim 540$ s letting t_0 as a free parameter. The best fit of this suggests that reference time is in fact the trigger time of the burst but since the χ^2 function is very flat in that region ($T \ll 500$ s), a definite minimum is difficult to estimate. This is in agreement with the theoretical prediction of Kobayashi & Zhang (2007) who claim that the reference time should be taken as T_0. The X-ray slope, which is at later times, is unaffected by changes in the reference time much less than the start time of the observations.

If the deceleration time is, as we claim, close to the trigger time, the flat optical light curve from 70 s – 310 s is then likely due to external shock. The blast wave model (Zhang & Mészáros 2004) in a slow-cooling wind-driven medium predicts a temporal slope $\alpha_{\rm opt} = 0$, in agreement with the observations ($\alpha_{\rm opt} = 0.10 \pm 0.10$), for all values of p if $\nu < \nu_{\rm m} < \nu_{\rm c}$ where $\nu_{\rm m}$ is the peak frequency.

We suggest that the rebrightening of $\alpha_{\rm opt} = -0.9$ in the optical light curve after 310 seconds could be explained by the change from a wind-driven medium to one of a higher, constant density as detailed by Pe'er & Wijers (2006). If, as expected, the progenitor of this burst is a massive star, the circumburst medium is composed of the wind from the star moving into the ISM. This causes a forward shock into the ISM and a reverse shock into the wind, separated by a region of shocked wind with a constant density profile. When the blast wave crosses the reverse shock - shocked wind discontinuity, there is a drop in the cooling frequency. This may shift the optical out of the $\nu < \nu_{\rm m} < \nu_{\rm c}$ regime into either $\nu < \nu_{\rm c} < \nu_{\rm m}$ or $\nu_{\rm c} < \nu < \nu_{\rm m}$. If this is matched by the standard evolution of the peak frequency, the optical may end up in the $\nu_{\rm m} < \nu < \nu_{\rm c}$ or $\nu_{\rm m,c} < \nu$ regime. The shocked wind has a higher density than the unshocked wind, necessitating

Table 8.5 — Observed late afterglow temporal decays. The possible X-ray break is at $7.4^{+2.1}_{-1.6}$ hr.

X-ray (power-law)	1.11 ± 0.02
X-ray (pre-break)	0.89 ± 0.05
X-ray (post-break)	1.35 ± 0.06
Optical	1.154 ± 0.013

a flux increase, causing the observed rebrightening. However, as we shall show in §8.4.5, the fine tuning of the energetics and circumburst medium parameters make this explanation of the rebrightening less likely.

8.4.4 Late afterglow

The X-ray spectral index of the late afterglow, $\beta = 1.14 \pm 0.03$ (§8.3.2), implies an electron power-law index, $p = 2.28 \pm 0.06$, assuming that the cooling and peak frequencies are below the X-rays (Zhang & Mészáros 2004). If the observed X-ray break was a jet break, we would expect the temporal index after the break to be $\alpha_X = p = 2.28$ which is inconsistent with the observed decay of $\alpha = 1.35$. This, in conjunction with the early time of the break ($1.5^{+0.4}_{-0.3}$ hr in the rest frame of the GRB), makes a jet break highly unlikely. In the absence of a jet break, the electron power-law index, p, implies an X-ray temporal decay index of $\alpha_X = 1.21 \pm 0.05$ in all media, which is not consistent with either of the broken power-law indices (Table 8.5). It could however, be in agreement with the single power-law.

Assuming that the optical is in the same frequency regime as the X-rays i.e. above the cooling and peak frequencies, the expected optical temporal decay and spectral indices are predicted to be the same as the X-ray indices, $\alpha_X = \alpha_{\rm opt} = 1.21, \beta_X = \beta_{\rm opt} = 1.14$. This temporal decay index is in agreement with the observed value of $\alpha_{\rm opt} = 1.15 \pm 0.04$ and consistent with the spectral index assuming host extinction. If the optical is not in the high-frequency regime, i.e. above either the cooling or peak frequencies, we can rule out a fast cooling regime ($\nu_c < \nu < \nu_m$) as that would imply $\alpha = 0.25$, which is clearly an underestimate. A slow cooling regime ($\nu_m < \nu < \nu_c$) implies a decay of $\alpha = 0.96 \pm 0.05$ in a homogeneous circumburst medium or one of $\alpha = 1.46 \pm 0.05$ in a wind driven medium, each with a spectral index of $\beta = 0.64 \pm 0.06$.

8.4.5 Blast wave energetics and circumburst medium

From the measured quantaties we can constrain various physical parameters of the relativistic blast wave and its surroundings; the jet opening angle, the energy of the blast wave, the density and structure of the circumburst medium, the energy in the magnetic field and the relativistic electrons that emit the synchrotron radiation. In order to obtain these constraints we use the formulas from Van der Horst, Wijers & Van den Horn (submitted to A&A), while adopting $p = 2.28$ and a luminosity distance $d_L = 7.97 \times 10^{28}$ cm ($\Omega_M = 0.27$, $\Omega_\Lambda = 0.73$, $H_0 = 71\,\mathrm{km\,s^{-1}\,Mpc^{-1}}$).

Since the temporal behaviour of ν_m, ν_c and the peak flux $F_{\nu,\mathrm{max}}$ depends on the structure of the circumburst medium, we derive constraints on the physical parameters in two cases: a homogeneous medium, in which the density is constant, and a stellar wind, in which the density as a function of radius is a power-law with index $k = -2$. In the homogeneous case $F_{\nu,\mathrm{max}}$ is constant, and ν_m and ν_c are decaying power-laws in time, which gives the constraints: $F_{\nu,\mathrm{max}} > F_{\nu_I}$, $\nu_m < \nu_I$ and $\nu_c < \nu_I$, all at 600 seconds. A fourth constraint comes from the measured I-band flux at 600 seconds, corrected for galactic and host extinction, $F_{\nu_I} = 150$ mJy. In the stellar wind case three of the four constraints are the same, except for ν_c, because its value increases in time; this means that $\nu_c < \nu_I$ at 7×10^3 seconds.

The limits on the isotropic equivalent energy we derive are lower limits of 5×10^{54} erg for the homogeneous medium and 2×10^{55} erg for the stellar wind. Since these limits are quite large, we assume that the energies are not much larger. This results in values for the fractional energies in electrons and magnetic field of $\varepsilon_e \sim \varepsilon_B \sim 10^{-2}$ (homogeneous) and $\varepsilon_e \sim \varepsilon_B \sim 5 \times 10^{-3}$ (wind). The density of the homogeneous medium is then $\sim 10\,\mathrm{cm^{-3}}$, while the wind density parameter $A_* \sim 1$, i.e. a mass-loss rate of 10^{-5} solar masses per year and a wind velocity of $10^3\,\mathrm{km\,s^{-1}}$. With these numbers and the lower limit on the jet break time of $\sim 10^6$ s we derive a lower limit on the jet opening angle of 8°(homogeneous) or 2°(wind), resulting in collimation corrected energies of 5×10^{52} and 1×10^{52} erg respectively. These energies are quite large, but not impossible, especially if you consider that the early optical emission could be due to sustained energy injection by the progenitor, providing even more energy for the blast wave than there was for the prompt emission. Furthermore, we note that a blast wave at this redshift and suffering significant host extinction has to be very energetic to produce the observed fluxes.

We have suggested that the early optical behaviour could be explained by the transition from a massive stellar wind to a homogeneous medium. To get the correct temporal slopes this implies that $\nu_I < \nu_m < \nu_c$ from 70 – 310 s, and $\nu_{\rm m,c} < \nu_{\rm I}$ after 540 s. This requires some fine-tuning of the parameters, in particular $\nu_{\rm c}$ has to decrease significantly because of the density jump, and at the same time $\nu_{\rm m}$ has to pass through the I band, since the peak frequency does not depend on the density and only mildly on the density structure. The isotropic equivalent energy that one derives in this case is even higher than before, namely 6×10^{55} erg, while $\varepsilon_{\rm e} \sim 4 \times 10^{-3}$ and $\varepsilon_{\rm B} \sim 3 \times 10^{-3}$. The density of the homogeneous medium is again $\sim 10\,{\rm cm}^{-3}$, but $A_* \sim 0.15$ in this case. From these parameters we get a lower limit for the jet opening angle of 6° and a collimation corrected energy of 3×10^{53} erg. This value for the energy is very high and difficult to accommodate within current progenitor models, making the transition from a wind to a homogeneous medium a less likely explanation for the early optical emission.

We note that with these physical parameters the synchrotron self-absorption frequency, $\nu_{\rm a}$, lies well above 8.64 GHz at 3.95 days when the 3σ limit was obtained by Frail (2006). The radio limit is hence consistent with both a homogeneous and wind-driven circumburst medium.

8.4.6 Energy injection

Although the X-ray light curve is best fit with a broken power-law, it is difficult to accommodate the temporal slopes within our current afterglow models. The pre-break slope is shallower than the simultaneous optical slope, which is only possible if the circumburst medium is a stellar wind and $\nu_{\rm m} < \nu_{\rm opt} < \nu_{\rm c} < \nu_{\rm X}$. This would imply that the optical slope should be $\alpha_{\rm opt} = 1.46$ and that the X-ray slope $\alpha_{\rm X} = 1.21$, which is much higher than the observed pre-break values. Continued energy injection from the central engine (Nousek et al. 2006) would cause this slope to be shallower for the period of injection before reverting to the original value. For the optical temporal slope this means that the energy has to increase as $t^{0.37\pm0.07}$, while the pre-break X-ray slope indicates $t^{0.30\pm0.08}$. The break in the X-ray light curve at ~ 7.4 hr is then the end of the energy injection phase. The post-break X-ray temporal slope is consistent with the spectral slope at a 2σ level for $\nu_{\rm m,c} < \nu_{\rm X}$. The temporal break can not be due to the passage of $\nu_{\rm c}$, since there is no spectral change observed between the pre-break and post-break spectra.

From the constraints on the ordering of the peak, cooling and observing frequencies we can again obtain limits on the physical parameters of the blast wave and its surroundings. For the calculations we adopt that the isotropic equivalent energy is proportional to $t^{0.34}$, changing the temporal scaling laws of the peak flux, peak frequency and cooling frequency into $F_{\nu,\rm max} \propto t^{-0.33}$, $\nu_{\rm m} \propto t^{0.67}$ and $\nu_{\rm c} \propto t^{-1.33}$. The values for the physical parameters we derive are quite similar to the values in §8.4.5: $\varepsilon_B \sim 10^{-3}$, $\varepsilon_e \sim 10^{-2}$, $A_* \sim 1$, the isotropic equivalent energy at the end of the energy injection phase $\sim 5 \times 10^{55}$ erg, the jet-opening angle > 2°, and the collimation corrected energy $\sim 2 \times 10^{52}$ erg. So again, while the energy requirements are at the high end of the distribution, they are not unprecedented.

8.5 Conclusion

We have analysed the optical, X-ray and γ-ray data of GRB 060210 from the time of the prompt emission up until the X-ray afterglow was no longer detectable by *Swift*-XRT.

The early flaring X-ray & γ-ray emission implies internal shocks, indicative of prolonged engine activity. The light curves of the two regimes match well, even displaying a common flare at ~ 100 s. The agreement of the X-ray flares to the curvature effect and the clearly demonstrated spectral evolution support the claim that the flares are indeed due to internal shocks. The simultaneous optical emission, on the other hand, is consistent with an external shock afterglow with a frequency below that of both the peak & cooling frequencies. We have shown that such an external shock's deceleration time is close to the trigger time and should hence dominate the optical emission at the time of our observations.

The late afterglow ($\gtrsim 600$ s) may be explained by either of two models with an electron power-law index, $p = 2.28$, derived from the X-ray spectral index, β_X: a single temporal power-law in both optical and X-rays with both observing bands above the cooling frequency; or a broken power-law in X-rays in which optical and pre-break X-ray temporal slopes can be explained by continued activity of the central engine. In the latter case the cooling frequency is between the optical and X-ray frequencies and the observed X-ray temporal break indicates the termination of the central engine activity. Though both are consistent with the temporal and spectral slopes, we favour the continued central engine activity since the χ^2 of the single power-law fit is significantly worse. The collimation corrected energy requirements of $\sim 10^{52}$ erg in both cases, are at the high end of the distribution for GRBs but are certainly not unprecedented.

Comparing the column density in the host to the optical extinction we find a higher than expected value which supports the notion that GRBs can cause destruction of dust in the circumburst environment.

Acknowledgements PAC acknowledges the support of NWO under grant 639.043.302 and of the University of Leicester SPARTAN exchange visit programme, funded by the European Union Framework 6 Marie Curie Actions. APB, CPH, PTOB, KLP, ER and RW gratefully acknowledge support from PPARC. We thank R. Starling for useful discussions regarding host extinction. The Faulkes Telescopes are operated by the Las Cumbres Observatory Global Telescope Network. The authors acknowledge benefits from collaboration within the EU FP5 Research Training Network "Gamma-Ray Bursts: An Enigma and a Tool" (HPRN-CT-2002-00294). This research has made use of data obtained through the High Energy Astrophysics Science Archive Research Center Online Service, provided by the NASA/Goddard Space Flight Center.

9

An expanding radio nebula produced by a giant flare from the magnetar SGR 1806–20

B.M. Gaensler, C. Kouveliotou, J.D. Gelfand, G.B. Taylor, D. Eichler,
R.A.M.J. Wijers, J. Granot, E. Ramirez-Ruiz, Y.E. Lyubarsky, R.W. Hunstead,
D. Campbell-Wilson, A.J. van der Horst, M.A. McLaughlin, R.P. Fender,
M.A. Garrett, K.J. Newton-McGee, D.M. Palmer, N. Gehrels & P.M. Woods
Nature 434, 1104 (2005)

9.1 Introduction

Soft gamma repeaters (SGRs) are “magnetars”, a small class of slowly spinning neutron stars with extreme surface magnetic fields, $B \sim 10^{15}$ gauss (Duncan & Thompson 1992; Kouveliotou et al. 1998; Woods & Thompson 2006). On 2004 December 27, a giant flare (Borkowski et al. 2004) was detected from the magnetar SGR 1806–20(Kouveliotou et al. 1998), the third such event ever recorded (Mazets et al. 1979; Hurley et al. 1999a). This burst of energy was detected by a variety of instruments (Palmer et al. 2005; Hurley et al. 2005) and even caused an ionospheric disturbance in the Earth’s upper atmosphere recorded around the globe (Campbell et al. 2005). Here we report the detection of a fading radio afterglow produced by this outburst, with a luminosity 500 times larger than the only other detection of a similar source (Frail et al. 1999). From day 6 to day 19 after the flare from SGR 1806–20, a resolved, linearly polarized, radio nebula was seen, expanding at approximately a quarter the speed of light. To create this nebula, at least 4×10^{43} ergs of energy must have been emitted by the giant flare in the form of magnetic fields and relativistic particles. The combination of spatially resolved structure and rapid time evolution allows a study in unprecedented detail of a nearby analog to supernovae and gamma-ray bursts.

9.2 Results

Almost seven days after the 2004 Dec. 27 giant flare, we observed SGR 1806–20 with the Very Large Array (VLA) in its highest resolution configuration (maximum baseline length 36.4 km). We identified a bright but fading radio source designated VLA J180839–202439 (see Fig. 9.1), whose position was consistent with the previously reported localization (Kaplan et al. 2002) of the SGR. This close juxtaposition, plus the transient nature of the emission, makes it certain that VLA J180839–202439 is the radio afterglow of the giant flare from SGR 1806–20. For a distance (Corbel & Eikenberry 2004) to SGR 1806–20 of $15d_{15}$ kiloparsecs, the 1.4-GHz flux density of this source at first detection implies an isotropic spectral luminosity of $5d_{15}^2 \times 10^{15}$ W Hz^{-1}, approximately 500 times larger than the radio afterglow seen from SGR 1900+14 after a giant flare in 1998 (Frail et al. 1999). No other magnetar has been detected in the radio band, either in quiescence or during active periods (Lorimer & Xilouris 2000; Kouveliotou et al. 2001).

Given the very bright nature of this afterglow, we organized an international campaign over a broad range of frequencies, 0.35 to 16 GHz, to track the decay of the radio emission of VLA J180839–202439. Here we present a subset of these observations, made on days 6 to 19 after the giant flare, consisting of images made using the VLA, the Australia Telescope Compact Array (ATCA), the Westerbork Synthesis Radio Telescope (WSRT) and the Molonglo Observatory Synthesis Telescope (MOST).

Figure 9.2 shows the combined light curves from these four telescopes covering the frequency range 0.84 to 8.5 GHz. These data are consistent with a sudden increase in the decay rate at day 8.8, as summarised in Table 9.1 and shown by the linear fits in Figure 9.2. Specifically, if we assume that $S_\nu \propto t^\delta$ (where S_ν is the flux density at frequency ν), after day 8.8 we find an achromatic and rapid decline, $\delta \approx -2.7$, in six independent frequency bands (a similarly rapid decline was also observed (Frail et al. 1999) for the radio afterglow of SGR 1900+14 in 1998). After carefully accounting for the instrumental response of the VLA antennas we find that VLA J180839–202439 is significantly linearly polarized (see Fig. 9.3), which indicates that the emission mechanism is synchrotron radiation. In our earliest observations this emission was already optically thin, but showed clear evidence for a spectral steepening at high frequencies (see caption to Fig. 9.2). From day 11.2 onward, the spectrum was consistent with an unbroken power-law from 0.84 to 8.5 GHz with $\alpha = -0.75 \pm 0.02$ (where $S_\nu \propto \nu^\alpha$), again similar to the 1998 afterglow of SGR 1900+14. This implies a power-law energy distribution of the emitting electrons, $dN/dE \propto E^{-p}$, with

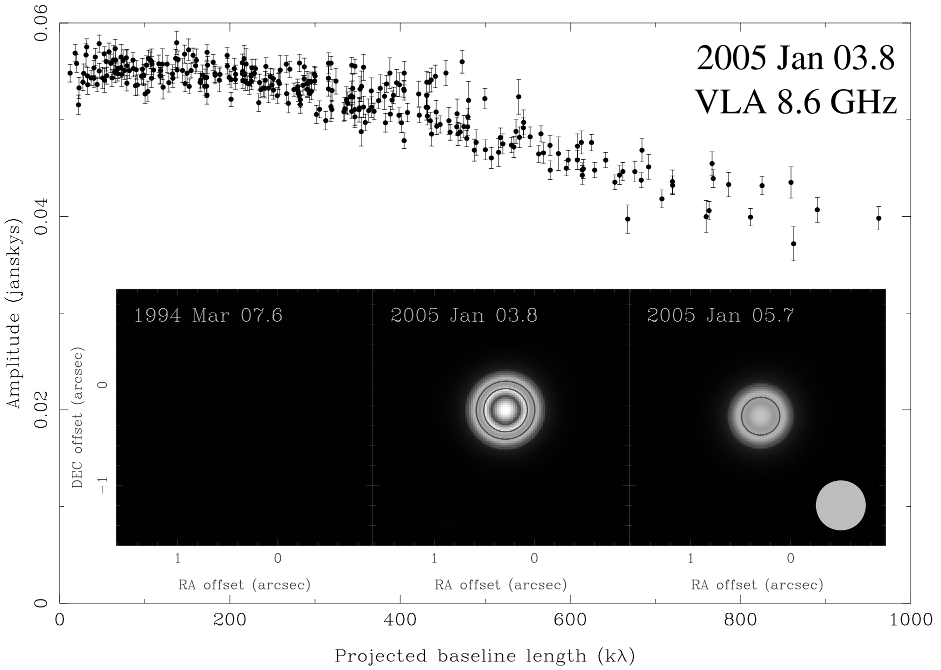

Figure 9.1 — Radio emission from VLA J180839–202439 at 8.5 GHz. The main panel shows the visibility amplitude as a function of projected baseline length (in units of thousands of wavelengths; 100 kλ $\approx$ 3.5 kilometers) at epoch 2005 Jan 03.8 (6.9 days after the giant flare), as seen by the VLA. The data have been self-calibrated in phase until the solution converged, and each baseline has then been time-averaged over the entire observation of duration 40 minutes. The error bars show the standard error in the mean of the amplitude on each baseline. The decrease in amplitude as a function of increasing baseline length clearly indicates that the source is resolved. The inset shows the image of the source at three epochs, smoothed to a uniform resolution of $0\farcs5$ (indicated by the green circle at lower right). The origin of the coordinate axes is the position of SGR 1806–20 measured with the *Chandra X-ray Observatory* (Kaplan et al. 2002), which has an uncertainty of $0\farcs3$ in each coordinate. The false-colour representation is on a linear scale, ranging from –0.3 to the peak brightness of 53 mJy beam $^{-1}$. The contours are drawn at levels of 20%, 40%, 60% and 80% of this peak. No source is seen in archival 8.5-GHz data from 1994 March, down to a 5-σ upper limit of 0.1 mJy. In the days after the giant flare, a bright but rapidly fading source is now seen at this position. The precise location of VLA J180839–202439 was determined by phase referencing to several nearby calibrators with well-determined positions. Our best measurement was on Jan. 16.6, for which we measured a position for VLA J180839–202439 (equinox J2000) of Right Ascension (R.A.) $18^{\rm h}08^{\rm m}39\fs343 \pm 0\fs002$, Declination (Dec.) $-20^\circ24'39\farcs80 \pm 0\farcs04$. The source's proper motion over the time span presented in this paper is -2.8 ± 6.5 mas day $^{-1}$ in R.A. and -2.2 ± 6.5 mas day^{-1} in Dec.

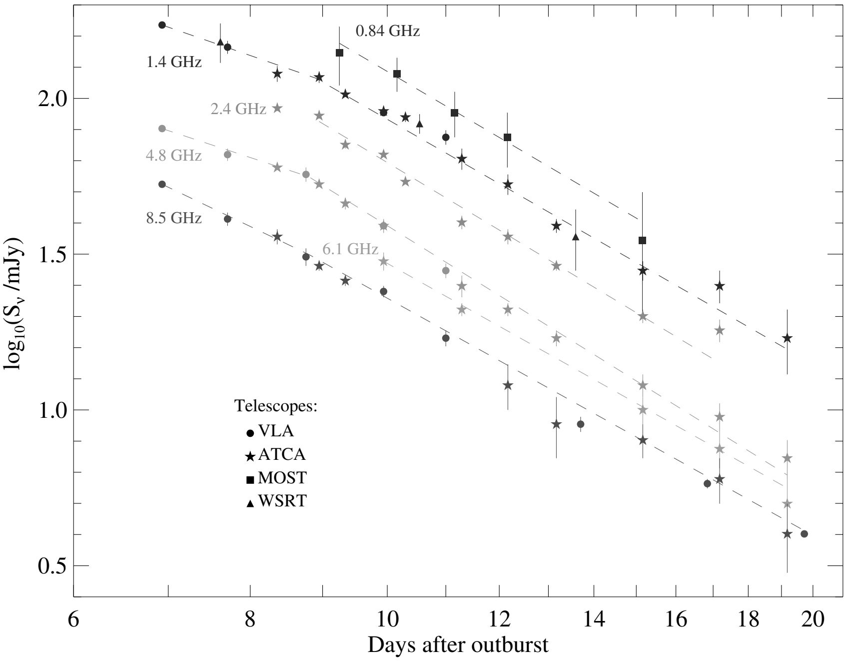

Figure 9.2 — Time evolution of the radio flux density from VLA J180839–202439. The x-axis indicates days since the giant flare was detected from SGR 1806–20, on 2004 Dec 27.90 UT. The radio data originate from ATCA, MOST and WSRT measurements made in six independent frequency bands. Each symbol represents a different telescope, while each colour indicates a different frequency. Measurement uncertainties are indicated at the 1-σ level. Fits to the data are indicated by dashed lines, and represent the results of applying the broken power-law model described in Table 9.1 to the data. Significant deviations from this fit are seen at both 1.4 and 2.4 GHz, suggesting short-term time-variability in the source (most notably the possible "bump" in the 1.4 GHz light curve seen with multiple telescopes on days 10–11 after the flare). These data also allow us to compute the evolution of the radio spectral index, α (defined as $S_\nu \propto \nu^\alpha$). At three epochs with good frequency coverage between 8.4 and 9.9 days after the flare, there is clear evidence for a spectral break, from $\alpha \approx -0.66$ below $\sim$ 5 GHz to $\alpha \approx -1.0$ above. Other data cannot rule out this break being present from day 6.9 (when the source was first detected) through to day 11.0. From day 11.2 onward, the spectrum has been consistent with an unbroken power-law from 0.84 to 8.5 GHz with $\alpha = -0.75 \pm 0.02$. In addition to the data shown here, on 2004 December 29, we used the Parkes Radio Telescope at 1.4 GHz to search for radio pulsations from SGR 1806–20. For dispersion measures in the range 0 to 2000 parsecs cm^{-3}, we found no pulsed signal at or near the star's X-ray period (Kouveliotou et al. 1998) of 7.5 sec down to a level of $\approx$ 0.2 mJy (these data provide no constraint on the unpulsed flux).

Table 9.1 — The rate of decay of the radio emission from VLA J180839–202439 at six independent frequencies. At each frequency, ν, it has been assumed that the radio flux density decays as $S_\nu \propto t^{\delta_\nu}$, with a break in the power-law index, δ_ν, at time t_0. To determine values of t_0 and δ_ν, a weighted least squares fit of a broken power-law has been applied to each data-set, with t_0 a free parameter. In each case, the fit shown is the only local minimum in χ^2 which meets the requirements that there are at least two data-points on either side of the break, the change in temporal index on either side of the break is larger than its uncertainties, and the power-law fits on either side of the break meet at the break point. Before day 8.8, we find that δ_ν possibly decreases with ν; after day 8.8, the flux decays rapidly at all frequencies with a power-law index $\delta \approx -2.7$, independent of ν.

ν (GHz)	t_0 (days)	δ_ν ($t < t_0$)	δ_ν ($t > t_0$)
0.84	≤ 10.2	...	-2.7 ± 0.8
1.4	$9.0^{+0.4}_{-0.6}$	-1.6 ± 0.2	-2.61 ± 0.09
2.4	≤ 9.0	...	-2.74 ± 0.07
4.8	$8.8^{+0.2}_{-0.4}$	-1.5 ± 0.1	-2.84 ± 0.08
6.1	≤ 11.3	...	-2.6 ± 0.2
8.5	$8.8^{+0.2}_{-0.4}$	-2.2 ± 0.2	-2.54 ± 0.04

$p = 1 - 2\alpha = 2.50 \pm 0.04$.

Our highest resolution measurements are those made with the VLA at 8.5 GHz. The visibility data from these observations, as shown for one epoch in Figure 9.1, demonstrate that VLA J180839–202439 is resolved. A Gaussian is a good fit to the visibilities at each epoch, with no significant persistent residuals (forthcoming higher resolution images from the VLBA and MERLIN will test the validity of this model). Figure 9.3 demonstrates that from day 6.9 to day 19.7, the data were consistent with constant isotropic expansion since outburst at a speed $v/c = (0.27 \pm 0.10)d_{15}$, with no noticeable deceleration as of day 19.7. Other than in one observation at day 16.8, the source was significantly elliptical, with an axial ratio ~ 0.6 and with the major axis oriented $\approx 60^\circ$ west of north.

9.3 Discussion & Conclusions

The spectrum and angular size of VLA J180839–202439 allow us to apply standard equipartition arguments for synchrotron sources (Pacholczyk 1970), implying a minimum magnetic field $B_{\rm min} = 0.02 d_{15}^{-2/7}[(1+\kappa)F_{100}/f]^{2/7}\theta_{50}^{-6/7}$ gauss, where $100F_{100}$ mJy is the flux density of VLA J180839–202439 at 1.4 GHz, κ the ratio of the energy in heavy particles to that in electrons, f is the volume

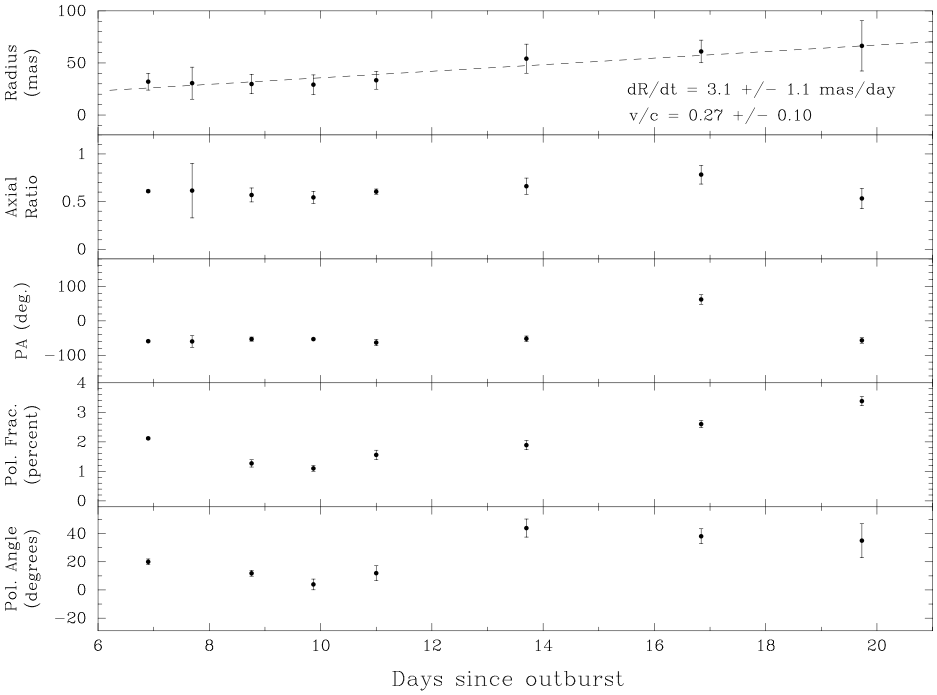

Figure 9.3 — Structural and polarization properties of VLA J180839–202439 as a function of time, as seen with the VLA at 8.5 GHz. The x-axis indicates days since the giant flare. The uppermost panel plots the radius of the source, determined by modelling (Staveley-Smith et al. 1993) the visibilities at each epoch as a two-dimensional Gaussian function in the Fourier plane of arbitrary position, amplitude, diameter, axial ratio and orientation, and then taking the geometric mean of the semi-major and semi-minor axes. The broken line shows a weighted linear least squares fit to the data. The indicated expansion velocity assumes two-sided or isotropic expansion at a distance of 15 kiloparsecs. The two panels below this show the axial ratio and position angle (measured north through east) of this best-fit Gaussian at each epoch. The fourth panel shows the fractional linear polarization of VLA J180839–202439 at 8.5 GHz. We find that the position angle of this linearly polarized emission is a linear function of ν^{-2} at each epoch, indicating the presence of Faraday rotation from foreground magnetised plasma. We measure a Faraday rotation measure (RM) of +272 ± 10 rad m^{-2} at multiple epochs, similar to the value RM = +290 ± 20 rad m^{-2} obtained for the adjacent calibrator, MRC B1817–254, and typical of RMs seen through the Galactic plane (Brown et al. 2003). Any contribution to the RM from the immediate environment of the magnetar must thus be small. The fifth panel shows the position angle of the electric field vector of linear polarization from VLA J180839–202439 after correction for this foreground Faraday rotation. Uncertainties at the 1-σ level are indicated for all data.

filling factor of magnetic fields and relativistic particles, and $50\theta_{50}$ mas is the source's angular diameter. The minimum energy in particles and magnetic fields in the emitting region is $E_{\rm min} = 4 \times 10^{43}\ d_{15}^{17/7}[(1+\kappa)F_{100}]^{4/7} f^{3/7}\theta_{50}^{9/7}$ ergs. The spectra show no evidence of self-absorption at frequencies above 0.6 GHz at early times (Chandra 2005), which is consistent with these parameters provided that the emitting medium has a density $n_0 \lesssim 0.1 f$ cm^{-3}. We can derive an additional independent energy estimate because of this rare opportunity to measure the expansion velocity directly. From the constant expansion speed observed over the first 20 days, we infer $E_{\rm min} \approx 6 \times 10^{42}\ \Omega(n_0/0.01\ {\rm cm}^{-3})(v/0.27c)^5$ ergs, where Ω is the opening solid angle of the ejected material.

Giant flares from magnetars are thought to result from shearing and reconnection of the extreme magnetic fields near the neutron star surface (Thompson & Duncan 2001, 1995). The inferred minimum energy in the radio nebula is somewhat smaller than the emitted gamma-ray energy (Palmer et al. 2005; Hurley et al. 2005), but is much larger than the electron/positron pair luminosity that would be expected to survive annihilation close to the magnetar. This suggests that baryons may have been ablated off the surface by the intense illumination of the flaring magnetosphere (Thompson & Duncan 2001, 1995). The radio nebula could be naturally created by these baryons, which move off the magnetar at high velocity, $\gtrsim 0.5c$, and then shock the ambient medium.

The very steep decay of the radio emission after day 8.8, $\delta \approx -2.7$, combined with the observed sub-luminal expansion velocity of VLA J180839–202439, is difficult to produce in standard gamma-ray burst blast-wave models (Rhoads 1999; Granot et al. 1999a; Cheng & Wang 2003). The light curves may thus represent an adiabatically expanding population of electrons accelerated at a particularly active phase, such as might occur if the ejecta collided with a pre-existing shell. Such a shell is naturally made by SGR 1806–20 itself, since its quiescent wind (Thompson et al. 2000) of luminosity (Woods et al. 2002) $\sim 10^{34}$ ergs s^{-1} will sweep up a bow shock (Wilkin 1996; Gaensler et al. 2002) of stand-off distance $\sim 10^{16}$ cm (corresponding to an angular extent $\sim 40 d_{15}^{-1}$ mas) as it moves through the interstellar medium (ISM) at a typical neutron star velocity (Arzoumanian et al. 2002) of $\sim$ 200 km s^{-1}. The star's motion creates a cigar-shaped cavity, mostly as a wake that trails the bow shock. If this pre-existing shell is hit by $\sim 10^{43}$–10^{44} ergs of energy from the SGR's giant flare, it will be shocked and swept outward, resulting in a violent episode of particle acceleration that puts much of the energy into a steadily expanding synchrotron-emitting shell 4 to 8 days after the giant flare. If we suppose that this shell maintains constant thickness and constant expansion speed, then its volume, V, increases as t^2, and the magnetic field will decay as $V^{-1/2}$ if directed within the tangent plane of the shell ($V^{-2/3}$ if tangled in three dimensions). This predicts a power-law index for the radio decay $\delta = (7\alpha - 3)/3 = -2.75 \pm 0.05$ (for $B \propto V^{-1/2}$) or $\delta = (8\alpha - 4)/3 = -3.33 \pm 0.05$ (for $B \propto V^{-2/3}$), consistent with the steep decay observed here. The overall evolution can be complicated by the fact that the ejecta may be somewhat collimated, and may hit the shell at different places and times — we defer detailed modelling to later papers, pending higher resolution images from MERLIN and the VLBA.

At early times, the polarization position angle on the sky is approximately perpendicular to the axis of the radio source (see Fig. 9.3), suggesting that the magnetic field in the emitting plasma (on average) is aligned preferentially along this axis. This is consistent with the shock producing a preferred magnetic anisotropy in the shock plane. Between observations at days 11.0 and 13.7 the polarized fraction and polarization angle both changed noticeably and a possible bump in the 1.4-GHz light curve is apparent; at day 16.8, the position angle of the major axis of the source also changed considerably. These results suggest that a different part of the outflow may have assumed the dominant role in the emission, as can occur if one region fades faster than another.

The intensity of this radio afterglow confirms the conservative inference made from the X- and gamma-ray detections (Palmer et al. 2005; Hurley et al. 2005) that this event was $\gtrsim 2$ orders of magnitude more energetic than the 1998 giant flare from SGR 1900+14. It is difficult to attribute the difference to beaming effects, because the measured expansion velocity ($\sim 0.3c$) appears to be modest. A release of $> 10^{46}$ ergs in a single magnetar flare (Palmer et al. 2005; Hurley et al. 2005) suggests that a rather large fraction, $\sim$ 10 percent, of the total magnetic energy can be released at once. Continued measurements of the morphology of the expanding radio source can provide an indication of whether the energy release took place at a specific location on the star's surface, or was a truly global phenomenon that rearranged the crust or even the entire interior.

Acknowledgements We thank Jim Ulvestad, Joan Wrobel, Bob Sault, Tony Foley and Rene Vermeulen for rapid scheduling of the VLA, ATCA and WSRT; Tracey DeLaney, Ger de Bruyn and Crystal Brogan for assistance with data analysis; and Dick Manchester, Dale Frail and Mark Wieringa for help with the observations. NRAO is a facility of the NSF operated under cooperative agreement by AUI. The Australia Telescope is funded by the Commonwealth of Australia for operation as a National Facility managed by CSIRO. The MOST is operated by the University of Sydney and supported in part by grants from the ARC. The WSRT is operated by ASTRON with financial support from NWO. B.M.G. acknowledges the support of NASA through a Long Term Space Astrophysics grant. D.E. acknowledge support from the Israel-U.S. BSF, the ISF, and the Arnow Chair of Physics. Y.L. acknowledges support from the German-Israeli Foundation. R.A.M.J.W and A.J.H. acknowledge support from NWO.

Table 9.2 — Flux density in mJy of VLA J180839–202439, the transient radio source coincident with SGR 1806–20. The epoch of the flare was 2004 Dec 27.89 UT. Uncertainties in each flux measurement are given at the 1-σ level. The absolute flux scales were set using bright standard calibrators; on several days, different telescopes observed the source nearly simultaneously and obtained near identical flux measurements, indicating the reliability of this calibration. Phase calibration was carried out using regular observations of nearby bright compact sources. At times when VLA J180839–202439 was bright enough, self-calibration in phase only was also applied. Fluxes were extracted in three ways: by integrating the surface brightness of the source, by fitting the image of the source to a Gaussian, and by modelling the source as a Gaussian in the complex visibility plane; results for total fluxes were consistent among these three approaches. The data with lower spatial resolution suffered from confusion from the bright radio source VLA J180840–202441 (Vasisht et al. 1995; Frail et al. 1997b), $14''$ to the east of SGR 1806–20, associated with the Luminous Blue Variable (LBV) 1806–20 (Hurley et al. 1999b). For these data, difference imaging and background subtraction were carefully applied to extract the radio flux of the transient source. The estimated uncertainties account for the systematic effects associated with this approach.

Mean Epoch (UT)	ΔT days	Telescope	0.84 GHz	1.4 GHz	2.4 GHz	4.8 GHz	6.1 GHz	8.5 GHz
Jan 03.83	6.93	VLA	...	172±4	...	80±1	...	53±1
Jan 04.52	7.62	WSRT	...	152±22	...	...	...	...
Jan 04.61	7.71	VLA	...	146±7	...	66±3	...	41±2
Jan 05.26	8.36	ATCA	...	120±7	93±2	60±1	...	36±2
Jan 05.66	8.76	VLA	...	...	...	57±3	...	31±2
Jan 05.85	8.95	ATCA	...	117±5	88±2	53±1	...	29±1
Jan 06.15	9.25	MOST	140±30	...	...	...	...	...
Jan 06.24	9.34	ATCA	...	103±2	71±2	46±2	...	26±1
Jan 06.85	9.95	ATCA	...	91±2	66±1	39±2	30±2	...
Jan 06.85	9.95	VLA	...	90±2	...	39±1	...	24±1
Jan 07.06	10.16	MOST	120±15	...	...	...	...	...
Jan 07.20	10.30	ATCA	...	87±3	54±1	...	...	...
Jan 07.44	10.54	WSRT	...	83±6	...	...	...	...
Jan 07.90	11.00	VLA	...	75±4	...	28±2	...	17±1
Jan 08.06	11.16	MOST	90±15	...	...	...	...	...
Jan 08.19	11.29	ATCA	...	64±5	40±2	25±2	21±1	...
Jan 09.06	12.16	MOST	75±15	...	...	...	...	...
Jan 09.07	12.17	ATCA	...	53±4	36±2	21±1	...	12±2
Jan 10.07	13.17	ATCA	...	39±2	29±1	17±1	...	9±2
Jan 10.49	13.59	WSRT	...	36±8	...	...	...	...
Jan 10.60	13.70	VLA	...	...	...	...	...	9.0±0.5
Jan 12.05	15.15	MOST	35±15	...	...	...	...	...
Jan 12.06	15.16	ATCA	...	28±2	20±1	12±1	10±1	8±1
Jan 13.74	16.84	VLA	...	...	...	...	...	5.8±0.2
Jan 14.08	17.18	ATCA	...	25±3	19±2	10±1	8±1	6±1
Jan 16.08	19.18	ATCA	...	17±4	...	7±1	5±2	4±1
Jan 16.62	19.72	VLA	...	...	...	...	...	4.0±0.1

10

Samenvatting

Gammaflitsers (“gamma-ray bursts”) zijn de krachtigste explosies in het heelal. Zoals de naam al doet vermoeden, zijn het korte flitsen van gammastraling, met een gemiddelde duur van een paar tientallen van seconden. De duur van de flits kan echter wel sterk verschillen: soms slechts een fractie van een seconde, en soms wel minuten lang. Gammaflitsers hebben een extreme helderheid: ze kunnen net zo helder zijn in gammastraling als de rest van het heelal bij elkaar. Na de ontdekking van gammaflitsers in 1967 heeft het 30 jaar geduurd voordat de aard van deze bijzondere fenomenen kon worden onthuld. Dit gebeurde toen in 1997 andere vormen van straling werden ontdekt die van de gammaflitsers af komen: röntgen-, ultraviolet, optische, infrarood-, millimeter-, en radiostraling. De ontdekking van deze zogenaamde nagloeier (“afterglow”) van gammaflitsers heeft een revolutie veroorzaakt in het onderzoek naar gammaflitsers. Door het waarnemen van alle verschillende soorten straling die van gammaflitsers af komen, kunnen de objecten en processen die gammaflitsers veroorzaken in detail bestudeerd worden. Het blijkt dat zowel de objecten als de processen zeer extreem zijn, wat het bestuderen van het nagloeien van gammaflitsers geschikt maakt om natuurkundige wetmatigheden te testen onder omstandigheden die we op de aarde niet kunnen nabootsen. In dit proefschrift geef ik een beschrijving van de natuurkundige processen die een rol spelen, en van methoden om uit allerlei verschillende waarneemgegevens, waar ik zelf ook een deel van heb vergaard, zo veel mogelijk informatie te halen, om zodoende een beter begrip te krijgen van de aard van gammaflitsers en hun nagloeiers.

10.1 Ontdekking van gammaflitsers en nagloeiers

Gammaflitsers zijn in 1967 per toeval ontdekt, en deze ontdekking was het gevolg van de Koude Oorlog tussen de Verenigde Staten en de Sovjet-Unie. Deze twee grootmachten hadden met elkaar afgesproken dat er geen kernproeven meer gedaan mochten worden, maar waren zeer wantrouwig tegenover elkaar. De Amerikanen waren bang dat de Russen deze proeven, in plaats van op de aarde, hoog in de aardatmosfeer of zelfs nog hoger gingen doen. Vandaar dat zij satellieten lanceerden die gammastraling konden detecteren. De militaire Vela satel-

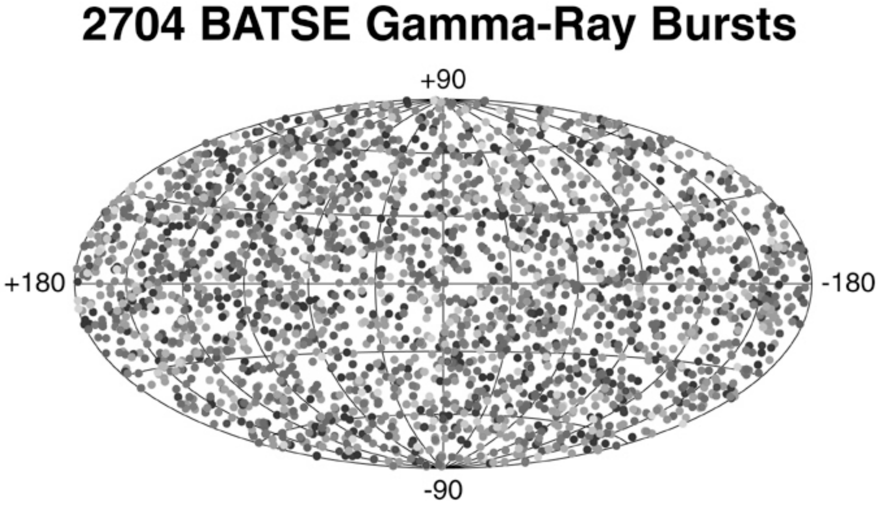

Figure 10.1 — De verdeling aan de hemel van gammaflitsers, die zijn gevonden door BATSE. De gammaflitsers zijn uniform over de hemel verdeeld, en er is dus geen voorkeur voor een bepaalde plaats aan de hemel, bijvoorbeeld ons zonnestelsel of onze eigen Melkweg. Dit was een belangrijke aanwijzing dat gammaflitsers buiten de Melkweg ontstaan, zelfs op miljarden lichtjaren hier vandaan.

lieten detecteerden inderdaad gammastraling, echter niet afkomstig van kernproeven van de Russen, maar van onbekende bronnen in het heelal: gammaflitsers.

Na deze eerste gammaflitser werden er nog velen ontdekt, maar het was onduidelijk waar ze vandaan kwamen. Er werden vele modellen ontwikkeld; iedereen had zijn eigen favoriete model en bijna geen enkel model kon worden ontkracht, omdat er één belangrijk gegeven ontbrak: de afstand. Dit probleem werd veroorzaakt door het feit dat de nauwkeurigheid waarmee de plaats aan de hemel bepaald kon worden, niet toereikend was om andere vormen van straling van deze bronnen te vinden. De eerste duidelijke aanwijzingen voor de afstand van gammaflitsers kwamen in het begin van de jaren negentig van de gammastralingdetector BATSE (Burst And Transient Source Experiment) aan boord van de satelliet Compton Gamma-Ray Observatory. De bijna drieduizend gammaflitsers die BATSE heeft waargenomen bleken uniform over de hemel verdeeld te zijn (Figuur 10.1). Er was dus geen voorkeur voor een bepaalde plaats aan de hemel, bijvoorbeeld ons zonnestelsel of onze eigen Melkweg. Dit betekende dat de modellen die gammaflitsers op die manier probeerden te verklaren, uitge-

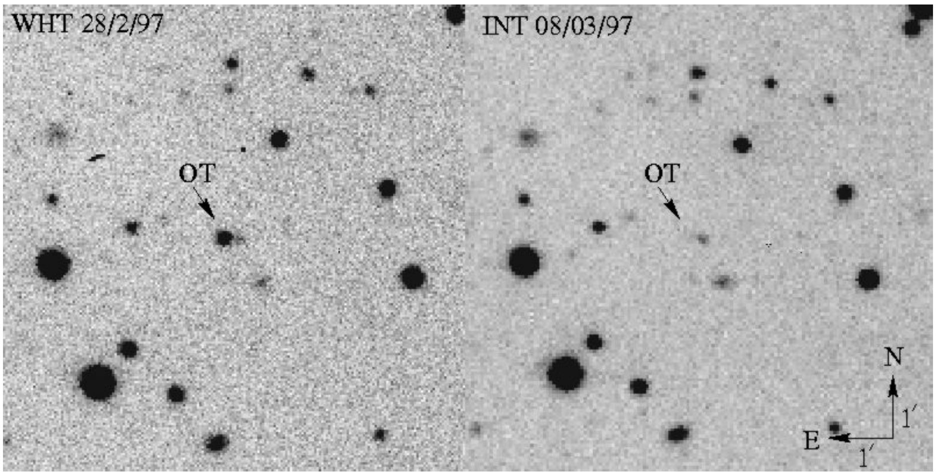

Figure 10.2 — Optisch plaatje van de hemel rond de positie van de optische nagloeier van de gammaflitser die 28 februari 1997 gevonden is. Het linker plaatje is een waarneming met de William Herschel Telescoop op 28 februari 1997, en het rechter plaatje is gemaakt met de Isaac Newton Telescoop een week later (8 maart). Bij de tweede waarneming was de optische bron, die op 28 februari gedetecteerd was, verdwenen. Dit was de eerste optische nagloeier van een gammaflitser, en het feit dat ze binnen een paar dagen verdwenen was, maakte duidelijk dat er snel gereageerd moest worden om de nagloeiers van gammaflitsers te vinden.

sloten werden. Alles leek er op te wijzen dat gammaflitsers buiten de Melkweg ontstaan, zelfs op miljarden lichtjaren hier vandaan (een lichtjaar is de afstand die het licht aflegt in 1 jaar, meer dan 9 biljoen kilometer).

Nog niet iedereen was overtuigd dat gammaflitsers op zogenaamde kosmologische afstanden staan, maar dit veranderde drastisch in 1997. Een Italiaans-Nederlandse satelliet, BeppoSAX genaamd, had twee camera's aan boord die harde röntgenstraling konden detecteren, en zeer nauwkeurig de positie van de bron aan de hemel konden bepalen. Op 28 februari 1997 werd op die manier voor het eerst de röntgennagloeier van een gammaflitser ontdekt, maar werd ook voor het eerst optische straling, oftewel zichtbaar licht, gedetecteerd. Een onderzoeksgroep in Amsterdam deed waarnemingen met de William Herschel Telescoop op de Canarische eilanden, en op diezelfde positie werd een bronnetje gedetecteerd, dat daarna zwakker werd. Toen dezelfde groep op 8 maart met de Isaac Newton Telescoop (ook op de Canarische eilanden) waarnemingen deed, was de optische bron geheel verdwenen (Figuur 10.2). Deze ontdekking van de röntgen- en optische nagloeier, en het feit dat ze binnen een paar dagen verdwenen was, maakte duidelijk dat er snel gereageerd moest worden om de nagloeiers van gammaflitsers te vinden.

Een paar maanden later, op 8 mei, werd er dankzij de Nederlandse camera's in BeppoSAX weer een nagloeier ontdekt, en werd er ook voor het eerst radiostraling gedetecteerd, met de Very Large Array in de Verenigde Staten en de Westerbork Synthese Radio Telescoop in Nederland. Daarnaast werd er ook voor het eerst een zogenaamd spectrum genomen, waarin te zien was dat gas en stof op ongeveer tien miljard lichtjaar hier vandaan een deel van het licht van de nagloeier hadden geabsorbeerd, wat meteen de minimale afstand tot dit object vastlegde. Hiermee was, 30 jaar na de ontdekking, het afstandsdebat opgelost: gammaflitsers staan op kosmologische afstanden.

10.2 De bron

De afstand naar de mysterieuze gammaflitsers was nu dus bepaald, en gezien hun extreme helderheid in gammastraling, moest de bron ook wel een extreem object zijn. Er waren ook al aanwijzingen dat er waarschijnlijk minstens twee verschillende soorten objecten moesten zijn om de waargenomen verschijnselen te kunnen verklaren. Bij het bestuderen van de gigantische hoeveelheid gammaflitsers die BATSE had waargenomen in de jaren negentig bleek namelijk dat er twee groepen gammaflitsers zijn: korte en lange gammaflitsers, waarbij de scheidslijn tussen de twee groepen bij een duur van ongeveer twee seconden ligt. Deze twee groepen hebben nog een groot verschil: de gammastraling van korte gammaflitsers is naar verhouding harder dan die van lange gammaflitsers.

Er was, tot twee jaar geleden, nog een belangrijk verschil tussen korte en lange gammaflitsers: op 9 mei 2005 werd namelijk pas voor het eerst de nagloeier van een korte gammaflitser ontdekt. In de tussenliggende acht jaar zijn er van de lange gammaflitsers vele nagloeiers ontdekt en in detail bestudeerd. Dit heeft een schat aan informatie opgeleverd over de objecten waar lange gammaflitsers uit ontstaan en hun omgeving, terwijl deze informatie voor korte gammaflitsers ontbrak. Van de korte gammaflitsers en hun nagloeiers zijn er daardoor tot nu toe veel minder waarnemingen, maar wel genoeg om te concluderen dat de eigenschappen van de gammaflitsers en hun omgeving verschillend zijn voor de lange en de korte groep.

10.2.1 Lange gammaflitsers

De eerste aanwijzing voor de bron van lange gammaflitsers kwam met de ontdekking in 1998 van een zogenaamde supernova, die zichtbaar werd op dezelfde plek in een sterrenstelsel waar kort daarvoor een gammaflitser was gezien. Een

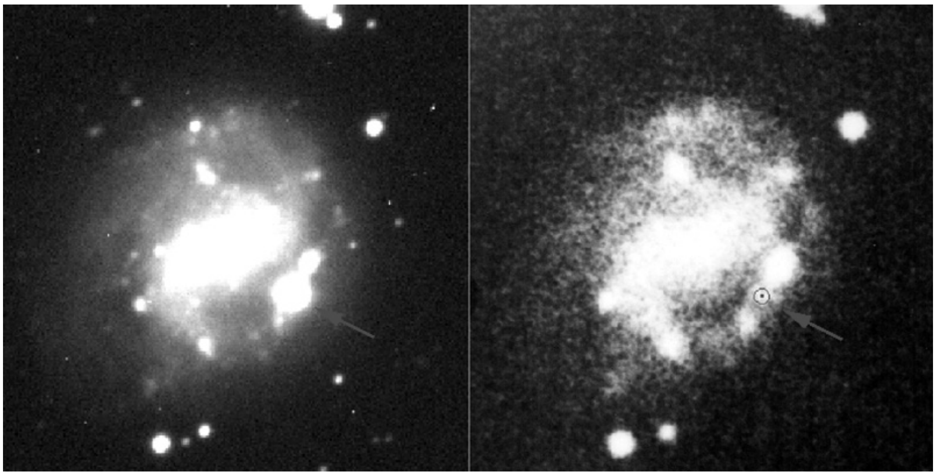

Figure 10.3 — Optisch plaatje van een sterrenstelsel waar in 1998 op dezelfde plek een gammaflitser en, kort daarna, een supernova gezien werd. Het linker plaatje is gemaakt toen de supernova het helderst was, en het rechter plaatje is een oude opname van het zelfde sterrenstelsel. De associatie tussen een gammaflitser en een supernova, die hier voor het eerst ontdekt is, was een belangrijke aanwijzing dat lange gammaflitsers zware sterren zijn die aan het einde van hun leven komen, net zoals de al bekende supernovae.

supernova is een gebeurtenis die plaats vindt aan het einde van het leven van een zeer zware ster. Tijdens het leven van een ster produceert zij energie door middel van kernfusie, wat er voor zorgt dat de ster niet in elkaar stort als gevolg van de zwaartekracht. Als echter de brandstof voor kernfusie in de ster op is, kan deze energie niet meer geproduceerd worden, en zal de kern van de ster onder invloed van de zwaartekracht in elkaar storten. Onze eigen zon doet er ongeveer 10 miljard jaar over om de brandstof op te maken, maar bij zwaardere sterren gaat dit proces veel sneller, en zal de eindklap ook veel heftiger zijn: een supernova. Bij die supernova wordt een zogenaamde neutronenster gevormd, een compact object dat bestaat uit extreem dicht op elkaar gepakte materie; en daarbij worden de buitenlagen van de ster met enorme snelheden de ruimte in geblazen. Onder nog extremere omstandigheden, bijvoorbeeld als de kern van de ster nog zwaarder is, kan ook die neutronenster de zwaartekracht niet meer weerstaan en stort alle materie in elkaar tot een zwart gat.

In 1998 was dus voor het eerst de associatie gemaakt tussen een lange gammaflitser en een supernova. Deze bron stond echter zo dichtbij, vele malen dichterbij dan alle andere gammaflitsers, dat het mogelijk was dat dit een speciaal geval was en niet representatief voor alle andere gammaflitsers. De associatie tussen gammaflitsers en supernovae werd echter versterkt door het feit dat in sterrenstelsels waar gammaflitsers te vinden zijn, veel stervorming plaats vindt; en wellicht het belangrijkste is dat in die sterrenstelsels veel zware sterren gevormd worden. In 2003 gebeurde datgene waar iedereen op had zitten wachten: het onomstotelijke bewijs dat gammaflitsers en supernovae verwant zijn. Op 29 maart van dat jaar werd er een extreem heldere gammaflitser gedetecteerd, met een van de helderste nagloeiers ooit. De radionagloeier was zelfs zo helder dat deze nu, vier jaar na de gammaflits, nog steeds zichtbaar is. Toen de optische nagloeier zwakker werd, begon opeens de vorm van het spectrum te veranderen, en er kwam het spectrum van een supernova te voorschijn die heel erg leek op de supernova uit 1998. Dit was het definitieve bewijs dat er een connectie is tussen lange gammaflitsers en supernovae.

Er worden echter veel vaker supernovae dan gammaflitsers ontdekt, dus er moet wel iets speciaals aan de hand zijn om een gammaflitser te kunnen zien. Het leidende model is dat er bij het in elkaar storten van de zware ster een zwart gat gevormd wordt, maar daarnaast ook materie en straling langs de rotatie-as van de ster weggeblazen wordt in een vrij nauwe bundel. Deze nauwe bundel wordt ook wel “jet” genoemd (Figuur 10.6) en is datgene wat uiteindelijk de gammaflits en het nagloeien veroorzaakt. Wij zien een gammaflitser dus slechts als de jet op ons gericht staat, anders zien we alleen maar de supernova. Daarmee missen we dus een groot aantal gammaflitsers, maar dat wil niet zeggen dat elke supernova die we zien, een gammaflitser is die toevallig een andere kant op gericht staat. Een groot deel van de supernovae produceert waarschijnlijk geen jet, of die jet is te zwak om door de buitenlagen van de ster heen te dringen en verdwijnt dan. Uit een gedetailleerde studie van een viertal relatief dichtbij staande gammaflitsers, waar veel informatie was over zowel de gammaflitser als de bijbehorende supernova, is gebleken dat de supernovae erg op elkaar lijken, maar dat de bijbehorende gammaflitsers zeer verschillend zijn, vooral in hoe krachtig de jet is. Het kan af en toe ook zo zijn dat er bij een gammaflitser, die duidelijk tot de groep lange gammaflitsers behoort, geen supernova wordt gezien, wat het geval was in mei en juni 2006 bij twee gammaflitsers. Al is er dus wel een duidelijke associatie tussen gammaflitsers en supernovae, deze is niet altijd even eenduidig, en meer waarnemingen van relatief dichtbij staande gammaflitsers zijn nodig om hier duidelijkheid in te scheppen.

10.2.2 Korte gammaflitsers

Van korte gammaflitsers weten we veel minder dan van de lange variant, vooral omdat de eerste nagloeier van een korte gammaflitser pas twee jaar geleden is ontdekt. Dit was mogelijk door de komst van een nieuwe satelliet, Swift genaamd, die speciaal is ontworpen voor het bestuderen van gammaflitsers. Deze

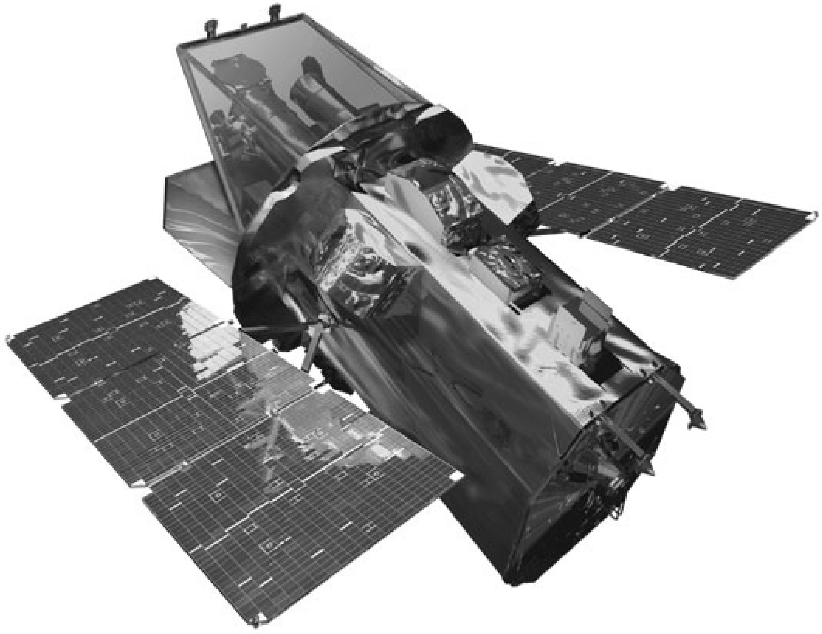

Figure 10.4 — De Swift satelliet, speciaal ontworpen voor het bestuderen van gammaflitsers. Swift kan zeer snel wenden, en heeft drie verschillende detectoren aan boord om gamma-, röntgen-, en ultraviolet en optische straling te meten. Als de gammastralingdetector een gammaflitser ontdekt, kan Swift meteen zo draaien dat de andere detectoren kunnen gaan meten. Dit betekent dat binnen een halve minuut na de gammaflits, en soms zelfs maar een paar seconden, het nagloeien waargenomen kan worden. Door het snelle reageren heeft Swift onder andere voor het eerst de nagloeier van een korte gammaflitser ontdekt.

satelliet kan namelijk zeer snel wenden, en heeft drie verschillende detectoren aan boord om gamma-, röntgen-, en ultraviolet en optische straling te meten. Als de gammastralingdetector een gammaflitser ontdekt, kan Swift meteen zo draaien dat de andere detectoren kunnen gaan meten. Dit betekent dat binnen een halve minuut na de gammaflits, en soms zelfs maar een paar seconden, het nagloeien waargenomen kan worden. In uitzonderlijke gevallen wordt er zelfs al röntgen- of optische straling waargenomen tijdens de gammaflits.

Door het snelle reageren van Swift (Figuur 10.4) werd in mei 2005 het nagloeien van een korte gammaflitser ontdekt. Dit was alleen nog maar röntgenstraling, maar was een enorme vooruitgang, omdat nu veel beter de locatie aan de hemel bepaald kon worden. Uit optische waarnemingen vanaf de aarde bleek dat de bron zeer waarschijnlijk hoorde bij een oud sterrenstelsel, dat er totaal anders uitzag dan de jonge, stervormende, sterrenstelsels waar lange gammaflitsers gevonden worden. Na deze ontdekking volgden er al snel meer nagloeiers van andere korte gammaflitsers, ook in optische en radiostraling. Het werd meteen duidelijk waarom het al die jaren zo lastig was geweest om de nagloeiers van korte gammaflitsers te vinden: ze zijn veel minder helder dan die van de lange gammaflitsers, al zitten er wel korte gammaflitsers bij die ongeveer even helder zijn. Het beeld van de sterrenstelsels waar korte gammaflitsers bij horen is niet eenduidig: zowel oude als jonge stelsels worden er gevonden. Het kan dus zo zijn dat een deel van de korte gammaflitsers op dezelfde manier gevormd wordt als lange gammaflitsers, al is er nog nooit een supernova gevonden bij een korte gammaflitser. Er is echter waarschijnlijk een andere bron voor korte gammaflitsers, waar compacte objecten een belangrijke rol bij spelen.

In het heelal vormen veel sterren een dubbelstersysteem samen met een andere ster. Deze twee sterren draaien onder invloed van de zwaartekracht om elkaar heen. Er zijn ook systemen met drie of zelfs meer sterren die om elkaar heen draaien. Het feit dat onze zon geen onderdeel is van een dubbelstersysteem, is dus eigenlijk niet zo vanzelfsprekend. In dubbelstersystemen kan een van de twee sterren ook een compact object zijn, bijvoorbeeld een neutronenster of een zwart gat, als een van de twee sterren met een supernova aan het einde van haar leven is gekomen. Ook beide objecten in het systeem kunnen een compact object zijn, zowel een neutronenster als een zwart gat. Als dit het geval is, vertelt de natuurkunde ons dat deze twee objecten, terwijl ze om elkaar heen draaien, heel langzaam dichter bij elkaar komen; de tijdschaal hiervoor kan variëren van honderdduizenden tot miljarden jaren. Als ze steeds dichter om elkaar heen gaan draaien, zal er ook een moment komen dat ze op elkaar botsen. Bij een dergelijke botsing van twee neutronensterren, of een neutronenster en een zwart gat, wordt er waarschijnlijk een zwart gat gevormd. Hierbij komt er een gigantische hoeveelheid energie vrij en wordt er wellicht ook een jet gevormd. Dit is het meest populaire model voor de korte gammaflitsers, al is het definitieve bewijs nog niet gevonden.

10.2.3 Gammaflikkeraars

Naast de dubbelsterren van twee neutronensterren, of een neutronenster en een zwart gat, is er nog een mogelijkheid om deel van de korte gammaflitsers te verklaren, namelijk een “superflits” van een zogenaamde gammaflikkeraar (“soft gamma repeater”). Gammaflikkeraars zijn eind jaren zeventig ontdekt, en leken in eerste instantie een aparte groep binnen de gammaflitsers te zijn. Wat gammaflikkeraars anders maakt dan gammaflitsers is dat zij niet na één flits verdwij-

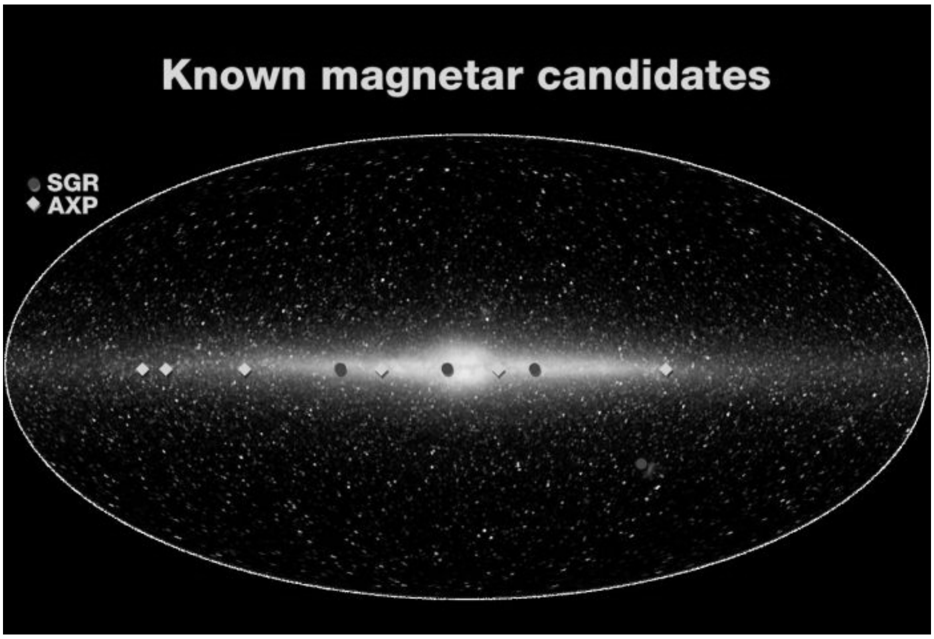

Figure 10.5 — De verdeling aan de hemel van “magnetars”, neutronensterren met een extreem sterk magneetveld. Gammaflikkeraars (“SGRs” in het kaartje) zijn ook magnetars. De baan van licht in het midden van het hemelkaartje is onze Melkweg. Het is duidelijk te zien dat, op één na, alle magnetars in het vlak van de Melkweg liggen. Er werd in eerste instantie gedacht dat gammaflikkeraars een groep binnen de gammaflitsers waren. Uit het vergelijken van dit hemelkaartje met die van gammaflitsers (Figuur 10.1), valt al op te maken dat de oorsprong van gammaflitsers en gammaflikkeraars verschillend is. Een nog duidelijker verschil is dat gammaflikkeraars niet na één flits verdwijnen zoals gammaflitsers, maar dat ze jaren lang actief zijn in het produceren van flitsen van gammastraling.

nen, maar dat ze jaren lang actief zijn in het produceren van flitsen van gammastraling. Deze flitsen komen vaak in groepen: een gammaflikkeraar kan een tijdje niets produceren en vervolgens een paar weken of maanden zeer actief zijn. Het blijkt dat deze zeldzame objecten iets anders zijn dan de bronnen van gammaflitsers, namelijk neutronensterren met een extreem sterk magneetveld, zogenaamde “magnetars”. Heel af en toe, er zijn er tot nu toe drie gedetecteerd, produceert een dergelijke gammaflikkeraar een superflits, die wel honderdduizend keer helderder kan zijn dan de gewone flitsen. De gammaflikkeraars die tot nu toe zijn gedetecteerd staan, op één na, allemaal in onze Melkweg (Figuur 10.5). Ze kunnen echter overal in het heelal voorkomen, maar ze staan dan te ver weg om de gewone flitsen te zien. Superflitsen van verder weg gelegen gammaflikkeraars zijn wel detecteerbaar, en die zouden er dan uitzien als een korte gammaflitser.

Op 27 december 2004 werd de helderste superflits van een gammaflikkeraar ooit gedetecteerd. Deze superflits was zo helder dat de detectoren op de Swift satelliet, die net daarvoor gelanceerd was, volledig overbelicht werd, terwijl de detectoren de andere kant op gericht waren, en de gammastraling dus volledig door de bepakking aan de achterkant heen ging. Ook satellieten die metingen aan de aardatmosfeer doen detecteerden deze superflits, omdat de eigenschappen van een deel van de aardatmosfeer kort veranderden toen de gammastraling de aarde bereikte. Naast deze grote hoeveelheid gammastraling, werd er ook een soort nagloeier van deze superflits gedetecteerd. Deze nagloeier was zeer helder in radiostraling en is waargenomen door radiotelescopen over de hele wereld. Omdat de bron van de straling in dit geval in onze eigen Melkweg stond in plaats van miljarden lichtjaren hier vandaan, was het mogelijk met zeer nauwkeurige radiowaarnemingen plaatjes van de nagloeier te maken, terwijl de nagloeiers van gammaflitsers normaal gesproken slechts puntjes aan de hemel zijn, omdat ze zo ver weg staan. Alleen voor de extreem heldere gammaflitser van maart 2003, waar voor het eerst het onomstotelijke bewijs is gevonden voor de bron van lange gammaflitsers, was het ook mogelijk om plaatjes te maken, maar die zijn lang niet zo gedetailleerd als die van deze superflits.

10.3 Nagloeiers en het schokmodel

Gammaflitsers worden gevonden door hun gammastraling, die zij in een flits uitzenden, variërend van een fractie van een seconde tot een paar minuten. De nagloeier in röntgenstraling wordt meestal een paar uur tot een paar dagen na de gammaflits te zwak om nog te detecteren; in het optisch is de nagloeier een paar dagen tot een paar weken na de gammaflits te zien, totdat het te zwak is om nog te detecteren, of dat het zwakker is dan het licht van het sterrenstelsel waar de gammaflitser in staat. De radiostraling van de nagloeier begint juist meestal zwak en wordt daarna helderder; na een week tot een paar maanden wordt hij dan weer zwakker, waarna hij op een gegeven moment echt niet meer detecteerbaar is, wat in sommige gevallen zelfs jaren na de oorspronkelijke gammaflits kan zijn. Door alle verschillende soorten straling die er van de bron afkomt te analyseren en met elkaar te vergelijken, kunnen eigenschappen worden bepaald van de gammaflitser en zijn omgeving. Om dit te kunnen doen wordt een model gebruikt dat beschrijft hoe al die straling geproduceerd wordt: het “schokmodel”.

Zoals al eerder vermeld, ontstaat in de modellen voor gammaflitsers een zwart gat, waarbij materie en straling wordt weggeblazen in een nauwe bun-

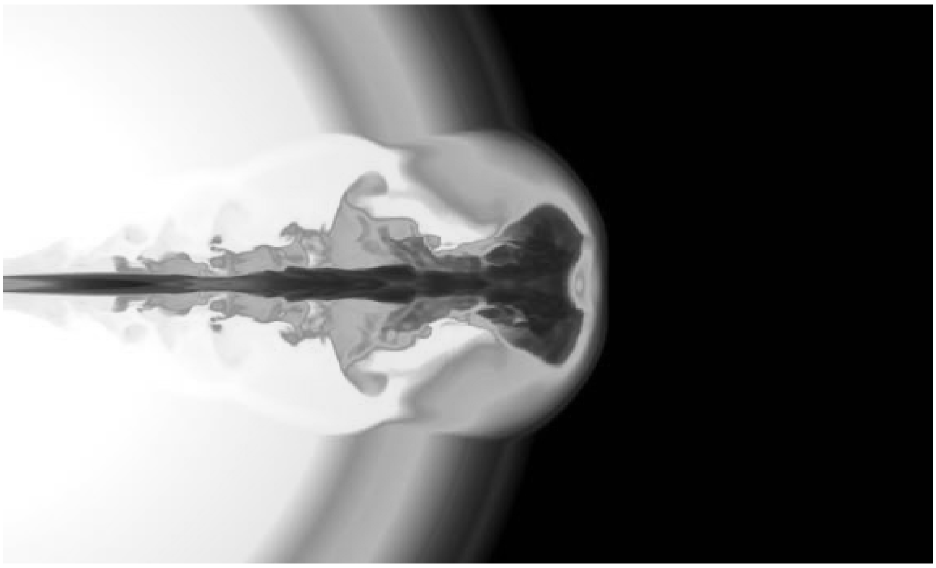

Figure 10.6 — Computersimulatie van een jet die geproduceerd wordt als een zware ster aan het einde van zijn leven komt en in elkaar stort. Vanwege de enorme energieën die hiermee gepaard gaan, wordt het materiaal in de jet versneld tot snelheden die bijna zo groot zijn als de lichtsnelheid. Deze jet moet door de buitenlagen van de ster heen, en deze opname van de computersimulatie laat het moment zien waarop de jet uit het oppervlak van de ster breekt.

del, de jet. Vanwege de enorme energieën die hiermee gepaard gaan, wordt het materiaal in deze uitstroom versneld tot snelheden die bijna zo groot zijn als de lichtsnelheid, wat de grootste snelheid in het heelal is. Deze snelheden worden relativistisch genoemd, omdat bij snelheden die bijna gelijk zijn aan de lichtsnelheid, de relativiteitstheorie van Einstein een rol gaat spelen. De materiestroom is niet een geleidelijke uitstroom, maar er kunnen schillen met materie ontstaan die verschillende snelheden hebben. Op het moment dat deze schillen op elkaar botsen, ontstaan er zogenaamde schokken: opeenhopingen van materie, waar de dichtheid en temperatuur van de materie opeens een sprong maken. Bij deze interne schokken in de uitstroom worden elementaire deeltjes, zoals electronen (één van de bouwstenen van de natuur), versneld, en deze deeltjes beginnen te stralen. De straling die hierbij geproduceerd wordt is gammastraling en dit is wat wij zien als de gammaflits.

Terwijl de materiestroom voortraast, zal er materie worden opgeveegd die de jet onderweg tegenkomt. Aan de voorkant van de jet is er ook een schok, de externe schok, en die veegt bij het voortbewegen meer materiaal op, waardoor hij afgeremd wordt. Ook deze externe schok zal electronen versnellen, die vervolgens gaan stralen, en dat nemen wij dan waar als de nagloeier van gammaflitsers. Na een paar dagen is de schok zoveel afgeremd, dat niet alle materie meer dezelfde richting op blijft bewegen in de jet, maar dat de jet opzij gaat expanderen. Na een paar maanden heeft de schok dan een snelheid gekregen die een stuk kleiner is dan de lichtsnelheid, en dus niet relativistisch meer, en is er van de jet niet veel meer over. De materie blijft nog steeds van de bron af bewegen, maar niet meer in een nauwe bundel, maar juist alle richtingen uit. Deze laatste fase van de schok kan in sommige gevallen nog een paar jaar bestudeerd worden, maar dan alleen in radiostraling en als ze daarvoor helder genoeg is.

10.4 Straling van nagloeiers ontleed

In het algemeen kunnen de waarnemingen van nagloeiers goed worden beschreven met het schokmodel. Aangezien het bij nagloeiers voornamelijk om de externe schok gaat, kunnen we met alle verschillende soorten straling die we meten, vooral de materie waar de jet doorheen beweegt goed bestuderen en ook bepaalde eigenschappen van de jet zelf. Daarnaast kunnen we ook de natuurkundige processen, die een rol spelen bij het produceren van de straling, in detail bestuderen. Om dit te kunnen doen moeten er wel waarnemingen van een bepaalde nagloeier gedaan worden in röntgen-, optische, en radiostraling. Alleen door de informatie uit waarnemingen van al deze stralingssoorten op een aantal verschillende tijdstippen met elkaar te combineren, kunnen alle eigenschappen van de schok en zijn omgeving bepaald worden.

10.4.1 Energie van de schok en de bron

Een belangrijke eigenschap van de schok die bepaald kan worden is zijn energie. Deze energie in de schok zegt iets over de energie die er bij de vorming van het zwarte gat is vrij gekomen. De laatstgenoemde energie is namelijk minimaal zo groot als de energie in de schok; het zou zelfs veel meer kunnen zijn, afhankelijk van hoe efficiënt de bron is in het produceren van de jet. Daarnaast kan er nog allerlei energie verloren gaan op het moment dat de materie-uitstroom versneld wordt en de jet nog niet waargenomen kan worden. De energie van de schok geeft dus een minimale hoeveelheid energie die er geproduceerd wordt, en dat is een belangrijk gegeven voor de modellen voor de bronnen van gammaflitsers. Het geeft bijvoorbeeld aan wat voor soort eigenschappen de zware sterren moeten hebben die een lange gammaflitser produceren, en ook welke bronnen de juiste eigenschappen hebben om korte gammaflitsers te produceren.

Hoeveel energie er echt geproduceerd wordt door de bron en welke fractie daarvan uiteindelijk door ons waargenomen wordt, is iets dat met de huidige waarnemingen niet opgelost kan worden, maar waar in de komende jaren mogelijk wel antwoorden op gevonden kunnen worden. Er worden namelijk op dit moment detectoren gebouwd, of zijn zelfs al (deels) in gebruik, die andere vormen van straling kunnen detecteren, zoals gammastraling met energieën die nog hoger zijn dan de energieën die we nu kunnen meten; maar ook zwaartekrachtsstraling, die geproduceerd wordt op het moment dat er sprake is van extreme zwaartekracht, bijvoorbeeld bij twee compacte objecten die om elkaar heen draaien en op elkaar botsen, zoals wordt verwacht voor (een deel van) de korte gammaflitsers. Daarnaast worden er ook detectoren gebouwd om “exotische” deeltjes uit de ruimte te detecteren, zoals de zogenaamde neutrino’s, bijna gewichtsloze deeltjes die heel moeilijk te detecteren zijn omdat ze bijna geen interacties aangaan met andere deeltjes. Deze neutrino’s kunnen ons een nieuwe blik geven op de processen die een rol spelen bij de vorming van het zwarte gat en in de materiestroom.

10.4.2 De jet en zijn omgeving

Uit de waarnemingen van nagloeiers kan vrij direct een eigenschap van de jet afgeleid worden, namelijk de openingshoek van de nauwe bundel. Deze openingshoek varieert per bron, van een paar graden tot enkele tientallen graden, en is belangrijk in het precies bepalen van de hoeveelheid energie die de schok heeft. Naast de openingshoek van de jet, kan in sommige gevallen ook de structuur van de jet bepaald worden. Met de structuur van de jet wordt bedoeld of de materie overal in de jet even snel stroomt en of de energie gelijkmatig over alle materie verdeeld is, of dat de materie in het midden van de jet meer energie heeft dan de buitenkant (of juist andersom). Deze structuur is lastig te bepalen, maar wel belangrijk voor modellen die het produceren van de jet beschrijven.

Van de materie waar de jet in voortbeweegt kan zowel de dichtheid als de structuur bepaald worden. Die opgeveegde materie is in het geval van een lange gammaflitser de sterrenwind die de ster aan het einde van zijn leven langzaam heeft weggeblazen (Figuur 10.7). Ook de zon heeft een sterrenwind, de zonnewind, maar deze is lang niet zo sterk als de sterrenwind van de zware sterren die lange gammaflitsers produceren. In het geval van korte gammaflitsers, aangenomen dat ze ontstaan bij de botsing van twee compacte objecten, wordt er interstellaire materie opgeveegd, de losse materie die tussen de sterren zweeft. De dichtheid van de massieve sterrenwind is voor veel lange gammaflitsers bepaald. Er zijn daarentegen nog niet zoveel nagloeiers van korte gammaflitsers geweest waarbij veel verschillende stralingssoorten zijn gedetecteerd, zodat

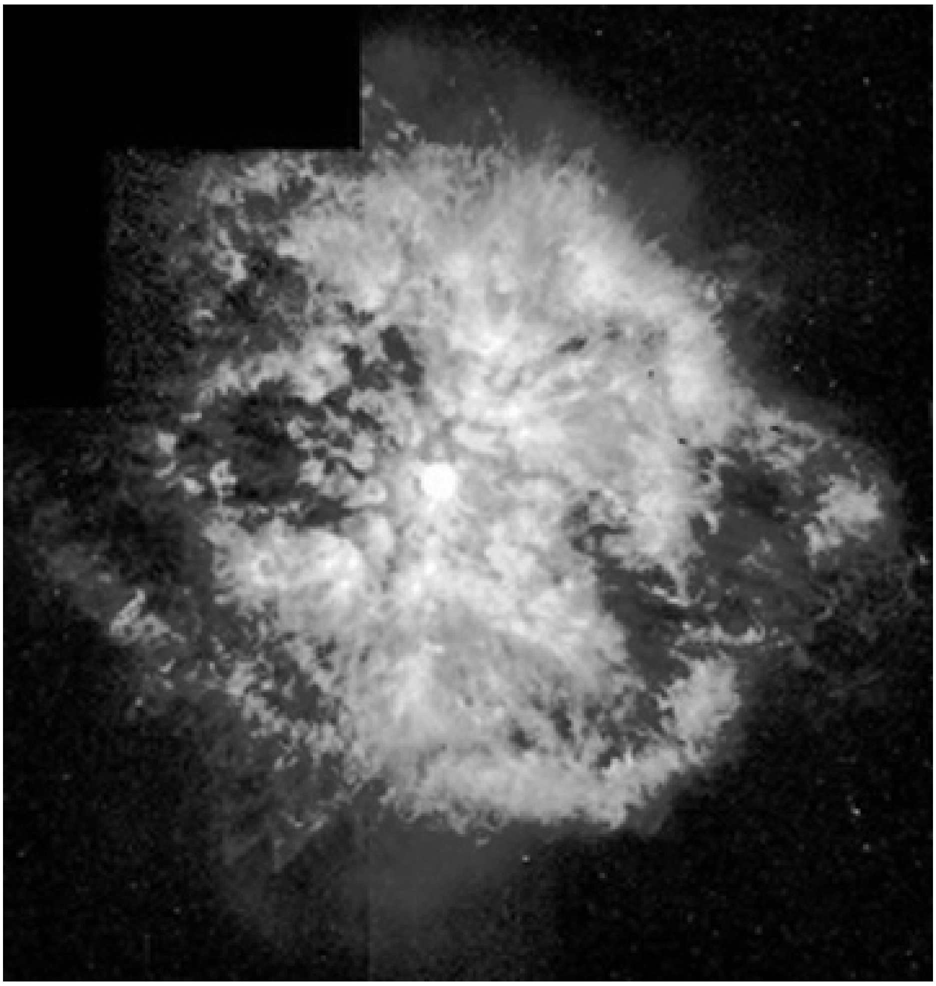

Figure 10.7 — Een zware ster, met de naam M1-67, in de nadagen van haar leven. De ster heeft al veel materiaal uit haar buitenlagen weggeblazen door middel van een sterrenwind. Het is goed te zien dat de weggeblazen materie niet gelijkmatig verdeeld is, maar dat er complexe structuren zijn ontstaan. Deze complexiteit wordt onder andere veroorzaakt door de interacties tussen de sterrenwind en de interstellaire materie.

de dichtheid van de interstellaire materie rondom deze objecten slechts enkele keren is bepaald.

De structuur van de materie waar de schok doorheen gaat, is ook verschillend voor korte en lange gammaflitsers. Interstellaire materie is gelijkmatig verspreid, oftewel homogeen, terwijl dit voor een sterrenwind niet het geval is. Een sterrenwind heeft een structuur dusdanig dat naar buiten toe, vanaf de centrale ster gezien, de dichtheid afneemt, en wel op een zeer karakteristieke manier. Deze karakteristieke manier van afnemen van de dichtheid wordt echter lang niet altijd waargenomen. De verklaring hiervoor is dat de sterrenwind interstellaire materie opveegt, waarna ook daar schokken gevormd kunnen worden. Deze schokken kunnen de structuur van het medium waar de schok van de nagloeier doorheen beweegt zeer gecompliceerd maken. De structuur kan zelfs zo veranderen dat het homogeen wordt, waardoor het gaat lijken op het interstellaire medium, terwijl het dat niet is. Hoe de structuur verandert hangt af van de dichtheid van het interstellaire medium, maar ook van eigenschappen van de sterrenwind. Het bestuderen van de structuur van het medium kan ons dus iets leren over het leven van de ster voordat zij aan het einde van haar leven kwam en een gammaflitser produceerde.

10.4.3 Kosmische deeltjesversnellers

Om de straling te kunnen produceren die wij waarnemen, moeten er in de schok een aantal natuurkundige processen plaats vinden die wij op aarde moeilijk, of zelfs helemaal niet, kunnen nabootsen. Zo moeten er elementaire deeltjes, zoals electronen, in grote hoeveelheden versneld worden tot snelheden van bijna de lichtsnelheid, en moeten er ook sterke magneetvelden aanwezig zijn. Over de details van hoe de deeltjes versneld worden en hoe de magneetvelden zo sterk gemaakt worden, is weinig bekend. Er zijn in ruwe lijnen wel modellen voor, maar voor de precieze uitwerkingen zijn grootschalige computersimulaties nodig, omdat er zoveel natuurkundige processen een rol spelen. Met de huidige computers zijn hier al wel eerste stappen in gemaakt, maar het blijkt lastig te zijn om de resultaten van die simulaties in overeenstemming te brengen met de waarnemingen. Er wordt bijvoorbeeld verwacht dat door de schok een zeer sterk magneetveld wordt geproduceerd. Computersimulaties laten zien dat dit inderdaad mogelijk is, maar dat het magneetveld achter de schok dan ook weer snel in sterkte afneemt, terwijl de waarnemingen ons lijken te vertellen dat de magneetvelden over een veel grotere lengte hun sterkte behouden.

Deeltjesversnelling komt in heel veel verschillende soorten bronnen in het heelal voor. Op aarde zijn daar grote deeltjesversnellers voor gebouwd, maar in het heelal kunnen we dat op veel verschillende plekken ook zien gebeuren. Zo ook bij de schokken van gammaflitsers, waar electronen versneld worden, maar waarvan de details niet goed bekend zijn. Bij de computersimulaties die hiervan gedaan worden blijken de aannames cruciaal te zijn die gedaan worden over welke processen wel of niet belangrijk zijn. Zo zijn er simulaties die aangeven dat de mechanismen voor deeltjesversnelling voor alle gammaflitsers hetzelfde moeten zijn, en dat die mechanismen zodanig zijn, dat de snelheden waar de electronen naar versneld worden altijd op dezelfde manier verdeeld zijn over alle electronen. Er zijn echter ook simulaties waar iets heel anders uit blijkt, namelijk dat er allerlei verschillende snelheidsverdelingen mogelijk zijn. Gedetailleerde waarnemingen, analyses en simulaties moeten hier uiteindelijk uitsluitsel over kunnen geven.

10.5 Dit proefschrift

In dit proefschrift begin ik met een theoretische beschrijving van het schokmodel voor de nagloeiers van gammaflitsers, en pas ik dit vervolgens toe op verschillende nagloeiers. Naast dit theoretische werk en modelleren van verschillende nagloeiers om de eigenschappen te bepalen van de gammaflitsers en zijn nabije omgeving, heb ik ook waarnemingen gedaan van een groot aantal radionagloeiers met de Westerbork Synthese Radio Telescoop (Figuur 10.8), waarvan de meest opvallende resultaten ook in dit proefschrift zijn opgenomen.

In *Hoofdstuk 1* leid ik mijn proefschrift in, op een soortgelijke wijze als ik dat in deze samenvatting gedaan heb. De theoretische basis van dit proefschrift is *Hoofdstuk 2*, waarin we alle vergelijkingen afleiden voor de stralingsmechanismen en de evolutie van de schok. Daarnaast geven we ook de methode die we gebruiken voor het modelleren van de waarnemingen, oftewel hoe uit alle waarnemingen van al die verschillende stralingssoorten de eigenschappen van de schok en zijn omgeving te bepalen zijn. Hierbij besteden we veel aandacht aan de structuur van de materie die de schok opveegt, wat nog nooit eerder in dergelijk detail is gebeurd. We bepalen die eigenschappen voor het klassieke voorbeeld van de nagloeier van 8 mei 1997, en vinden met grote nauwkeurigheid dat de materie rondom de schok in dit geval homogeen verdeeld is. *Hoofdstuk 3* borduurt hier op voort, door voor tien nagloeiers, waaronder die van 8 mei 1997, uit alleen de optische en röntgenwaarnemingen de structuur van het omringende medium en de snelheidsverdeling van de electronen te bepalen. Wij laten zien dat voor deze tien nagloeiers alleen die van 8 mei 1997 beschreven kan worden met materie dat homogeen verdeeld is, en dat voor vier anderen de structuur er uit ziet als een sterrenwind. Voor de overige vijf waren de waarnemingen niet nauwkeurig genoeg, om de structuur precies te kunnen bepalen. We tonen ook aan dat voor deze tien nagloeiers de snelheden van de electronen in de schok niet op dezelfde manier verdeeld zijn over alle electronen. Dit resultaat is belangrijk voor de computersimulaties voor deeltjesversnelling die gedaan worden.

In de *Hoofdstukken 4 & 5* presenteren we de resultaten van meer dan drie jaar waarnemingen met de Westerbork Synthese Radio Telescoop van de radionagloeier van de gammaflitser van 29 maart 2003. In *Hoofdstuk 5* presenteren we

Figure 10.8 — Luchtfoto van de Westerbork Synthese Radio Telescoop in het Drentse Westerbork. De veertien radiotelescopen, met elke een diameter van 25 meter, vormen samen één van de beste radiotelescopen ter wereld. Het is zelfs één van de weinige radiotelescopen in de wereld die gevoelig genoeg kan meten om de nagloeiers van gammaflitsers te detecteren. Een aantal hoofdstukken in dit proefschrift is gebaseerd op waarnemingen die zijn gedaan met deze telescoop.

ook nog waarnemingen van dezelfde nagloeier met de Giant Metrewave Radio Telescoop in India. Met deze gigantische hoeveelheid waarnemingen kunnen we de eigenschappen van de schok volgen van 1 tot 1128 dagen na de gammaflits, wat nog nooit eerder voor een nagloeier mogelijk was. We vergelijken de resultaten van het bestuderen van de schok als hij bijna met de lichtsnelheid beweegt, dus relativistisch is, en wanneer hij niet meer relativistisch is. Op die manier kunnen we zeer nauwkeurig de energie van de schok bepalen, en ook in detail bestuderen wat er gebeurt als de jet zijwaarts gaat expanderen. Deze bron is de enige nagloeier van een gammaflitser waarvoor het ook mogelijk was om met radiowaarnemingen de grootte van de bron te meten en te zien veranderen, en we vergelijken die resultaten met de resultaten van onze waarnemingen.

Ook in *Hoofdstuk 6* zijn waarnemingen met de Westerbork Synthese Radio Telescoop verwerkt, en wel van een zogenaamde donkere gammaflitser. Deze gammaflitser was zeer helder in röntgen- en radiostraling, maar er is geen optische straling gedetecteerd, vandaar de term "donker". Dit is al voor meer gammaflitsers gezien, al is dit één van de weinigen die wel een radionagloeier heeft. De vraag is of deze donkere nagloeiers zelf weinig optische straling uitzenden, of dat deze straling geabsorbeerd wordt door de zeer dichte materie er omheen. Doordat we voor deze gammaflitser veel röntgen- en radiowaarnemingen hebben, kunnen we bijna alle eigenschappen van de schok en de materie eromheen bepalen. We laten ook zien dat het gebrek aan optische straling in dit geval verklaard kan worden met een grote hoeveelheid absorptie van de straling door zeer dichte materie om de bron heen.

De *Hoofdstukken 7 & 8* zijn de resultaten van studies naar twee nagloeiers, die zijn gedetecteerd met de Swift satelliet. Door de komst van Swift en robotische optische telescopen zijn er nu heel veel waarnemingen van nagloeiers in de eerste minuten en uren na de gammaflits. Deze vroege waarnemingen laten allerlei nieuwe fenomenen zien, zoals röntgenflitsen en langere activiteit van de bron (soms uren in plaats van seconden). De röntgenwaarnemingen van Swift op latere tijden lijken er op te wijzen dat gammaflitsers helemaal niet zulke nauwe jets hebben als gedacht, als ze er al zijn. In *Hoofdstuk 7* laten we echter zien dat hier pas echt conclusies over kunnen worden getrokken als zowel naar optische als röntgenwaarnemingen wordt gekeken. Dit kan alleen goed gebeuren als er minimaal waarnemingen zijn tot een paar dagen na de gammaflits, wat helaas lang niet altijd mogelijk is. In *Hoofdstuk 8* worden optische en röntgenwaarnemingen gepresenteerd en geanalyseerd in de eerste uren na een bepaalde gammaflitser. We presenteren een methode om de zoveel mogelijk informatie te halen uit waarnemingen met veel verschillende optische telescopen, en bepalen ook voor de nagloeier de eigenschappen van de schok en zijn omgeving.

Hoofdstuk 9 is het laatste hoofdstuk, waarin we de resultaten presenteren van de radiowaarnemingen die wij gedaan hebben van de helderste superflits van een gammaflikkeraar ooit. Deze nagloeier hebben we waargenomen met een aantal verschillende radiotelescopen over de hele wereld, waaronder de Westerbork Synthese Radio Telescoop, en we laten zien dat het een heldere bron is die zwakker wordt in de tijd, maar ook groter wordt. Het model wat we gebruiken om deze nagloeier te verklaren is ook een schokmodel, dat in grote lijnen het zelfde is als het schokmodel voor de nagloeier van gammaflitsers. Er zijn wel wat verschillen, namelijk dat de schok niet zo een hoge snelheid heeft als die van gammaflitsers, en dat er minder energie door de bron vrij gemaakt wordt.

Dankwoord

Dit proefschrift is het resultaat van vier jaar onderzoek op een fantastisch instituut. Ik heb in die periode mogen samenwerken met heel veel goede, leuke en gezellige mensen, zowel op het instituut als daar buiten. Ik wil een aantal personen speciaal bedanken voor alles wat zij voor mij betekend hebben. Als eerste is dat Ralph Wijers, die mij de afgelopen vier jaar begeleid heeft en mij heel veel heeft geleerd over het doen van sterrenkundig onderzoek. Ralph, jouw enorme enthousiasme voor de sterrenkunde, en vele andere zaken in het leven, hebben zeer zeker bijgedragen tot mijn plezier in het doen van onderzoek. Ik wil je graag heel hartelijk bedanken voor alle mogelijkheden die je mij hebt geboden om aan interessante projecten te werken, en de ruimte die je me hebt gegeven om mezelf in allerlei richtingen te ontplooien.

Ik wil ook graag alle (ex-)leden van de GRB-groep op het API bedanken voor een meer dan plezierige samenwerking, en in het bijzonder Evert Rol, Klaas Wiersema, Rhaana Starling en Peter Curran. Jullie zijn niet alleen zeer goede collega's met wie het fijn werken is, maar jullie zijn ook geweldige mensen naast het werk. I would like to thank Chryssa Kouveliotou for her contributions to my work, the things she has tought me and opportunities she has offered me. Chryssa, I am looking forward to go to Huntsville and work on the latest opportunity you have offered me.

In dit proefschrift zijn veel waarnemingen met de WSRT verwerkt en mijn dank is groot naar een aantal mensen die mij geholpen hebben bij het verkrijgen en verwerken van de data, in het bijzonder Richard Strom. Richard, je hebt me veel geleerd over radiowaarnemingen en je bent altijd een grote steun geweest bij het GRB-project op WSRT. Tevens wil ik Tom Oosterloo en Rob Fender bedanken voor hun lessen in radiodata-analyse. Mijn dank gaat ook zeker uit naar de twee heren die ik altijd kon bellen als er een GRB waargenomen moest worden en dan ook altijd zeer behulpzaam waren: Tony Foley en Rene Vermeulen. Daarnaast wil ik ook de WSRT-waarnemers, Bert Harms, Geert Kuper en Jurjen Sluman, bedanken voor de zeer prettige samenwerking. Furthermore, I would like to thank the GMRT GRB-group, Dipankar Bhattacharya, Atish Kamble and Resmi, for the nice projects we have done together.

I cannot thank all the people I've worked with in the last four years in person, but I've enjoyed all the collaborations, conferences and working visits, and I'ld like to thank all my collaborators and other GRB friends for that. It is also not possible to thank everyone at the API and all the ex-APIs of the past four years in person. I've always enjoyed the great atmoshpere at the institute, the coffee table, cola breaks, ping games, Sinterklaas parties, quizzes, squash tournaments, etcetera. It’s a fantastic place to work and thank you all for making it like that.

Naast al deze collega’s en vrienden gaat mijn dank uit naar mijn familie en vrienden die mijn leven kleur geven. Een aantal daarvan zijn helaas niet meer in ons midden, maar ik wil van hun in het bijzonder mijn vader en mijn opa noemen, omdat zij altijd een zeer belangrijke rol in mijn leven hebben gespeeld en zullen blijven spelen. Het is fijn om te weten dat je een thuis hebt waar mensen zijn die je steunen in alles wat je doet. Daarvoor wil ik mijn broertje en mijn moeder uit de grond van mijn hart bedanken. Mama, dit boekwerkje is voor u, omdat u altijd een fantastische moeder voor mij bent geweest en ook altijd zult blijven.

List of publications

Refereed publications

Broadband modeling of gamma-ray burst afterglows: GRB 970508 revisited
A.J. van der Horst, R.A.M.J. Wijers & L.J. van den Horn
Submitted to Astronomy & Astrophysics

GRB 030329: three years of radio afterglow monitoring
A.J. van der Horst, A. Kamble, L. Resmi, R.A.M.J. Wijers, D. Bhattacharya, B. Scheers, E. Rol, R. Strom, C. Kouveliotou, T. Oosterloo & C.H. Ishwara-Chandra
Submitted to Astronomy & Astrophysics

Gamma-ray burst afterglows as probes of environment and blast wave physics II: circumburst media and the distribution of p
R.L.C. Starling, **A.J. van der Horst**, E. Rol, R.A.M.J. Wijers, C. Kouveliotou, K. Wiersema, P. Curran & P. Weltevrede
Submitted to Astrophysical Journal

Spectroscopy and multiband photometry of the afterglow of intermediate duration gamma-ray burst 040924 and its host galaxy
K. Wiersema, **A.J. van der Horst**, D.A. Kann, E. Rol, R.L.C. Starling, P.A. Curran, J. Gorosabel, A.J. Levan, J.P.U. Fynbo, A. de Ugarte Postigo, R.A.M.J. Wijers, A.J. Castro-Tirado, S. Guziy, A. Hornstrup, J. Hjorth, M. Jelínek, B.L. Jensen, M. Kidger, F. Martín-Luis, N.R. Tanvir, P. Tristram & P.M. Vreeswijk
Submitted to Astronomy & Astrophysics

Radio observations of candidate magnetic O stars
R.S. Schnerr, K.L.J. Rygl, **A.J. van der Horst**, T.A. Oosterloo, J.C.A. Miller-Jones, H.F. Henrichs, T.A.Th. Spoelstra & A.R. Foley
Submitted to Astronomy & Astrophysics

GRB 060206 and the quandary of achromatic breaks in afterglow light curves
P.A. Curran, **A.J. van der Horst**, R.A.M.J. Wijers, R.L.C. Starling, A.J. Castro-Tirado, J.P.U. Fynbo, J. Gorosabel, A.S. Järvinen, D. Malesani, E. Rol, N.R. Tanvir, K. Wiersema, M.R. Burleigh, S.L. Casewell, P.D. Dobbie, S. Guziy, P. Jakobsson, M. Jelínek, P. Laursen, A.J. Levan, C.G. Mundell, J. Näränen & S. Piranomonte
Accepted for Publication, Monthly Notices of the Royal Astronomical Society

GRB 051022: physical parameters and extinction of a prototype dark burst
E. Rol, **A.J. van der Horst**, K. Wiersema, S.K. Patel, A. Levan, M. Nysewander, C. Kouveliotou, R.A.M.J. Wijers, N. Tanvir, D. Reichart, A.S. Fruchter, J. Graham, R.L.C. Starling, P.T. O'Brien, J. Hjorth, J. Fynbo, P. Jonker, W. van Ham, D.N. Burrows, J.-E. Ovaldsen, A.O. Jaunsen & R. Strom
Accepted for Publication, Astrophysical Journal

The prompt to late-time multiwavelength analysis of GRB 060210
P.A. Curran, **A.J. van der Horst**, A.P. Beardmore, K.L. Page, E. Rol, A. Melandri, I.A. Steele, C.G. Mundell, A. Gomboc, P.T. O'Brien, D.F. Bersier, M.F. Bode, D. Carter, C. Guidorzi, J.E. Hill, C.P. Hurkett, S. Kobayashi, A. Monfardini, C.J. Mottram, R.J. Smith, R.A.M.J. Wijers & R. Willingale
2007, Astronomy & Astrophysics, 467, 1049

Gamma-ray burst afterglows as probes of environment and blast wave physics I: absorption by host galaxy gas and dust
R.L.C. Starling, R.A.M.J. Wijers, K. Wiersema, P. Curran, E. Rol, C. Kouveliotou, **A.J. van der Horst** & M.H.M. Heemskerk
2007, Astrophysical Journal, 661, 787

Prompt and afterglow emission properties of gamma-ray bursts with spectroscopically identified supernovae
Y. Kaneko, E. Ramirez-Ruiz, J. Granot, C. Kouveliotou, S.E. Woosley, S.K. Patel, E. Rol, J.J.M. in 't Zand, **A.J. van der Horst**, R.A.M.J. Wijers & R. Strom
2007, Astrophysical Journal, 654, 385

The radio afterglow of GRB 030329 at centimeter wavelengths: evidence for a structured jet or non-relativistic expansion
A.J. van der Horst, E. Rol, R.A.M.J. Wijers, R. Strom, L. Kaper & C. Kouveliotou
2005, Astrophysical Journal, 634, 1166

An expanding radio nebula produced by a giant flare from the magnetar SGR 1806-20
B.M. Gaensler, C. Kouveliotou, J.D. Gelfand, G.B. Taylor, D. Eichler, R.A.M.J. Wijers, J. Granot, E. Ramirez-Ruiz, Y.E. Lyubarsky, R.W. Hunstead, D. Campbell-Wilson, **A.J. van der Horst**, M.A. McLaughlin, R.P. Fender, M.A. Garrett, K.J. Newton-McGee, D.M. Palmer, N. Gehrels & P.M. Woods
2005, Nature, 434, 1104

Conference proceedings

Probing gamma-ray burst environments via their spectral energy distributions
R.L.C. Starling, R.A.M.J. Wijers, K. Wiersema, E. Rol, P. Curran, C. Kouveliotou & **A.J. van der Horst**
Proceedings of the Meeting "070228: The Next Decade of GRB Afterglows"

GRB 030329: three years of radio afterglow monitoring
A.J. van der Horst, A. Kamble, R.A.M.J. Wijers, L. Resmi, D. Bhattacharya, E. Rol, R. Strom, C. Kouveliotou, T. Oosterloo & C.H. Ishwara-Chandra
2007, Philosophical Transactions of the Royal Society A, 365, 1241
Proceedings of the Royal Society Scientific Discussion Meeting "Recent developments in the study of Gamma-Ray Bursts"

GRB 030329: three years of radio afterglow monitoring
A.J. van der Horst, A. Kamble, R.A.M.J. Wijers, L. Resmi, D. Bhattacharya, E. Rol, R. Strom, C. Kouveliotou, T. Oosterloo & C.H. Ishwara-Chandra
Accepted for publication in Il Nuovo Cimento B, 121
Proceedings of the Congress "Swift and GRBs: Unveiling the Relativistic Universe"

Radio observations of candidate magnetic O stars
R.S. Schnerr, K.L.J. Rygl, **A.J. van der Horst**, T.A. Oosterloo, J.C.A. Miller-Jones & H.F. Henrichs
Proceedings of the Meeting "Mass loss from stars and the evolution of stellar clusters"

Radio afterglows of gamma-ray bursts
A.J. van der Horst
2005, Memorie della Societa Astronomica Italiana, 76, 635
Proceedings of the Workshop "Stellar end products"

Broadband modeling of gamma-ray burst afterglows
A.J. van der Horst, R.A.M.J. Wijers & E. Rol
2005, Il Nuovo Cimento C, 28, 467
Proceedings of the 4th Workshop "Gamma-Ray Bursts In the Afterglow Era"

GRB Coordinates Network Circulars

GRB 070612A: second epoch WSRT radio observations
A.J. van der Horst, R.A.M.J. Wijers, K. Wiersema & E. Rol
2007, GCN Circular 6576

GRB 070612A: possible WSRT radio detection
A.J. van der Horst, R.A.M.J. Wijers, K. Wiersema & E. Rol
2007, GCN Circular 6549

GRB 070125: WSRT radio detection
A.J. van der Horst
2007, GCN Circular 6063

GRB 070125: WSRT radio observations
A.J. van der Horst
2007, GCN Circular 6042

GRB 061121: second epoch ATCA radio observations
A.J. van der Horst, R.A.M.J. Wijers & E. Rol
2006, GCN Circular 5874

GRB 061121: ATCA & WSRT radio observations
A.J. van der Horst, R.A.M.J. Wijers & E. Rol
2006, GCN Circular 5871

GRB 061007: third epoch ATCA radio observations
A.J. van der Horst, R.A.M.J. Wijers & E. Rol
2006, GCN Circular 5787

GRB 061007: second epoch ATCA radio observations
A.J. van der Horst & E. Rol
2006, GCN Circular 5726

GRB 061007: ATCA radio observations
A.J. van der Horst & E. Rol
2006, GCN Circular 5720

GRB 060801: second epoch WSRT radio observations
A.J. van der Horst
2006, GCN Circular 5408

GRB 060801: WSRT radio observations
A.J. van der Horst
2006, GCN Circular 5390

GRB 060206: WSRT radio observations
A.J. van der Horst
2006, GCN Circular 4715

GRB 051221A: WSRT radio observations
A.J. van der Horst
2005, GCN Circular 4385

GRB 051022: WSRT radio detection
A.J. van der Horst, E. Rol & R.A.M.J. Wijers
2005, GCN Circular 4158

GRB 050925: second epoch WSRT radio observations
A.J. van der Horst
2005, GCN Circular 4057

GRB 050925: WSRT radio observations
A.J. van der Horst
2005, GCN Circular 4039

GRB 050730: third epoch WSRT radio observations
A.J. van der Horst & E. Rol
2005, GCN Circular 3810

GRB 050730: WSRT radio observations
A.J. van der Horst & E. Rol
2005, GCN Circular 3781

GRB 050509B: WSRT radio observations
A.J. van der Horst, K. Wiersema & R.A.M.J. Wijers
2005, GCN Circular 3405

GRB 050502A: WSRT radio observations
A.J. van der Horst, R.A.M.J. Wijers & K. Wiersema
2005, GCN Circular 3341

GRB 041219: second epoch WSRT radio observations
A.J. van der Horst, E. Rol & R. Strom
2005, GCN Circular 2759

GRB 041219: WSRT radio afterglow detection
A.J. van der Horst, E. Rol & R. Strom
2005, GCN Circular 2894

GRB 040924: second epoch WSRT radio observations
A.J. van der Horst, E. Rol & R.A.M.J. Wijers
2005, GCN Circular 2759

GRB 040924: WSRT radio observations
A.J. van der Horst, E. Rol & R.A.M.J. Wijers
2005, GCN Circular 2746

Bibliography

Abbey, T., Carpenter, J., Read, A., et al. 2006, in ESA SP-604: The X-ray Universe 2005, ed. A. Wilson, 943

Achterberg, A., Gallant, Y. A., Kirk, J. G., & Guthmann, A. W. 2001, MNRAS, 328, 393

Akerlof, C., Balsano, R., Barthelmy, S., et al. 1999, Nature, 398, 400

Alard, C. 2000, A&AS, 144, 363

Alatalo, K., Perley, D., & Bloom, J. S. 2006, GRB Coordinates Network, 4702

Amati, L. 2006, MNRAS, 372, 233

Amati, L., Frontera, F., Tavani, M., et al. 2002, A&A, 390, 81

Arnaud, K. A. 1996, in Astronomical Society of the Pacific Conference Series, Vol. 101, Astronomical Data Analysis Software and Systems V, ed. G. H. Jacoby & J. Barnes, 17

Arzoumanian, Z., Chernoff, D. F., & Cordes, J. M. 2002, ApJ, 568, 289

Band, D., Matteson, J., Ford, L., et al. 1993, ApJ, 413, 281

Baring, M. G. 2004, Nuclear Physics B Proceedings Supplements, 136, 198

Barraud, C., Olive, J.-F., Lestrade, J. P., et al. 2003, A&A, 400, 1021

Barthelmy, S. D., Barbier, L. M., Cummings, J. R., et al. 2005, Space Science Reviews, 120, 143

Beardmore, A., Barthelmy, S., Boyd, P., et al. 2006, GRB Coordinates Network, 4724

Berger, E. 2007, ArXiv Astrophysics e-prints 0702694

Berger, E., Cowie, L. L., Kulkarni, S. R., et al. 2003a, ApJ, 588, 99

Berger, E., Kulkarni, S. R., Fox, D. B., et al. 2005a, ApJ, 634, 501

Berger, E., Kulkarni, S. R., Pooley, G., et al. 2003b, Nature, 426, 154

Berger, E., Price, P. A., Cenko, S. B., et al. 2005b, Nature, 438, 988

Berger, E. & Wyatt, P. 2005, GRB Coordinates Network, 4148

Bhat, P. N., Fishman, G. J., Meegan, C. A., et al. 1994, ApJ, 426, 604

Bhattacharya, D. 2001, Bulletin of the Astronomical Society of India, 29, 107

Bhattacharya, D. & Resmi, L. 2004, in Astronomical Society of the Pacific Conference Series, Vol. 312, Astronomical Society of the Pacific Conference Series, ed. M. Feroci, F. Frontera, N. Masetti, & L. Piro, 411

Björnsson, G., Hjorth, J., Pedersen, K., & Fynbo, J. U. 2002, ApJ, 579, L59

Blandford, R. D. & McKee, C. F. 1976, Physics of Fluids, 19, 1130

Bloom, J. S., Frail, D. A., Kulkarni, S. R., et al. 1998, ApJ, 508, L21

Bloom, J. S., Frail, D. A., & Sari, R. 2001, AJ, 121, 2879

Bloom, J. S., Kulkarni, S. R., Djorgovski, S. G., et al. 1999, Nature, 401, 453

Boggs, S. E., Zoglauer, A., Bellm, E., et al. 2007, ApJ, 661, 458

Bolzonella, M., Miralles, J.-M., & Pelló, R. 2000, A&A, 363, 476

Borkowski, J., Gotz, D., Mereghetti, S., et al. 2004, GRB Coordinates Network, 2920

Bremer, M., Castro-Tirado, A. J., & Neri, R. 2005, GRB Coordinates Network, 4157

Bremer, M., Krichbaum, T. P., Galama, T. J., et al. 1998, A&A, 332, L13

Brown, J. C., Taylor, A. R., & Jackel, B. J. 2003, ApJS, 145, 213

Burrows, D. N., Hill, J. E., Nousek, J. A., et al. 2005, Space Science Reviews, 120, 165

Burrows, D. N. & Racusin, J. 2007, Il Nuovo Cimento C, in press (ArXiv Astrophysics e-prints 0702633)

Butler, N. R., Ricker, G. R., Lamb, D. Q., et al. 2005a, GRB Coordinates Network, 4165

Butler, N. R., Ricker, G. R., Lamb, D. Q., et al. 2005b, GRB Coordinates Network, 4170

Cameron, P. B. & Frail, D. A. 2005, GRB Coordinates Network, 4154

Campbell, P., Hill, M., Howe, R., et al. 2005, GRB Coordinates Network, 2932

Castro-Tirado, A. J., McBreen, S., Jelínek, M., et al. 2006, in American Institute of Physics Conference Series, Vol. 836, Gamma-Ray Bursts in the Swift Era, ed. S. S. Holt, N. Gehrels, & J. A. Nousek, 79–84

Cavallo, G. & Rees, M. J. 1978, MNRAS, 183, 359

Chandra, P. 2005, GRB Coordinates Network, 2947

Chary, R., Neugebauer, G., Morris, M., et al. 1998, ApJ, 498, L9

Cheng, K. S. & Wang, X. Y. 2003, ApJ, 593, L85

Chevalier, R. A. & Li, Z.-Y. 1999, ApJ, 520, L29

Chevalier, R. A. & Li, Z.-Y. 2000, ApJ, 536, 195

Christensen, L., Hjorth, J., & Gorosabel, J. 2005, ApJ, 631, L29

Colgate, S. A. 1968, Canadian Journal of Physics, 46, 476

Corbel, S. & Eikenberry, S. S. 2004, A&A, 419, 191

Cordes, J. M. & Lazio, T. J. W. 2002, ArXiv Astrophysics e-prints 0207156

Costa, E., Frontera, F., Heise, J., et al. 1997, Nature, 387, 783

Cucchiara, A., Fox, D. B., & Berger, E. 2006, GRB Coordinates Network, 4729

Curran, P. A., Kann, D. A., Ferrero, P., Rol, E., & Wijers, R. A. M. J. 2006, ArXiv Astrophysics e-prints 0610067

Curran, P. A., van der Horst, A. J., Beardmore, A. P., et al. 2007, A&A, 467, 1049

Dai, X. & Stanek, K. Z. 2006, GRB Coordinates Network, 5147

Dai, Z. G. & Lu, T. 2002, ApJ, 565, L87

de Pasquale, M., Piro, L., Gendre, B., et al. 2006, A&A, 455, 813

Dickey, J. M. & Lockman, F. J. 1990, ARA&A, 28, 215
Djorgovski, S. G., Frail, D. A., Kulkarni, S. R., et al. 2001, ApJ, 562, 654
Draine, B. T. & Hao, L. 2002, ApJ, 569, 780
Duncan, R. C. & Thompson, C. 1992, ApJ, 392, L9
Eldridge, J. J. 2007, MNRAS, 377, L29
Evans, P. A., Beardmore, A. P., Page, K. L., et al. 2007, A&A, 469, 379
Fender, R., Braun, R., Stappers, B., et al. 2006a, ArXiv Astrophysics e-prints
Fender, R. P., Muxlow, T. W. B., Garrett, M. A., et al. 2006b, MNRAS, 367, L6
Fitzpatrick, E. L. 1985, ApJ, 299, 219
Fox, D. B. & Cenko, S. B. 2006, GRB Coordinates Network, 4723
Fox, D. B., Frail, D. A., Price, P. A., et al. 2005, Nature, 437, 845
Frail, D. A. 2006, GRB Coordinates Network, 4761
Frail, D. A., Kulkarni, S. R., & Bloom, J. S. 1999, Nature, 398, 127
Frail, D. A., Kulkarni, S. R., Nicastro, L., Feroci, M., & Taylor, G. B. 1997a, Nature, 389, 261
Frail, D. A., Kulkarni, S. R., Sari, R., et al. 2001, ApJ, 562, L55
Frail, D. A., Kulkarni, S. R., Sari, R., et al. 2000a, ApJ, 534, 559
Frail, D. A., Soderberg, A. M., Kulkarni, S. R., et al. 2005, ApJ, 619, 994
Frail, D. A., Vasisht, G., & Kulkarni, S. R. 1997b, ApJ, 480, L129
Frail, D. A., Waxman, E., & Kulkarni, S. R. 2000b, ApJ, 537, 191
Fruchter, A., Burud, I., Rhoads, J., & Levan, A. 2001a, GCN Circulars, 1087
Fruchter, A., Krolik, J. H., & Rhoads, J. E. 2001b, ApJ, 563, 597
Fukugita, M., Ichikawa, T., Gunn, J. E., et al. 1996, AJ, 111, 1748
Fynbo, J. P. U., Starling, R. L. C., Ledoux, C., et al. 2006a, A&A, 451, L47
Fynbo, J. P. U., Watson, D., Thöne, C. C., et al. 2006b, Nature, 444, 1047
Fynbo, J. U., Jensen, B. L., Gorosabel, J., et al. 2001, A&A, 369, 373
Gaensler, B. M., Jones, D. H., & Stappers, B. W. 2002, ApJ, 580, L137
Gal-Yam, A., Berger, E., Fox, D. B., et al. 2005, GRB Coordinates Network, 4156
Galama, T. J., Groot, P. J., van Paradijs, J., et al. 1998a, ApJ, 497, L13
Galama, T. J., Tanvir, N., Vreeswijk, P. M., et al. 2000, ApJ, 536, 185
Galama, T. J., Vreeswijk, P. M., van Paradijs, J., et al. 1998b, Nature, 395, 670
Galama, T. J. & Wijers, R. A. M. J. 2001, ApJ, 549, L209
Galama, T. J., Wijers, R. A. M. J., Bremer, M., et al. 1998c, ApJ, 500, L101
Garcia, M. R., Callanan, P. J., Moraru, D., et al. 1998, ApJ, 500, L105
Gehrels, N., Chincarini, G., Giommi, P., et al. 2004, ApJ, 611, 1005
Gehrels, N., Sarazin, C. L., O'Brien, P. T., et al. 2005, Nature, 437, 851
Gendre, B. & Boër, M. 2005, A&A, 430, 465
Ghirlanda, G., Ghisellini, G., & Lazzati, D. 2004, ApJ, 616, 331

Ginzburg, V. L. & Syrovatskii, S. I. 1965, ARA&A, 3, 297

Golenetskii, S., Aptekar, R., Mazets, E., et al. 2005, GRB Coordinates Network, 4150

Goodman, J. 1997, New Astronomy, 2, 449

Gorosabel, J., Castro-Tirado, A. J., Ramirez-Ruiz, E., et al. 2006, ApJ, 641, L13

Granot, J. 2007, in Revista Mexicana de Astronomia y Astrofisica Conference Series, Vol. 27, Revista Mexicana de Astronomia y Astrofisica, vol. 27, 140–165

Granot, J., Königl, A., & Piran, T. 2006, MNRAS, 370, 1946

Granot, J. & Loeb, A. 2003, ApJ, 593, L81

Granot, J., Nakar, E., & Piran, T. 2003, Nature, 426, 138

Granot, J., Piran, T., & Sari, R. 1999a, ApJ, 513, 679

Granot, J., Piran, T., & Sari, R. 1999b, A&AS, 138, 541

Granot, J., Ramirez-Ruiz, E., & Loeb, A. 2005, ApJ, 618, 413

Granot, J. & Sari, R. 2002, ApJ, 568, 820

Greiner, J., Peimbert, M., Estaban, C., et al. 2003, GCN Circulars, 2020

Groot, P. J., Galama, T. J., van Paradijs, J., et al. 1998, ApJ, 493, L27+

Guidorzi, C., Monfardini, A., Gomboc, A., et al. 2006, PASP, 118, 288

Gunn, J. E. & Peterson, B. A. 1965, ApJ, 142, 1633

Haislip, J. B., Nysewander, M. C., Reichart, D. E., et al. 2006, Nature, 440, 181

Halpern, J. P., Kemp, J., Piran, T., & Bershady, M. A. 1999, ApJ, 517, L105

Hearty, F., Bayliss, M., Lamb, D. Q., et al. 2006, GRB Coordinates Network, 4753

Henden, A. 2005, GRB Coordinates Network, 4184

Hill, J. E., Angelini, L., Morris, D. C., et al. 2005, in UV, X-Ray, and Gamma-Ray Space Instrumentation for Astronomy XIV. Edited by Siegmund, Oswald H. W. Proceedings of the SPIE, Volume 5898, pp. 313-328 (2005)., ed. O. H. W. Siegmund, 313–328

Hill, J. E., Burrows, D. N., Nousek, J. A., et al. 2004, in X-Ray and Gamma-Ray Instrumentation for Astronomy XIII. Edited by Flanagan, Kathryn A.; Siegmund, Oswald H. W. Proceedings of the SPIE, Volume 5165, pp. 217-231 (2004)., ed. K. A. Flanagan & O. H. W. Siegmund, 217–231

Hjorth, J., Sollerman, J., Møller, P., et al. 2003, Nature, 423, 847

Hjorth, J., Watson, D., Fynbo, J. P. U., et al. 2005, Nature, 437, 859

Horváth, I. 1998, ApJ, 508, 757

Houck, J. C. & Denicola, L. A. 2000, in Astronomical Society of the Pacific Conference Series, Vol. 216, Astronomical Data Analysis Software and Systems IX, ed. N. Manset, C. Veillet, & D. Crabtree, 591

Hurley, K., Boggs, S. E., Smith, D. M., et al. 2005, Nature, 434, 1098

Hurley, K., Cline, T., Mazets, E., et al. 1999a, Nature, 397, 41
Hurley, K., Kouveliotou, C., Cline, T., et al. 1999b, ApJ, 523, L37
in 't Zand, J. J. M., Amati, L., Antonelli, L. A., et al. 1998, ApJ, 505, L119
Jakobsson, P., Frail, D. A., Fox, D. B., et al. 2005, ApJ, 629, 45
Jakobsson, P., Fynbo, J. P. U., Ledoux, C., et al. 2006a, A&A, 460, L13
Jakobsson, P., Hjorth, J., Fynbo, J. P. U., et al. 2004, ApJ, 617, L21
Jakobsson, P., Levan, A., Fynbo, J. P. U., et al. 2006b, A&A, 447, 897
Jester, S., Schneider, D. P., Richards, G. T., et al. 2005, AJ, 130, 873
Jóhannesson, G., Björnsson, G., & Gudmundsson, E. H. 2006, ApJ, 640, L5
Kaneko, Y., Ramirez-Ruiz, E., Granot, J., et al. 2007, ApJ, 654, 385
Kaplan, D. L., Fox, D. W., Kulkarni, S. R., et al. 2002, ApJ, 564, 935
Kaplan, S. A. & Tsytovich, V. N. 1973, Plasma astrophysics (International Series of Monographs in Natural Philosophy, Oxford: Pergamon Press, 1973)
King, A., O'Brien, P. T., Goad, M. R., et al. 2005, ApJ, 630, L113
Kirk, J. G., Guthmann, A. W., Gallant, Y. A., & Achterberg, A. 2000, ApJ, 542, 235
Klebesadel, R. W., Strong, I. B., & Olson, R. A. 1973, ApJ, 182, L85
Kobayashi, S. & Zhang, B. 2007, ApJ, 655, 973
Königl, A. & Granot, J. 2002, ApJ, 574, 134
Kouveliotou, C., Dieters, S., Strohmayer, T., et al. 1998, Nature, 393, 235
Kouveliotou, C., Meegan, C. A., Fishman, G. J., et al. 1993, ApJ, 413, L101
Kouveliotou, C., Tennant, A., Woods, P. M., et al. 2001, ApJ, 558, L47
Kulkarni, S. R., Frail, D. A., Sari, R., et al. 1999, ApJ, 522, L97
Kumar, P. & Panaitescu, A. 2000, ApJ, 541, L51
Kuno, N., Sato, N., Nakanishi, H., et al. 2004, PASJ, 56, L1
Kuulkers, E., Antonelli, L. A., Kuiper, L., et al. 2000, ApJ, 538, 638
Lamb, D. Q. 1995, PASP, 107, 1152
Landolt, A. U. 1992, AJ, 104, 340
Laros, J. G., Fenimore, E. E., Klebesadel, R. W., et al. 1987, ApJ, 320, L111
Levan, A., Fruchter, A., Rhoads, J., et al. 2006, ApJ, 647, 471
Li, W. 2006, GRB Coordinates Network, 4727
Li, Z. & Song, L. M. 2004, ApJ, 614, L17
Liang, E. W., Zhang, B., O'Brien, P. T., et al. 2006, ApJ, 646, 351
Lin, L., Koo, D. C., Weiner, B. J., et al. 2007, ApJ, 660, L51
Lipkin, Y. M., Ofek, E. O., Gal-Yam, A., et al. 2004, ApJ, 606, 381
Lorimer, D. R. & Xilouris, K. M. 2000, ApJ, 545, 385
MacFadyen, A. I. & Woosley, S. E. 1999, ApJ, 524, 262
MacFadyen, A. I., Woosley, S. E., & Heger, A. 2001, ApJ, 550, 410
Madau, P. 1995, ApJ, 441, 18

Marshall, F. & Swank, J. H. 2003, GCN Circulars, 1996

Martin, N., Maurice, E., & Lequeux, J. 1989, A&A, 215, 219

Masetti, N., Palazzi, E., Pian, E., et al. 2001, A&A, 374, 382

Mazets, E. P. & Golenetskii, S. V. 1981, Ap&SS, 75, 47

Mazets, E. P., Golentskii, S. V., Ilinskii, V. N., Aptekar, R. L., & Guryan, I. A. 1979, Nature, 282, 587

Meegan, C. A., Fishman, G. J., Wilson, R. B., et al. 1992, Nature, 355, 143

Mészáros, P. & Rees, M. J. 1997, ApJ, 476, 232

Mészáros, P., Rees, M. J., & Wijers, R. A. M. J. 1998, ApJ, 499, 301

Metzger, M. R., Djorgovski, S. G., Kulkarni, S. R., et al. 1997, Nature, 387, 878

Monfardini, A., Kobayashi, S., Guidorzi, C., et al. 2006, ApJ, 648, 1125

Nakagawa, Y. E., Yoshida, A., Sugita, S., et al. 2006, PASJ, 58, L35

Nakar, E. 2007, ArXiv Astrophysics e-prints 0703129

Nakar, E., Piran, T., & Granot, J. 2003, New Astronomy, 8, 495

Nicastro, L., Amati, L., Antonelli, L. A., et al. 1999, A&AS, 138, 437

Nousek, J. A., Kouveliotou, C., Grupe, D., et al. 2006, ApJ, 642, 389

Oates, S. R., Mundell, C. G., Piranomonte, S., et al. 2006, MNRAS, 372, 327

O'Brien, P. T., Willingale, R., Osborne, J., et al. 2006, ApJ, 647, 1213

Odewahn, S. C., Djorgovski, S. G., Kulkarni, S. R., et al. 1997, International Astronomical Union Circulars, 6735

Oke, J. B. & Gunn, J. E. 1983, ApJ, 266, 713

Olive, J.-F., Ricker, G., Atteia, J.-L., et al. 2005, GRB Coordinates Network, 4131

Oren, Y., Nakar, E., & Piran, T. 2004, MNRAS, 353, L35

Ovaldsen, J.-E., Jaunsen, A. O., Fynbo, J. P. U., et al. 2007, ApJ, 662, 294

Pacholczyk, A. G. 1970, Radio astrophysics. Nonthermal processes in galactic and extragalactic sources (Series of Books in Astronomy and Astrophysics, San Francisco: Freeman, 1970)

Paczyński, B. 1995, PASP, 107, 1167

Padoan, P., Cambrésy, L., Juvela, M., et al. 2006, ApJ, 649, 807

Pagani, C., Morris, D. C., Kobayashi, S., et al. 2006, ApJ, 645, 1315

Palmer, D., Barbier, L., Barthelmy, S., et al. 2006, GRB Coordinates Network, 4697

Palmer, D. M., Barthelmy, S., Gehrels, N., et al. 2005, Nature, 434, 1107

Panaitescu, A. & Kumar, P. 2001, ApJ, 560, L49

Panaitescu, A. & Kumar, P. 2002, ApJ, 571, 779

Panaitescu, A., Mészáros, P., Burrows, D., et al. 2006, MNRAS, 369, 2059

Panaitescu, A., Mészáros, P., & Rees, M. J. 1998, ApJ, 503, 314

Patel, S., Kouveliotou, C., & Rol, E. 2005, GRB Coordinates Network, 4163

Pe'er, A. & Wijers, R. A. M. J. 2006, ApJ, 643, 1036

Pei, Y. C. 1992, ApJ, 395, 130

Perley, D. A., Bloom, J. S., Butler, N. R., et al. 2007, ArXiv Astrophysics e-prints 0703538

Pian, E., Soffitta, P., Alessi, A., et al. 2001, A&A, 372, 456

Pihlström, Y. M., Taylor, G. B., Granot, J., & Doeleman, S. 2007, ArXiv Astrophysics e-prints 0704.2085, 704

Piran, T. 2003, Nature, 422, 268

Piro, L., Amati, L., Antonelli, L. A., et al. 1998, A&A, 331, L41

Piro, L., Frail, D. A., Gorosabel, J., et al. 2002, ApJ, 577, 680

Predehl, P. & Schmitt, J. H. M. M. 1995, A&A, 293, 889

Press, W. H., Teukolsky, S. A., Vetterling, W. T., & Flannery, B. P. 1992, Numerical recipes in C. The art of scientific computing (Cambridge: University Press, —c1992, 2nd ed.)

Prochaska, J. X., Chen, H.-W., Dessauges-Zavadsky, M., & Bloom, J. S. 2007, ArXiv Astrophysics e-prints 0703665

Quimby, R. M., Rykoff, E. S., Yost, S. A., et al. 2006, ApJ, 640, 402

Racusin, J., Burrows, D., & Gehrels, N. 2005a, GRB Coordinates Network, 4141

Racusin, J., Kennea, J., Fox, D., et al. 2005b, GRB Coordinates Network, 4169

Ramaprakash, A. N., Kulkarni, S. R., Frail, D. A., et al. 1998, Nature, 393, 43

Ramirez-Ruiz, E., Celotti, A., & Rees, M. J. 2002, MNRAS, 337, 1349

Ramirez-Ruiz, E., Dray, L. M., Madau, P., & Tout, C. A. 2001, MNRAS, 327, 829

Ramirez-Ruiz, E., García-Segura, G., Salmonson, J. D., & Pérez-Rendón, B. 2005, ApJ, 631, 435

Rao, A. P., Ishwara-Chandra, C. H., & Bhattacharya, D. 2003, GCN Circulars, 2073

Rees, M. J. & Mészáros, P. 1992, MNRAS, 258, 41P

Rees, M. J. & Mészáros, P. 1998, ApJ, 496, L1

Resmi, L., Ishwara-Chandra, C. H., Castro-Tirado, A. J., et al. 2005, A&A, 440, 477

Rhoads, J. E. 1997, ApJ, 487, L1

Rhoads, J. E. 1999, ApJ, 525, 737

Ricker, G. R., Atteia, J.-L., Crew, G. B., et al. 2003, in American Institute of Physics Conference Series, Vol. 662, Gamma-Ray Burst and Afterglow Astronomy 2001: A Workshop Celebrating the First Year of the HETE Mission, ed. G. R. Ricker & R. K. Vanderspek, 3–16

Rol, E., Osborne, J. P., Page, K. L., et al. 2007, MNRAS, 374, 1078

Rol, E., Wijers, R. A. M. J., Kouveliotou, C., Kaper, L., & Kaneko, Y. 2005, ApJ, 624, 868

Roming, P. W. A., Kennedy, T. E., Mason, K. O., et al. 2005, Space Science Reviews, 120, 95

Rossi, E., Lazzati, D., & Rees, M. J. 2002, MNRAS, 332, 945

Rossi, E. M., Lazzati, D., Salmonson, J. D., & Ghisellini, G. 2004, MNRAS, 354, 86

Röttgering, H. J. A., Braun, R., Barthel, P. D., et al. 2006, ArXiv Astrophysics e-prints 0610596

Rybicki, G. B. & Lightman, A. P. 1979, Radiative processes in astrophysics (New York, Wiley-Interscience, 1979. 393 p.)

Rykoff, E. S., Mangano, V., Yost, S. A., et al. 2006, ApJ, 638, L5

Sahu, K. C., Livio, M., Petro, L., et al. 1997, ApJ, 489, L127

Sari, R. 1999, ApJ, 524, L43

Sari, R. & Mészáros, P. 2000, ApJ, 535, L33

Sari, R., Piran, T., & Halpern, J. P. 1999, ApJ, 519, L17

Sari, R., Piran, T., & Narayan, R. 1998, ApJ, 497, L17

Sato, R., Kawai, N., Suzuki, M., et al. 2003, ApJ, 599, L9

Savage, B. D. & Mathis, J. S. 1979, ARA&A, 17, 73

Savaglio, S. & Fall, S. M. 2004, ApJ, 614, 293

Schady, P., Mason, K. O., Page, M. J., et al. 2007, MNRAS, 377, 273

Schaefer, B. E. 2005, GRB Coordinates Network, 4132

Schaefer, B. E., Gerardy, C. L., Höflich, P., et al. 2003, ApJ, 588, 387

Schlegel, D. J., Finkbeiner, D. P., & Davis, M. 1998, ApJ, 500, 525

Shen, R., Kumar, P., & Robinson, E. L. 2006, MNRAS, 371, 1441

Sheth, K., Frail, D. A., White, S., et al. 2003, ApJ, 595, L33

Skrutskie, M. F., Cutri, R. M., Stiening, R., et al. 2006, AJ, 131, 1163

Smith, I. A., Tilanus, R. P. J., Tanvir, N., et al. 2005, A&A, 439, 981

Smith, J. A., Tucker, D. L., Kent, S., et al. 2002, AJ, 123, 2121

Soderberg, A. M., Berger, E., Kasliwal, M., et al. 2006, ApJ, 650, 261

Sokolov, V. V., Kopylov, A. I., Zharikov, S. V., et al. 1998, A&A, 334, 117

Stanek, K. Z., Dai, X., Prieto, J. L., et al. 2007, ApJ, 654, L21

Stanek, K. Z., Garnavich, P. M., Jha, S., et al. 2001, ApJ, 563, 592

Stanek, K. Z., Garnavich, P. M., Kaluzny, J., Pych, W., & Thompson, I. 1999, ApJ, 522, L39

Stanek, K. Z., Matheson, T., Garnavich, P. M., et al. 2003, ApJ, 591, L17

Starling, R. L. C., van der Horst, A. J., Rol, E., et al. 2007a, ArXiv Astrophysics e-prints 0704.3718, 704

Starling, R. L. C., Wijers, R. A. M. J., Hughes, M. A., et al. 2005, MNRAS, 360, 305

Starling, R. L. C., Wijers, R. A. M. J., Wiersema, K., et al. 2007b, ApJ, 661, 787
Staveley-Smith, L., Manchester, R. N., Kesteven, M. J., Tzioumis, A. K., & Reynolds, J. E. R. 1993, Proceedings of the Astronomical Society of Australia, 10, 331
Stratta, G., Fiore, F., Antonelli, L. A., Piro, L., & De Pasquale, M. 2004, ApJ, 608, 846
Tan, G. H. 1991, in Astronomical Society of the Pacific Conference Series, Vol. 19, IAU Colloq. 131: Radio Interferometry. Theory, Techniques, and Applications, ed. T. J. Cornwell & R. A. Perley, 42–46
Tanvir, N. R., Barnard, V. E., Blain, A. W., et al. 2004, MNRAS, 352, 1073
Taylor, G. B., Frail, D. A., Berger, E., & Kulkarni, S. R. 2004, ApJ, 609, L1
Taylor, G. B., Momjian, E., Pihlström, Y., Ghosh, T., & Salter, C. 2005, ApJ, 622, 986
Thoene, C. C., Fynbo, J. P. U., Oestlin, G., et al. 2007, ArXiv Astrophysics e-prints 0703407
Thompson, C. & Duncan, R. C. 1995, MNRAS, 275, 255
Thompson, C. & Duncan, R. C. 2001, ApJ, 561, 980
Thompson, C., Duncan, R. C., Woods, P. M., et al. 2000, ApJ, 543, 340
Tiengo, A., Mereghetti, S., Ghisellini, G., Tavecchio, F., & Ghirlanda, G. 2004, A&A, 423, 861
Tody, D. 1986, in Presented at the Society of Photo-Optical Instrumentation Engineers (SPIE) Conference, Vol. 627, Instrumentation in astronomy VI; Proceedings of the Meeting, Tucson, AZ, Mar. 4-8, 1986. Part 2 (A87-36376 15-35). Bellingham, WA, Society of Photo-Optical Instrumentation Engineers, 1986, p. 733., ed. D. L. Crawford, 733
Tokunaga, A. T. & Vacca, W. D. 2005, PASP, 117, 1459
Torii, K. 2005, GRB Coordinates Network, 4130
Trentham, N., Ramirez-Ruiz, E., & Blain, A. W. 2002, MNRAS, 334, 983
Usov, V. V. 1994, MNRAS, 267, 1035
Van der Horst, A. J., Rol, E., & Wijers, R. A. M. J. 2005a, GRB Coordinates Network, 4158
Van der Horst, A. J., Rol, E., Wijers, R. A. M. J., et al. 2005b, ApJ, 634, 1166
Van Marle, A. J., Langer, N., Achterberg, A., & Garcaía-Segura, G. 2006, A&A, 460, 105
Van Paradijs, J., Groot, P. J., Galama, T., et al. 1997, Nature, 386, 686
Vanderspek, R., Crew, G., Doty, J., et al. 2003, GCN Circulars, 1997
Vanderspek, R., Sakamoto, T., Barraud, C., et al. 2004, ApJ, 617, 1251
Vasisht, G., Frail, D. A., & Kulkarni, S. R. 1995, ApJ, 440, L65
Vaughan, S., Goad, M. R., Beardmore, A. P., et al. 2006, ApJ, 638, 920

Vreeswijk, P. M., Galama, T. J., Owens, A., et al. 1999, ApJ, 523, 171
Vreeswijk, P. M., Ledoux, C., Smette, A., et al. 2007, A&A, 468, 83
Walker, M. A. 1998, MNRAS, 294, 307
Wang, X. & Loeb, A. 2000, ApJ, 535, 788
Watson, D., Hjorth, J., Fynbo, J. P. U., et al. 2007, ApJ, 660, L101
Waxman, E. & Draine, B. T. 2000, ApJ, 537, 796
Weiler, K. W., van Dyk, S. D., Sramek, R. A., & Panagia, N. 2004, New Astronomy Review, 48, 1377
White, R. L., Becker, R. H., Helfand, D. J., & Gregg, M. D. 1997, ApJ, 475, 479
Wijers, R. A. M. J. 2001, in Gamma-ray Bursts in the Afterglow Era, ed. E. Costa, F. Frontera, & J. Hjorth, 306
Wijers, R. A. M. J. & Galama, T. J. 1999, ApJ, 523, 177
Wijers, R. A. M. J., Rees, M. J., & Mészáros, P. 1997, MNRAS, 288, L51
Wilkin, F. P. 1996, ApJ, 459, L31
Willingale, R., Osborne, J. P., O'Brien, P. T., et al. 2004, MNRAS, 349, 31
Woods, P. M., Kouveliotou, C., Göğüş, E., et al. 2002, ApJ, 576, 381
Woods, P. M. & Thompson, C. 2006, Soft gamma repeaters and anomalous X-ray pulsars: magnetar candidates (Compact stellar X-ray sources), 547–586
Woosley, S. E. 1993, ApJ, 405, 273
Woosley, S. E., Heger, A., & Weaver, T. A. 2002, Reviews of Modern Physics, 74, 1015
Woźniak, P. R., Vestrand, W. T., Wren, J. A., et al. 2006, ApJ, 642, L99
Yost, S. A., Frail, D. A., Harrison, F. A., et al. 2002, ApJ, 577, 155
Yost, S. A., Harrison, F. A., Sari, R., & Frail, D. A. 2003, ApJ, 597, 459
Yost, S. A., Swan, H. F., Rykoff, E. S., et al. 2007, ApJ, 657, 925
Zeh, A., Klose, S., & Kann, D. A. 2006, ApJ, 637, 889
Zhang, B., Fan, Y. Z., Dyks, J., et al. 2006, ApJ, 642, 354
Zhang, B. & Mészáros, P. 2004, International Journal of Modern Physics A, 19, 2385
Zhang, W., Woosley, S. E., & MacFadyen, A. I. 2003, ApJ, 586, 356
Zharikov, S. V. & Sokolov, V. V. 1999, A&AS, 138, 485